Investigating Spatio-temporal Dynamics of Non-linear Dispersive Nano-plasmonics with Advanced Time-domain Simulation Methods

Fabian Renn-Giles

28th February 2016

Department of Physics, Imperial College London

A thesis submitted for the degree of Doctor of Philosophy of Imperial College London and Diploma of the Imperial College

I dedicate this doctorate thesis to my beautiful and loving wife Danica

"The little wife of my heart"

Abstract

Over the last few decades, nano-fabrication techniques have evolved to such precision that novel optical material responses can be tailor-made to challenging specifications. This development has opened a new avenue to research areas such as nano-plasmonics and metamaterials, which investigate the behaviour of light on the nano-scale and promise a range of exciting new applications. A valuable tool for a better understanding of these systems are numerical simulations. However, the correct description of the phenomena in this new regime is however challenging as it inherently involves theories of multiple length and time scales, often including non-linear phenomena. This thesis discusses several simulation techniques and investigates their suitability for describing such systems. The focus lies on the Finite-Difference-Time-Domain technique (FDTD) - a method originally developed for the study of radio and microwave electro-magnetics. Unlike frequency-domain solvers, the FDTD method can naturally describe non-linear dynamics due to its time-domain nature. However, two main challenges must be overcome to extend the FDTD method to the nano-plasmonic regime: first, an accurate time-domain description of frequency-dependent, dispersive materials such as metals must be found and second - due to its lack of adaptive meshing - the FDTD method struggles to computationally efficiently calculate systems with features over a wide range of length scales. Both challenges are discussed in detail, along with suggestions on how to overcome them. In the second part of the thesis, the FDTD method is applied to the investigate the behaviour of a non-linear, nano-plasmonic dimer system - two infinitely long and nearly touching silver nanowires, coated with an active material (such as Rh800 dye). Although there have been many studies treating the purely plasmonic system - the silver nanowires - and the non-linear system - the dye coating - individually, describing the combined system with computer simulations has been challenging due to the reasons mentioned above. This system is therefore not only physically highly relevant but also offers a benchmark for the proposed numerical methods in this thesis.

Acknowledgements

First and foremost I would like to thank my principal supervisor Prof. Dr. Ortwin Hess. Not only did he give me the opportunity to work in his research group but also guided me with his continuous support and advice. Finding a suitable research theme can be a difficult task and I, in particular, required several approaches until I finally settled with my research topic. Ortwin was tremendously patient and accommodating to my constant varying research themes in this initial time of orientation. For this I would like to thank him.

I would also like to thank my supervisor Dr. Andrew Horsfield for agreeing to supervise my work. The regular meetings with him and his other PhD students were not only a valuable source of guidance and support but also gave me an opportunity to regularly present my work. In addition to my supervisors, I would like to thank Prof. Francisco J. García Vidal for kindly accepting to assess this thesis.

I am extremely grateful to the enormous support I received by Dr. Joachim Hamm. The countless discussions and meetings with him - often several times a day - are beyond what any PhD student can expect and have helped shape the ideas that went into this thesis. In addition to his academic support, I would like to thank Joachim for all his continuous moral support and encouragement which were equally vital for the success of this thesis.

Apart from the mentors mentioned above, many have contributed in discussions and advice to particular topics covered in this thesis: I would like to thank Dr. Andreas Pusch for his helpful discussions on two- and four-level models, Dr. Sebastian Wüstner for his support in understanding many aspects of the energy dynamics involved in lossy materials and Peter Fox for the many valuable discussions on strongly-coupled systems.

I would like to extend my gratitude to all who have proof-read my thesis. In particular, I am grateful to Dr. Doris Reiter who spent a considerable amount of time proof-reading the many drafts of this thesis. Her suggestions and comments greatly improved the readability and correctness of this thesis.

I would also like to thank my family and friends who were there to assist me in the many difficult times of this thesis. In particular, I would like to thank my friends Benjamin and Gabi for their continuous support, patience and hospitality, my siblings for their constant encouragements and my parents for offering so much help and advice along the way.

However, if one person requires singling out then it has to be my lovely wife Danica: not only did she assist me with various tasks such as tirelessly proof-reading my drafts or taking over most of the house-hold chores, but also by continuously strengthening me with motivation and valuable advice. Without her constant en-

couragements and belief in my work I would have long given-up in completing this thesis. I truly cannot express in words how grateful I am for all her support and love along the way.

Declaration of Originality

I hereby declare, that, unless stated otherwise, the work contained within this thesis is my own. This thesis has not been submitted in whole or in part for any other award at this or any other university.

Declaration of Copyright

Contents

[1] The derivation of this section is largely based on the work of S. Wüstner et al. [1]

Introduction

The last two decades have seen an exponential increase in the number of publications in the field of nano-plasmonics [2], the study of nano-scale metal based optics. The sharp rise in interest in this topic can be attributed to the unusual properties of plasmonic excitations while being relatively easily accessible to experimental realisation [2, 3, 4]. For instance, the extreme light concentrating properties of surface-plasmon excitations at near singular surface geometry points result in very effective coupling between the electro-magnetic fields and nearby microscopic systems such as quantum-dots or single molecules. This phenomenon has led to prospects of exciting applications such as cost-effective, single molecule sensors or nano-cavity lasers [5, 6, 7, 8].

Computational simulations of nano-plasmonic systems are an important tool in investigating the behaviour of such systems. Simulations not only allow a researcher to scan a vast parameter space to select the most promising systems for experimental investigation but also provide a way to directly probe a wide range of observables which are difficult to access by experiment - such as local field amplitudes, confinement factors, phase factors and many more.

Unfortunately, the interesting properties often associated with nano-plasmonic systems, such as extreme field enhancement factors, make computer simulations of these systems extremely challenging. The most popular methods for simulating passive nano-plasmonic systems are frequency-domain based solvers [11] such as finite element methods (FEM) [12] or the method of moments (MoM) [13] which both employ an adaptive meshing to be able to capture the often orders of magnitude variations in length scales of geometric features found in such systems (see figure 0.0.1a). Traditional frequency-domain based methods solve the entire system for only a single frequency and therefore cannot be used, for example, to describe systems which contain materials with non-linear responses, as this generally results in the presence of electro-magnetic waves of multiple frequencies even if there is only a single excitation frequency. Important non-linear effects such as saturation effects or lasing dynamics cannot be described by these solvers which make them unsuitable for simulating the full dynamics of a wide range of nano-plasmonic devices such as nano-cavity lasers, frequency converters, optical switches and modulators and a

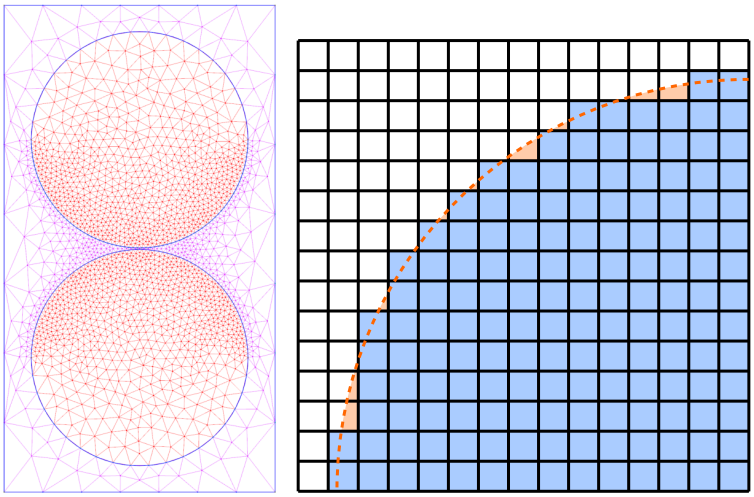

(a) (b)

Figure 0.0.1: a) Typical frequency-domain based solvers (such as COMSOL [9]) employ an adaptive meshing to capture the various length scales of geometric features often found in nano-plasmonic systems. The image shows the result of such a meshing procedure [10] on a system of two nearly touching, infinitely long wires. b) The "staircasing" effect: in the traditional FDTD method, the voxels must be completely filled with a single material (blue filling). This leads to a jagged appearance of the material boundaries.

variety of nano-sensors. As a result, the vast majority of current theoretical publications on such devices rely on analytical models to capture the non-linear behaviour of the device[2].

This thesis aims to close this gap by determining if and how the Finite-Difference-Time-Domain (FDTD) method [14, 15] can be extended to solve non-linear, nano-plasmonic systems. In contrast to the frequency-domain based methods mentioned above, the FDTD method is formulated in the time-domain. Therefore it has the advantage of the description of non-linear material responses being relatively straightforward as will be shown in this thesis. However, as the method is traditionally used to simulate systems in the microwave or radio frequency regime, its application to nano-plasmonic systems comes with its own set of challenges.

Many nano-plasmonic systems are specifically designed to measure minuscule variations in their environment such as the presence of a single molecule. Therefore it is not surprising that such systems are very sensitive to any numerical inaccuracies to the surface geometry of the material interfaces introduced by the algorithm of the simulation. Unfortunately, the traditional FDTD method requires the discretisation of space into a set of "voxels" [14], tiny cubes of equal volume, each filled with only a single material. Similar to the pixels of a low-resolution bitmap image the voxels of a low-resolution FDTD simulation will fail to capture the details of a curved surface

[2] based on an online literature review conducted by the author of the top thirty cited publications on non-linear nano-plasmonic devices according to the online Web of Science literature database

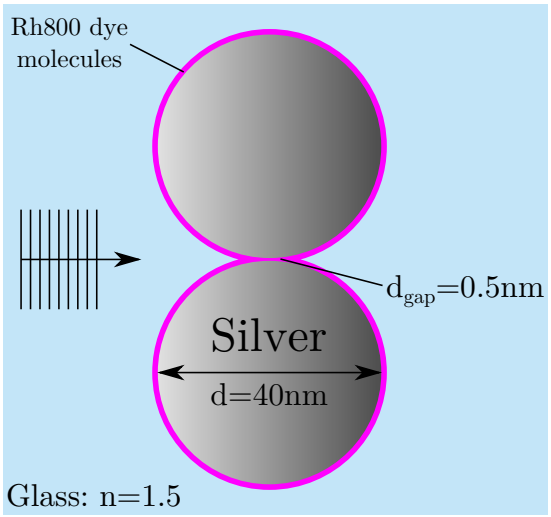

Figure 0.0.2: A sketch of a non-linear, nano-plasmonic system consisting of two infinitely long silver nanowires. The system is discussed in detail in chapter 5 of this thesis.

of a material interface (see figure 0.0.1b). Hence a computationally infeasibly high resolution is often required to accurately simulate aforementioned nano-plasmonic systems [16].

An additional challenge is the correct and computationally efficient description of materials with a dispersive and/or frequency-dependent response. As the FDTD method was traditionally developed for microwave applications, it only includes the description of perfect conductors or materials with a static dielectric response ε_∞, a good approximation for many materials in the microwave regime. In contrast to the straightforward description of dispersive, frequency-dependent materials in frequency-based solvers, a computationally efficient extension of the FDTD method to dispersive, frequency-dependent materials is surprisingly involved.

The challenges in extending the FDTD method to a broader range of applications such as nano-plasmonics is well-known and a wide variety of solutions has been suggested in the literature [15]. This thesis will review various techniques to simulate dispersive, frequency-dependent materials and place them in a single theoretical framework. Additionally, this thesis proposes new techniques to overcome some of the challenges associated with the currently available techniques to simulate such materials.

In order to validate the accuracy and viability of the various techniques, the results of the FDTD simulations are compared to the results of more proven computational methods such as commercially available frequency-domain based solvers [9]. However, in order to prove that the FDTD method can be used to investigate systems previously inaccessible to traditional frequency-domain solvers, a significant proportion of the thesis is dedicated to the investigation of a non-linear, nano-plasmonic

dimer system: a pair of nearly touching, infinitely long, silver nanowires with a coating consisting of laser dye molecules (see figure 0.0.2). Such dimer systems are currently of great interest to the nano-plasmonics community [17, 18, 19, 20, 21] as analytical calculations show that within the classical approximation electric field amplitudes can reach up to $\approx 1.5 \cdot 10^3$ of the incident field amplitude in the limit where both cylinders are infinitesimally close [17, 22]. The strong field enhancements allow for very efficient coupling between the plasmonic and gain-dye molecules and FDTD simulations in this thesis will predict phenomena often associated with strongly coupled systems such as Rabi splitting [23]. The strong field confinement factor of the system makes the computational simulation extremely demanding and, to the author's knowledge, this is the first publication to present full-vectorial, computational simulations of the complete system including the description of the coupling to a material with a non-linear response.

The thesis includes five chapters with the following content and structure. The first chapter introduces the FDTD method and begins by deriving the key equations to numerically propagate the electro-magnetic fields in time and space. Various properties of the equations are discussed along with related important concepts such as the Yee cell. As the propagation equations alone are not sufficient for any useful numerical simulation, key methods are introduced to, for example, inject incident fields into the computational domain. Additionally, methods to terminate the boundary of the computational domain are discussed, along with methods to calculate well-known quantities, such as absorption or scattering cross sections, from the numerical results of the simulation. The chapter concludes by presenting a typical FDTD simulation set-up that will be used throughout this thesis.

The second chapter is dedicated to the numerical description of *linear* materials in the context of the FDTD method. In essence, the electro-magnetic response of any material can be described by its electric or magnetic polarization functionals $\mathbf{P}[\mathbf{E}, \mathbf{H}]$, $\mathbf{M}[\mathbf{H}, \mathbf{E}]$. To be able to numerically simulate such a material, a discretised time-domain algorithm must be found to calculate these polarization functionals. The chapter begins by discussing the particularly simple case of a material which can be described by a single static dielectric permittivity ε_∞ or permeability μ_∞, as the FDTD method in its original form was limited to such simple materials only. However, as nano-plasmonic systems require the accurate description of metals by their very definition, this chapter then moves on to deriving algorithms that calculate commonly used polarization responses of metals, such as the Drude response, in the form needed by the FDTD method. It is shown that all of these algorithms can be written as linear recursive update equations, and a general relationship between any linear, recursive time-domain polarization update equation and its

frequency-dependent response is derived. After discussing the numerical stability of recursive update equations in general, a computational algorithm is presented which autonomously finds a set of coefficients for recursive update equations, which can be used to simulate the response of a given complex-valued, frequency-dependent permittivity or permeability within a given error. The chapter then concludes by generalising the discussed methods to anisotropic materials.

The third chapter extends the previous chapter's discussion to materials with non-linear responses and investigates if the FDTD method is suited to describe systems which exhibit behaviour typically associated with quantum phenomena. The chapter begins by deriving two algorithms to simulate non-linear materials: the first describes the response of a χ^3-material and the second simulates the response of a material consisting of an ensemble of two- or four-level dipole systems. The latter can be used to simulate certain types of laser dye, for example. The chapter continues by arguing that the FDTD method naturally describes certain phenomena typically associated with quantum systems. The chapter concludes by deriving a semi-classical model for Rabi splitting which not only shows that the FDTD method can naturally describe such phenomena but will also help interpret the results of numerical calculations conducted in chapter five.

The fourth chapter investigates the problem of accurately simulating curved surfaces between material interfaces. As mentioned above, the FDTD method divides space into voxels of equal volume. With the traditional FDTD method only a single material can be assigned to each voxel, leading to the jagged appearance of material interfaces in low-resolution FDTD simulations, often referred to as the "staircasing effect". Various popular methods to "smooth out" the response of such interface cells are discussed. It is shown that depending on the choice of region over which the response is smoothed, the electro-magnetic field values as integrated by the FDTD equations must be interpreted differently. However, regardless of the exact choice of smoothing region, a computationally efficient algorithm must be found, that accurately calculates the response of a smoothed-out voxel containing a material interface. Various algorithms found in the literature are discussed, along with two algorithms that were developed as part of this thesis. The chapter concludes by comparing the performance of the various methods on a particularly challenging nano-plasmonic system.

The fifth and final chapter applies the FDTD method and the various extensions discussed and derived in previous chapters to a nearly touching, infinitely long, silver nanowire system with a laser-dye coating. The chapter focuses first on the purely plasmonic system, i.e. the nanowires without any coating. It is shown that there is a symmetry in the system that results in two strong resonances with nearly identical frequencies yet significantly different spatial electric field profiles. Both resonances

exhibit high field confinement factors in the gap region between both nanowires. The chapter then turns to nanowires with a thin coating, which is modelled with the two-level system response discussed in chapter three. Due to the strong coupling between the "quantum" coating and the plasmonic nanowires, Rabi splitting can be observed along with inherently non-linear phenomena, such as saturation effects, typically associated with strongly coupled systems. Next, the two-level model is replaced with a four-level model, and it is shown that the strong field enhancements found in the system allow for an efficient "pumping"[3] of the four-level model. After the system has been inverted, an intense stimulated emission pulse can be observed on a predominantly "dark" mode.

The thesis concludes with a summary of the main results and suggestions for further research.

[3]the process of inverting a four-level system by the absorption of photons of a continuous, incident "pump" field is often referred to as "pumping"

Chapter 1

The FDTD method

This chapter describes the Finite-Difference-Time-Domain (FDTD) method [15, 14] which is an efficient numerical algorithm to simulate electro-magnetic systems in the time-domain. Originally, this method was developed to describe electromagnetic propagation in the microwave and radio frequency regime. However, due to its near perfect linear computational scaling on multi-processor systems [24, 25], the method has received much attention in the last two decades, also in the optical regime.

Strictly speaking, the FDTD method only includes the equations to propagate the electromagnetic fields. As the name of the method implies, the field propagators operate in time- and real space. The core of these field propagators is a pair of update equations which advance the current state of the electromagnetic field by one time step. Therefore, the electromagnetic fields only need to be stored in memory for all positions at the respective current time steps.

The derivation of these update equations is surprisingly simple: the derivatives in Maxwell's curl equations are discretised with difference quotients and then solved for the field value at the next time step. The resulting equations can be easily implemented computationally with a few lines of code (see appendix A.1). The simplicity of the FDTD method is certainly a major reason for its success. However, in contrast to this simplicity, difficulties arise in determining the subtle theoretical implications of this discretisation process, some of which have been fully understood only recently [26]. For example, the free-space electromagnetic Green's function of the FDTD method is a complicated function of propagation angle which is only identical to the real physical free-space Green's function in the limit where the discretisation resolution becomes infinite [15, 27]. Consequently, there are still ongoing discussions on many aspects of FDTD, such as how to interpret correctly the calculated field value at a material interface, which will be discussed in chapter 4.

Although in most textbooks on FDTD [15] the field update equations are already derived for an electro-magnetic wave propagating in a static dielectric medium, it is more effective for this thesis to separate the discussions of the field propagation

and the material response aspects. Therefore, this chapter will leave the electric and magnetic polarization responses $\mathbf{P}$, $\mathbf{M}$ unspecified. Responses for different materials and their numerical implementations will be discussed in chapters 2 and 3.

1.1 Discretised Maxwell's Equations

We begin by stating the microscopic Maxwell's Equations, where all the material specific properties are completely described by the polarisation functionals:

$$\frac{d\mathbf{E}(\mathbf{r},t)}{dt} = c\left[\nabla \times \mathbf{H}(\mathbf{r},t)\right] - \frac{d\mathbf{P}[\mathbf{E},\mathbf{H}]}{dt} \tag{1.1.1}$$

$$\frac{d\mathbf{H}(\mathbf{r},t)}{dt} = -c\left[\nabla \times \mathbf{E}(\mathbf{r},t)\right] - \frac{d\mathbf{M}[\mathbf{H},\mathbf{E}]}{dt} \tag{1.1.2}$$

$$\nabla \cdot \mathbf{E} = \rho_{const} + \rho_{micro} \tag{1.1.3}$$

$$\nabla \cdot \mathbf{H} = 0, \tag{1.1.4}$$

where c is the speed of light and $\mathbf{P}$ and $\mathbf{M}$ are the electric and magnetic polarisation field respectively. Note, that the above equations are in Lorentz-Heaviside units [28] which will be used throughout the remaining chapters of this thesis. By using these units and writing Maxwell's Equations in terms of $\mathbf{E}$ and $\mathbf{H}$, the above equations become more symmetric and this convention is used throughout FDTD literature.

Further, the above equations account for the possibility of a magnetic material response $\mathbf{M} \neq 0$ which can often be neglected in real systems. For brevity, it will sometimes be beneficial to drop the magnetic material response. This simplifies the equations and most derivations can easily be extended to $\mathbf{M} \neq 0$ by treating the magnetic polarisation field $\mathbf{M}$ in an analogous manner as the electric polarisation field $\mathbf{P}$.

Furthermore, it should be noted that we have not divided the above charges into "free" and "microscopic" or "bound" charges as is often done with Maxwell's equations (see for example [29]). Here, $\rho_{constant}$ is referring to charges which are constant in time. All other charges ρ_{micro} must be completely described by the polarisation functional, i.e. $\rho_{micro} = -\nabla \cdot \mathbf{P}$.

It is evident that the coupling to any material is included via the polarisation functionals $\mathbf{P}[\mathbf{E},\mathbf{H}]$, $\mathbf{M}[\mathbf{H},\mathbf{E}]$ which will not be specified further in this chapter. Note, however, that in general these functionals can be non-linear, non-local and non-instantaneous. Depending on the material, the calculation of the polarisation functionals may require a complex numerical algorithm on its own. For the remainder of this chapter, however, we shall not be interested in the exact material system and only focus on finding an efficient algorithm to evolve the electromagnetic fields.

The implementation of different material models, both quantum-mechanical and classical, will be discussed in chapters 2 and 3.

1.1.1 The discretised curl equations

It is beneficial to begin by discretising the curl equations (equation 1.1.1 and 1.1.2) and ignore Gauss's Law (equation 1.1.3 and 1.1.4) for the time being. It will be shown that Gauss's Law imposes certain constraints for the initial condition and the functionals $\mathbf{P}[\mathbf{E}, \mathbf{H}]$ and $\mathbf{M}[\mathbf{H}, \mathbf{E}]$.

For simplicity, Maxwell's equations are stated here for a system with a 1-D geometry, i.e. the polaration functionals only depend on the x coordinate - the method can easily be extended to higher dimensions and this will be shown later. Furthermore, the system is excited in such a way that only the field components E_y and H_z are non-zero. For such a system, Ampère's Law is

$$\frac{dE_y(\mathbf{r},t)}{dt} = -c \cdot \frac{\partial H_z(\mathbf{r},t)}{\partial x} - \frac{dP_y(\mathbf{r},t)}{dt}. \tag{1.1.5}$$

If space and time is evenly divided into voxels and time steps of width Δx,Δt respectively, then the above equation reads:

$$\left.\frac{dE_y}{dt}\right|_{t=n\cdot\Delta t, x=k\cdot\Delta x} = -c \cdot \left.\frac{\partial H_z}{\partial x}\right|_{t=n\cdot\Delta t, x=k\cdot\Delta x} - \left.\frac{dP_y}{dt}\right|_{x=k\cdot\Delta x, t=n\cdot\Delta t}, \tag{1.1.6}$$

where k refers to the k-th voxel and n refers to the n-th time step. It is further possible to approximate all derivatives in the above equation with different quotients - for example with a forward difference quotient:

$$\left.\frac{df}{dx}\right|_{x=k\cdot\Delta x} \approx \frac{f((k+1)\cdot\Delta x) - f(k\cdot\Delta x)}{\Delta x}. \tag{1.1.7}$$

Doing this for both temporal and spatial derivatives in Ampère's Law (equation 1.1.1) leads to:

$$\frac{E_y|_k^{n+1} - E_y|_k^n}{\Delta t} = c \cdot \frac{H_z|_k^n - H_z|_{k+1}^n}{\Delta x} - \frac{P_y|_k^{n+1} - P_y|_k^n}{\Delta t}, \tag{1.1.8}$$

where we have additionally adopted a new notation which is commonly used throughout FDTD literature [15]:

$$f|_k^n := f(k\cdot\Delta x, n\cdot\Delta t). \tag{1.1.9}$$

Solving the above discretised equation for $E_y|_k^{n+1}$ leads to

$$E_y|_k^{n+1} = E_y|_k^n + c \cdot \frac{\Delta t}{\Delta x} \left(H_z|_k^n - H_z|_{k+1}^n \right) - P_y|_k^{n+1} + P_y|_k^n \,. \tag{1.1.10}$$

The above equation is an update equation in time, for example, given E_y, H_z and P_y at an earlier time step we can now advance the electric field by one time step. Currently irritating is the fact that the RHS of the above equation depends on the polarisation P_y at time step $n+1$, i.e. the polarisation at the next time step. In chapter 2, however, it will be shown that this will only require special attention for some material models.

A similar discretisation can be done with Faraday's Law (equation 1.1.2):

$$H_z|_k^{n+1} = H_z|_k^n - c \cdot \frac{\Delta t}{\Delta x} \left(E_y|_{k+1}^{n+1} - E_y|_k^{n+1} \right), \tag{1.1.11}$$

where any magnetic polarisation fields were neglected and a backward difference quotient for the time derivative was used. It will later be shown that both the forward and backward difference quotients are associated with large errors and a formulation based on central differences will be preferred. However, equations 1.1.10 and 1.1.11 together with a currently unspecified update equation for the polarisation functional $P_y|^{n+1} = P_y|^n + ...$ are nevertheless sufficient for an iterative electromagnetic solver in real-space and time-domain: the solver starts with an initial solution for the fields $H|_k^n$, $E|_k^n$ for all k at time step n. With equation 1.1.10, the field $E|_k^n \rightarrow E_k^{n+1}$ can be advanced for all k, after which the magnetic field $H_k^n \rightarrow H_k^{n+1}$ can be advanced for all k. This can be repeated until the duration of the simulation has been reached. This update loop is depicted schematically in figure 1.1.1.

Until now, Gauss's Law in Maxwell's Equations (equation 1.1.3 and 1.1.4) has been neglected. However, Gauss's Law is automatically fulfilled as long as the following constraint for the initial conditions are observed:

$$\nabla \cdot \mathbf{E}\left(\mathbf{r}, t = 0\right) = \rho_{const} \tag{1.1.12}$$

$$\nabla \cdot \mathbf{H}\left(\mathbf{r}, t = 0\right) = 0. \tag{1.1.13}$$

This can be shown by taking the time derivative of the LHS of Gauss's Law and using Ampère's Law:

$$\frac{d}{dt}\left(\nabla \cdot \mathbf{E}\right) = \nabla \cdot \frac{d\mathbf{E}}{dt} = \nabla \cdot \nabla \times \mathbf{H} - \nabla \cdot \mathbf{J} = -\nabla \cdot \mathbf{J} = \frac{d\rho_{micro}}{dt}. \tag{1.1.14}$$

Note that the above equation hasn't used Gauss's Law (equation 1.1.3) - it simply

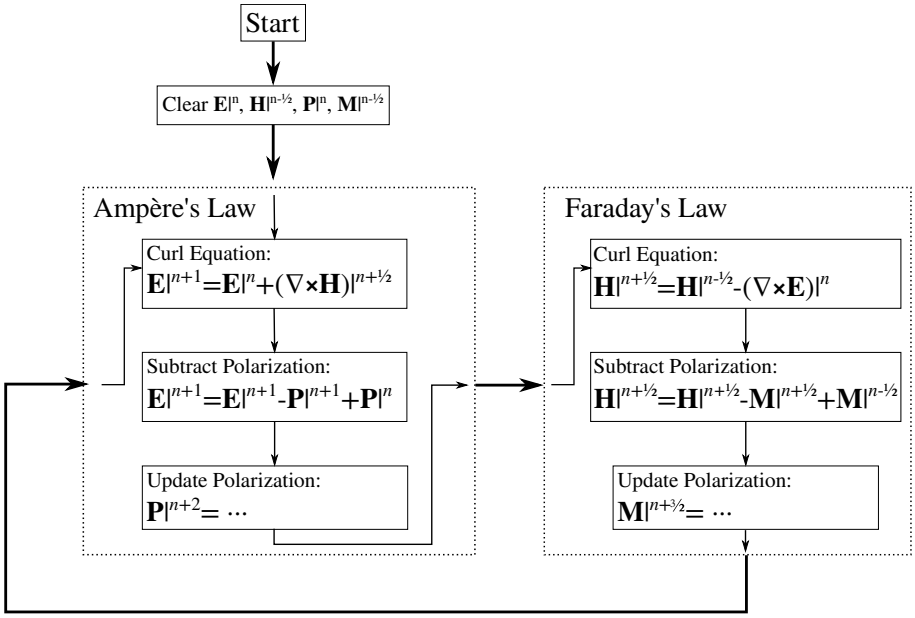

Figure 1.1.1: A schematic of the FDTD update loop: the algorithm alternates between updating the electric field (Ampère's Law) and the magnetic field (Faraday's Law). The update equations for the electric and magnetic polarization are not specified and is the subject of chapter 2.

transformed the LHS of Gauss's Law and used the definition of ρ_{micro}. Integrating the above equation, however, recovers Gauss's Law by equating the integration constant with ρ_{const}:

$$\nabla \cdot \mathbf{E} = \rho_{const} + \rho_{micro}. \tag{1.1.15}$$

The same is also valid for the magnetic field $\mathbf{H}$.

1.1.2 Discretisation Error

It can easily be shown that the above discretisation leads to undesirable large errors. This is due to the forward and backward difference quotient being only first order accurate:

$$\frac{f|_{k+1} - f|_k}{\Delta x} = \frac{1}{\Delta x}\left[\left(f|_k + \partial_x f|_k \cdot \Delta x + \mathcal{O}\left(\Delta x^2\right)\right) - f|_k\right] = \partial_x f|_k + \mathcal{O}\left(\Delta x\right), \tag{1.1.16}$$

where a Taylor expansion of the field f was used. The same is true for a backward difference quotient. However, a central difference quotient results in a second order accurate approximation:

$$\begin{aligned} \frac{f|_{k+\frac{1}{2}} - f|_{k-\frac{1}{2}}}{\Delta x} &= \frac{1}{\Delta x}\left[\left(f|_k + \frac{1}{2}\,\partial_x f|_k \cdot \Delta x + \frac{1}{4}\,\partial_x^2 f|_k \cdot \Delta x^2 + \mathcal{O}\left(\Delta x^3\right)\right)\right. \\ &- \left.\left(f|_k - \frac{1}{2}\,\partial_x f|_k \cdot \Delta x + \frac{1}{4}\,\partial_x^2 f|_k \cdot \Delta x^2 + \mathcal{O}\left(\Delta x^3\right)\right)\right] \\ &= \partial_x f|_k + \mathcal{O}\left(\Delta x^2\right). \end{aligned} \tag{1.1.17}$$

Unfortunately, simply replacing the forward and backward difference quotients in equations 1.1.10 and 1.1.11 leads to uncoupled equations:

$$E_y|_k^{n+\frac{1}{2}} = E_y|_k^{n-\frac{1}{2}} + c \cdot \frac{\Delta t}{\Delta x}\left(H_z|_{k-\frac{1}{2}}^n - H_z|_{k+\frac{1}{2}}^n\right) - P_y|_k^{n+\frac{1}{2}} + P_y|_k^{n-\frac{1}{2}} \tag{1.1.18}$$

$$H_z|_k^{n+\frac{1}{2}} = H_z|_k^{n-\frac{1}{2}} - c \cdot \frac{\Delta t}{\Delta x}\left(E_y|_{k+\frac{1}{2}}^n - E_y|_{k-\frac{1}{2}}^n\right). \tag{1.1.19}$$

This is because Ampère's Law in the above equation calculates the electric field at positions and time steps k and $n + 1/2$. Yet, Faraday's Law requires the electric field at positions and time steps $k + 1/2$ and n. The solution is to shift Ampère's and Faraday's Law by a half time step and voxel width:

$$E_y|_k^{n+1} = E_y|_k^n + c \cdot \frac{\Delta t}{\Delta x}\left(H_z|_{k-\frac{1}{2}}^{n+\frac{1}{2}} - H_z|_{k+\frac{1}{2}}^{n+\frac{1}{2}}\right) - P_y|_k^{n+1} + P_y|_k^n \tag{1.1.20}$$

$$H_z|_{k-\frac{1}{2}}^{n+\frac{1}{2}} = H_z|_{k-\frac{1}{2}}^{n-\frac{1}{2}} - c \cdot \frac{\Delta t}{\Delta x}\left(E_y|_k^n - E_y|_{k-1}^n\right) \tag{1.1.21}$$

This so-called co-location of the field components in time and space results in the desired second order accurate numerical scheme. Although not apparent in the simple form above, the co-location will result in an increased complexity not only when modelling sources, materials and boundary conditions, but also in the implementation of diagnostic and post-processing algorithms.

1.1.3 The Yee cell

The spatial and temporal positions of the electric and magnetic field components become more involved when extending the above equations to geometries with higher dimensions. For example, the co-location of the update equations 1.1.20 and 1.1.21 in the 2-D trans-magnetic case leads to:

$$E_x|_{j,k-\frac{1}{2}}^{n+1} = E_x|_{j,k-\frac{1}{2}}^n + c \cdot \frac{\Delta t}{\Delta y}\left(H_z|_{j+\frac{1}{2},k-\frac{1}{2}}^{n+\frac{1}{2}} - H_z|_{j-\frac{1}{2},k-\frac{1}{2}}^{n+\frac{1}{2}}\right) - P_x|_{j,k-\frac{1}{2}}^{n+1} + P_x|_{j,k-\frac{1}{2}}^n \tag{1.1.22}$$

$$E_y|_{j+\frac{1}{2},k}^{n+1} = E_y|_{j+\frac{1}{2},k}^n + c \cdot \frac{\Delta t}{\Delta x}\left(H_z|_{j+\frac{1}{2},k-\frac{1}{2}}^{n+\frac{1}{2}} - H_z|_{j+\frac{1}{2},k+\frac{1}{2}}^{n+\frac{1}{2}}\right) - P_y|_{j+\frac{1}{2},k}^{n+1} + P_y|_{j+\frac{1}{2},k}^n \tag{1.1.23}$$

$$\begin{aligned} H_z|_{j+\frac{1}{2},k-\frac{1}{2}}^{n+\frac{1}{2}} = H_z|_{j+\frac{1}{2},k-\frac{1}{2}}^{n-\frac{1}{2}} \quad &+ \quad c \cdot \tfrac{\Delta t}{\Delta y}\left(E_x|_{j+1,k-\frac{1}{2}}^n - E_x|_{j,k-\frac{1}{2}}^n\right) \\ &+ \quad c \cdot \tfrac{\Delta t}{\Delta x}\left(E_y|_{j+\frac{1}{2},k-1}^n - E_y|_{j+\frac{1}{2},k}^n\right) \end{aligned}. \tag{1.1.24}$$

The positions of the different field components in the above 2-D equations are depicted in figure 1.1.2a. Obviously, the 3-D update equations become yet more complex (see figure 1.1.2b) and we refrain from listing them here. The depicted cells in figure 1.1.2 are commonly referred to as the "Yee cell" after the inventor of the

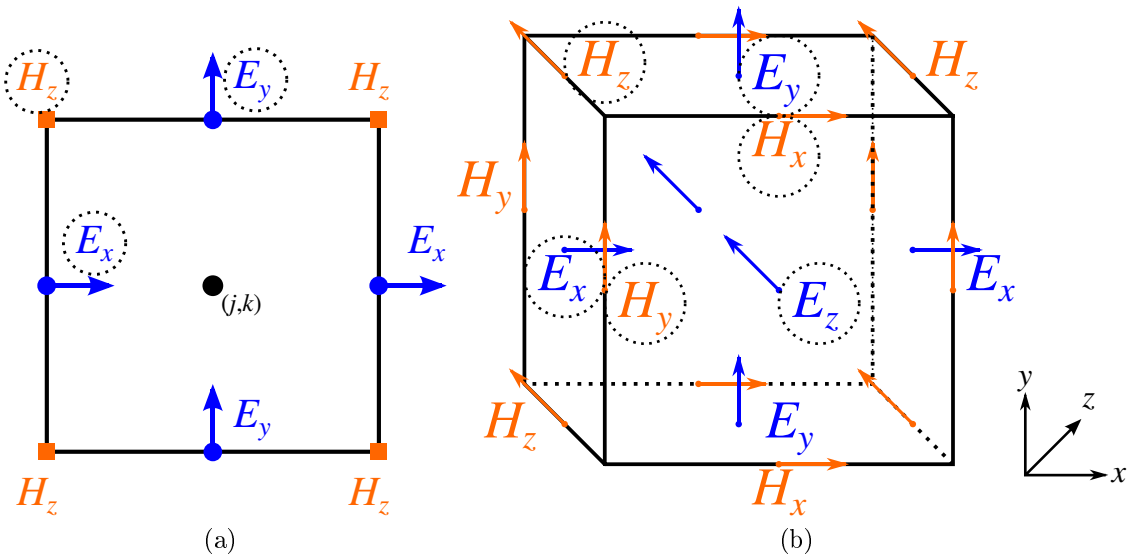

Figure 1.1.2: The unique Yee cell arrangement of the electric- and magnetic field components in a 2D (a) and 3D (b) FDTD simulation. The field components which are stored at the ijk-th memory location are encircled. All other components are stored at other memory locations as they can be associated with neighbouring Yee cells.

FDTD method Kane Yee [14]. It is this unique arrangement of the Yee cell that allows a second order accurate integration scheme.

Some of the properties of the Yee cell shall be noted here. First of all, in the 2-D or 3-D case, not only are the fields co-located but also the individual components of each field. In fact, no two field components either electric or magnetic are located at the same position in space. The unique spatial arrangement can also be derived from the integral form of Maxwell's equations, for example, Faraday's Law relates the magnetic field to an integration over a closed loop of the electric field. In fact, it will be shown in chapter 4 that deriving FDTD from the integral form of Maxwell's equations provides further insight into the numerical characteristics of the FDTD method.

Another convention within the Yee arrangement used in this thesis is that the position i, j, k is put at the centre of the i, j, k-th Yee cell (or voxel) where in fact no field component is located. This leads to more symmetric update equations regarding the indices of the field components, as any other choice would coincide with a single field component and thus distinguish this field component from all of the others. Unfortunately, this is at odds with text-book literature on FDTD [15] where the i, j, k position coincides with the E_x component.

1.1.4 Computational implementation

Although the interleaved evaluation of the above electric and magnetic update equations fully specifies the numerical algorithm for propagating the electromagnetic fields, there are some further considerations and useful properties regarding the computational implementation of the scheme. First of all, it should be noted that when embarking on a computational implementation, one must further select which field components *belong* to the i, j, k-th Yee cell, for example, it can easily be seen in figure 1.1.2a that both $E_x|_{j,k-1/2}$ and $E_x|_{j,k+1/2}$ lie on the edge of the j, k-th Yee cell. However, in a computational implementation the E_x must be stored in a 2-D array which is accessed with integers j, k. Therefore an implementation must specify which field of the two components is associated with the j, k-th array entry. The convention used in this thesis is shown in figure 1.1.2 by encircling field components that "belong" to the depicted Yee cell.

Secondly, as the electric and magnetic update equations are evaluated in turn, each location of either field can be updated completely independent from each other. For example, the magnetic field update equation only depends on electric field components (which already have been calculated everywhere in space in the previous half time step) or on the magnetic field component at the same location. Therefore, every magnetic field voxel can be calculated in parallel allowing a massively parallel execution of the update equations. The same is true for the electric field voxels. Furthermore, the relative simplicity of the update equations, i.e. only additive terms and multiplication with constant factors, allows for execution on GPU processing units [25, 30, 31, 32] which are specialised in massively parallel execution of simple equations on large sets of voxels [33]. This property has contributed to the recent rise in popularity of the FDTD method.

1.1.5 Notation conventions

Due to the Yee cell arrangement, the exact form of a single update equation will depend both on the number of dimensions of the geometry of the system and on the particular field component in question. This makes the discussion of general properties of the update equations cumbersome. To overcome this, the following general notation for the update equations can be found

$$\mathbf{E}|^{n+1} = \mathbf{E}|^{n} + (\nabla \times \mathbf{H})|^{n+\frac{1}{2}} - \mathbf{P}|^{n+1} + \mathbf{P}|^{n} \tag{1.1.25}$$

$$\mathbf{H}|^{n+\frac{1}{2}} = \mathbf{H}|^{n-\frac{1}{2}} - (\nabla \times \mathbf{E})|^{n} - \mathbf{M}|^{n+\frac{1}{2}} + \mathbf{M}|^{n-\frac{1}{2}}\,, \tag{1.1.26}$$

by introducing the short notation $(\nabla \times \mathbf{H})|^{n+\frac{1}{2}}$ and $(\nabla \times \mathbf{E})|^{n}$ for the curl part of the update equations. Although, this notation is convenient, in some cases, it can

be misleading. For example, consider the following equation

$$\mathbf{P}|^n = \chi\, \mathbf{E}|^n\,, \tag{1.1.27}$$

where it may seem as if there is a single scalar χ for all x, y and z components. However, if χ has a spatial dependency, then, due to the co-location of the electric field components, every field component will be multiplied with a different value of χ.

1.1.6 Dispersion relation and numerical stability of the FDTD update equations

Although the general convergence behaviour has been shown in section 1.1.2, the conditions under which the scheme is numerically stable has yet to be shown. A common tool to investigate the behaviour of discretised systems is the z-transform [34]. As the general 3-D update equations are lengthy and complex, the numerical stability criteria will first be derived for a 1-D system and then extended to higher dimensions.

The update equation of the electric and magnetic fields of a system with a 1-D geometry excited with a trans-magnetic (TM) plane-wave are as follows

$$\begin{aligned} E_y|_k^{n+1} &= E_y|_k^n + c\tfrac{\Delta t}{\Delta x}\left(H_z|_{k-\frac{1}{2}}^{n+\frac{1}{2}} - H_z|_{k+\frac{1}{2}}^{n+\frac{1}{2}}\right) \\ H_z|_{k-\frac{1}{2}}^{n+\frac{1}{2}} &= H_z|_{k-\frac{1}{2}}^{n-\frac{1}{2}} - c\tfrac{\Delta t}{\Delta x}\left(E_y|_k^n - E_y|_{k-1}^n\right). \end{aligned}$$

By substituting the latter equation into the former, the discretised version of Helmholtz's Equation is found

$$E_y|_k^{n+1} - 2\,E_y|_k^n + E_y|_k^{n-1} = c^2\frac{\Delta t^2}{\Delta x^2}\left(E_y|_{k+1}^n - 2\,E_y|_k^n + E_y|_{k-1}^n\right).$$

The definition of the 2-D z-transform is

$$\tilde{F}\left(z,\eta_x\right) = \sum_{n,k=0}^{\infty} F|_k^n\, z^{-n}\eta_x^{-k},$$

where $F|_k^n$ stands for any field component and $\tilde{F}\left(z,\eta_x\right)$ is the 2-D z-transform of $F|_k^n$. The 2-D z-transform is identical to a 2-D Discrete-Time-Fourier-Transform (DTFT) with the following substitutions

$$z \;\rightarrow\; \exp\left(i\omega\Delta t\right) \tag{1.1.28}$$

$$\eta_x \;\rightarrow\; \exp\left(ik_x\Delta x\right). \tag{1.1.29}$$

An important property of the z-transform (or DTFT) which will be useful to find the z-transform of the discretised Helmholtz Equation is the following [35]

$$\mathcal{Z}\left[F|_{k+j}^{n+m}\right] = \tilde{F}\left(z,\eta_x\right) z^{-m}\eta_x^{-j},$$

where $\mathcal{Z}\left[F|_k^n\right]$ denotes the z-transform of $F|_k^n$ and n, j are integers. With this property, the 2-D z-transform can be applied to both sides of the discretised Helmholtz Equation and after dividing both sides by $\tilde{E}_y\left(z,\eta_x\right)$ one obtains

$$\left(z^{-1}-2+z\right) = c^2\frac{\Delta t^2}{\Delta x^2}\left(\eta_x^{-1}-2+\eta_x\right)$$

or

$$\left(z^{-\frac{1}{2}}-z^{\frac{1}{2}}\right)^2 = c^2\frac{\Delta t^2}{\Delta x^2}\left(\eta_x^{-\frac{1}{2}}-\eta_x^{\frac{1}{2}}\right)^2$$

and by using the substitutions 1.1.28 and 1.1.29

$$\sin^2\left(\frac{1}{2}\omega\Delta t\right) = \pm c^2\frac{\Delta t^2}{\Delta x^2}\sin^2\left(\frac{1}{2}k_x\Delta x\right). \tag{1.1.30}$$

The above equation can be solved for ω by requiring the following criteria

$$\Delta x = c\Delta t;\ -\pi \leq \omega\Delta t \leq \pi,$$

known as the 1-D Courant condition of the FDTD equations [15, 36, 37]. By substituting this into equation 1.1.30, the numerical dispersion relation for the 1-D FDTD update equations is found

$$\omega = c\left|k_x\right|,$$

which is identical to the physical dispersion relation of a plane-wave for any choice of Δt, Δx as long as they fulfil the Courant condition. Unfortunately, this is only true for the 1-D case which will be shown now.

The 4-D z-transform of the 3-D discretised Helmholtz Equation is

$$\begin{aligned}\tfrac{1}{c^2\Delta t^2}\left(z^{-1}-2+z\right) = \tfrac{1}{\Delta x^2}\left(\eta_x^{-1}-2+\eta_x\right) &+ \tfrac{1}{\Delta y^2}\left(\eta_y^{-1}-2+\eta_y\right)\\ &+ \tfrac{1}{\Delta z^2}\left(\eta_z^{-1}-2+\eta_z\right)\end{aligned}$$

and after applying the same algebra as was done in the 1-D case, the numerical dispersion relation for the 3-D FDTD update equations is found [27, 15]:

$$\omega = \frac{2\arcsin\left(c\Delta t\sqrt{\tfrac{1}{\Delta x^2}\sin^2\left(\tfrac{1}{2}k_x\Delta x\right)+\tfrac{1}{\Delta y^2}\sin^2\left(\tfrac{1}{2}k_y\Delta y\right)+\tfrac{1}{\Delta z^2}\sin^2\left(\tfrac{1}{2}k_z\Delta z\right)}\right)}{\Delta t}. \tag{1.1.31}$$

To achieve numerical stability, ω must be remain real-valued, as otherwise $E|^n \propto$

$\exp(in\omega\Delta t)$ could grow exponentially. This is the case as long as the absolute value of the argument of the arcsin function remains smaller than one:

$$c\Delta t\sqrt{\frac{1}{\Delta x^2}\sin^2\left(\frac{1}{2}k_x\Delta x\right)+\frac{1}{\Delta y^2}\sin^2\left(\frac{1}{2}k_y\Delta y\right)+\frac{1}{\Delta z^2}\sin^2\left(\frac{1}{2}k_z\Delta z\right)}\leq 1.$$

Numerical inaccuracies, such as floating-point round-off errors, will result in the presence of plane-waves with frequencies unrelated to any of the source excitations. Therefore the above inequality must also be valid for any frequency or wavelength. The LHS has it's maximum for $k_x^{max}=k_y^{max}=k_z^{max}=\pi/\Delta x$. Inserting this into the above inequality results in the FDTD Courant condition gives

$$c\Delta t\sqrt{\frac{1}{\Delta x^2}+\frac{1}{\Delta y^2}+\frac{1}{\Delta z^2}}\leq 1. \tag{1.1.32}$$

Often, the FDTD grid is cubic ($\Delta x=\Delta y=\Delta z$) and the above criteria can be written as

$$\Delta t\leq\frac{1}{c}\frac{\Delta x}{\sqrt{d}},$$

where d is the number of dimensions of the simulation. In practice, Δt is never chosen to be exactly equal to the RHS of the above equations, as numerical inaccuracies may still render the equations unstable. The following upper-limit has been established from practical experience when solving the FDTD equations with double-precision floating point numbers:

$$\Delta t\leq 0.98\frac{1}{c}\frac{\Delta x}{\sqrt{d}}.$$

It can easily be verified that the expression for the numerical dispersion relation converges towards the physical dispersion relation for $\Delta t,\Delta x,\Delta y,\Delta z\to 0$ as long as the Courant condition is fulfilled. Nevertheless, the exact expression for the numerical dispersion relation remains important to correctly simulate sources (see, for example, section 1.2.3) and boundary conditions.

Obviously, to achieve the maximum computational efficiency, it is beneficial to choose Δt and Δx as large as possible while still being able to resolve the incident excitation and the geometry of the materials. In nano-plasmonics, the structures are commonly much smaller than the excitation wavelength (sub-wavelength regime) and therefore, in this regime, Δx is limited by the geometry, which in turn limits Δt via the Courant condition. Therefore, the computational complexity of the FDTD algorithm in this regime is given by

$$\mathcal{O}\left(L^{d+1}\right),$$

where L is the sidelength of the computational domain in pixels and d is the number of dimensions of the simulation. This means, for example, that the computational processing time increases sixteen times if the resolution of a 3-D simulation is doubled.

1.2 Sources

This section discusses the methods commonly used within FDTD to inject an electromagnetic field into the computational simulation domain. A variety of source injection methods exist for the different types of desired numerical experiments and only the most common techniques and their applications will be discussed here.

1.2.1 Time-evolution of sources

Depending on the nature of the numerical experiment, different wave-forms of the injection amplitude are required. For example, to measure scattering or absorption cross-sections over a wide frequency range, it is convenient to inject a narrow pulse in time-domain. On the other hand, pump-probe experiments (see section 1.5.3) rely on the injection of a monochromatic wave in the pump phase.

Irrespective of the type of source, the initial field conditions must fulfil Gauss's Law (equation 1.1.12 and 1.1.13) which may require the knowledge of the solution for the particular injection waveform (for example, if a monochromatic wave is injected, then the initial total electromagnetic fields must already solve Maxwell's equations for an incident monochromatic field). To avoid this, the initial electromagnetic field will be zero everywhere ($\mathbf{E} = \mathbf{H} = 0$) and all sources will be "switched off" at the beginning of the simulation. This setup will always fulfil Gauss's Law for the initial conditions (equation 1.1.12 and 1.1.13). Only then will the energy injected by the sources be "ramped up". The ramp-up phase must be sufficiently slow so that the desired spectral width is achieved.

For these reasons, all injection techniques share a common set of parameters to specify the injection waveform. Typically, a monochromatic wave is modulated with a pulse waveform that consists of an attack, sustain and decay phase. A typical excitation waveform is depicted in figure 1.2.1. The attack and decay phase

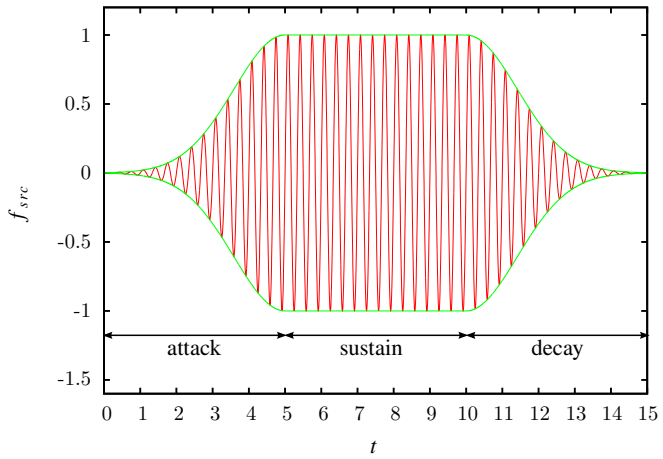

Figure 1.2.1: The amplitude f_{src} of a typical incident wave-form as given by equation 1.2.1 (red) with $t_{attack} = 1$, $\sigma_{attack} = 1$, $t_{sustain} = 5$, $t_{decay} = 1$, $\sigma_{decay} = 1$ and $t_{offset} = 4$. The modulation wave-form is shown in green.

are modelled with a Gaussian pulse and the complete waveform can be given by:

$$\begin{aligned} f_{src}(t) := \quad & \Big[\quad \Theta\left(t_{attack} - t + t_{offset}\right) \cdot \exp\left(-\left(\tfrac{t - t_{offset} - t_{attack}}{2\sigma_{attack}}\right)^2\right) \\ & + \quad \Theta\left(t - t_{ofsset} - t_{attack}\right) \Theta\left(t_{attack} + t_{sustain} - t + t_{offset}\right) \\ & + \quad \Theta\left(t - t_{offset} - \left(t_{attack} + t_{sustain}\right)\right) \cdot \exp\left(-\left(\tfrac{t - t_{offset} - t_{attack} - t_{sustain}}{2\sigma_{decay}}\right)^2\right)\Big] \\ & \cdot \quad f_{amp} \sin\left(\omega_0 \cdot \left(t - t_{offset}\right)\right), \end{aligned} \tag{1.2.1}$$

where $\Theta(t)$ is the Heaviside function.

1.2.2 Dipole Sources

The easiest injection source from an implementation standpoint is the injection of an electromagnetic wave from a single infinitesimally small dipole source. This injection is commonly referred to as a "Hard Dipole Source" and is sketched in figure 1.2.2a. The polarisation current of such a dipole located at position $\mathbf{r}_0$ and oriented along the unit vector $\mathbf{e}_{dipole}$ is simply given by:

$$\mathbf{P}(\mathbf{r}, t) = \delta^3(\mathbf{r} - \mathbf{r}_0) \cdot \mathbf{e}_{dipole} \cdot f_{src}(t). \tag{1.2.2}$$

The above dipole current is injected into the electromagnetic fields via the polarisation current in the update equations 1.1.22 and 1.1.23. Strictly, $\mathbf{r}_0$ and $\mathbf{e}_{dipole}$ must exactly coincide with the position and orientation of one of the electric field components in the Yee cell. If this is not the case then the polarisation current must be interpolated appropriately over several electric field components in the Yee cell.

A line of these dipoles is sometimes referred to as a "Hard Side Source". This

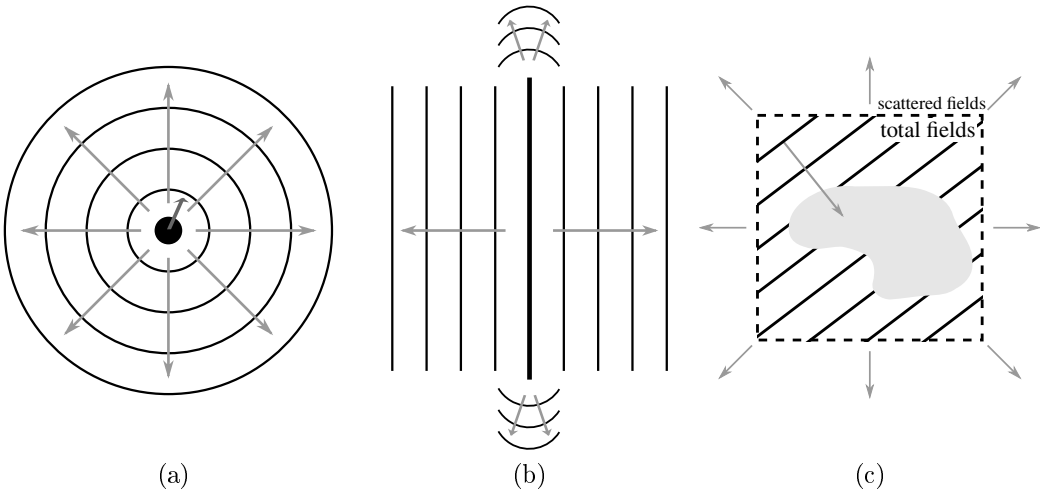

Figure 1.2.2: Sketches of the most common incident field injection methods used in FDTD simulations. (a) The hard dipole source emits radiation in all directions (b) The hard side source is a line of dipoles which injects waves travelling in all directions perpendicular to the dipole line. Some energy also travels in other directions due to the finite length of the dipole line. (c) A total-field-scattered-field box (TFSF) can be used to inject any analytically given incident field. Inside the TFSF box (dotted), the FDTD algorithm integrates the total electro-magnetic fields. The incident field is subtracted at the boundary of the TFSF box with only the scattered fields remaining outside.

method is often used to simulate a plane-wave or pulse excitation (the excitation comes from the "side") and is depicted in figure 1.2.2b. Obviously, the dipoles will radiate symmetrically along their orientation axes and therefore this source will emit two plane-waves in opposite direction. To avoid this, the line of dipoles can be placed along one of the edges of the computational region which is terminated by a perfect electric conductor boundary (see section 1.3.1) acting as a perfect mirror. However, this will also reflect any scattered waves travelling in the direction of the source. Therefore, this source type is often used in wave-guide simulations where there is little or no backscattering of the incident wave. Additionally, the finite length of the dipole line will diminish the quality of the plane-wave.

1.2.3 Total-Field-Scattered-Field Box

The Total-Field-Scattered-Field (TFSF) box is the most common injection source used in the FDTD method and does not suffer from the limitations described above. It can be used to inject a wide variety of incident electromagnetic fields E_{inc}, H_{inc}. It uses the fact that both the scattered electromagnetic fields $\mathbf{E}_{scat}$, $\mathbf{H}_{scat}$ as well as the total electromagnetic fields $\mathbf{E}_{tot} = \mathbf{E}_{inc} + \mathbf{E}_{scat}$, $\mathbf{H}_{tot} = \mathbf{H}_{inc} + \mathbf{H}_{scat}$ solve Maxwell's equations individually. Therefore, the computational domain can be divided into a region where only the total fields and a region where only the scattered fields

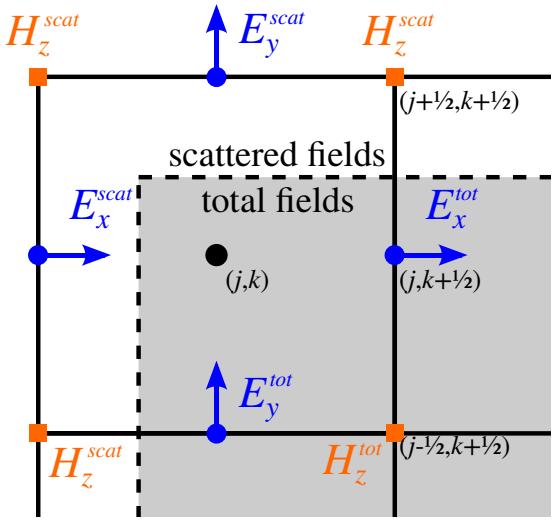

Figure 1.2.3: The top-left corner of a 2-D TFSF-box (grey box). The displayed Yee cells have electro-magnetic field components both inside and outside the TFSF box.

are solved. This is sketched in figure 1.2.2c. The analytically calculated incident electromagnetic field E_{inc}, H_{inc} is added or subtracted accordingly at the boundary of the total field region. This total field region is referred to as the Total-Field-Scattered-Field (TFSF) box.

The top-left corner of a TFSF-box in 2-D TM setup is shown in figure 1.2.3. As indicated in this figure, due to the unique Yee cell arrangement, some field components will be outside and some field components will be inside of the TFSF-box region. Therefore, at the boundary of the TFSF-box the incident field must be added or subtracted accordingly. For example, the $E_x|_{j,k+1/2}$ component at the right edge of the shown Yee cell is inside the total field region. Therefore, the RHS of its update equation must also only include total field quantities:

$$E_x^{tot}\big|_{j,k+\frac{1}{2}}^{n+1} = E_x^{tot}\big|_{j,k+\frac{1}{2}}^{n} + c \cdot \frac{\Delta t}{\Delta y}\left[H_z^{tot}\big|_{j+\frac{1}{2},k+\frac{1}{2}}^{n+\frac{1}{2}} - H_z^{tot}\big|_{j-\frac{1}{2},k+\frac{1}{2}}^{n+\frac{1}{2}}\right]. \tag{1.2.3}$$

Although this is correct, the field component $H_z^{tot}|_{j+\frac{1}{2},k+\frac{1}{2}}$ is not readily available as this lies outside the total field region where only H^{scat} is available as can be seen in figure 1.2.3. However, we can easily calculate the total field by adding the analytically calculated incident field to the scattered field at this location:

$$E_x^{tot}\big|_{j,k+\frac{1}{2}}^{n+1} = E_x^{tot}\big|_{j,k+\frac{1}{2}}^{n} + c \cdot \frac{\Delta t}{\Delta y}\left[\left(H_z^{scat}\big|_{j+\frac{1}{2},k+\frac{1}{2}}^{n+\frac{1}{2}} + H_z^{inc}\big|_{j+\frac{1}{2},k+\frac{1}{2}}^{n+\frac{1}{2}}\right) - H_z^{tot}\big|_{j-\frac{1}{2},k+\frac{1}{2}}^{n+\frac{1}{2}}\right]. \tag{1.2.4}$$

A similar technique can be done for boundary field components outside of the TFSF box. For example, the update equation for the $H_z|_{j+1/2,k+1/2}$ component at the top-right corner of the shown Yee cell must only include scattered field quantities. However, it will also depend on $E_x|_{j,k+1/2}$ which is inside the total field region and

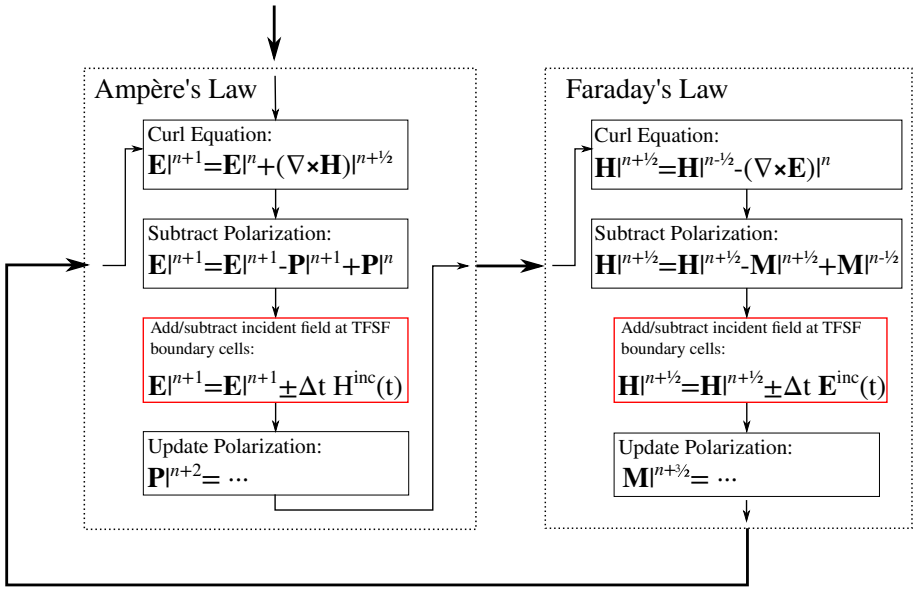

Figure 1.2.4: The FDTD computation loop of a simulation containing a TFSF-box. The additional steps are highlighted in red.

therefore the incident field must be subtracted from this component:

$$H_z^{scat}\big|_{j+\frac{1}{2},k+\frac{1}{2}}^{n+\frac{1}{2}} = H_z^{scat}\big|_{j+\frac{1}{2},k+\frac{1}{2}}^{n+\frac{1}{2}} + c\cdot\frac{\Delta t}{\Delta y}\left[E_x^{scat}\big|_{j+1,k+\frac{1}{2}}^{n} - \left(E_x^{tot}\big|_{j,k+\frac{1}{2}}^{n} - E_x^{inc}\big|_{j,k+\frac{1}{2}}^{n}\right)\right] + c\cdot\frac{\Delta t}{\Delta x}\left[E_y^{scat}\big|_{j+\frac{1}{2},k}^{n} - E_y^{scat}\big|_{j+\frac{1}{2},k+1}^{n}\right]. \tag{1.2.5}$$

The above corrections need only be done for some of the field components which are located immediately at the boundary of the TFSF box. A typical computational implementation of the TFSF-box will therefore first update the electric field everywhere in the computational domain with the unaltered electric field update equations 1.1.22 and 1.1.23, after which, the analytically calculated incident field is added or subtracted from the electric field components located at the boundary of the TFSF-box. For example, the two examples discussed above would be augmented with the following equations after the corresponding unaltered update equations have been processed:

$$\begin{aligned} E_x^{tot}\big|_{j,k+\frac{1}{2}}^{n+1} &= E_x^{tot}\big|_{j,k+\frac{1}{2}}^{n} + c\cdot\frac{\Delta t}{\Delta y}\cdot H_z^{inc}\big|_{j+\frac{1}{2},k+\frac{1}{2}}^{n+\frac{1}{2}} \\ H_z^{scat}\big|_{j+\frac{1}{2},k-\frac{1}{2}}^{n+\frac{1}{2}} &= H_z^{scat}\big|_{j+\frac{1}{2},k-\frac{1}{2}}^{n+\frac{1}{2}} + E_x^{inc}\big|_{j,k-\frac{1}{2}}^{n}. \end{aligned} \tag{1.2.6}$$

The augmented FDTD update loop is depicted in figure 1.2.4.

There are several advantages of a TFSF box compared to other injection methods. First of all, as already mentioned, when the TFSF box is used to inject a plane-wave or pulse incident field, the wave or pulse travels only in the desired direction and not also in the opposite direction as is the case with hard sources. Furthermore,

the TFSF box does not suffer from the same quality degradation due to the finite length of the dipole line source. The spatial separation of a total and scattered field also has some additional advantages. For example, the scattering and absorption cross sections of the scatterer can easily be calculated by integrating the Poynting Vector on the surface of a box either outside or inside the TFSF box respectively (see section 1.5). Furthermore, the scattering field typically carries less energy than the total field and therefore the back reflection due to numerical inaccuracies for certain types of computational domain boundary methods is minimised.

In addition to the parameters required by the time evolution of the incident field discussed above (equation 1.2.1), the origin of the incident wave $\mathbf{r}_0$, the propagation constant $\mathbf{k} = |\mathbf{k}| \cdot \cos\varphi_k \cdot \sin\theta_k \cdot \mathbf{e}_x + |\mathbf{k}| \cdot \sin\varphi_k \cdot \sin\theta_k \cdot \mathbf{e}_y + |\mathbf{k}| \cdot \cos\theta_k \cdot \mathbf{e}_z$ and the polarisation angle Ψ need to be specified to fully define the incident field. With these parameters, the incident field at any point along the boundary of the TFSF box can then be calculated with the following analytic equation:

$$\begin{aligned} \mathbf{E}^{inc}(\mathbf{r},t) &= [\cos\Psi \cdot \mathbf{e}_\varphi + \sin\Psi \cdot \mathbf{e}_\theta]\, f_{src}\left(t - (\mathbf{r}-\mathbf{r}_0)\cdot\mathbf{k}\right) \\ \mathbf{H}^{inc}(\mathbf{r},t) &= \sqrt{\tfrac{\varepsilon}{\mu}}\,[\cos\Psi \cdot \mathbf{e}_\theta - \sin\Psi \cdot \mathbf{e}_\varphi]\, f_{src}\left(t - (\mathbf{r}-\mathbf{r}_0)\cdot\mathbf{k}\right). \end{aligned} \tag{1.2.7}$$

Although the above equations describe the analytic fields in a real physical system, it is strictly only a good approximation for the incident fields in the FDTD method. This is because the physical free-space dispersion relation $\omega = c \cdot |\mathbf{k}|$ was assumed, which is only identical to the dispersion relation of the FDTD method in the limit of $\Delta x \to 0$ as was discussed in section 1.1.6. A modern TFSF implementation will therefore solve the FDTD dispersion relation equation 1.1.31 with an iterative solver [15] such as Newton-Raphson.

1.3 Boundaries

Obviously, the computational domain cannot be infinite and boundary conditions must be formulated. This can already be seen by the structure of the update equations 1.1.20 and 1.1.21 which always require the field values of neighbouring points creating an infinite chain of spatial dependencies. This section discusses the most common boundary conditions used within the FDTD method. Surprisingly, the most natural boundary condition - a boundary which simulates infinite space - is the most difficult to achieve.

1.3.1 PEC and PMC, PBC boundary conditions

The simplest boundary conditions are boundaries which represent perfect electrical conductors (PEC) or perfect magnetic conductors (PMC). Any electrical field inside

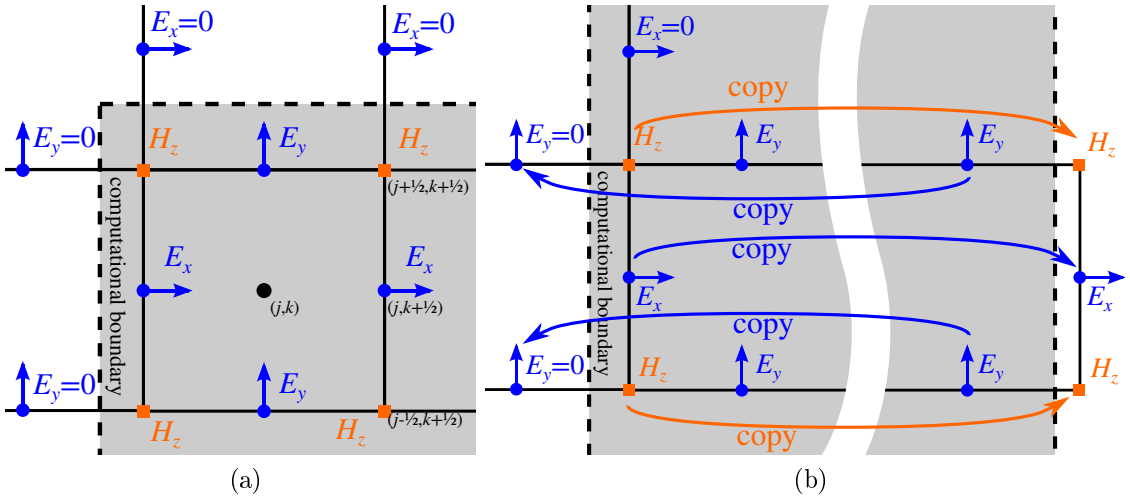

Figure 1.3.1: A Yee cell located at various types of computational boundaries (dotted). (a) A PEC boundary refrains from updating the outer electric field components and therefore remain zero. (b) A PBC boundary copies the values from one side of the computational domain to the other.

the PEC is instantaneously compensated by an infinitely fast re-arrangement of electrical charges at the surface: $\mathbf{E} = 0$. Similarly, in a PMC no magnetic field can occur: $\mathbf{H} = 0$.

A Yee cell at the boundary of the computational domain is depicted in figure 1.3.1. For a PEC, the update equations for the magnetic field immediately inside the boundary must be altered to not include the electric fields outside the boundary. Similarly, for the PMC, the update equations for the electric field components must be modified accordingly. From an implementation standpoint it is easier to leave the update equations unaltered and just refrain from updating the appropriate electric field components of the outer most Yee cells and therefore these field components remain zero. A sketch of the PEC boundary is shown in figure 1.3.1a.

A related boundary condition is the periodic boundary condition (PBC) which is used to simulate a system where the polarisation current functionals are spatially periodic, i.e. they fulfil the following condition:

$$\begin{aligned} \mathbf{P}\left(\mathbf{r}+\mathbf{p},t\right)\left[\mathbf{E},\mathbf{H}\right] &= \mathbf{P}\left(\mathbf{r},t\right)\left[\mathbf{E},\mathbf{H}\right] \quad \forall \quad \mathbf{r}\in V \\ \mathbf{M}\left(\mathbf{r}+\mathbf{p},t\right)\left[\mathbf{H},\mathbf{E}\right] &= \mathbf{M}\left(\mathbf{r},t\right)\left[\mathbf{H},\mathbf{E}\right] \quad \forall \quad \mathbf{r}\in V \end{aligned} \tag{1.3.1}$$

As the electromagnetic fields are completely specified by the polarisation current functionals (which includes all sources and materials), the fields must be periodic in space as well:

$$\begin{aligned} \mathbf{E}\left(\mathbf{r}+\mathbf{p},t\right) &= \mathbf{E}\left(\mathbf{r},t\right) \quad \forall \quad \mathbf{r}\in V \\ \mathbf{H}\left(\mathbf{r}+\mathbf{p},t\right) &= \mathbf{H}\left(\mathbf{r},t\right) \quad \forall \quad \mathbf{r}\in V \end{aligned} \tag{1.3.2}$$

If additionally, one of the computational axes equals $\mathbf{p}$, then the update equation at

the edge of the computational region will depend on a field component whose value is identical to a field component at the opposite side of the computational domain. A PBC boundary will copy the appropriate field components from one side to the other which is depicted in figure 1.3.1b.

1.3.2 Absorbing boundary conditions (ABCs)

The most common boundary problem encountered when modelling electromagnetic systems are such, that an infinitely large empty space surrounds a region where interactions between the electromagnetic field and a material take place.

A naïve exact solution to this problem is to dynamically extend the computational domain so that the electromagnetic fields never hit the boundary during the duration of the simulation. Obviously, this solution is computationally inefficient and is only used for benchmarking. Surprisingly, although exact solutions to the infinite boundary problem based on the Green's function exist, these solutions are either mathematically identical to or have similar unfavourable computational efficiency in comparison with the naïve solution in the 2-D and 3-D case [38, 39]. Therefore, a perfect absorbing boundary is only feasible in the 1-D case and certain approximations must be made for higher dimensions. The first second-order accurate and numerically stable approximation for such an absorbing boundary condition was formulated by Mur [40] in 1981 and brief derivation of the main results follow.

As mentioned in the above discussions, the inherent problem in calculating the update equation for a boundary Yee cell is that the electromagnetic field $\mathbf{E}_{bound}$, $\mathbf{H}_{bound}$ will always depend on at least one field component value which is outside of the computational region $\mathbf{E}_{outside}$, $\mathbf{H}_{outside}$. For example, assuming that the outer-left computational boundary of a 3-D simulation is located at $x = -\frac{1}{2}\Delta x$, then the update equation for the H_z field component located along this boundary is:

$$H_z|^{n+\frac{1}{2}}_{i,j+\frac{1}{2},k=-\frac{1}{2}\Delta x} = H_z|^{n-\frac{1}{2}}_{i,j+\frac{1}{2},k=-\frac{1}{2}\Delta x} + c\Delta t \left[\partial_y E_x|^{n}_{i,j+\frac{1}{2},k=-\frac{1}{2}\Delta x} - \partial_x E_y|^{n}_{i,j+\frac{1}{2},k=-\frac{1}{2}\Delta x}\right], \tag{1.3.3}$$

which involves the term $\partial_x E_y|^{n}_{i,j+\frac{1}{2},k=-\frac{1}{2}\Delta x}$. In a standard FDTD update equation, this term would typically be approximated with the following central difference

$$\partial_x E_y|^{n}_{i,j+\frac{1}{2},k=-\frac{1}{2}\Delta x} \approx \frac{1}{\Delta x}\left[E_y|^{n}_{i,j+\frac{1}{2},k=\Delta x} - E_y|^{n}_{i,j+\frac{1}{2},k=-\Delta x}\right]. \tag{1.3.4}$$

However, this is not possible as the above equation relies on the field-component $E_y|^{n}_{i,j+\frac{1}{2},k=-\Delta x}$ which is located outside of the computational domain. It is therefore, essential, to find another expression for the spatial derivative $\partial_x E_y|^{n}_{i,j+\frac{1}{2},k=-\frac{1}{2}\Delta x}$ which only involves field components residing inside the computational domain.

Theoretically, this should be possible as the electric field and its spatial derivatives is fully defined by the electric polarization response $\mathbf{P}[\mathbf{E}]$ which is only located inside the computational domain. This can be expressed mathematically with the Green's function:

$$\partial_x \mathbf{E}(\mathbf{r}_0, t) = C \cdot \int_{V_{src}} \int_{t_0}^{t} \partial_x \hat{\mathbf{G}}(\mathbf{r}_0, \mathbf{r}', t, t') \circ \dot{\mathbf{P}}(\mathbf{r}', t')\, d^3r' dt' \tag{1.3.5}$$

where $\mathbf{r}_0$ is a point along the computational boundary, $\hat{\mathbf{G}}$ is the electric field Green's dyad, V_{src} is the smallest volume which contains all sources and material responses $\mathbf{P}$ and C is a constant. The electromagnetic Green's dyad can always be written as a dyad depending only on the absolute value of the coordinate differences:

$$\hat{\mathbf{G}}(\mathbf{r}, \mathbf{r}', t, t') = \hat{\mathbf{G}}(u_x(x, x'), u_y(y, y'), u_z(z, z'), u_t(t, t')), \tag{1.3.6}$$

with

$$\begin{aligned} u_x(x, x') &\equiv |x - x'| \\ u_y(y, y') &\equiv |y - y'| \\ u_z(z, z') &\equiv |z - z'| \\ u_t(t, t') &\equiv |t - t'| \quad = t - t', \end{aligned}$$

where the last equation above used the fact that the system is casual. Obviously, the Green's Dyad must fulfil Helmholtz' Equation

$$\left[\frac{1}{c^2}\partial_{u_t}^2 - \left(\partial_{u_x}^2 + \partial_{u_y}^2 + \partial_{u_z}^2\right)\right] \hat{\mathbf{G}}(u_x, u_y, u_z, u_t) = C' \cdot \delta(u_x)\,\delta(u_y)\,\delta(u_z)\,\delta(u_t), \tag{1.3.7}$$

where δ is the Dirac delta distribution and C' is another constant. Note, that in an FDTD simulation the computational domain V_{comp} is always larger than V_{src} and therefore, any point on the computational boundary $\mathbf{r_0}$ must be outside V_{src}. Consequently, the RHS of the above equation will always be zero when evaluated in an integral similar to equation 1.3.5.

With this, it is now possible to re-express the x-derivative at a point $\mathbf{r}_0$ with only field components residing inside the computational domain. This is particularly simple in the 1-D case where the above equation reduces to

$$\partial_{u_x}^2 \hat{\mathbf{G}}(u_x, u_t) = \frac{1}{c^2}\partial_{u_t}^2 \hat{\mathbf{G}}(u_x, u_t), \tag{1.3.8}$$

or[1]

$$\partial_{u_x}\hat{\mathbf{G}}\left(u_x,u_t\right)=\frac{1}{c}\partial_{u_t}\hat{\mathbf{G}}\left(u_x,u_t\right).$$

By replacing the derivatives of u_x and u_t with derivatives of x and t, the above equation can be written as

$$\left(\partial_x u_x\right)^{-1}\partial_x\hat{\mathbf{G}}\left(x,x',t,t'\right)=\frac{1}{c}\partial_t\hat{\mathbf{G}}\left(x,x',t,t'\right).$$

If x_0 lies on the right boundary, then $\partial_x\, u_x\left(x,x'\right)|_{x=x_0}=\partial_x\left(x-x'\right)=1$ and therefore $\partial_x\hat{\mathbf{G}}=\frac{1}{c}\partial_t\hat{\mathbf{G}}$. If x_0 lies on the left boundary, then an additional minus sign will appear. Inserting this into equation 1.3.5 it follows:

$$\partial_x E_y\left(x_0,t\right)=\pm\frac{1}{c}\partial_t E_y\left(x_0,t\right), \tag{1.3.9}$$

where the sign of the above equation depends on which boundary x_0 refers to. With this it is now possible to calculate the update equation 1.3.3 of a field-component located on a boundary Yee cell in the 1-D case.

Higher order dimensions follow a similar pattern where the Helmholtz' Equation 1.3.7 is solved for one of the spatial derivatives. For example, for a boundary perpendicular to the x-axes in a 3-D simulation one finds

$$\partial_{u_x}\hat{\mathbf{G}}\left(u_x,u_t\right)=\sqrt{\frac{1}{c^2}\partial_{u_t}^2-\left(\partial_{u_y}^2+\partial_{u_z}^2\right)}\hat{\mathbf{G}}\left(u_x,u_t\right)=\frac{1}{c}\partial_{u_t}\sqrt{1-\frac{c^2}{\partial_{u_t}^2}\left(\partial_{u_y}^2+\partial_{u_z}^2\right)}\hat{\mathbf{G}}\left(u_x,u_t\right)$$

or, with a similar replacement $u_t\rightarrow t$, $u_x\rightarrow x$,... as was done in the 1-D case, this can be written as a derivative of the electric field

$$\partial_x E_y=\frac{1}{c}\partial_t\sqrt{1\pm\frac{c^2}{\partial_t^2}\left(\partial_y^2+\partial_z^2\right)}E_y,$$

where once again the $\pm$ symbol depends on which boundary is being updated.

The square root function in the above equations must be interpreted as a Taylor series of differential operators. This is the reason why the 2-D and 3-D analytic boundary conditions can only ever be approximations of an infinite computational domain. The accuracy of this approximation will depend on the order of the above Taylor expansion. For example, the 2-D case reduces to the 1-D case if only first

[1] this can be proven by taking the 2-D Fourier-Transform of both sides, observing the dispersion relation that is implied by equation 1.3.7 and Fourier-Transforming back again. Additionally, only the positive square root branch was taken as, for boundary Yee cells, only waves propagating away from the scatterer exist $k_{u_x}>0$.

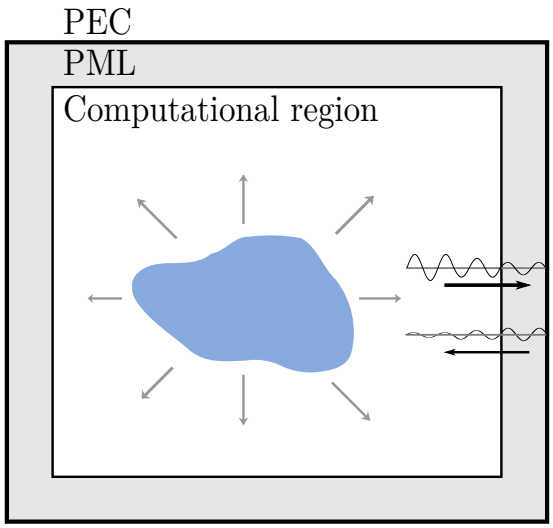

Figure 1.3.2: The operation of the absorbing perfectly matched layers (PMLs) which are used to terminate the computational domain: a scattered wave traverses the PML which attenuates the wave's energy. The wave is reflected at a perfect electrical conductor (PEC) boundary and traverses the PMLs a second time further attenuating the wave.

order terms are retained:

$$\partial_x E_y = \frac{1}{c}\partial_t \sqrt{1 \pm \frac{c^2}{\partial_t^2}\partial_y^2} E_y \approx \pm \frac{1}{c}\partial_t E_y \tag{1.3.10}$$

1.3.3 Perfectly matched layer (PML)

The discussion of the ABCs in the previous section showed that simulating an infinitely large computational domain with acceptable errors is surprisingly difficult for the 2-D and 3-D case. Maybe this is not so surprising, as a single FDTD Yee cell layer must absorb all the energy of the impeding electromagnetic waves. This interpretation of the boundary layer as an absorbing material has led to completely new approach: the perfectly matched layer (PML) [41, 42]. The PML is strictly not a boundary - it is a fictitious material model which absorbs the electromagnetic energy of a traversing electromagnetic wave with the least possible amount of back reflection. This material can now be used at the edge of the computational region to absorb as much energy as possible before the waves hit the boundary cells. In fact, if the computational domain is terminated with a PEC (see section 1.3.1), then the remaining energy of the wave is reflected at the PEC boundary and will be attenuated again when the wave travels through the PML a second time. The typical layout of PMLs is sketched in figure 1.3.2.

With this approach, the infinite boundary problem is effectively divided into two sub-problems: first, it is necessary to find material properties (such as ε and μ) that

absorb a maximum amount of energy while minimising back reflection - irrespective of the FDTD method - and secondly, one must find a suitable polarisation functional to numerically implement this material in FDTD. We refrain from discussing the latter in this thesis as the derivation is lengthy and does not add much insight to the functioning of the PMLs.

A simple PML material can easily be found for the 1-D case. Assume, for instance, an electromagnetic plane-wave with angular frequency ω_0 travelling in the $-\mathbf{e}_x$ direction impeding on a lossy material at $x = 0$. The total electromagnetic fields will have the following form in the region outside of the absorbing material $x > 0$ (region 1):

$$H_z^1(x) = H_z^0 \cdot (1 + \Gamma \cdot \exp(2 \cdot i \cdot k_1 \cdot x)) \cdot \exp(-i \cdot k_1 \cdot x) \tag{1.3.11}$$

$$E_y^1(x) = H_z^0 \cdot \frac{k_1}{\omega_0 \cdot \varepsilon_1} \cdot (1 + \Gamma \cdot \exp(2 \cdot i \cdot k_1 \cdot x)) \cdot \exp(-i \cdot k_1 \cdot x) \tag{1.3.12}$$

where Γ is the reflection coefficient and ε_1, $k_1 = \omega_0/\sqrt{\varepsilon_1 \cdot \mu_1}$ is the dielectric and propagation constant of the material in the $x > 0$ region respectively. The total field in the region $x < 0$ (region 2) is given by the following equations:

$$H_z^2(x) = H_z^0 \cdot \tau \cdot \exp(-i \cdot k_2 \cdot x) \tag{1.3.13}$$

$$E_y^2(x) = H_z^0 \cdot \frac{k_2}{\omega_0 \cdot \varepsilon_2} \cdot \tau \cdot \exp(-i \cdot k_2 \cdot x) \tag{1.3.14}$$

where τ is the transmission coefficient and ε_2, $k_2 = \omega/\sqrt{\varepsilon_2 \cdot \mu_2}$ is the dielectric and propagation constant of the material in the $x < 0$ region respectively. Enforcing the continuity of the tangential fields across the $x = 0$ boundary leads to:

$$\Gamma = \frac{\eta_1 - \eta_2}{\eta_1 + \eta_2}; \qquad \tau = 1 + \Gamma \tag{1.3.15}$$

where η_1 and η_2 is the impedance of regions $x > 0$ and $x < 0$ respectively:

$$\eta_1 := \sqrt{\frac{\mu_1}{\varepsilon_1}}; \qquad \eta_2 := \sqrt{\frac{\mu_2}{\varepsilon_2}} \tag{1.3.16}$$

As stated above, the goal is to minimise the impedance mismatch on the boundary while maximising the absorption in the material, i.e. maximise the imaginary part of k_2. In 1-D this can be achieved exactly, by setting the material properties of the $x < 0$ region as follows:

$$\varepsilon_2 = \varepsilon_1 + \sigma \cdot i; \qquad \mu_2 = \mu_1 + \frac{\sigma \cdot \mu_1}{\varepsilon_1} \cdot i \tag{1.3.17}$$

with this the impedance mismatch vanishes:

$$\eta_2 = \sqrt{\frac{\mu_2}{\varepsilon_2}} = \sqrt{\frac{\mu_1 + \frac{\sigma \cdot \mu_1}{\varepsilon_1} \cdot i}{\varepsilon_1 + \sigma \cdot i}} = \sqrt{\frac{\mu_1 \cdot \left(1 + \sigma \cdot \varepsilon_1^{-1}\right) \cdot i}{\varepsilon_1 \cdot \left(1 + \sigma \cdot \varepsilon_1^{-1}\right) \cdot i}} = \eta_1 \tag{1.3.18}$$

while the exponential absorption of the electromagnetic wave is preserved in the region $x < 0$:

$$k_2 = \sqrt{\varepsilon_2 \cdot \mu_2} \cdot \omega_0 = \sqrt{\varepsilon_1 \cdot \mu_1} \cdot \left(1 + \frac{\sigma}{\varepsilon_1} \cdot i\right) \cdot \omega_0 = \left(1 + \frac{\sigma}{\varepsilon_1} \cdot i\right) \cdot k_1 \tag{1.3.19}$$

Thus, in 1-D, the goal of finding an absorbing material with minimal back reflection has been achieved and a suitable numerical implementation of the magnetic and electric polarisation functional for such an absorbing material will be discussed in chapter 2.

As before, the 2-D and 3-D case is not as simple. This is because the impeding electromagnetic wave will not necessarily transverse the PML material at a normal incidence angle. Here only the 2-D TM case ($H_x = H_y = 0$, $E_z = 0$) is discussed as this sufficient to understand the motivation behind the PML technique.

By splitting the RHS of Faraday's Law (equation 1.1.2) into a part that depends only on E_x and only E_y, it is possible to split the magnetic field component H_z into a portion H_{zx} which travels in the $\pm\mathbf{e}_x$ direction and a portion H_{zy} which travels in the $\pm\mathbf{e}_y$ direction:

$$\begin{array}{rcl} \frac{\partial H_z}{\partial t} & = & \frac{\partial H_{zx}}{\partial t} + \frac{\partial H_{zy}}{\partial t} \\ \frac{\partial H_{zx}}{\partial t} & = & -\mu_{zx}^{-1} \cdot \frac{\partial E_y}{\partial x} \\ \frac{\partial H_{zy}}{\partial t} & = & \mu_{zy}^{-1} \cdot \frac{\partial E_x}{\partial y} \end{array} \tag{1.3.20}$$

Note that $H_z = H_{zx} + H_{zy}$ still fulfils Ampère's Law. Also, if the wave is travelling in the $\pm\mathbf{e}_x$ direction then $E_x = 0$ and therefore only $H_{zx} \neq 0$ and vice versa. Unfortunately, it is not possible to find a single pair of material properties ε, μ to minimise reflection and maximise absorption for both H_{zx}, H_{zy} at the same time. However, it is possible to introduce material properties in such a way that μ_{zx}, μ_{zy} is only applied to the above temporal derivative of H_{zx}, H_{zy} respectively. Obviously, this results in a non-physical material where H_{zx} and H_{zy} experience different material properties, however, the material needn't be physical as long as it achieves the goal of minimal reflection and maximum absorption and can be numerically implemented in FDTD. Note, that this is different from an anisotropic material, where a different material response is applied depending on the direction of the field component. Here, the direction of H_{zx} and H_{zy} is always in the $\pm\mathbf{e}_z$ direction.

The derivation of the exact values for ε, μ_{zx} and μ_{zy} is lengthy, yet straightfor-

ward and similar to the 1-D case and can be found in popular text-books on the FDTD method [15]. Further, mathematical transformation can be found to achieve a more symmetric representation of the material, however, all formulations split the physical electromagnetic fields **E**, **H** into two auxiliary fields for which different material responses apply. The exception is the 1-D case treated above, which does not require the introduction of auxiliary fields.

1.4 Post-processing

FDTD simulations of nano-plasmonic systems typically require tens of millions of simulation time steps. Writing the electro-magnetic field values at every voxel for every time step would easily produce terabytes of data and is not a viable option and some form of post-processing and filtering is required.

1.4.1 Scattering-, extinction- and absorption cross sections

Many quantum-optical phenomena, such as Rabi splitting, manifest themselves as electromagnetic resonances and therefore the calculation of the frequency-resolved extinction, scattering or absorption cross section is beneficial. The cross section is a hypothetical area which describes the likelihood of an incident particle being scattered or absorbed. In classical electro-magnetics, this is equivalent to the fraction of power which is extinct, scattered or absorbed:

$$\sigma_i = \frac{W_i}{\frac{1}{2}\sqrt{\varepsilon_0/\mu_0}\,|\mathbf{E}^0_{inc}|^2} \tag{1.4.1}$$

where $\mathbf{E}^0_{inc}$ is the amplitude of the incident field and W_i refers to the extinct, scattered or absorbed power. In this context, absorption refers to an inelastic process, for example, energy being lost due to non-radiative processes such as Joule-Heating of a metal etc. The extinction cross section is the likelihood of energy being extinct - irrespective of it being absorbed or scattered:

$$\sigma_{ext} = \sigma_{abs} + \sigma_{scat} \tag{1.4.2}$$

Furthermore, if the system only contains purely dielectric, non-dispersive materials then no energy will be lost to non-radiative processes and $\sigma_{abs} = 0$. In this case the scattering and extinction cross sections are identical.

The scattered energy of the entire simulation can easily be determined by integrating the electromagnetic energy that passes through a surface surrounding the TFSF box as only the scattered fields will emerge from the outside of the TFSF box

(see section 1.2.3). This is done by calculating Poynting's Vector along a surface outside of the TFSF box:

$$W = \int_{t_0}^{t} dt' \int_{\partial V} d\mathbf{a}' \cdot (\mathbf{E}(\mathbf{r}', t') \times \mathbf{H}(\mathbf{r}', t')) \tag{1.4.3}$$

where, in this case, $W = W_{scat}$ is the scattered energy and ∂V is the surface of a region containing the TFSF box. Similarly, the absorbed energy W_{abs} can be calculated by determining the missing energy inside the total field region. This is done by integrating the energy that passes through the surface surrounding the scatterer **inside** the TFSF box. The injected incident field passing through this surface is registered as a negative energy contribution. If the scatterer is completely elastic then this energy will either pass through unaltered or be elastically scattered. In any case, the same amount of energy will pass through the surface once again as an outgoing wave and registered as a positive energy contribution. This will exactly cancel the earlier registered negative energy and thus the total integrated energy will be zero. However, if the scatterer is inelastic, the absorbed energy will be missing in the outgoing wave and the integrated energy passing through the boundary will not cancel the negative energy contribution of the incident field and hence, the total registered energy calculated by equation 1.4.3 will equal the absorbed energy multiplied by minus one: $W_{abs} = -W$.

In a numerical implementation of equation 1.4.3, the integrals must be replaced by discrete sums:

$$W \approx \sum_n \Delta t \sum_{ijk \in \partial V} \Delta A_{ijk} \left(\mathbf{E}|_{ijk}^n \times \mathbf{H}|_{ijk}^n \right),$$

where ∂V is now the surface of a box either inside or outside of the TFSF box (depending on whether an absorption or scattering cross section is desired) and ΔA_{ijk} denotes the area of the face of the ijk-th Yee cell which is parallel to the face of the ∂V-box on which the ijk-th Yee cell lies. Additionally, the magnetic and/or electric field in the above equation would need to be interpolated so that the field values can be obtained at the same position in space and time before calculating the cross term. However, the error by neglecting the co-location is small and therefore the interpolation is usually not performed.

In general, the absorbed or scattered energy will depend on the incident frequency. A frequency resolved cross section spectrum can be calculated by performing a whole host of individual FDTD simulations in which a nearly perfect incident plane-wave is injected by the TFSF box. In each simulation the plane-wave has a different frequency and therefore determines one point in the cross section spectrum.

However a computationally more effecient way exists which calculates the entire

spectrum with a single simulation. This is done by injecting a spectrally broad incident pulse and then Fourier-Transforming the fields in time. Assume, for instance, that the frequency range of interest lies between the frequencies ω_{min} and ω_{max}. In this case, the spectral components of the incident pulse must be non-zero and sufficiently large in the range between ω_{min} and ω_{max}. This can be achieved by an incident pulse described by equation 1.2.1 and the following parameters:

$$\omega_0 = \tfrac{1}{2}\left(\omega_{max} + \omega_{min}\right); \quad \sigma_{attack} = \sigma_{decay} = \tfrac{2\pi}{|\omega_{max} - \omega_{min}|} \tag{1.4.4}$$

The Fourier-Transform of an incident wave with the above time evolution is a Gaussian centred at frequency ω_0 and a standard width of $|\omega_{max} - \omega_{min}|$. With this incident pulse, the frequency resolved absorbed or scattered energy W_ω can be found by Fourier-Transforming the fields and averaging over one wave period in time:

$$\langle W_\omega \rangle = \frac{\omega}{2\pi} \int_{\frac{2\pi}{\omega}} dt' \int_{\partial V} d\mathbf{a}' \cdot \left(\mathrm{Re}\left[\tilde{\mathbf{E}}_\omega\left(\mathbf{r}'\right) \cdot \exp\left(i \cdot \omega \cdot t'\right)\right] \times \mathrm{Re}\left[\tilde{\mathbf{H}}_\omega\left(\mathbf{r}'\right) \cdot \exp\left(i \cdot \omega \cdot t'\right)\right] \right) \tag{1.4.5}$$

and after some simple algebra the above expression can be simplified to obtain:

$$\langle W_\omega \rangle = \frac{1}{2} \int_{\partial V} d\mathbf{a}' \cdot \mathrm{Re}\left[\tilde{\mathbf{E}}_\omega\left(\mathbf{r}'\right) \times \tilde{\mathbf{H}}^*_\omega\left(\mathbf{r}'\right)\right], \tag{1.4.6}$$

or

$$\langle W_\omega \rangle \approx \frac{1}{2} \sum_{ijk \in \partial V} \Delta A_{ijk} \mathrm{Re}\left[\tilde{\mathbf{E}}_\omega\Big|_{ijk} \times \tilde{\mathbf{H}^*}_\omega\Big|_{ijk}\right] \tag{1.4.7}$$

after the discretisation of the integral. Practically, the frequency resolved absorbed or scattered energy $\left\langle W^\omega_{abs,scat} \right\rangle$ is calculated by storing the field values $\mathbf{E}|_{ijk}$ and $\mathbf{H}|_{ijk}$ at every time step and position along the surface of the ∂V-box. After the simulation, a Fourier-Transform in time is performed for all $\mathbf{E}|_{ijk}$ and $\mathbf{H}|_{ijk}$ individually resulting in complex electromagnetic field amplitudes $\tilde{\mathbf{E}}_\omega|_{ijk}$ and $\tilde{\mathbf{H}}_\omega|_{ijk}$ along the boundary from which the absorbed or scattered energy $\left\langle W^\omega_{abs,scat} \right\rangle$ can be calculated with the above formula. As the incident pulse itself, is not uniform in energy across the frequencies of interest, it is then necessary to divide $\left\langle W^\omega_{abs,scat} \right\rangle$ by the analytically calculated incident field intensity of the same frequency $\frac{1}{2}\sqrt{\varepsilon_0/\mu_0}\left|\mathbf{E}^0_{inc}\left(\omega\right)\right|^2$.

1.5 A typical FDTD setup

Apart from material models which will be discussed in chapter 2, all the building blocks are in place to introduce the setup which is commonly used in this thesis.

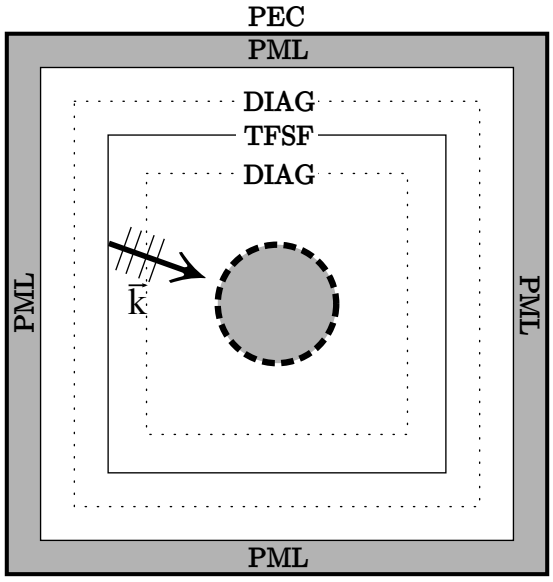

Figure 1.5.1: A typical FDTD setup: incident fields are injected by the total-field-scattered-field (TFSF) box which are scattered by the materials contained in the computational domain. The energy of the total and scattered fields are recorded at the dotted boxes labelled with "DIAG". The fields then reach the PMLs where they are attenuated and reflected off a perfect electrical conductor (PEC) boundary. The reflected waves are attenuated once more and only negligible energy is reflected back into the computational region.

1.5.1 Scattering/Absorption cross section simulation

A typical FDTD setup which is used to calculate the absorption and scattering cross section is depicted in figure 1.5.1. In the innermost region lies the material or scatterer of interest surrounded by a fictitious box at which the Poynting-Vector is integrated to obtain the absorption cross section (see section 1.4.1). This in turn is surrounded by the TFSF box (see section 1.2.3) which injects the incident field $\mathbf{E}_{inc}$ into the total field region. Outside of this box only the scattered fields emerge. The TFSF box is itself surrounded by another fictitious box at which the Poynting-Vector is again integrated to obtain the scattering cross section. Surrounding this box are the PMLs (see section 1.3.3) which attenuate the out-going waves. The computational-domain is terminated by a perfect electrical conductor.

The time-line of such a simulation is straightforward: the simulation starts by injecting a spectrally broad pulse. After the pulse has traversed the computational domain, the simulation continues until the energy inside the computational domain becomes negligible. After this the simulation terminates and the cross section spectra are calculated as described in section 1.4.1.

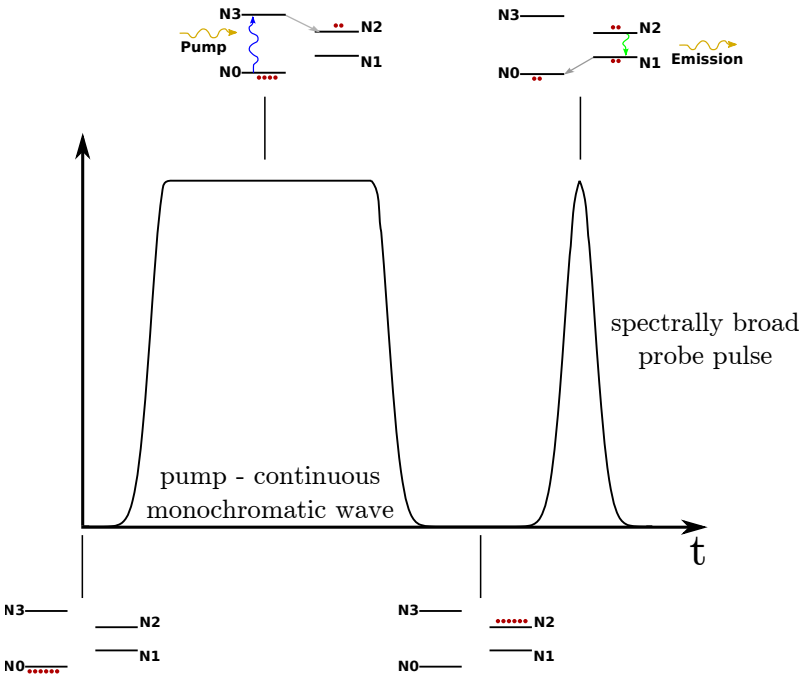

Figure 1.5.2: Time line of the incident field amplitude of a pump probe experiment. The simulation begins by injecting a long monochromatic pump incident wave. The energy is absorbed by the laser-dye exciting electrons to a higher energy state. After the pump excitation and any remaining electro-magnetic field energy has decayed, a spectrally broad probe-pulse is injected from which frequency-resolved cross sections of the pumped system can be obtained.

1.5.2 Spatial field-profile

Often it is beneficial to obtain the spatial field profile of a certain mode in a system. To obtain this, a similar setup as described above can be used. However, instead of injecting a spectrally broad pulse, a continuous plane-wave with a ramp-up phase is injected (see section 1.2.1). To minimise the spectral width of the incident wave one can either increase the ramp-up time or add buffer phase where sufficient amount of extra simulation time steps are added after the ramp-up has completed but before any data is extracted. The latter will ensure that any foreign frequency components from the ramp-up phase will have sufficiently dissipated. After the buffer phase is finished, the field-values of every voxel, at every time step in the region of interest is stored while the plane-wave continues to excite the system. This data-collection phase typically lasts one wave-period after which the simulation is terminated. A Fourier-Transform in time of the stored field data results in the desired complex-valued spatial field profile.

1.5.3 Pump-probe experiment

The FDTD method is often used to investigate systems with an embedded gain material such as they occur in laser systems. For these systems it is common to do a so-called "pump-probe" experiment. The simulation begins by "pumping" the gain material: a monochromatic plane-wave at the pump-frequency with a ramp-up is injected similar to the simulation described above. After the ramp-up, the plane-wave continues to excite the system until the desired inversion in the gain material has been achieved. After this pump phase, the monochromatic plane-wave is ramped-down again. It is crucial that the ramping down is done slow enough so that only negligible frequency components are produced at the emission frequency of the laser. Otherwise, the ramp-down phase will prematurely deplete the inversion. After the decay of the monochromatic pump, a buffer phase is necessary which is long enough to ensure that only negligible electro-magnetic energy remains in the computational domain, however, short enough so that the inversion does not significantly deplete by other non-radiative processes (see chapter 3 for details on the implementation of gain media in FDTD). After this buffer-phase, the system is "probed" by a spectrally broad probe pulse and the cross sections are calculated as described in section 1.5.1. The probe pulse must be sufficiently weak in amplitude to not significantly change the inversion levels during the course of the simulation. The time-line of such simulation is sketched in figure 1.5.2.

Chapter 2

Materials and the FDTD method

The previous chapter discusses a numerical algorithm to propagate electro-magnetic fields in vacuum. It is shown that all material processes can be described by the polarisation functionals $\mathbf{P}[\mathbf{E}, \mathbf{H}]$ and $\mathbf{M}[\mathbf{H}, \mathbf{E}]$. Effectively, this breaks down the problem of numerical simulation of such systems into two sub-problems: finding a numerical algorithm to propagate the electro-magnetic fields and formulating the material interactions as polarisation functionals. As the numerical implementation for the former was discussed in the previous chapter, this chapter now focuses on a range of polarisation functionals for different classes of materials.

The original FDTD method is limited to materials that can only be described by a single static, frequency-independent permittivity ε_∞ or permeability μ_∞ [14]. As is shown in this chapter, such materials only require a modification of a constant pre-factor in the FDTD update equations. Unfortunately, a key requirement for simulating nano-plasmonic systems with FDTD is the accurate description of lossy and dispersive metals that require a complex, frequency-dependent permittivity $\varepsilon(\omega)$ or permeability $\mu(\omega)$.

In contrast to the relatively straightforward numerical implementation of such materials in frequency-based solvers, the FDTD method requires a set of auxiliary update equations to appropriately calculate the time-domain response [15, 43]. In the last decade, various methods to find the auxiliary update equations for a range of complex, frequency-dependent permittivity $\varepsilon(\omega)$ or permeability $\mu(\omega)$ have been discovered, of which the most common are discussed in this chapter [15, 44, 43, 45]. It is shown that the auxiliary update equations behind these techniques can all be written as discretised, recursive update equations [46]. A large proportion of this chapter is therefore dedicated to the investigation of the properties of such recursive update equations.

Although a wide range of materials, including metals, are now standard features of many modern FDTD solvers, finding a computationally efficient auxiliary update equation remains challenging for any material for which an auxiliary update

equation does not yet exist. Even the leading commercial FDTD software packages [47] require laborious manual fitting of parameters in order to find, for example, an auxiliary update equation for a material response that sufficiently matches a given complex, frequency-dependent permittivity $\varepsilon(\omega)$ or permeability $\mu(\omega)$ [48]. To overcome this limitation, an algorithm that automatically finds these auxiliary update equations was developed as part of this thesis and is presented in this chapter.

The chapter concludes by extending the above discussion of material responses to anisotropic materials. It should be noted that this chapter only discusses materials with a linear response functional; the extension to non-linear materials, such as simple quantum systems and χ^3 materials, will be discussed in chapter 3.

2.1 Conventional techniques to model materials in FDTD

The following is an account of the conventional techniques used to model materials in FDTD solvers.

2.1.1 Simple Dielectric Materials

The simplest class of materials from an implementation standpoint are materials that can be described by a frequency-independent, real-valued and positive permittivities $\varepsilon_\infty(\mathbf{r})$ and permeabilities $\mu_\infty(\mathbf{r})$. The suffix ∞ is used to differentiate the above permittivity and permeability from frequency-dependent material properties, i.e. ε_∞ and μ_∞ describe the material response at infinitely long wavelengths. A material with these properties has the following simple polarisation functionals:

$$\begin{aligned} \mathbf{P}\left[\mathbf{E}\right](\mathbf{r},t) &= \left(\varepsilon_\infty(\mathbf{r})-1\right)\mathbf{E}(\mathbf{r},t) \\ \mathbf{M}\left[\mathbf{H}\right](\mathbf{r},t) &= \left(\mu_\infty(\mathbf{r})-1\right)\mathbf{H}(\mathbf{r},t) \end{aligned} \tag{2.1.1}$$

The discretisation of the polarisation functionals is straightforward. For example, in the 2-D TM case ($H_z \neq 0$ and $E_x \neq 0$, $E_y \neq 0$) the discretised polarization functionals are:

$$\begin{aligned} P_x|^n_{j,k-\frac{1}{2}} &= \left(\varepsilon_\infty|_{j,k-\frac{1}{2}} - 1\right) E_x|^n_{j,k-\frac{1}{2}} \\ P_y|^n_{j+\frac{1}{2},k} &= \left(\varepsilon_\infty|_{j+\frac{1}{2},k} - 1\right) E_y|^n_{j+\frac{1}{2},k} \\ M_z|^{n+\frac{1}{2}}_{j+\frac{1}{2},k-\frac{1}{2}} &= \left(\mu_\infty|_{j+\frac{1}{2},k-\frac{1}{2}} - 1\right) H_z|^{n+\frac{1}{2}}_{j+\frac{1}{2},k-\frac{1}{2}}, \end{aligned} \tag{2.1.2}$$

where the Yee cell component arrangement of the previous chapter was used. Unfortunately, it is not possible to directly use the above polarisation in the FDTD

update equations as the FDTD update equations require the polarization functionals one time step in advance with regards to the current available field values (see section 1.1.1). For example, the update equation for the x-component of the electric field in the 2-D TM case reads:

$$E_x|^{n+1}_{j,k-\frac{1}{2}} = E_x|^{n}_{j,k-\frac{1}{2}} + c\frac{\Delta t}{\Delta y}\left(H_z|^{n+\frac{1}{2}}_{j+\frac{1}{2},k-\frac{1}{2}} - H_z|^{n+\frac{1}{2}}_{j-\frac{1}{2},k-\frac{1}{2}}\right) - P_x|^{n+1}_{j,k-\frac{1}{2}} + P_x|^{n}_{j,k-\frac{1}{2}}\,, \tag{2.1.3}$$

which depends on $P_x|^{n+1}$. It is possible to work around this problem by simply inserting the polarization equation 2.1.2 and solving for $\mathbf{E}|^{n+1}$:

$$\begin{aligned}
E_x|^{n+1}_{j,k-\frac{1}{2}} &= E_x|^{n}_{j,k-\frac{1}{2}} + c\,\varepsilon_\infty^{-1}|_{j,k-\frac{1}{2}}\,\tfrac{\Delta t}{\Delta y}\left(H_z|^{n+\frac{1}{2}}_{j+\frac{1}{2},k-\frac{1}{2}} - H_z|^{n+\frac{1}{2}}_{j-\frac{1}{2},k-\frac{1}{2}}\right)\\
E_y|^{n+1}_{j+\frac{1}{2},k} &= E_y|^{n}_{j+\frac{1}{2},k} + c\,\varepsilon_\infty^{-1}|_{j+\frac{1}{2},k}\,\tfrac{\Delta t}{\Delta x}\left(H_z|^{n+\frac{1}{2}}_{k-\frac{1}{2}} - H_z|^{n+\frac{1}{2}}_{k+\frac{1}{2}}\right)\\
H_z|^{n+\frac{1}{2}}_{j+\frac{1}{2},k-\frac{1}{2}} &= H_z|^{n-\frac{1}{2}}_{j+\frac{1}{2},k-\frac{1}{2}} + c\,\mu_\infty^{-1}|_{j+\frac{1}{2},k-\frac{1}{2}}\,\tfrac{\Delta t}{\Delta y}\left(E_x|^{n}_{j+1,k-\frac{1}{2}} - E_x|^{n}_{j,k-\frac{1}{2}}\right) +\\
&\qquad c\,\mu_\infty^{-1}|_{j+\frac{1}{2},k-\frac{1}{2}}\,\tfrac{\Delta t}{\Delta x}\left(E_y|^{n}_{j+\frac{1}{2},k-1} - E_y|^{n}_{j+\frac{1}{2},k}\right)
\end{aligned} \tag{2.1.4}$$

Effectively, this alters the spatial derivatives of the FDTD update equations only by a pre-factor. This does not effect the computational complexity of the algorithm in any way as the FDTD update equations already require a pre-factor of $c\Delta t\Delta x^{-1}$ even in vacuum.

Obviously, the above update equations for a simple dielectric could have been derived directly from the macroscopic Maxwell Equations and many derivations of the FDTD update equations found in literature [15] choose to include the permittivity and permeability from the start. This thesis, however, considers the strict separation of electro-magnetic field propagation and material interaction to be more beneficial.

It is important to note that introducing a permittivity and/or permeability can alter the numerical stability and the order of accuracy of the FDTD update equations. For example, the proof of second order accuracy of the central difference equation (see section 1.1.2) assumed a continuous field in space which is not necessarily valid at material boundaries [49]. A more detailed discussion and ways to mitigate the numerical errors will be detailed in chapter 4. Nevertheless, it should be noted here, that in practice, as the errors are only introduced at a small number of material interface Yee cells, the overall error remains largely acceptable.

2.1.2 Auxiliary differential equation method

Originally, the FDTD method was limited to non-dispersive, frequency-independent permittivities and permeabilities as these can easily be included via a scalar pre-factor in the FDTD update equations as was shown in the previous section. However,

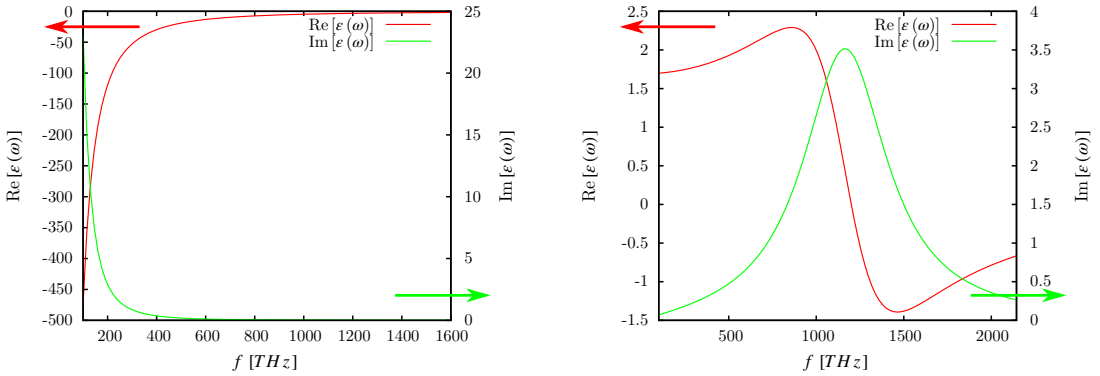

Figure 2.1.1: The real (red) and imaginary (green) parts of the permittivity $\varepsilon(\omega)$ of a (a) Drude response ($\omega_p = 13697$ THz, $\gamma_D = 0.581$ ps^{-1}) and (b) Lorentzian response ($\omega_0 = 7540$ THz, $\gamma_L = 1839$ ps^{-1}, $\Delta\epsilon = 1.69$).

plasmonic simulations require accurate material responses of various conductors. Such materials can only be described by frequency-dependent, complex polarisation functionals. Often, simple differential equations governing these functionals can be found, and a widely used method to convert these into FDTD update equations shall now be presented [50] by discussing two commonly found material responses: the Drude model and the Lorentzian resonance response.

2.1.2.1 Drude-like materials

The most common model to describe the response of a metal is the Drude model [51, 52]. The Drude model assumes that electrons can be treated as classical particles with an effective mass m^* and an empirical "drag" term γ_D caused by scattering events. The equation of motion for such a particle in an electric field is given by

$$m^*\ddot{\mathbf{x}} = -m^*\gamma_D\dot{\mathbf{x}} + e\mathbf{E}(\mathbf{x}) \tag{2.1.5}$$

and $\mathbf{x}$ is the displacement of the charge carrier from its equilibrium position. Further, assuming that the macroscopic polarization can be written as a sum of all microscopic dipole moments $\mathbf{P} = N\mu = Ne\mathbf{x}$, the following differential equation for the polarization of a Drude material is found:

$$\ddot{P} + \gamma_D\dot{P} = \omega_p^2 E \ , \tag{2.1.6}$$

where ω_p is the plasmon resonance frequency which is given by:

$$\omega_p = \sqrt{\frac{Ne^2}{m^*}} \ . \tag{2.1.7}$$

Solving the differential equation 2.1.6 with a time harmonic ansatz leads to the well-known dielectric response function of a Drude metal (see figure 2.1.1a):

$$\varepsilon_{drude}(\omega) = \varepsilon_\infty - \frac{\omega_p^2}{\omega(\omega + i\gamma_D)} \ . \tag{2.1.8}$$

However, in pursuit of finding a time-domain polarization update equation, it is beneficial to remain in the time-domain and discretise the Drude polarization differential equation 2.1.6 by replacing the time-derivatives with central difference quotients:

$$\frac{\mathbf{P}|^{n+1} - 2\,\mathbf{P}|^n + \mathbf{P}|^{n-1}}{(\Delta t)^2} + \gamma_D \frac{\mathbf{P}|^{n+\frac{1}{2}} - \mathbf{P}|^{n-\frac{1}{2}}}{\Delta t} = \omega_p^2\,\mathbf{E}|^n \ . \tag{2.1.9}$$

The second term on the LHS in the above equation requires an extra time averaging step as the polarization functionals are only given at full time steps $\mathbf{P}|^{n-1}$, $\mathbf{P}|^n$, $\mathbf{P}|^{n+1}$, ...:

$$\frac{\mathbf{P}|^{n+1} - 2\,\mathbf{P}|^n + \mathbf{P}|^{n-1}}{(\Delta t)^2} + \gamma_D \frac{\mathbf{P}|^{n+1} - \mathbf{P}|^{n-1}}{2\Delta t} = \omega_p^2\,\mathbf{E}|^n \ . \tag{2.1.10}$$

Solving the above equation for $\mathbf{P}|^{n+1}$ gives the following update equation:

$$\mathbf{P}|^{n+1} = \frac{2}{\frac{1}{2}\gamma_D\Delta t + 1}\,\mathbf{P}|^n + \frac{\frac{1}{2}\gamma_D\Delta t - 1}{\frac{1}{2}\gamma_D\Delta t + 1}\,\mathbf{P}|^{n-1} + \frac{(\Delta t)^2\,\omega_p^2}{\frac{1}{2}\gamma_D\Delta t + 1}\,\mathbf{E}|^n \ . \tag{2.1.11}$$

This is the final polarization update equation for a Drude model which is integrated along-side the FDTD update equation. It is a recursive update equation as it depends on previously calculated polarization values and therefore, strictly, one must investigate if the integration scheme is numerically stable for all expected inputs. A proper stability analysis will be done for the general case in section 2.3.

In the Drude case, the above update equation requires two previous polarization functional values $P|^n$ and $P|^{n-1}$. In practice, however, the update equation only requires the storage of the current and the polarization value at the previous time step. This is because the oldest polarization value can always be overwritten by the newest calculated polarization value immediately. Therefore, the implementation of a Drude model in FDTD requires $2dV_{drude}$ extra memory storage, where d is the number of components of the electric field vector and V_{drude} is the number of Yee cells that are within the boundaries of a Drude material.

In the previous chapter a potential problem for the update equation of the electric field was identified: the electric field update equation (see, for example, equation 2.1.3) $E|^{n+1} = E|^n + ...$ already requires the polarization functional of the next time

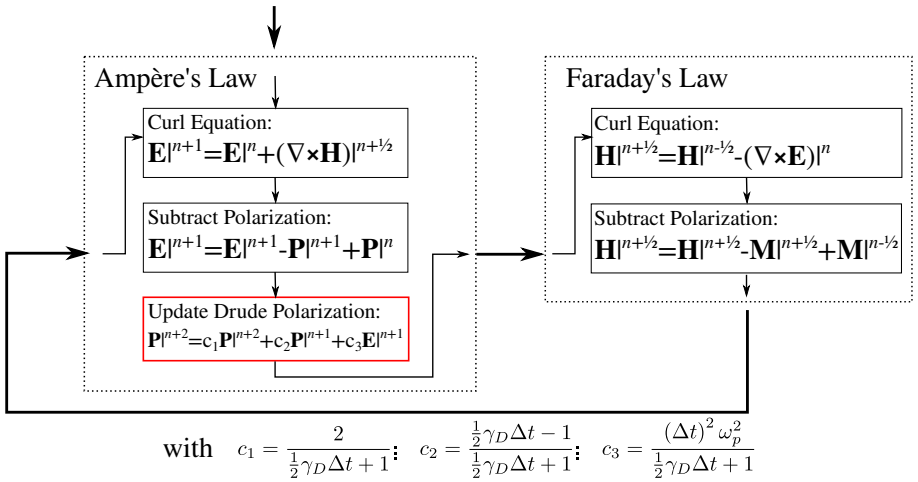

Figure 2.1.2: A sketch of the FDTD update algorithm simulating a system containing a material with a Drude polarization response. The changes to the core FDTD algorithm are highlighted in red.

step $P|^{n+1}$. However, for the Drude model, this turns out to be unproblematic as the above polarization update equation naturally calculates the polarization functional at a future time step $P|^{n+1}$ given an electric field value one time step in the past $E|^{n}$. In section 2.2.1, it will be shown that any physical and linear polarizability $\chi(\omega)$ can be composed of a non-instantaneous polarizability $\chi(\omega)$ and a real-valued, static dielectric constant.

The update cycle of a single FDTD simulation time step with a Drude like material response is depicted in figure 2.1.2.

2.1.2.2 Lorentz resonance response

For some metals it is important to include resonant behaviour in the polarizability which can arise, for example, due to inter-band transitions in a metal. A common way to model such resonances is with a Lorentzian response [53, 54] (see figure 2.1.1b). The differential equation of a Lorentzian resonance is similar to the Drude response, but additionally includes a restoring force term:

$$m^*\ddot{\mathbf{x}} = -m^*2\gamma_L\dot{\mathbf{x}} - k\mathbf{x} + e\mathbf{E}(\mathbf{x}), \tag{2.1.12}$$

where k is the restoring-force constant. With $\mathbf{P} = N\mu = Ne\mathbf{x}$, the following differential equation for the polarization can be found:

$$\ddot{\mathbf{P}} + 2\gamma_L\dot{\mathbf{P}} + \frac{k}{m^*}\mathbf{P} = \frac{Ne^2}{k}\frac{k}{m^*}\mathbf{E}(\mathbf{x}) \tag{2.1.13}$$

or

$$\ddot{\mathbf{P}} + 2\gamma_L\dot{\mathbf{P}} + \omega_0^2\mathbf{P} = \Delta\epsilon\omega_0^2\mathbf{E}, \tag{2.1.14}$$

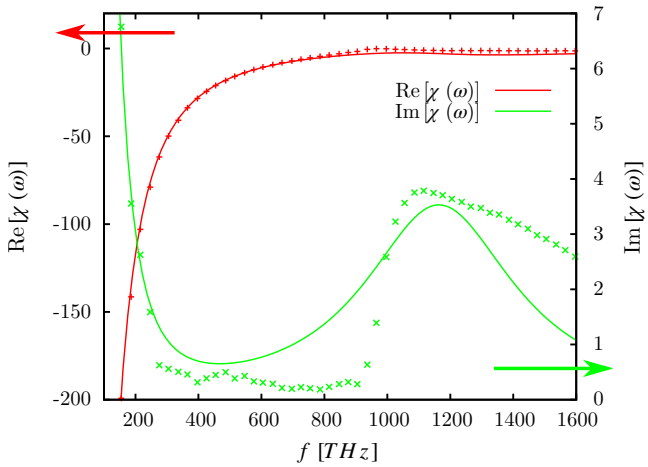

Figure 2.1.3: The real (red) and imaginary (green) parts of the experimentally derived polarizability $\chi(\omega)$ of silver (crosses) and that of a combined Lorentzian and Drude response (solid lines). The parameters for the latter were fitted to achieve a reasonable agreement with the experimental data.

where the following definitions were used

$$\omega_0 := \sqrt{\frac{k}{m^*}}; \quad \Delta\epsilon := \frac{Ne^2}{k}. \tag{2.1.15}$$

After discretising equation 2.1.14 and solving for $\mathbf{P}|^{n+1}$ the following update equation for a Lorentzian resonance is found

$$\mathbf{P}|^{n+1} = \frac{2-\omega_0^2(\Delta t)^2}{1+\gamma_L\Delta t}\mathbf{P}|^n + \frac{\gamma_L\Delta t-1}{\gamma_L\Delta t+1}\mathbf{P}|^{n-1} + \frac{\Delta\epsilon\omega_0^2(\Delta t)^2}{1+\gamma_L\Delta t}\mathbf{E}|^n. \tag{2.1.16}$$

2.1.2.3 Superposition of Lorentz- and Drude responses

As the polarisation functionals $\mathbf{P}[\mathbf{E}]$ for a Drude or Lorentzian are linear, it is possible to use linear combinations of both to create more complex total polarization responses $\mathbf{P}[\mathbf{E}]$. This method shall now be demonstrated to find a reasonably accurate response functional $\mathbf{P}[\mathbf{E}]$ to describe the response of silver.

The complex-valued polarizability $\chi(\omega)$ of silver (solid blue and green lines) is plotted in figure 2.1.3. The values are obtained from reflectivity measurements done by Johnson and Christie [55] and are widely used in the plasmonic community. It can easily be seen that the overall response is Drude-like with a region of strong absorption at ≈ 1200 THz. We therefore choose to fit this curve with a combination of a static dielectric response ε_∞, a Drude and a Lorentzian response. The static dielectric constant ε_∞ and the parameters of the Lorentzian and Drude were determined by the `Gnuplot` fitting algorithm after an already reasonable agreement was

achieved by eye. The parameters were determined as follows:

$$\varepsilon_\infty = 1.174; \quad \omega_p = 13697 \text{ THz}; \quad \gamma_D = 30.581 \text{ ps}^{-1};$$

$$\omega_0 = 7540 \text{ THz}; \quad \gamma_L = 1839 \text{ ps}^{-1}; \quad \Delta\epsilon = 1.69$$

and the resulting polarizability $\chi(\omega)$ is plotted in figure 2.1.3. Both the experimentally obtained data and the numerical implementation have a reasonably good agreement.

2.2 General frequency-dependent and dispersive material responses

The superposition method of simple individual material responses (such as Drude and Lorentzian) described above is widely used in the FDTD community. Although the numerical implementation of the superposition method is relatively straightforward, the process of obtaining the various parameters of the constituent material responses is tedious and cannot be easily automated. This is a major disadvantage in comparison to frequency-based solvers which can easily operate with either analytically given or experimentally derived permittivities or permeabilities $\varepsilon(\omega)$, $\mu(\omega)$ with very little user interaction. Therefore, several methods to automatically find a computationally efficient, discretised time-domain polarization update equations $\mathbf{P}[\mathbf{E}]$, $\mathbf{M}[\mathbf{H}]$ for given permittivities or permeabilities $\varepsilon(\omega)$, $\mu(\omega)$ were developed during the course of this thesis and shall now be presented and discussed.

For the sake of readability, this section will only deal with the derivation of a time-domain polarization update equation $P|^{n+1} = ...$ from a given frequency-dependent polarizability $\chi(\omega) := \varepsilon(\omega) - 1$. The derivation of a magnetic polarization update equation $M|^{n+\frac{1}{2}} = ...$ from a given permeability is identical and will therefore not be discussed here.

2.2.1 Theoretical time-domain response functional

The goal of this section is to find a time-domain polarisation update equation $P|^{n+1} = ...$ from a known polarizability $\chi(\omega)$. In frequency space, the relation between the electric and polarization field is straightforward:

$$\tilde{\mathbf{P}}(\omega) = \chi(\omega)\,\tilde{\mathbf{E}}(\omega), \tag{2.2.1}$$

where $\tilde{\mathbf{E}}(\omega)$ and $\tilde{\mathbf{P}}(\omega)$ are the discrete-time Fourier-Transform [56] (DTFT, not to be confused with the discrete Fourier Transform DFT) of the time discretised electric

field $\mathbf{E}|^n$ and polarization current $\mathbf{P}|^n$:

$$\tilde{\mathbf{E}}(\omega) = \sum_{n=-\infty}^{\infty} \mathbf{E}|^n \exp(-i\omega n\Delta t) \tag{2.2.2}$$

$$\tilde{\mathbf{P}}(\omega) = \sum_{n=-\infty}^{\infty} \mathbf{P}|^n \exp(-i\omega n\Delta t). \tag{2.2.3}$$

The time-domain representation of 2.2.1 can be found by taking the inverse DTFT and observing the correlation property [56]:

$$\mathbf{P}|^n = \sum_{m=-\infty}^{\infty} \mathbf{E}|^{n-m} \chi|^m, \tag{2.2.4}$$

where $\chi|^n$ is given by [56]

$$\chi|^n = \frac{1}{2\omega_{max}} \int_{-\omega_{max}}^{\omega_{max}} \chi(\omega') \exp(i\omega' n\Delta t)\, d\omega' \tag{2.2.5}$$

and $\omega_{max} = \pi/\Delta t$ is the highest possible frequency in a time-domain simulation (Nyquist frequency).

In principle, the convolution expression in equation 2.2.4 is already an update equation for the polarization field in the time-domain. However, practically, this expression cannot be used in a numerical integration scheme as it depends on an infinite amount of electric field values. Nevertheless, some important mathematical properties of polarization currents can be discussed by analysing the polarisation and electric field relationship in the time-domain.

One important consequence of equation 2.2.4 is that the time-domain representation of the polarizability $\chi|^n$ must be real-valued for the polarization and electromagnetic fields to remain physical:

$$\mathrm{Im}\left[\chi|^n\right] = \mathrm{Im}\left[\frac{1}{2\omega_{max}} \int_{-\omega_{max}}^{\omega_{max}} \chi(\omega') \exp(i\omega' n\Delta t)\, d\omega'\right] = 0. \tag{2.2.6}$$

which, after some straightforward algebra, leads to the following condition on the polarizability in frequency space $\chi(\omega)$:

$$\chi(\omega) = \chi^*(-\omega). \tag{2.2.7}$$

In particular, equation 2.2.6 also states that the instantaneous response $\chi|^0$ must be real. Consequently, it is always possible to split any instantaneous polarizability

$\chi_{instant}(\omega)$ into a static dielectric ε_∞ and non-instantaneous material response $\chi(\omega)$:

$$\chi_{instant}(\omega) = (\varepsilon_\infty - 1) + \chi(\omega)$$

with

$$\varepsilon_\infty \equiv \chi|^0 + 1.$$

As discussed in section 2.1.1, static dielectric materials can easily be incorporated into the FDTD update equations and hence, the following discussions are limited to non-instantaneous $\chi|^0 = 0$ polarizations only.

An additional requirement for a physical polarizability is that the update equation 2.2.4 remains casual, i.e. it only depends on current or past electric field values:

$$\chi|^n = 0 \text{ for } n < 0. \tag{2.2.8}$$

For non-vanishing and non-instantaneous polarizations, the above condition implies

$$\chi|^n \neq \chi|^{-n}, \tag{2.2.9}$$

and consequently any non-instantaneous physical polarizability must have a non-vanishing imaginary component:

$$\mathrm{Im}\left[\chi(\omega)\right] \neq 0. \tag{2.2.10}$$

2.2.2 Windowing method

Although the time-domain relationship between the polarization and electric field has been found in equation 2.2.4, a computationally efficient way of calculating the infinite sum must be found. One simple method is to modify the convolution kernel $\hat{\chi}|^n$ by a window function $w|^n$ with limited support ΔN.

$$\mathbf{P}|^n = \sum_{m=0}^{\Delta N} \mathbf{E}|^{n-m} \hat{\chi}|^m, \tag{2.2.11}$$

where

$$\hat{\chi}|^n := w|^n \chi|^n \tag{2.2.12}$$

and

$$w|^n = \begin{cases} 1 & \text{for } 0 \leq n \leq \Delta N \\ 0 & \text{otherwise} \end{cases}. \tag{2.2.13}$$

Obviously, it is important to understand how the introduction of such a window function will alter the polarizability $\chi(\omega)$. If $\tilde{w}(\omega)$ denotes the DTFT of the window

function $w|^n$, then the modified polarizability is given by:

$$\hat{\chi}(\omega) = \frac{1}{\omega_{max}} \int_{-\frac{1}{2}\omega_{max}}^{\frac{1}{2}\omega_{max}} \tilde{w}(\omega') \chi(\omega - \omega') d\omega', \tag{2.2.14}$$

where $\tilde{w}(\omega)$ is the Fourier-Transform of $w|^n$:

$$\tilde{w}(\omega) = \frac{\Delta t \Delta N}{\sqrt{2\pi}} \text{sinc}\left(\frac{\omega \Delta t \Delta N}{2}\right) \exp\left(i \frac{\omega \Delta N \Delta t}{2}\right).$$

This convolution expression shows, that the errors introduced by the windowing operation will vanish the more delta-like $\tilde{w}(\omega)$ is:

$$\tilde{w}(\omega) \to \delta(\omega) \Longrightarrow \hat{\chi}(\omega) \to \chi(\omega). \tag{2.2.15}$$

Unfortunately, to achieve a more delta-like $\tilde{w}(\omega)$, an increased number of coefficients ΔN is necessary

$$\tilde{w}(\omega) \to \delta(\omega) \text{ for } \Delta N \to \infty$$

and hence will negatively affect the computational efficiency. This is illustrated in figure 2.2.1 which shows the result of integrating several polarization update equations based on equation 2.2.11 for various different window sizes (100, 200, 400, 800, 1600). Ultimately a compromise between the accuracy and the computational complexity of the polarization update equation must be found.

2.2.3 Recursive update equations

The above windowing method is far from computationally optimal. This is because the polarization update equation 2.2.11 is not recursive, i.e. it does not make use of previously calculated polarization values. As was shown in the Drude and Lorentzian case, this can increase computational efficiency by orders of magnitude. Indeed, one may argue that many empirical or measured polarizabilities $\chi(\omega)$ are the result of relatively simple temporal differential equations as, for example, the equation of motion in the Drude case. The discretisation of such a differential equation will typically result in a recursive equation with a relatively small number of coefficients.

We start by writing down the most general, linear recursive time-domain update equation:

$$P|^{n+1} = \sum_{n=0}^{N_A} (-a_m)\, P|^{n-m} + \sum_{m=0}^{N_B} b_m\, E|^{n-m} \quad . \tag{2.2.16}$$

where a_m and b_m are the recursion coefficients, N_A, N_B denote the number of recursion coefficients and $P|^n$, $E|^n$ are components of the polarization and electric field vector respectively. The goal is to find a relationship between the desired polar-

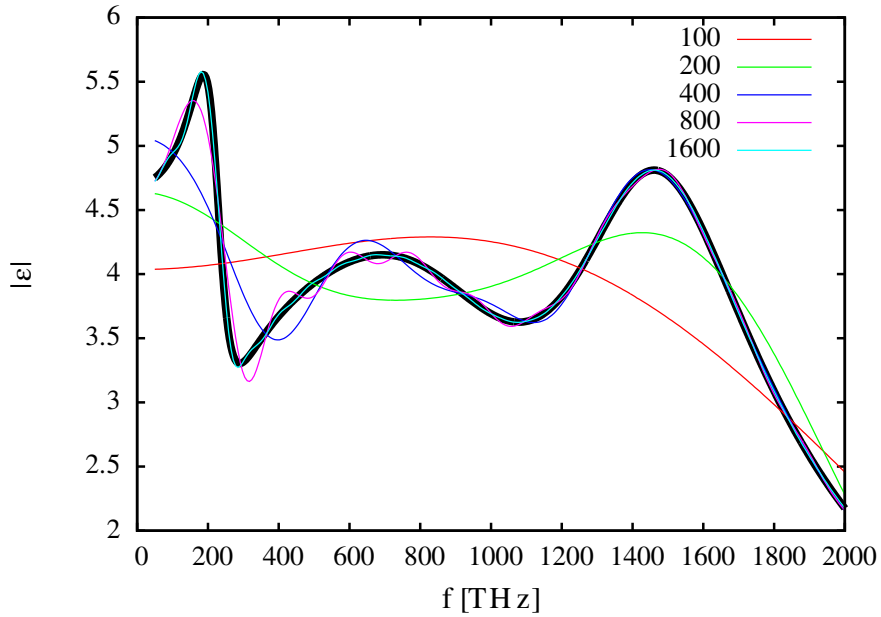

Figure 2.2.1: The accuracy of a discretised, time-domain polarization response update equation $\mathbf{P}[\mathbf{E}]$ based on equation 2.2.11 vs. an increasing number of coefficients ΔN. The bold black line is a reference dielectric function $x(\omega)$ of a complex material. The thin lines represent the retrieved dielectric function after running short FDTD simulations with the discretised polarization update equation. Various line colours show increasing numbers of coefficients ΔN. It can clearly be seen that the accuracy increases with increasing ΔN.

izability $\chi(\omega)$ and the recursion coefficients a_m, b_m. After some re-arrangements, equation 2.2.16 reads:

$$\sum_{m=-1}^{N_A} a_m \, P|^{n-m} = \sum_{m=0}^{N_B} b_m \, E|^{n-m} \quad . \tag{2.2.17}$$

where $a_{-1} := 1$ was defined. To find the frequency response of this recursive update equation, it is beneficial to introduce the z-transform[1] of the polarization current $P|^n$ and electric field $E|^n$:

$$P(z) = \sum_{n=-\infty}^{\infty} P|^n \, z^{-n} \tag{2.2.18}$$

$$E(z) = \sum_{n=-\infty}^{\infty} E|^n \, z^{-n} \tag{2.2.19}$$

With this and the cross-correlation theorem for z-transforms, the recursive update equation 2.2.17 in z-space reads:

$$P(z) \sum_{m=-1}^{N_A} a_m z^{-m} = E(z) \sum_{m=0}^{N_B} b_m z^{-m} \tag{2.2.20}$$

and with some additional re-arrangements the polarizability in z-space $\tilde{\chi}(z)$ is found [34]

$$\tilde{\chi}(z) = \frac{P_i(z)}{E_i(z)} = \frac{\sum_{m=0}^{N_A} b_m z^{-m}}{\sum_{m=-1}^{N_B} a_m z^{-m}}. \tag{2.2.21}$$

Evaluating the above equation on the complex unit circle $z = \exp(-i\varphi\Delta t)$ results in the frequency-dependent polarizability:

$$\chi(\omega) = \tilde{\chi}(\exp(-i\omega\Delta t)) = \frac{\sum_{m=0}^{N_A} b_m \exp(i\omega m\Delta t)}{\sum_{m=-1}^{N_B} a_m \exp(i\omega m\Delta t)}, \tag{2.2.22}$$

which concludes the search for a relationship between the frequency-dependent polarizability $\chi(\omega)$ and the recursion coefficients a_m, b_m.

2.2.4 Finding the recursion coefficients a_m, b_m for a given polarizability $\chi(\omega)$

The question arises if there is a method which can find the optimal values for the recursion coefficients a_m, b_m for given A, B so that the resulting recursion equation is both numerically stable (see section 2.3) and is the best approximate for a given

[1] using a discrete Fourier-Transform leads to identical results, however, the z-transform is a more natural choice when discussing the stability of the recursion equations

polarizability $\chi(\omega)$. Two methods shall now be presented which are based on key findings of control theory and the study of filter systems.

2.2.4.1 Finding recursion coefficients a_m, b_m for a given analytic expression of the polarizability $\chi(\omega)$

The following substitution method was developed by the author to automatically find the recursion coefficients a_m, b_m for simple analytic expressions of a dielectric function. It involves substituting powers of ω with trigonometric functions. As will be shown below, such an ansatz will only lead to accurate results for very low frequencies $\omega \ll \frac{1}{\Delta t}$ and therefore is a poor choice for typical control theory or filter systems. However, in FDTD, $\omega \ll \frac{1}{\Delta t}$ is a good assumption, especially for nano-plasmonic systems (see section 1.1.6).

The method works best if the polarizability $\chi(\omega)$ can be written as a rational polynomial

$$\chi(\omega) = \frac{\sum_{m=0} \tilde{c}_m \omega^m}{\sum_{m=0} \tilde{d}_m \omega^m}, \tag{2.2.23}$$

where $\tilde{c}_m$, $\tilde{d}_m$ are now the coefficients of the rational polynomial. It will be useful to stress the fact that the coefficients $\tilde{c}_m$, $\tilde{d}_m$ can be complex, by introducing the following notation

$$\chi(\omega) = \frac{\sum_{m=0} \left(c_m + ic_m^\dagger\right) \omega^m}{\sum_{m=0} \left(d_m + id_m^\dagger\right) \omega^m}, \tag{2.2.24}$$

where $c_m := \mathrm{Re}[\tilde{c}_m]$, $c_m^\dagger := \mathrm{Im}[\tilde{c}_m]$, $d_m := \mathrm{Re}[\tilde{d}_m]$ and $d_m^\dagger := \mathrm{Im}[\tilde{d}_m]$. In section 2.2.1, certain conditions on the polarizability were derived, for example:

$$\chi(-\omega) = \chi^*(\omega). \tag{2.2.25}$$

Substituting equation 2.2.24 into the LHS of the above condition gives:

$$\chi(-\omega) = \frac{\sum_{m=0} \left(c_{2m} + ic_{2m}^\dagger\right) \omega^{2m} - \sum_{m=0} \left(c_{2m+1} + ic_{2m+1}^\dagger\right) \omega^{2m+1}}{\sum_{m=0} \left(d_{2m} + id_{2m}^\dagger\right) \omega^{2m} - \sum_{m=0} \left(d_{2m+1} + id_{2m+1}^\dagger\right) \omega^{2m+1}}, \tag{2.2.26}$$

where we have split the sum into even and odd terms. On the other hand, substituting equation 2.2.24 into the RHS of the above condition gives

$$\chi^*(\omega) = \frac{\sum_{m=0} \left(c_{2m} - ic_{2m}^\dagger\right) \omega^{2m} - \sum_{m=0} \left(-c_{2m+1} + ic_{2m+1}^\dagger\right) \omega^{2m+1}}{\sum_{m=0} \left(d_{2m} - id_{2m}^\dagger\right) \omega^{2m} - \sum_{m=0} \left(-d_{2m+1} + id_{2m+1}^\dagger\right) \omega^{2m+1}}. \tag{2.2.27}$$

It can be shown any rational polynomial 2.2.23 can always be brought into a form

where equations 2.2.26 and 2.2.27 are equivalent when the following conditions are met

$$\begin{array}{l} c_n = d_n = 0 \quad \text{for} \quad n \text{ is odd} \\ c_n^\dagger = d_n^\dagger = 0 \quad \text{for} \quad n \text{ is even} \end{array}, \tag{2.2.28}$$

and therefore, any analytically given polarizabilities $\chi(\omega)$ can be written in the following form [57]

$$\chi(\omega) = \frac{\sum_{m=0} c_{2m}\omega^{2m} + i\sum_{m=0} c_{2m+1}^\dagger \omega^{2m+1}}{\sum_{m=0} d_{2m}\omega^{2m} + i\sum_{m=0} d_{2m+1}^\dagger \omega^{2m+1}}. \tag{2.2.29}$$

In the Drude case (equation 2.1.8), for example, the coefficients of the rational polynomial are

$$c_0 = -\omega_p^2;\ d_1^\dagger = \gamma;\ d_2 = 1. \tag{2.2.30}$$

To bring equation 2.2.29 into the form required by equation 2.2.22, it is necessary to replace the powers of ω with trigonometric functions. A suitable substitution can be motivated by observing the following Taylor-Expansions:

$$\sin(\omega\Delta t) \approx \omega\Delta t;\ \cos(\omega\Delta t) \approx 1 - \frac{1}{2}\Delta t^2\omega^2, \tag{2.2.31}$$

which is a good approximation when $\omega \ll \omega_{max} = \pi\Delta t^{-1}$ which is generally valid for FDTD simulations especially in the nano-plasmonic regime. After re-arranging,

$$\omega \approx \frac{\sin(\omega\Delta t)}{\Delta t};\ \omega^2 \approx \frac{2 - 2\cos(\omega\Delta t)}{\Delta t^2}, \tag{2.2.32}$$

the following substitution rules can be found

$$\begin{array}{rcl} \omega^{2m} & \rightarrow & \left[\frac{2-\exp(i\omega\Delta t)-\exp(-i\omega\Delta t)}{\Delta t^2}\right]^m = \left[\frac{2-z^{-1}-z}{\Delta t^2}\right]^m \\ i\omega^{2m+1} & \rightarrow & (-1)^m\left[\frac{\exp(i\omega\Delta t)-\exp(-i\omega\Delta t)}{2\Delta t}\right]^{2m+1} = (-1)^m\left[\frac{z^{-1}-z}{2\Delta t}\right]^{2m+1} \end{array}. \tag{2.2.33}$$

With these substitutions, the coefficients a_m and b_m can easily be determined for any analytic polarizability $\chi(\omega)$ which is of the form 2.2.29.

For example, applying these substitution rules 2.2.33 on the frequency-dependent polarizability $\chi(\omega)$ of the Drude model

$$\chi(\omega) = -\frac{\omega_p^2}{\omega(\omega + i\gamma_D)}$$

results in the following equation for $\tilde{\chi}(z)$:

$$\tilde{\chi}(z) \approx \frac{\omega_p^2\Delta t^2}{\left(1 + \frac{1}{2}\gamma\Delta t\right)z^1 - 2z^0 + \left(1 - \frac{1}{2}\gamma\Delta t\right)z^{-1}}, \tag{2.2.34}$$

from which the following recursion coefficients can be determined by comparing the above equation with equation 2.2.21:

$$b_0 = \omega_p^2 \Delta t^2;\ a_{-1} = \frac{1}{2}\gamma\Delta t + 1;\ a_0 = -2;\ a_1 = 1 - \frac{1}{2}\gamma\Delta t. \tag{2.2.35}$$

Inserting these into equation 2.2.17 and dividing both sides by a_{-1} leads to the same polarization update equation 2.1.11 which was already found in section 2.1.2.1. The Lorentz response can be derived in a similar manner as many other analytic polarizabilities.

The above method was translated into a computational algorithm and integrated into an FDTD solver which was written by the author. It allows the user to specify an analytic polarization response, from which it will calculate the recursion coefficients a_m, b_m while ensuring numerical stability (see section 2.3). More details on the implementation of this algorithm are given in section 2.3.3.

2.2.4.2 Finding recursion coefficients a_m, b_m for an experimentally given polarizability $\chi(\omega)$

Often the analytic expression for a polarizability $\chi(\omega)$ is unknown, cannot easily be written as a rational polynomial or is only available as experimental data. In these cases it is possible to determine the recursion coefficients a_m, b_m in equation 2.2.22 by fitting them to the desired polarizability $\chi(\omega)$. Let us assume that ω_j, $\chi(\omega_j)$ is the i-th data-point in a set of N data-points describing the desired polarizability $\chi(\omega)$ and that we wish to find N_A number of coefficients in the denominator and N_B number of coefficients in the nominator of equation 2.2.22. Then the following set of equations can be found by re-arranging equation 2.2.22:

$$\begin{aligned}
\sum_{k=0}^{N_B} b_k \exp\left(i\omega_1 k\Delta t\right) &= \chi(\omega_1) \sum_{k=-1}^{N_A} a_k \exp\left(i\omega_1 k\Delta t\right) \\
\sum_{k=0}^{N_B} b_k \exp\left(i\omega_2 k\Delta t\right) &= \chi(\omega_2) \sum_{k=-1}^{N_A} a_k \exp\left(i\omega_2 k\Delta t\right) \\
\vdots \qquad\qquad & \vdots \qquad\qquad\qquad \vdots \\
\sum_{k=0}^{N_B} b_k \exp\left(i\omega_N k\Delta t\right) &= \chi(\omega_N) \sum_{k=-1}^{N_A} a_k \exp\left(i\omega_N k\Delta t\right)
\end{aligned} \tag{2.2.36}$$

To ensure accurate results, it is important that the data-points in the above equations contain any asymptotic behaviour. By observing that $a_{-1} = 1$, the above set of equations can be brought into a system of linear equations:

$$\mathbf{Mx} = \mathbf{b}, \tag{2.2.37}$$

where

$$\mathbf{M} := \begin{pmatrix} \gamma_1^0 & \gamma_1^2 & \cdots & \gamma_1^B & -\chi_1\gamma_1^0 & -\chi_1\gamma_1^1 & \cdots & -\chi_1\gamma_1^A \\ \gamma_2^0 & \gamma_2^2 & \cdots & \gamma_2^B & -\chi_2\gamma_2^0 & -\chi_2\gamma_2^1 & \cdots & -\chi_2\gamma_2^A \\ & & \vdots & & & & \vdots & \\ \gamma_N^0 & \gamma_N^2 & \cdots & \gamma_N^B & -\chi_N\gamma_N^0 & -\chi_N\gamma_N^1 & \cdots & -\chi_N\gamma_N^A \end{pmatrix};$$

$$\mathbf{x} := \begin{pmatrix} b_0 \\ b_1 \\ \vdots \\ b_B \\ a_0 \\ a_1 \\ \vdots \\ a_A \end{pmatrix}; \qquad \mathbf{b} := \begin{pmatrix} \chi_1\gamma_1^{-1} \\ \chi_2\gamma_2^{-1} \\ \vdots \\ \chi_N\gamma_N^{-1} \end{pmatrix} \tag{2.2.38}$$

and $\gamma_j := \exp(i\omega_j \Delta t)$ and $\chi_j := \chi(\omega_j)$ was defined. Additionally it is required that the recursion coefficients remain real-valued for the polarization field to be physical. To ensure this, the above rows need to be split into equations for the imaginary and real parts:

$$\begin{pmatrix} \mathrm{Re}\,[\mathbf{M}] \\ \mathrm{Im}\,[\mathbf{M}] \end{pmatrix} \mathbf{x} = \begin{pmatrix} \mathrm{Re}\,[\mathbf{b}] \\ \mathrm{Im}\,[\mathbf{b}] \end{pmatrix} \tag{2.2.39}$$

The above system of linear equations can be solved for the recursion coefficients a_m, b_m by inverting the matrix (Re[$\mathbf{M}$] Im[$\mathbf{M}$]). Additionally the following condition on N_A, N_B and N is required to ensure a square matrix:

$$N_A + N_B + 2 = 2N. \tag{2.2.40}$$

In many situations there are far more data-points available than the number of fitting control points $\frac{1}{2}(N_A + N_B + 2)$ given by the desired number of recursion coefficients N_A, N_B. Therefore, better fitting algorithms than the one described above seem attractive. The most popular numerical algorithms to fit a rational polynomial to a set of data-points is the Remez algorithm[2] [58, 59]. From the experience gathered during the author's thesis, however, it was observed that the numerical stability of the algorithm was extremely fragile and tedious manual conditioning of an initial guess was required which defeats the object of having an automatic recursion coefficient finder.

The method described above was also translated into a computational algorithm and incorporated into the FDTD solver written by the author. The user must

[2] sometimes referred to as the minmax algorithm

only specify a data-file containing the values of a dielectric function, the expected asymptotic behaviour and the desired RMS error of the numerical implementation. The program will then automatically calculate the recursion coefficients a_m, b_m. It does this by successively increasing $N_A + N_B$ until the desired error is reached. More details on the implementation of this program are given in section 2.3.3.

Figure 2.2.2a) shows the spectral responses of the resulting polarization update equations with coefficients a_m, b_m determined by the aforementioned computer algorithm. The experimentally derived polarizability $\chi(\omega)$ of silver (see section 2.1.2.3) was used as an input data-set. Depending on the desired RMS error, the algorithm produced update equations with varying number of coefficients A, B. Excellent agreement is achieved with only a small number of coefficients.

2.3 Numerical Stability

The above methods will automatically determine the recursion coefficients a_m, b_m, which, when evaluated with equation 2.2.22, will be a good approximation for a given polarizability $\chi(\omega)$. However, it is yet to be shown if the recursion coefficients a_m, b_m lead to a stable numerical time-domain update equation.

There are two important factors for the overall numerical stability of a recursive update equation. Firstly, the recursion coefficients a_m, b_m must fulfil certain conditions (derived below) to be theoretically stable. Secondly, even if a set of coefficients a_m, b_m was found that fulfil these conditions, any computational implementation will lead to quantization or round-off errors which can negatively affect the numerical stability.

2.3.1 Round-off errors

As a rule of thumb, any recursion equation with $A > 3$ is known to be problematic when evaluated with single precision floating point arithmetic [34, 60]. To overcome this limitation, any higher order recursion equation $\mathbf{P}_{tot}[\mathbf{E}]$ is split into a composition of several lower order recursion equations $\mathbf{P}_\nu$

$$\mathbf{P}_{tot}[\mathbf{E}] = \mathbf{P}_N[\mathbf{P}_{N-1}[\mathbf{P}_{N-2}[\cdots\mathbf{P}_1[\mathbf{E}]]]] \tag{2.3.1}$$

each having no more than three feedback coefficients $A \leq 3$. Such lower order recursion equations are commonly referred to as "biquads[3]" and the cascaded evaluation

[3] if the inverse response $\chi^{-1}(\omega)$ should also be stable then an additional requirement is $B \leq 3$. In this case the polynomials in the numerator and denominator will both be of second order (quadratic) for $A = B = 3$, hence the name "biquad".

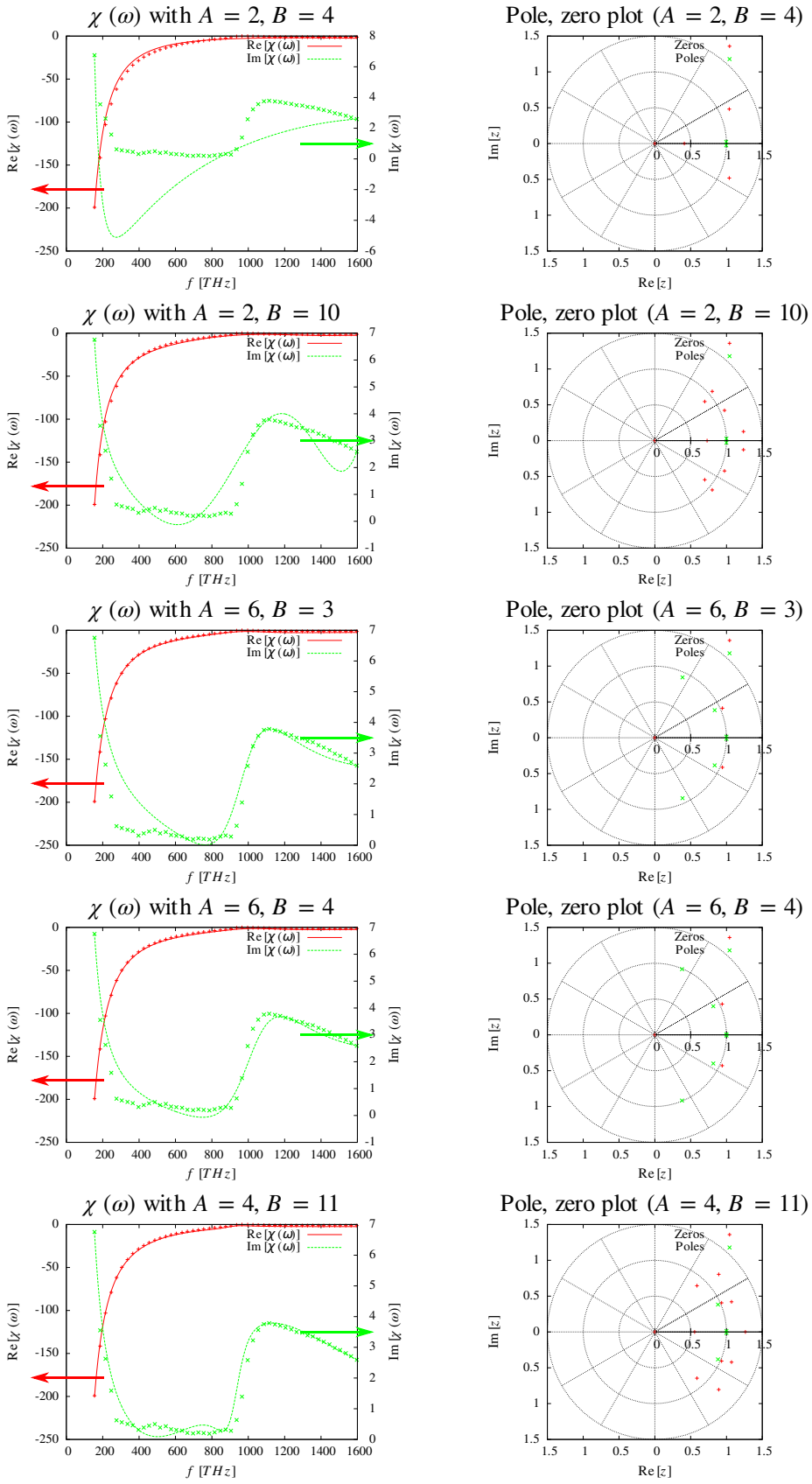

Figure 2.2.2: The result of a computational algorithm to determine the recursion coefficients a_m, b_m by fitting a rational polynomial to experimentally obtained polarization $\chi(\omega)$ of silver (green and red lines). Each row shows the result of the algorithm for a different set of number of desired coefficients A, B. a) the spectral response of the resulting time-domain update equation and b) their corresponding pole-zero plots.

of a set of biquads is referred to as a cascaded biquad filter. As each individual biquad is known to not suffer from round-off errors for all possible inputs, the overall recursion equation must also be numerically stable.

In frequency domain, each biquad $\mathbf{P}_\nu$ in equation 2.3.1 is a simple multiplication with the biquad's frequency response $\tilde{\chi}_\nu(\omega)$. Therefore, in frequency domain, the above equation reads

$$\tilde{\mathbf{P}}_{tot}\left[\tilde{\mathbf{E}}(\omega)\right] = \tilde{\chi}_N(\omega) \cdot \tilde{\chi}_{N-1}(\omega) \cdots \tilde{\chi}_1(\omega) \cdot \tilde{\mathbf{E}}(\omega)$$

and therefore the transfer function of such a polarizability in z-space is

$$\tilde{\chi}(z) = \frac{P(z)}{E(z)} = \frac{\sum_m b_m z^{-m}}{\sum_m a_m z^{-m}} = \left(\frac{\sum_m b_m^N z^{-m}}{\sum_m a_m^N z^{-m}}\right) \cdot \left(\frac{\sum_m b_m^{N-1} z^{-m}}{\sum_m a_m^{N-1} z^{-m}}\right) \cdots \left(\frac{\sum_m b_m^1 z^{-m}}{\sum_m a_m^1 z^{-m}}\right),$$

where a_m^ν, b_m^ν are now the recursion coefficients of the individual biquad update equations.

To find these coefficients it is necessary to bring the original transfer function into the following form:

$$\tilde{\chi}(z) = \frac{P(z)}{E(z)} = \frac{\prod_m^B (z^{-1} - \xi_m)}{\prod_m^A (z^{-1} - \eta_m)},$$

where ξ_m, η_m are the zeros of the polynomial in the numerator and denominator respectively. The above transfer function can now easily be split into a product of several transfer functions

$$\tilde{\chi}(z) = \frac{P(z)}{E(z)} = \left(\frac{\prod_m^B (z^{-1} - \xi_m)}{\prod_m^A (z^{-1} - \eta_m)}\right) \cdot \left(\frac{\prod_m^B (z^{-1} - \xi_m)}{\prod_m^A (z^{-1} - \eta_m)}\right) \cdots \left(\frac{\prod_m^B (z^{-1} - \xi_m)}{\prod_m^A (z^{-1} - \eta_m)}\right)$$

and by expanding the product in the numerator and denominator of each biquad, their recursion coefficients a_m^ν, b_m^ν can be found.

2.3.2 Theoretical stability condition

The theoretical condition for which a set of coefficients a_m, b_m leads to a stable update equation in time-domain shall now be derived [34]. Let us assume, that a_m, b_m denote the coefficients of a recursive update equation for which the stability shall be tested. It is beneficial to decompose the transfer function of this update equation into a transfer function with only feedback coefficients a_m and a transfer function with only input coefficients b_m:

$$\tilde{\chi}(z) = \frac{P_{tot}(z)}{E(z)} = \frac{\sum_m b_m z^{-m}}{\sum_m a_m z^{-m}} = \left(\frac{1}{\sum_m a_m z^{-m}}\right) \cdot \left(\frac{\sum_m b_m z^{-m}}{1}\right).$$

The product on the RHS of the above equation corresponds to the following coupled recursive update equations in the time-domain:

$$\begin{aligned} P^{tot}\big|^{n+1} &= \textstyle\sum_{m=0}^{N_A} a_m \, P^{tot}\big|^{n-m} + P^1\big|^n \\ P^1\big|^{n+1} &= \textstyle\sum_{m=0}^{N_B} b_m \, E\big|^{n-m} . \end{aligned}$$

The latter update equation is a discrete convolution, which is stable for any choice of b_m. Therefore, the stability of the entire update equation does not depend on the b_m coefficients.

Let us now examine the first update equation (involving the a_m) by further decomposing it into several first order transfer functions:

$$\frac{1}{\sum_m a_m z^{-m}} = \left(\frac{1}{z^{-1} - \eta_N}\right) \cdot \left(\frac{1}{z^{-1} - \eta_{N-1}}\right) \cdots \left(\frac{1}{z^{-1} - \eta_1}\right), \tag{2.3.2}$$

where η_m is the m-th zero of the polynomial $\sum_m a_m z^{-m}$. For the entire update equation to be stable, each individual update equation corresponding to each individual factor in the above transfer function must be stable. The corresponding update equation in time-domain of one of the above products is:

$$P^m\big|^{n+1} = \eta_m \, P^m\big|^n + E\big|^n$$

It is evident that any $|\eta_m| > 1$ will lead to successively increasing $P^m|^n$ with each time step, i.e. an unstable first-order filter. This is true for all of the individual first-order update equations in equation 2.3.2 and therefore, the stability of a general recursive update equation with coefficients a_m, b_m is found:

$$|\eta_m| < 1 \text{ for } 0 \leq m \leq A.$$

where η_m is the m-th pole of the update equation's transfer function (equation 2.2.21).

Interestingly, the stability of an update equation for a polarization response $\mathbf{P}|^n$ when used in an FDTD algorithm is somewhat relaxed. This is because, the polarization $\mathbf{P}\,[\mathbf{E}]$ only ever enters the FDTD update equations as a temporal difference between the current and previous time steps (see equation 2.1.3) to approximate a discretised current density $\mathbf{J}|^{n+\frac{1}{2}}$:

$$\mathbf{J}\big|^{n+\frac{1}{2}} = \frac{\mathbf{P}^{n+1}\,[\mathbf{E}] - \mathbf{P}^n\,[\mathbf{E}]}{\Delta t}.$$

The above equation can also be interpreted as a recursion equation and will have

the following transfer function

$$\frac{J(z)}{E(z)} = \frac{J(z)}{P(z)}\tilde{\chi}(z) = \frac{z^{-1}-1}{\Delta t \cdot z^{\frac{1}{2}}} \cdot \tilde{\chi}(z) = \left(\frac{z^{-1}-1}{\Delta t \cdot z^{\frac{1}{2}}}\right) \cdot \left(\frac{\sum_m b_m z^{-m}}{\sum_m a_m z^{-m}}\right).$$

Consequently, any pole at $\eta_m = 1$ of the original transfer function for $\mathbf{P}[\mathbf{E}]$ will be cancelled if used in an FDTD algorithm and therefore, the stability criteria for the recursive update equation of a material polarization response $\mathbf{P}[\mathbf{E}]$ in FDTD is

$$|\eta_m| < 1 \text{ or } \eta_m = 1 \text{ for } 0 \leq m \leq A.$$

For example, the following recursion coefficients were found for the Drude response discussed in section 2.1.2.1:

$$b_0 = \omega_p^2 \Delta t^2;\ a_{-1} = \frac{1}{2}\gamma_D \Delta t + 1;\ a_0 = -2;\ a_1 = 1 - \frac{1}{2}\gamma_D \Delta t.$$

With these coefficients, equation 2.2.21 has the following poles:

$$z_0 = 1; \quad z_1 = \frac{1 - \frac{1}{2}\gamma_D \Delta t}{1 + \frac{1}{2}\gamma_D \Delta t}$$

and therefore the Drude response is stable for any positive Drude decay rate $\gamma_D > 0$.

2.3.3 Automated computer algorithm to find recursion coefficients a_m, b_m

As mentioned in section 2.2.4, a computer algorithm was designed by the author to automatically calculate the recursion coefficients a_m, b_m for a given analytic or experimentally derived polarizability $\chi(\omega)$. The algorithm will ensure the stability of the resulting time-domain update equation. To achieve this, the following sequence of execution was developed: First, the recursion coefficients a_m, b_m are found by either replacing powers of ω with trigonometric functions (see section 2.2.4.1) or by fitting a rational polynomial to a given data-set (see section 2.2.4.2). After this, the poles and zeros of the resulting transfer function are determined. The transfer function is deemed stable if all the poles are within the complex unit circle $|\eta_m| < 1$ or are equal to one $\eta_m = 1$. For the sake of argument, let us assume that $N_{A,unstable}$ poles were found which render the transfer function unstable. These poles are removed by multiplying both sides of equation 2.2.21 with $\prod_m^{A_{unstable}} \left(z^{-1} - \eta_m^{unstable}\right)$. The remaining poles and zeros are split into groups of three - each group representing the transfer function of a stable biquad. The recursion coefficients a_m^ν, b_m^ν of each biquad are then determined by expanding the numerator and denominator of each biquad's transfer function. The result of this first iteration is a cascaded, stable,

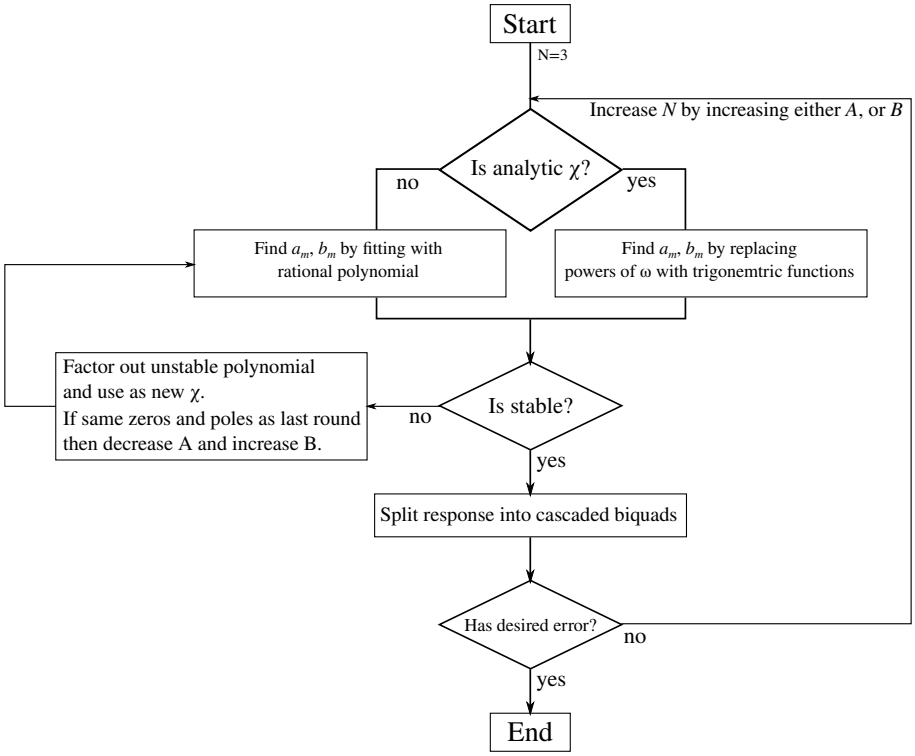

Figure 2.3.1: An algorithm to find the recursion coefficients a_m, b_m for a desired polarizability $\chi(\omega)$ and maximum error. Details of the algorithm can be found in the text.

time-domain polarization functional $\mathbf{P}|^n$ which has the following frequency domain response

$$\frac{\tilde{P}(\omega)}{\tilde{E}(\omega)} = \chi(\omega) \prod_{m=0}^{N_{A,unstable}} \left(\exp(i\omega\Delta t) - \eta_m^{unstable}\right).$$

Obviously, if no unstable poles were found then $N_{A,unstable} = 0$ and the product on the RHS of the above equation will evaluate to one and the algorithm is finished. Otherwise, the program starts a second iteration by trying to find the recursion coefficients for the following new polarization response:

$$\chi^{II}(\omega) = \frac{1}{\sum_{m=0}^{N_{A,unstable}} \left(\exp(i\omega\Delta t) - \eta_m^{unstable}\right)},$$

where $\chi^{II}(\omega)$ denotes that this is the polarization response of the second pass of the computer algorithm. To ensure that not the same poles are found again, the number of recursion coefficients of the second iteration pass is modified, for example, by decreasing the number of feedback coefficients and increasing the number of B coefficients:

$$N = N_{A,unstable} - 1; \quad B = 2.$$

In the worst case, the resulting transfer function will have one less pole than the previous iteration ensuring the overall convergence of the algorithm. Each iteration will produce a set of stable cascaded biquads, which will result in the desired approximation for the initial polarizability $\chi(\omega)$ when evaluated in total. A simplified flow-chart of the complete algorithm is depicted in figure 2.3.1.

Although, the recursion coefficients produced by the algorithm result in polarization responses which have an excellent agreement with the desired polarizability $\chi(\omega)$ (shown in figure 2.2.2), the algorithm must be considered in the prototype stage as it has several limitations. As was already mentioned above, the fitting algorithm to find the recursion coefficients a_m, b_m based on equations 2.2.37-2.2.38 will only have $\frac{1}{2}(N_A + N_B + 2)$ fitting control points. Thus, for small N_A, N_B, the resulting polarization response is only expected to match the given polarizability $\chi(\omega)$ at very few points. Additionally, in the current implementation of the algorithm, the inversion of the matrix (Re[$\mathbf{M}$] Im[$\mathbf{M}$]) becomes singular for $N_A + N_B > 19$ due to floating-point rounding errors. Finally, it was observed that only certain combinations of A, B lead to stable recursion coefficients with low errors. This was independent of the choice of the input polarizability $\chi(\omega)$ - at least for the polarizabilities tested during the course of this thesis. Further investigation would be needed for the origin of this phenomena which may lead to further optimizations of the above algorithm.

2.4 Anisotropic materials

The above discussions were limited to isotropic materials, i.e. materials which can be described by scalar-valued polarization functional or dielectric constant. The extension of the FDTD method to anisotropic materials is useful so that a wider range of materials can be studied. An additional motivation for anisotropic response functions is to accommodate a method known as "sub-pixel" averaging which will be discussed in chapter 4. In short, the sub-pixel averaging method replaces the material response of a Yee cell containing a boundary between several materials, with an anisotropic response function, even if the original materials are all isotropic. In fact, it will be shown that the sub-pixel averaging method is a key requirement for the accurate simulation of nano-plasmonic systems.

The challenges associated with anisotropic materials, stem from the co-location of the electro-magnetic fields within the FDTD method. For example, the x-component of the update equation for the electric field within an anisotropic material with the response $\mathbf{P}[\mathbf{E}]$ reads

$$E_x|^{n+1}_{i,j,k-\frac{1}{2}} = E_x|^{n}_{i,j,k-\frac{1}{2}} + (\nabla \times \mathbf{H})_x|^{n}_{i,j,k-\frac{1}{2}} - P_x|^{n+1}_{i,j,k-\frac{1}{2}} + P_x|^{n}_{i,j,k-\frac{1}{2}},$$

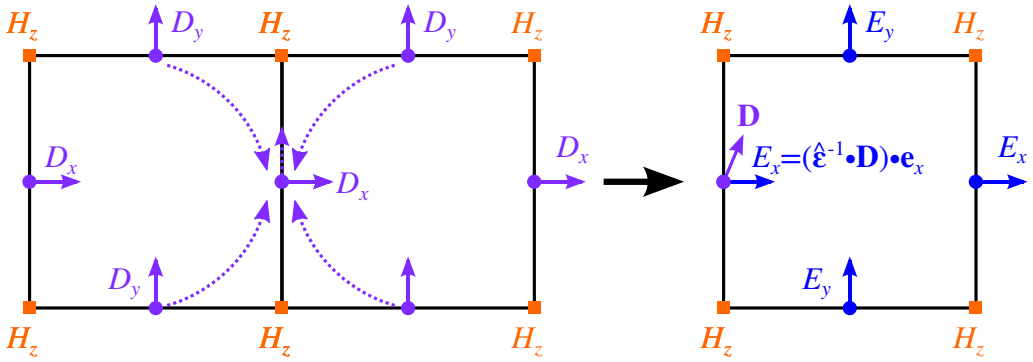

Figure 2.4.1: Diagram on how to apply an isotropic material response by spatially interpolating the components which are not available at a particular Yee cell location (offset spatial averaging). To simplify the diagram, it was assumed that the material response can be written as a static dielectric tensor $\hat{\varepsilon}$. The procedure is only shown for the x-component and must be repeated for all other components.

where $P_x|_{i,j,k-\frac{1}{2}}$ depends on the *entire* electric field vector $\mathbf{E}$

$$P_x|_{i,j,k-\frac{1}{2}} = \mathbf{e}_x \cdot \mathbf{P}\left[\mathbf{e}_x\, E_x|_{i,j,k-\frac{1}{2}} + \mathbf{e}_y\, E_y|_{i,j,k-\frac{1}{2}} + \mathbf{e}_z\, E_z|_{i,j,k-\frac{1}{2}}\right]. \tag{2.4.1}$$

Unfortunately, due to the co-location of the fields, only the x-component of the electric field is known at the position $\mathbf{r}_{i,j,k-\frac{1}{2}}$ (see for example figure 1.1.2 in the previous chapter).

2.4.1 Offset spatial averaging

To overcome this limitation, some form of spatial interpolation is necessary. One option, for example, is to linearly interpolate the unknown field components $E_y|_{i,j,k-\frac{1}{2}}$, $E_z|_{i,j,k-\frac{1}{2}}$ to the location of the $E_x|_{i,j,k-\frac{1}{2}}$ component [61]. With this the above equation reads

$$\begin{aligned} P_x|_{i,j,k-\frac{1}{2}} = \mathbf{e}_x \cdot \mathbf{P}\Big[\mathbf{e}_x\, E_x|_{i,j,k-\frac{1}{2}} \;&+\; \tfrac{1}{4}\mathbf{e}_y \Big(E_y|_{i,j+\frac{1}{2},k} + E_y|_{i,j+\frac{1}{2},k-1} \\ &+\; E_y|_{i,j-\frac{1}{2},k} + E_y|_{i,j-\frac{1}{2},k-1}\Big) \\ &+\; \tfrac{1}{4}\mathbf{e}_z \Big(E_z|_{i+\frac{1}{2},j,k} + E_z|_{i+\frac{1}{2},j,k-1} \\ &+\; E_z|_{i-\frac{1}{2},j,k} + E_z|_{i-\frac{1}{2},j,k-1}\Big) \end{aligned}$$

2.4.2 Symmetric, cell-centred spatial interpolation

Another, more symmetric interpolation method is to linearly interpolate all electric field components to a single point [61], for example, the centre of the Yee cell, where

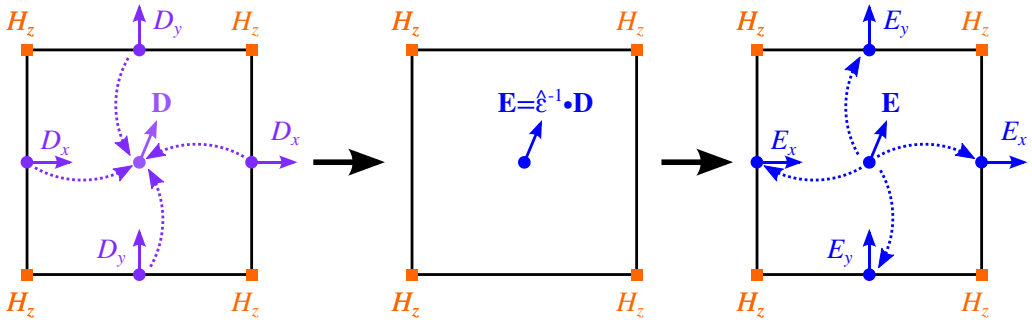

Figure 2.4.2: Diagram on how to apply an isotropic material response by spatially interpolating all components to the Yee cell centre (cell-centred spatial averaging). To simplify the diagram, it was assumed that the material response can be written as a static dielectric tensor $\hat{\varepsilon}$. After the displacement current $\mathbf{D}$ has been centred and the electric field calculated $\mathbf{E}$, the field must be spread-out again to its original locations.

the anisotropic polarization functional can now be applied

$$\mathbf{P}|_{ijk} = \mathbf{P}\left[\tfrac{1}{2}\left(E_x|_{ij,k-\frac{1}{2}} + E_x|_{ij,k+\frac{1}{2}}\right)\mathbf{e}_x \quad +\tfrac{1}{2}\left(E_y|_{i,j+\frac{1}{2},k} + E_y|_{i,j+\frac{1}{2},k}\right)\mathbf{e}_y \right.$$
$$\left. +\tfrac{1}{2}\left(E_z|_{i+\frac{1}{2},j,k} + E_z|_{i-\frac{1}{2},j,k}\right)\mathbf{e}_z\right].$$

Once calculated, the polarization vector must be spread out again to the original positions in the Yee cell

$$P_x|_{i,j,k-\frac{1}{2}} = \frac{1}{2}\left(\mathbf{P}|_{i,j,k}\cdot\mathbf{e}_x + \mathbf{P}|_{i,j,k-1}\cdot\mathbf{e}_x\right)$$

$$P_y|_{i,j+\frac{1}{2},k} = \frac{1}{2}\left(\mathbf{P}|_{i,j,k}\cdot\mathbf{e}_y + \mathbf{P}|_{i,j+1,k}\cdot\mathbf{e}_y\right)$$

$$P_z|_{i-\frac{1}{2},j,k} = \frac{1}{2}\left(\mathbf{P}|_{i,j,k}\cdot\mathbf{e}_z + \mathbf{P}|_{i-1,j,k}\cdot\mathbf{e}_z\right),$$

after which the update equation for the electric field can be executed.

Both of the above interpolation methods have been sketched in figure 2.4.1 and figure 2.4.2 respectively. The former method has the advantage that the diagonal components of the polarization tensor do not require spatial interpolation, whereas the latter method is appealing due to its symmetry. In a systematic analysis [61], it was shown that the offset spatial averaging technique produces less errors than the cell-centred spatial interpolation. Both methods, however, have the same computational complexity.

2.5 Conclusion

This chapter derived a set of numerical methods to accurately model the response of complex, anisotropic and dispersive media within an FDTD integration scheme. It was shown that translating any non-trivial frequency-dependent response into a computationally efficient time-domain polarization update equation is highly non-trivial. In general, any linear polarization update equation can be written as a general recursive update equation with recursion coefficients a_m, b_m. The difficulty lies in finding a minimum number of a_m, b_m coefficients that result in an update equation that has a frequency response sufficiently similar to the desired frequency domain polarizability $\chi(\omega)$.

Two methods which are suitable for analytically and experimentally given polarizabilities $\chi(\omega)$, respectively, were developed to find these coefficients. However, none of these methods ensure that the coefficients result in a numerically stable recursion equation. Therefore, a third algorithm was presented on how to transform a set of possibly unstable recursion coefficients a_m, b_m into a set of cascaded biquads, several recursion equations evaluated in composition, each having no more than three feedback coefficients a_m. Such low-order biquads are known to improve stability. The practical relevance of the developed algorithms was demonstrated by applying them to the experimentally derived polarizability of silver. It was shown that excellent agreement with the experimental data can be achieved with $N_A + N_B \leq 15$ recursion coefficients. Limitations of the algorithm, such as the number of fitting control points being determined by the number of recursion coefficients N_A, N_B, were also discussed.

The final section of this chapter showed that some form of spatial interpolation is necessary to correctly model anisotropic materials and presented two common spatial interpolation schemes.

Chapter 3

Non-linear Materials and Semi-classical Systems

The overall goal of this thesis is to investigate if the FDTD method can be used as a computationally efficient solver for non-linear, nano-plasmonic systems. Therefore, the discussion of material responses shall now be extended to non-linear material responses. Two non-linear material models will be derived in the first section of this chapter: the polarization response of a χ^3 material and the response of a two- or four-level system.

In addition to the responses of non-linear materials, the question arises, if it is generally possible to describe quantum phenomena with the FDTD method. Strictly, the answer to this question must be "no" as the FDTD equations were derived from classical equations. However, in physics, it is common practice to substitute a quantum system with a quasi-classical "surrogate" model - a model which has a sufficiently similar response to the quantum system but can be solved with classical equations. In this context, it is a valid question if the FDTD method is a more suitable tool to solve typical semi-classical phenomenon than other popular electro-magnetic solvers due to its time-domain nature.

The answer to this question is by no means obvious: for example, the equation predicting the quantum phenomena of decay due to spontaneous emission is of nearly identical form to the equation describing the free-space decay of a classical harmonic oscillator model [62]. Even if the harmonic oscillator is not damped ($\gamma_L = 0$ in equation 2.1.14 in section 2.1.2.2), the harmonic oscillator will decay in a *finite* amount of time due to the back-coupling of the electro-magnetic waves produced by the oscillator [63]. Although a classical phenomena, a typical frequency based solver will fail to capture some aspects of this decay, as will be shown in this chapter. Therefore, one can say that the FDTD method captures phenomena associated with spontaneous emission more naturally.

The second section of this chapter will show that the FDTD method can be used to describe another important semi-classical phenomena typically associated with strongly coupled quantum systems: Rabi splitting. This model will additionally be used to interpret the numerical results of chapter 5.

3.1 χ^3-materials

The polarization response of a χ^3-material in time-domain is straightforward:

$$\mathbf{P}_\chi|^n = \chi \left(\mathbf{E}|^n\right)^3, \tag{3.1.1}$$

where $\mathbf{P}_\chi|^n$ denotes the polarization due to the χ^3 non-linear material. The challenge, however, lies in the fact that the response is instantaneous, yet non-linear. The difficulty can be easily be seen by inserting the above polarization response into the update equation for the electric field:

$$\mathbf{E}|^{n+1} = \mathbf{E}|^n + c\Delta t \left(\nabla \times \mathbf{H}\right)|^{n+\frac{1}{2}} - \chi \left(\mathbf{E}|^{n+1}\right)^3 + \chi \left(\mathbf{E}|^n\right)^3, \tag{3.1.2}$$

where the RHS depends on the electric field of the next time step $\mathbf{E}|^{n+1}$. If the instantaneous response were linear, then χ can be absorbed in the pre-factor $c\Delta t$ as was done in the case for simple dielectric materials (section 2.1.1). In theory, it is also possible to solve the above equation for $\mathbf{E}|^{n+1}$, for example, with an iterative solver. However, such an approach would break the overall architecture of the FDTD algorithm, for example, it would require significant modification of the core FDTD update equations and all other non-instantaneous material models which potentially also exist in the system.

A simple trick can be used to avoid such modifications: instead of numerically integrating the physical electro-magnetic fields with the FDTD update equations, it is possible to introduce a new auxiliary field

$$\tilde{\mathbf{E}}\Big|^n := \mathbf{E}|^n + \mathbf{P}_\chi|^n. \tag{3.1.3}$$

This auxiliary field was chosen in such a way, that the update equation of the auxiliary field matches the original form of the FDTD update equations *as if there weren't any instantaneous responses*:

$$\tilde{\mathbf{E}}\Big|^{n+1} = \tilde{\mathbf{E}}\Big|^n + c\Delta t \left(\nabla \times \mathbf{H}\right)|^{n+\frac{1}{2}} - \sum_i \mathbf{P}_i|^{n+1} + \sum_i \mathbf{P}_i|^n, \tag{3.1.4}$$

where $\mathbf{P}_i|^n$ is the i-th non-instantaneous response which may also be present in the system. With this simple redefinition, the form of the FDTD update equations can

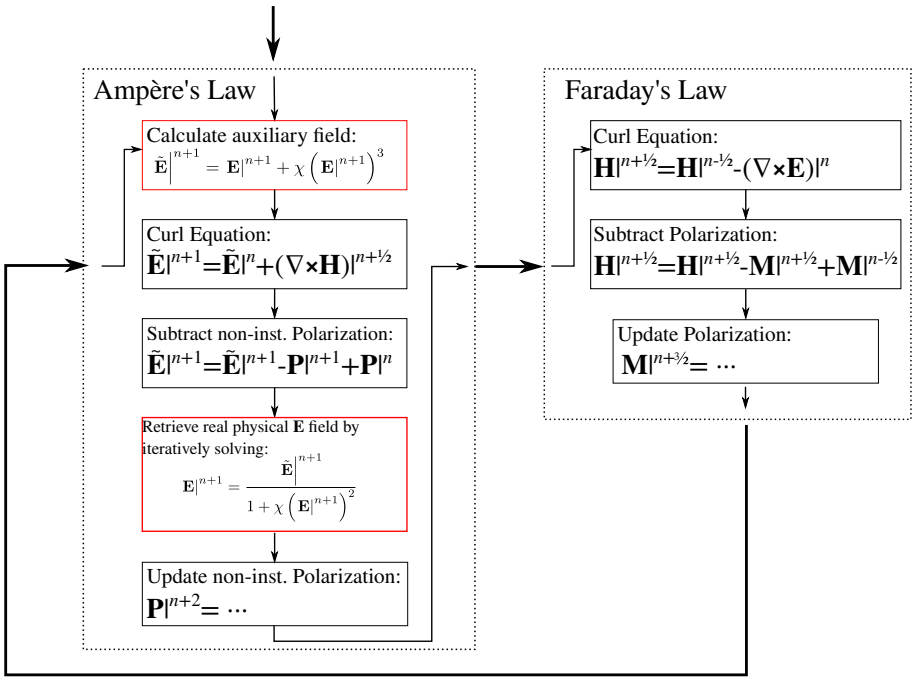

Figure 3.1.1: Diagram of the computational algorithm required to simulate a system containing a χ^3 non-linearity. Steps which are not in the core FDTD update loop are highlighted in red. Details of the algorithm can be found in the text.

be preserved.

Unfortunately, the update equations for the non-instantaneous responses $\mathbf{P}_i|^{n+2} = ...$ and the update equation for the magnetic field $\mathbf{H}|^{n+\frac{3}{2}} = ...$ of the subsequent time step will still depend on the real physical electric field $\mathbf{E}|^{n+1}$. Therefore, before the polarization and magnetic field update equations for the next time step are executed, the auxiliary field $\tilde{\mathbf{E}}|^{n+1}$ must be transformed into the real physical field $\mathbf{E}|^{n+1}$. This can be achieved by substituting equation 3.1.1 into equation 3.1.3 and re-arranging

$$\mathbf{E}|^{n+1} = \frac{\tilde{\mathbf{E}}\big|^{n+1}}{1+\chi\left(\mathbf{E}|^{n+1}\right)^2}, \tag{3.1.5}$$

which can be solved with an iterative approach, i.e. by replacing $\mathbf{E}|^{n+1}$ on the RHS of the above equation with the result (LHS) of the previous iteration. The auxiliary field $\tilde{\mathbf{E}}|^{n+1}$ can be used as an initial guess. After the iteration loop has converged and the real electric field has been found, the non-instantaneous polarization update equations $\mathbf{P}_i|^{n+1} = ...$ can be executed along with Faraday's Law (the magnetic field update equations). However, before, the next electric field update equation is executed, the physical electric field must now be re-replaced with the axillary field again. Luckily, this step is straightforward:

$$\tilde{\mathbf{E}}\big|^{n+1} = \mathbf{E}|^{n+1} + \chi\left(\mathbf{E}|^{n+1}\right)^3. \tag{3.1.6}$$

In summary, to include a non-linear instantaneous material response such as a χ^3 material, it is necessary to add two additional steps to the core FDTD algorithm (see figure 3.1.1): an additional step directly after the electric field update equation, which transforms the auxiliary field into a physical electric field $\tilde{\mathbf{E}}|^{n+1} \rightarrow \mathbf{E}|^{n+1}$, and an additional step directly before the electric field update equation, which does the reverse $\mathbf{E}|^{n+1} \rightarrow \tilde{\mathbf{E}}|^{n+1}$. The core update equations and any update equations for any other non-instantaneous polarizations need not be modified in any way.

Although this method of calculating χ^3 non-linearities is not new [64], the order of evaluation of the polarization functional and the technique of introducing an auxiliary field will be benefecial for the discussion of material boundaries in chapter 4.

3.2 Two- and Four-Level quantum system[1]

The optical Bloch equations describe the dynamics of a two-level quantum system interacting with an electro-magnetic field [65, 66]. The Maxwell-Bloch equations are an approximation derived with the Jaynes-Cummings Hamiltonian [67] which includes an interaction term effectively coupling a classical electro-magnetic field and a two-level quantum system. Thus the quantum nature of the electro-magnetic fields are neglected - a good approximation for fields with energies much greater than $\hbar\omega$. The Maxwell-Bloch equations are formulated as equations of motion for the density matrix $\tilde{\rho}$ of the two-level quantum system:

$$\begin{array}{rcrcl} \partial_t\tilde{\rho}_{00} & = & -\partial_t\tilde{\rho}_{11} & = & i\hbar^{-1}\left(\tilde{\rho}^*_{01} - \tilde{\rho}_{01}\right)\boldsymbol{\mu}\cdot\mathbf{E} \\ \partial_t\tilde{\rho}_{01} & = & \partial_t\tilde{\rho^*}_{01} & = & -i\omega_0\tilde{\rho}_{01} + \gamma\tilde{\rho}_{01} - i\hbar^{-1}\left(\rho_{11} - \rho_{11}\right)\boldsymbol{\mu}\cdot\mathbf{E}, \end{array} \tag{3.2.1}$$

where ω_0 is the transition frequency between both energy levels, γ is the line-width of the transition and $\boldsymbol{\mu}$ is the microscopic dipole vector of the quantum system.

The above equations are not well suited for a numerical time-integration scheme as they contain mixed real and imaginary components. However, by splitting $\tilde{\rho}_{01}$ into real and imaginary parts $\tilde{\rho}_{01} := \rho_{01} + i\rho^\dagger_{01}$ the above equation can be decomposed into the following coupled equations

$$\partial_t\rho_{01} = \omega_0\rho^\dagger_{01} + \gamma\rho_{01} \tag{3.2.2}$$

$$\partial_t\rho^\dagger_{01} = -\omega_0\rho_{01} + \gamma\rho^\dagger_{01} - \hbar^{-1}\left(\rho_{22} - \rho_{00}\right)\boldsymbol{\mu}\cdot\mathbf{E} \tag{3.2.3}$$

$$\partial_t\rho_{11} = 2\hbar^{-1}\rho^\dagger_{01}\boldsymbol{\mu}\cdot\mathbf{E} \tag{3.2.4}$$

$$\rho_{00} + \rho_{11} = 1 \tag{3.2.5}$$

[1] The derivation of this section is largely based on the work of S. Wüstner et al. [1]

By further substituting equation 3.2.2 into equation 3.2.4 and equations 3.2.2, 3.2.3 into the time derivative of equation 3.2.2, it is possible to eliminate the dependency on all imaginary quantities:

$$\partial_t \rho_{11} = 2\hbar^{-1}\omega_0^{-1}\left(\partial_t \rho_{01} - \gamma\rho_{01}\right)\boldsymbol{\mu}\cdot\mathbf{E} \tag{3.2.6}$$

$$\partial_t^2 \rho_{01} = 2\gamma\partial_t\rho_{01} - \left(\omega_0^2+\gamma^2\right)\rho_{01} - \omega_0\hbar^{-1}\left(\rho_{11}-\rho_{00}\right)\boldsymbol{\mu}\cdot\mathbf{E} \tag{3.2.7}$$

The above equations depend on the individual orientation of the microscopic dipoles $\boldsymbol{\mu}$. By assuming that the microscopic dipoles $\boldsymbol{\mu}$ are randomly, yet uniformly oriented in every direction of space, the above equations can be written as

$$\partial_t \rho_{11}\boldsymbol{\mu} = \frac{2}{3}\hbar^{-1}\omega_0^{-1}\left(\partial_t \rho_{01} - \gamma\rho_{01}\right)|\mu|^2\,\mathbf{E} \tag{3.2.8}$$

$$\partial_t^2 \rho_{01}\boldsymbol{\mu} = 2\gamma\partial_t\rho_{01}\boldsymbol{\mu} - \left(\omega_0^2+\gamma^2\right)\rho_{01}\boldsymbol{\mu} - \frac{1}{3}\omega_0\hbar^{-1}|\mu|^2\,\mathbf{E}\left(\rho_{11}-\rho_{00}\right), \tag{3.2.9}$$

where both sides of the above equations were multiplied with $\boldsymbol{\mu}$ and averaged over each spatial direction.

The above equations can now be used in a numerical time-integration scheme such as the FDTD method. However, the back-coupling of the two-level system with the electro-magnetic field is still missing. This can be found by realizing that the macroscopic polarization $\mathbf{P}[\mathbf{E}]$ of an ensemble of many two-level systems is given by [68, 1]:

$$\mathbf{P} = \frac{N}{V}\left(\tilde{\rho}_{01}+\tilde{\rho}_{10}\right)\boldsymbol{\mu}, \tag{3.2.10}$$

where N/V is the density of the two-level systems. With $\tilde{\rho}_{01} = \tilde{\rho}_{10}^*$ the above equation reads

$$\mathbf{P} = 2\frac{N}{V}\rho_{01}\boldsymbol{\mu}, \tag{3.2.11}$$

and by multiplying both sides of equation 3.2.9 by $2\frac{N}{V}$ the following relation between the macroscopic polarization vector $\mathbf{P}$ and the electric field can be found $\mathbf{E}$:

$$\partial_t^2\hat{\mathbf{P}} - 2\gamma\partial_t\hat{\mathbf{P}} + \left(\omega_0^2+\gamma^2\right)\hat{\mathbf{P}} = -\frac{2\omega_0|\mu|^2\left(N_1-N_0\right)}{3\hbar V}\mathbf{E}, \tag{3.2.12}$$

where the occupation numbers $N_0 := N\rho_{00}$ and $N_1 := N\rho_{11}$ were introduced. Similarly, by multiplying both sides of equation 3.2.8 by the number of two-level systems N, equation 3.2.8 can be written as [1]:

$$\partial_t N_1 = -\partial_t N_0 = -\tau_{10}N_1 + \frac{1}{3}\hbar^{-1}\omega_0^{-1}V\mathbf{E}\left(\partial_t\mathbf{P} - \gamma\mathbf{P}\right), \tag{3.2.13}$$

where a non-radiative decay half-life τ_{10} from level N_1 to N_0 was also included. Equations 3.2.12 and 3.2.13 form a self-consistent set of coupled equations to numerically

integrate the polarization current induced by a quantum mechanical two-level system coupled to a classical electro-magnetic field. These equations can be integrated along-side the FDTD update equations.

Technically, the relation linking the macroscopic polarization to the components of the density matrix (equation 3.2.10) assumes that the microscopic two-level systems do not interact. However, the above derivation was done for the response of a single Yee cell. Consequently, equation 3.2.10 only assumes that the microscopic two-level systems are non-interacting within a single Yee cells. The two-level systems of separate Yee cells can still interact via the electro-magnetic fields solved by the FDTD update equations.

It is interesting to note that equation 3.2.12 is identical to the polarization of a Lorentzian response (see equation 2.1.14 in section 2.1.2.2) with the Lorentzian coupling factor $\Delta\epsilon$ given by [1]

$$\Delta\epsilon := \frac{2\left|\mu\right|^2}{3\omega_0 V\hbar}\left(N_0 - N_1\right), \tag{3.2.14}$$

i.e. the coupling strength of the Lorentzian is proportional to the occupation inversion $N_1 - N_0$ of the two-level system. As the latter is modified by the electric field strength $\mathbf{E}$ via equation 3.2.13, the overall response of the two-level system must be non-linear. However, if the electric field strength $\mathbf{E}$ is sufficiently small to not significantly modify the coupling strength, then the two-level system can be completely modelled by a linear Lorentzian response. This regime is often referred to as the small-signal-regime.

The extension of the above model to a four-level system is straightforward: both the absorption line $N_0 \to N_3$ and the emission line $N_1 \to N_2$ are modelled with two two-level systems [1]:

$$\begin{aligned}
\partial_t^2\mathbf{P}_{abs} - 2\gamma_{abs}\partial_t\mathbf{P}_{abs} + \left(\omega_{abs}^2 + \gamma_{abs}^2\right)\mathbf{P}_{abs} &= -2\omega_{abs}\frac{\left|\mu_{abs}\right|^2}{V\hbar}\left(N_3 - N_0\right)\mathbf{E} \\
\partial_t^2\mathbf{P}_{ems} - 2\gamma_{ems}\partial_t\mathbf{P}_{ems} + \left(\omega_{ems}^2 + \gamma_{ems}^2\right)\mathbf{P}_{ems} &= -2\omega_{ems}\frac{\left|\mu_{ems}\right|^2}{V\hbar}\left(N_2 - N_1\right)\mathbf{E}
\end{aligned}, \tag{3.2.15}$$

where the *abs*, *ems* indicates that the quantity belongs to the absorption, emission line respectively. Both update equations are coupled by including non-radiative transitions $N_3 \to N_2$ and $N_1 \to N_0$ in the rate equations for the occupation densities [1]

$$\begin{aligned}
\partial_t N_3 &= -\partial_t N_0 &&= -\tau_{30}N_3 - \tau_{10}N_1 + \hbar^{-1}\omega_{abs}^{-1}\mathbf{E}\left(\partial_t\mathbf{P}_{abs} - \gamma_{abs}\mathbf{P}_{abs}\right) \\
\partial_t N_2 &= -\partial_t N_1 &&= -\tau_{21}N_2 + \tau_{32}N_3 + \hbar^{-1}\omega_{ems}^{-1}\mathbf{E}\left(\partial_t\mathbf{P}_{ems} - \gamma\mathbf{P}_{ems}\right)
\end{aligned}. \tag{3.2.16}$$

This again forms a complete set of differential equations which can be numerically in-

tegrated along side the FDTD update equations by discretising the time-derivatives with central differences.

It may come as a surprise that a model for a two-level quantum system can be formulated by simply modulating the coupling factor $\Delta\epsilon$ of a Lorentz oscillator model with an additional, relatively simple auxiliary update equation. However, this is only one of many examples where the time-domain nature of the FDTD method can naturally describe phenomena typically associated with quantum system with only very little or no modification at all. For example, it will now be shown that when the optical Bloch equations are implemented in an FDTD scheme - as was done above - phenomena associated with the spontaneous emission of quantum two-level systems are qualitatively predicted. Another example, Rabi splitting, will be given in the next section of this chapter.

Although FDTD has no concept of photons, a free-space decay of an inverted two-level system can be seen in an FDTD simulation even if the line-width entering the Lorentzian resonance formula is infinitely sharp ($\gamma_L = 0$ in equation 2.1.16). In an FDTD simulation, this is solely due to the self-interaction of the Lorentzian oscillator with its own electro-magnetic fields (radiation reaction). Similar to spontaneous emission, the decay rate is proportional to the local density of states and will therefore be modified by its environment [69]. This analogy between the quantum and classical systems has often been pointed out in literature [62, 70] and is not unique to the FDTD method. However, a typical frequency-domain based solver cannot show this phenomena if it is not specifically accounted for by modifying the line-width which enters the Lorentzian resonance formula [71]. This is because a frequency-domain solver calculates the response of the system for each frequency ω of interest individually. For each frequency ω, a static, possibly complex, dielectric constant $\varepsilon = 1 + \chi_L(\omega)$ is assigned to the Lorentzian material where $\chi_L(\omega)$ is the polarizability of a Lorentzian resonance. If, for example, the Lorentzian resonance is infinitely sharp ($\gamma_L = 0$) then the Lorentzian material would be indistinguishable from vacuum for any simulation which is off-resonant as $\chi_L(\omega) = 0$ for any $\omega \neq \omega_0$.

3.3 Semi-classical model of strong coupling

To show that the FDTD method can correctly describe phenomena typically associated with quantum processes, a semi-classical model for the Rabi splitting of strongly coupled classical systems was developed in collaboration with Dr. Joachim Hamm. The results of this section will be used to validate numerical experiments in chapter 5.

The model assumes that the solution of the purely plasmonic or optical system is known and we treat the two- or four-level system as a first-order perturbation.

This perturbation approach can be expressed by including all plasmonic responses of the system in the dielectric constant $\varepsilon(\omega)$, while accounting for the remaining response of the two- or four-level system in a polarization current $\mathbf{P}_{QM}$. With this choice, the Helmholtz wave equation reads:

$$\partial_t^2 \mathbf{E}_{tot}(\mathbf{r},t) = -\varepsilon^{-1}\nabla\times\nabla\times\mathbf{E}_{tot}(\mathbf{r},t) - \varepsilon^{-1}\partial_t^2\mathbf{P}_{QM}(\mathbf{r},t)$$

As stated, we now assume that the solution for the purely plasmonic system is known as a set of eigenmodes $\mathbf{u}_m(\mathbf{r})\cdot\exp(i\cdot\tilde{\omega}_m\cdot t)$, i.e. each eigenmode fulfils the Helmholtz wave equation of the purely plasmonic system:

$$\nabla\times\nabla\times\mathbf{u}_m(\mathbf{r}) = -\varepsilon\tilde{\omega}_m^2\mathbf{u}_m(\mathbf{r}). \tag{3.3.1}$$

Strictly, the number of eigenmodes of a radiating plasmonic system can be infinitely dense. However, here we assume that one can describe the plasmonic system sufficiently well with a discrete set of eigenmodes with complex $\tilde{\omega}_m = \omega_m + i\cdot\gamma_m$, where the imaginary part of $\tilde{\omega}_m$ describes the decay of the mode, for example, due to radiative or ohmic losses. Further, we assume that the eigenmodes are orthonormal:

$$\int \mathbf{u}_n(\mathbf{r}')\cdot\mathbf{u}_m^*(\mathbf{r}')\,d^3r' = \delta_{nm}. \tag{3.3.2}$$

For this assumption to be valid, several other approximations may need to be invoked. For example, in many plasmonic system the resonances are well separated in frequency. In such as system, it is a good assumption to neglect all other eigenmodes apart from the resonance which lies closest to the emission/absorption lines of the quantum mechanical system. In this case, condition 3.3.2 always holds, as there is only a single eigenmode to consider. In the system which will be discussed in chapter 5, there are two eigenmodes - a symmetric and anti-symmetric mode - with nearly identical frequency. Due to the symmetry of the spatial profiles of these modes, it will be shown that condition 3.3.2 still holds (see section 5.2 for more details).

We now further assume that the quantum mechanical perturbation has little influence on the spatial mode profiles of the system, i.e. that the total electric field, which now includes both the quantum mechanical and the plasmonic response, can be written as a superposition of the eigenmodes:

$$\mathbf{E}_{tot}(\mathbf{r},t) \approx \sum_m \tilde{E}_m(t)\,\mathbf{u}_m(\mathbf{r})\exp(i\tilde{\omega}_m t). \tag{3.3.3}$$

This is generally a good assumption, if the volume of the quantum mechanical system V_{QM} is small compared to the volume of the plasmonic system. This becomes evident if one views the quantum mechanical system similar to an infinitesimally

small incident dipole source. In such a system the infinitesimally small spatially delta-like dipole will only excite the available spatial modes $\mathbf{u}_m$ of the system. If, on the other hand, the quantum mechanical system is spatially extended, then the effective dielectric constant of the quantum mechanical system will significantly alter the solutions of the plasmonic system $\mathbf{u}_m$.

Inserting the total electric field $\mathbf{E}_{tot}(\mathbf{r},t)$ into the Helmholtz equation and using equation 3.3.1 gives

$$\sum_m \left[\partial_t^2 \tilde{E}_m(t) + 2i\tilde{\omega}_m \partial_t \tilde{E}_m(t)\right] \mathbf{u}_m(\mathbf{r}) \cdot \exp(i\tilde{\omega}_m t) = -\varepsilon^{-1}(\mathbf{r})\, \partial_t^2 \mathbf{P}_{QM}(\mathbf{r},t).$$

We now use the slowly varying envelope approximation (SVEA) [72, 73] which assumes that the perturbation caused by the quantum system does not cause any fast oscillating terms in the electric field, i.e. $\partial_t^2 \tilde{E}_m(t) \approx 0$. With this and using the orthogonality condition 3.3.2 yields

$$\exp(i\tilde{\omega}_n t)\, \partial_t \tilde{E}_n(t) = \frac{1}{2} i\tilde{\omega}_n^{-1} \int \varepsilon^{-1}(\mathbf{r}')\, \mathbf{u}_n^*(\mathbf{r}') \cdot \partial_t^2 \mathbf{P}_{QM}(\mathbf{r}',t)\, d^3r'.$$

It is beneficial to write the LHS of the above equation in terms of an electric field quantity which includes all the temporal dependencies of the n-th eigenmode, i.e. we introduce the quantity $E_n(t) \equiv \tilde{E}_n(t) \cdot \exp(i\tilde{\omega}_n t)$:

$$\partial_t E_n(t) = i\tilde{\omega}_n E_n + \frac{1}{2} i\tilde{\omega}_n^{-1} \int \varepsilon^{-1}(\mathbf{r}')\, \mathbf{u}_n^*(\mathbf{r}') \cdot \partial_t^2 \mathbf{P}_{QM}(\mathbf{r}',t)\, d^3r'.$$

The above equation describes the evolution of a plasmonic eigenmode with frequency ω_n and spatial profile $\mathbf{u}(\mathbf{r})$ when coupled to a generic polarization response $\mathbf{P}_{QM}$. Further simplifications can be made if we assume that the polarization current can be written as a linear functional, i.e. $\mathbf{P}(\mathbf{r},t) = \chi(\mathbf{r})\, \mathbf{E}_{tot}(\mathbf{r},t)$, which, as was discussed in section 3.2, is a valid assumption in the small-signal regime. With this and equations 3.3.3 and 3.3.1 the above equation reads:

$$\partial_t E_n(t) = i\tilde{\omega}_n E_n - \frac{1}{2} i \sum_m \frac{\tilde{\omega}_m^2}{\tilde{\omega}_n} \int \varepsilon^{-1}(\mathbf{r}')\, \chi(\mathbf{r},t)\, \tilde{E}_m(t)\, \mathbf{u}_n^*(\mathbf{r}') \cdot \mathbf{u}_m(\mathbf{r})\, d^3r'$$

This can be further simplified by assuming that the polarizability of the quantum system $\chi(\mathbf{r},t)$ does not vary significantly in space:

$$\chi(\mathbf{r},t) \approx \chi_{QM}(t).$$

This is a good assumption if quantum systems has a sufficiently small volumes V_{QM} so that the electro-magnetic field values do not vary significantly within the

region of the quantum system V_{QM}. If we further introduce the expression $P_k(t) \equiv \chi_{QM}(t)\,\tilde{E}_k(t)$ then the above equation reads:

$$\partial_t E_n(t) = i\tilde{\omega}_n E_n - \frac{1}{2} i \sum_m \frac{\tilde{\omega}_m^2}{\tilde{\omega}_n} \Gamma_{nm} P_m, \tag{3.3.4}$$

where we have introduced the quantity Γ_{nm}:

$$\Gamma_{nm} \equiv \int_{V_{QM}} \mathbf{u}_n^*(\mathbf{r}') \cdot \mathbf{u}_m(\mathbf{r}')\,\varepsilon^{-1}(\mathbf{r}')\,d^3r'. \tag{3.3.5}$$

Equation 3.3.4 resembles a harmonic oscillator equation for the amplitude of the n-th plasmonic mode E_n which is coupled to P_m with a coupling strength of $\frac{1}{2}\tilde{\omega}_m^2\tilde{\omega}_n^{-1}\Gamma_{nm}$. In this model, the P_m quantities act like uncorrelated, independent polarizations which are only coupled via the electro-magnetic field. Together they form the total polarization response $\mathbf{P}_{QM}$:

$$\mathbf{P}_{QM}(\mathbf{r},t) = \sum_m \chi_{QM}(t)\,\tilde{E}_m(t)\,\mathbf{u}_m(\mathbf{r})\exp(i\tilde{\omega}_m t).$$

It should be noted that although the eigenmodes $\mathbf{u}_n(\mathbf{r})$ were assumed to be orthonormal, the off-diagonal components of Γ_{nm} can still be non-zero as the integral is evaluated only over the volume of the quantum emitter V_{QM}.

Interestingly, the diagonal elements of the above quantity Γ_{nn} are identical to the confinement factor Γ_n of the n-th plasmonic mode [74, 75, 76]:

$$\Gamma_{mm} = \int_{V_{QM}} \mathbf{u}_m^*(\mathbf{r}') \cdot \mathbf{u}_m(\mathbf{r}')\,\varepsilon^{-1}(\mathbf{r}')\,d^3r = \frac{\int_{V_{QM}} \mathbf{E}_m^*(\mathbf{r}') \cdot \mathbf{E}_m(\mathbf{r}')\,\varepsilon^{-1}(\mathbf{r}')\,d^3r}{\int_V \mathbf{E}_m^*(\mathbf{r}') \cdot \mathbf{E}_m(\mathbf{r}')\,\varepsilon^{-1}(\mathbf{r}')\,d^3r} = \Gamma_m.$$

The confinement factor Γ_n is a quantity which expresses the proportion of field energy which is confined to the region of the quantum system V_{QM}. It is linked to the effective mode volume of the n-th plasmonic mode $V_{n,eff}$ as follows [77]:

$$V_{n,eff} \equiv \frac{V_{QM}}{\Gamma_n}. \tag{3.3.6}$$

If the polarization $\mathbf{P}$ of the quantum system is described by the two- or four-level model derived above (see section 3.2), then the polarization response $\mathbf{P}$ can also be written as a harmonic oscillator equation with a complex resonant frequency $\tilde{\omega}_{QM} \equiv \omega_0 + i\gamma_L$ which is coupled to the electric field via a coupling constant $\Delta\epsilon$:

$$\partial_t \mathbf{P}(\mathbf{r},t) = i\tilde{\omega}_{QM}\mathbf{P}(\mathbf{r},t) + i\Delta\epsilon\mathbf{E}_{tot}(\mathbf{r},t), \tag{3.3.7}$$

where $\Delta\epsilon$ for a two-level system based on the Maxwell-Bloch equations is (see equation 3.2.14)

$$\Delta\epsilon = \frac{2\left|\mu\right|^2 N}{3\omega_0 \hbar V}. \tag{3.3.8}$$

Using equations 3.3.2, 3.3.3, 3.3.7 and $P_k(t) \equiv \chi_{QM}(t) \cdot \tilde{E}_k(t)$, an equation of motion for the partial polarization currents P_k is obtained

$$\partial_t P_n(t) = i\tilde{\omega}_{QM} P_n(t) + i\Delta\epsilon E_n(t). \tag{3.3.9}$$

Equations 3.3.4 and 3.3.9 form a complete set of coupled harmonic oscillator equations

$$\partial_t \begin{pmatrix} \mathbf{E} \\ \mathbf{P} \end{pmatrix} = i \begin{pmatrix} \Omega & -A \\ \Delta\epsilon \mathbb{1} & \tilde{\omega}_{QM}\mathbb{1} \end{pmatrix} \cdot \begin{pmatrix} \mathbf{E} \\ \mathbf{P} \end{pmatrix} \tag{3.3.10}$$

with the following definitions

$$\mathbb{1}_{ij} = \delta_{ij}; \quad \Omega_{ij} \equiv \delta_{ij}\tilde{\omega}_i; \quad A_{ij} \equiv \frac{1}{2}\frac{\tilde{\omega}_j^2}{\tilde{\omega}_i}\Gamma_{ij}; \quad \mathbf{E} \equiv \begin{pmatrix} E_1(t) \\ E_2(t) \\ \vdots \\ E_N(t) \end{pmatrix}; \quad \mathbf{P} \equiv \begin{pmatrix} P_1(t) \\ P_2(t) \\ \vdots \\ P_N(t) \end{pmatrix}$$

which can be used to predict and investigate coupling phenomena in the semi-classical limit.

A well-known phenomena of strong-coupling is Rabi splitting which can be predicted by the model derived above. For this we assume that the off-diagonal elements of Γ_{mn} are negligible:

$$\Gamma_{mn} \approx 0 \text{ for } m \neq n$$

This is true if there is only a single mode at the frequency of interest or if the spatial symmetry of the plasmonic modes $\mathbf{u}_m$, $\mathbf{u}_n$ is such that the integration in equation 3.3.10 vanishes. With this equation 3.3.10 becomes particularly simple

$$\partial_t E_n(t) = i\tilde{\omega}_n E_n - \frac{1}{2} i\tilde{\omega}_n \Gamma_{nn} P_n,$$

i.e. the different plasmonic modes in equation 3.3.10 completely de-couple. The equation of motion for a single plasmonic mode E_n, therefore only involves two harmonic oscillator equations:

$$\partial_t \begin{pmatrix} E_n \\ P_n \end{pmatrix} = i \begin{pmatrix} \tilde{\omega}_n & -\frac{1}{2}\tilde{\omega}_n\Gamma \\ \Delta\epsilon & \tilde{\omega}_{QM} \end{pmatrix} \cdot \begin{pmatrix} E_n \\ P_n \end{pmatrix}.$$

To calculate the maximum Rabi splitting, we now assume that there is no frequency

detuning between the plasmonic and quantum resonance ($\mathrm{Re}\left[\tilde{\omega}_0\right] = \mathrm{Re}\left[\tilde{\omega}_{QM}\right]$). By re-inserting the definitions for the complex frequencies ($\tilde{\omega}_n \equiv \omega_n + i\gamma_n$, $\tilde{\omega}_{QM} \equiv \omega_0 + i\gamma_L$) and using equations 3.3.6, 3.3.8, the following expression for the maximum Rabi splitting can be found:

$$\Delta\omega = \sqrt{\Omega^2 - (\gamma_n - \gamma_L)^2}, \tag{3.3.11}$$

with the Rabi frequency given by

$$\Omega^2 = 2\omega_n^2 \Gamma_{nn} \Delta\epsilon = \frac{2N\omega_n}{3V_{eff}\epsilon_0\hbar} \left|\mu\right|^2. \tag{3.3.12}$$

This is identical to the Rabi splitting found in literature for quantum-optical systems [23, 78].

3.4 Summary

This first section of this chapter derived numerical methods to simulate two commonly found non-linear systems: a χ^3 non-linearity and a two- or four-level system. For the latter, it was shown, that the response is identical to the response of a classical Lorentzian resonance as discussed in section 2.1.2.2 in chapter 2. However, as opposed to the Lorentzian response, the two- and four-level systems additionally integrate auxiliary update equations for the occupation densities N_0, N_1, N_2, N_3 of the energy levels. The occupation levels, in turn, determine the coupling of the Lorentzian response $\Delta\epsilon$ to the electro-magnetic field which results in an overall non-linear response.

The second section of this chapter derived a semi-classical model for the Rabi splitting phenomena found in strongly coupled systems and proves that the FDTD method can be used to describe such phenomena.

Chapter 4

Material Boundaries

As stated in the introduction, to date the FDTD method is a highly successful method for the simulation of electro-magnetic wave phenomena for objects that do not involve surface geometries on wide variety of length-scales and therefore, it cannot be used to simulater a wide range of nano-plasmonic systems. Therefore, the goal of this thesis is to investigate how the FDTD method can be extended for use also on these systems. The critical benefit of using FDTD instead of more established frequency based methods to simulate nano-plasmonic systems is the straightforward extension of the FDTD method to non-linear systems and its use as a tool for investigating the resulting, often complex temporal dynamics. Nevertheless, several key limitations of the method must be overcome for it to be an effective and efficient solver for nano-plasmonic systems. One such limitation is the inability of the traditional FDTD method to simulate key materials commonly found in nano-plasmonic systems such as metals or systems which have to be described by semi-classical models. A solution to this limitation was presented in the previous chapters.

A second, crucial limitation is the accurate modeling of material interfaces. This key aspect was intentionally excluded from those chapters as its discussion is surprisingly involved and therefore merits its own chapter. The original description of the FDTD method does not specify how Yee cells with material boundaries should be treated [14]. For example, the update equation for the x-component of the electric field E_x for a 2D TM simulation ($E_z = H_z = H_y = 0$) within a material with a dielectric constant of ε reads

$$E_x|_{j,k-\frac{1}{2}}^{n+1} = E_x|_{j,k-\frac{1}{2}}^{n+1} + \varepsilon^{-1}\big|_{j,k-\frac{1}{2}} \frac{c\Delta t}{\Delta y} \left(H_z|_{j+\frac{1}{2},k-\frac{1}{2}}^{n+\frac{1}{2}} - H_z|_{j-\frac{1}{2},k-\frac{1}{2}}^{n+\frac{1}{2}} \right) \tag{4.0.1}$$

but it remains unspecified what the exact value of $\varepsilon^{-1}\big|_{j,k-\frac{1}{2}}$ is for a Yee cell containing a material boundary. For systems which are traditionally solved by FDTD - such as microwave or radar wavelength simulations - the exact choice of $\varepsilon^{-1}\big|_{j,k-\frac{1}{2}}$ at a material interface Yee cell does not significantly change any macroscopically derived

properties such as energy cross section spectra. Hence, the exact specification of $\varepsilon^{-1}|_{j,k-\frac{1}{2}}$ for a Yee cell at a material interface is simply not necessary. This clearly changes when the FDTD method is used to simulate nano-plasmonic systems where many of the phenomena encountered are inherently linked to the surface structure, such as the occurrence of surface plasmon polaritons or strong field enhancements at nearly singular geometry points. In fact, it has been shown that convergence is at most first order accurate for $\Delta x \to 0$ when using a non-optimal value of $\varepsilon^{-1}|_{j,k-\frac{1}{2}}$ for a Yee cell containing a material boundary [79, 80, 81, 82, 83].

Three methods to determine an effective response of a Yee cell containing a material boundary stand out based on their popularity: the stair-casing method [82], the volume averaging method (DVA) [83], and the sub-pixel averaging method [84]. The vast majority of literature on these methods, as well as this topic in general, merely deals with identifying the effective material response of a Yee cell containing only materials that can be described by a single dielectric constant [82, 83, 84, 85]. This is not very useful for nano-plasmonics as a static dielectric constant cannot describe the response of essential materials used in nano-plasmonics, such as metals. This chapter will therefore re-derive these three popular methods for the more general case of identifying the correct effective polarization response $\mathbf{P}_{eff}[\mathbf{E}]$ of a Yee cell containing a boundary between materials described by the individual polarization responses $\mathbf{P}_\eta[\mathbf{E}]$.

4.1 Effective polarization responses of a Yee cell containing material boundaries

The goal of this section is to derive methods to determine the discretised effective polarization response $\mathbf{P}_{eff}|^n_{ijk}$ of a Yee cell containing boundaries between several materials $\mathbf{P}_\eta$, where $\mathbf{P}_\eta$ is the polarization response of the η-th material. In a system where the individual material responses are continuous, the total polarization response of a boundary Yee cell is simply the sum of the polarization responses $\mathbf{P}_\eta$

$$\mathbf{P}_{tot}(\mathbf{r},t) = \sum_\eta \mathbf{P}_\eta(\mathbf{r},t)\,\Theta_\eta(\mathbf{r}), \tag{4.1.1}$$

where $\Theta_\eta(\mathbf{r})$ is a geometry function which describes the extent of the η-th material and is given by

$$\Theta_\eta(\mathbf{r}) \equiv \begin{cases} 1 & \text{for } \mathbf{r} \in V_\eta \\ 0 & \text{for } \mathbf{r} \notin V_\eta \end{cases},$$

and V_η is the volume which is occupied by the η-th material. The explicit spatial dependence of the geometry function $\Theta_\eta(\mathbf{r})$ causes discontinuities in the overall polarization response and the goal is to find a discretised effective polarization response $\mathbf{P}_{eff}$ that ensures convergence for $\Delta V \to 0$ despite these discontinuities.

Additionally, it is assumed that the polarization functionals $\mathbf{P}_\eta$ are spatially local, isotropic and do not explicitly depend on $\mathbf{r}$. Often, the equations below will make use of the notation $\mathbf{P}_\eta[\mathbf{E}(\mathbf{r},t)]$ which shall mean, that the polarization $\mathbf{P}_\eta$ functional is evaluated with the value of the electric field vector $\mathbf{E}(\mathbf{r},t)$ at the location $\mathbf{r}$. However, the functional $\mathbf{P}_\eta[\mathbf{E}(\mathbf{r},t)]$ may also depend on previous time-values of $\mathbf{E}(\mathbf{r},t)$ (however, not on other spatial locations as the $\mathbf{P}_\eta$ are assumed to be local) and this is not explicitly noted.

4.1.1 Staircasing method

If one strictly follows the derivation of the FDTD equations as presented in chapter 1, then the update equation of the electric field at a Yee cell with a material boundary reads

$$\mathbf{E}|_{ijk}^{n+1} = \mathbf{E}|_{ijk}^{n} + c\Delta t\,(\nabla \times \mathbf{H})|_{ijk}^{n+\frac{1}{2}} - \mathbf{P}_{tot}|_{ijk}^{n+1} + \mathbf{P}_{tot}|_{ijk}^{n},$$

where the short notation of section 1.1.5 was used. In the above equation, $\mathbf{P}_{tot}|_{ijk}^{n}$ stands for

$$\mathbf{P}_{tot}|_{ijk}^{n} \equiv \mathbf{P}_{tot}(\mathbf{r}_{ijk}, n\Delta t) = \mathbf{P}_{\eta_{ijk}}[\mathbf{E}(\mathbf{r}_{ijk}, n\Delta t)],$$

where $\mathbf{r}_{ijk} \equiv i\Delta z\mathbf{e}_z + j\Delta y\mathbf{e}_y + k\Delta x\mathbf{e}_x$ and η_{ijk} is the index of the material that surrounds the point $\mathbf{r}_{ijk}$. This shows, that the polarization response ignores all but one material in the Yee cell and this is visually represented in figure 4.1.1a where the fill-colour of the Yee cell indicates which material polarization is used in the update equation. Due to the jagged appearance in this visual representation, the use of the above update equations is often called the "staircasing" method.

Although, having followed a correct derivation, the unsmooth properties of the traditional update equations result in some undesired consequences. For example, any spatial shift of the material boundaries which doesn't change the material surrounding the point $\mathbf{r}_{ijk}$ will have no effect on the simulation results. This is shown in figure 4.1.1b where several 1-D simulations were performed with varying spatial positions of a material boundary. It can be seen that the error of the simulation varies periodically with a period-length of exactly one Yee cell length Δx.

Motivated by the above short-comings, a sensible starting-point in the pursuit of finding an effective polarization response $\mathbf{P}_{eff}$ of a Yee cell containing a material

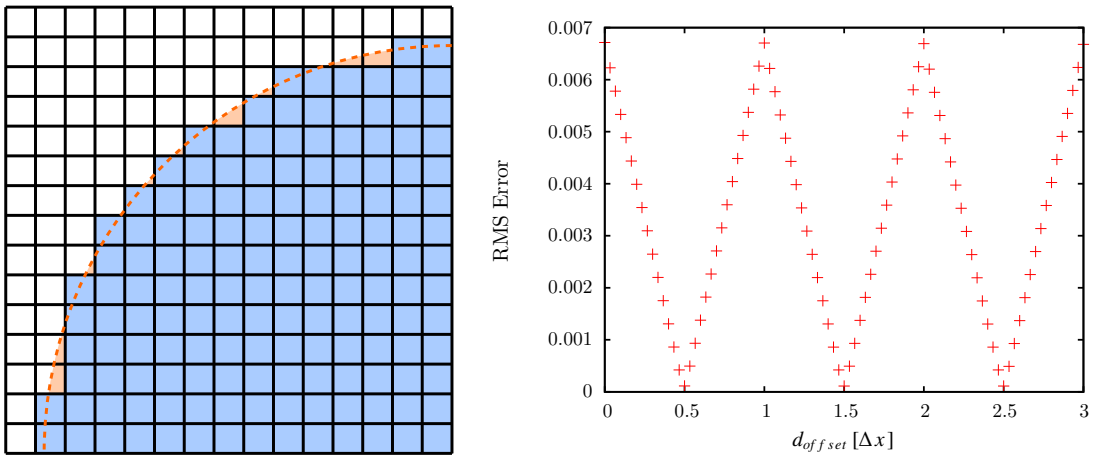

(a) (b)

Figure 4.1.1: (a) the "staircasing effect": in the traditional FDTD method, the Yee cells (outlined with black lines) must be completely filled with a single material (blue filling). This leads to a jaggered appearance of the material boundaries as compare to the real physical boundaries (orange) (b) RMS error of several 1-D FDTD simulations ($L = 256\Delta x$) with a varying location d_{offset} of a static dielectric material boundary ($\Delta\varepsilon = 4$). When the material boundary is at $x = m \cdot \Delta x + \frac{1}{2}\Delta x$ (and m is an integer, Δx is the Yee cell size), then either vacuum or the material will completely fill a Yee cell centred around E_y and the staircased representation of the material boundary becomes identical to the real geometry of the boundary. The RMS error was calculated compared to a perfect plane-wave with amplitude $A = 1$.

boundary is to apply some smoothing operation to the total polarization $\mathbf{P}_{tot}$

$$\mathbf{P}_{eff} = \frac{1}{\Delta\Gamma} \int_{\Gamma_{ijk}} \mathbf{P}_{tot}\left(\mathbf{r}', n\Delta t\right) d^3r', \tag{4.1.2}$$

where Γ_{ijk} is a region centred at $\mathbf{r}_{ijk}$ being no larger than the volume of a single Yee cell. Although not explicitly noted above, the smoothing region Γ_{ijk} may depend on the orientation of the polarization $\mathbf{P}_{tot}$ - for example the smoothing region Γ_{ijk} may be different when applied to a polarization component that is parallel or perpendicular to a material interface. It will be shown that the exact choice Γ_{ijk} will lead to different interpretations of the update equations and even on the overall macroscopic results of a simulation. For now, Γ_{ijk} will remain unspecified and two popular approximations for the above integral will now be derived which are compatible with the FDTD field update equations.

4.1.2 Volume averaging (VA)

To derive the VA approximation, it is useful to substitute the total polarization response $\mathbf{P}_{tot}$ (equation 4.1.1) into the smoothing integral of equation 4.1.2

$$\mathbf{P}_{eff} = \frac{1}{\Delta\Gamma} \int\limits_{\Gamma_{ijk}} \mathbf{P}_{tot}\left(\mathbf{r}', n\Delta t\right) d^3r' = \frac{1}{\Delta\Gamma} \int\limits_{\Gamma_{ijk}} \sum_{\eta} \mathbf{P}_{\eta}\left[\mathbf{E}\left(\mathbf{r}', t\right)\right] \Theta_{\eta}\left(\mathbf{r}\right) d^3r'.$$

The VA method uses the approximation

$$\mathbf{P}_{\eta}\left[\mathbf{E}\left(\mathbf{r}', t\right)\right] \approx \mathbf{P}_{\eta}\left[\mathbf{E}\left(\mathbf{r}_{ijk}, t\right)\right] = \mathbf{P}_{\eta}\left[\mathbf{E}|_{ijk}\right] \tag{4.1.3}$$

and with this, the effective polarization in the VA approximation is found

$$\mathbf{P}_{eff}^{VA} = \frac{1}{\Delta\Gamma} \sum_{\eta} \mathbf{P}_{\eta}\left[\mathbf{E}|_{ijk}\right] \int\limits_{\Gamma_{ijk}} \Theta_{\eta}\left(\mathbf{r}\right) d^3r' = \sum_{\eta} f_{\eta} \mathbf{P}_{\eta}\left[\mathbf{E}|_{ijk}\right], \tag{4.1.4}$$

where VA stands for volume averaging and the following definition for the filling factor f_{η} of the η-th material was used

$$f_{\eta} \equiv \frac{1}{\Delta\Gamma} \int\limits_{\Gamma_{ijk}} \Theta_{\eta}\left(\mathbf{r}\right) d^3r'. \tag{4.1.5}$$

It is obvious that the effective polarization within the VA approximation is compatible with the FDTD update equations, as it only requires the pre-multiplication of the individual polarization responses $\mathbf{P}_{\eta}$ with the filling factors f_{η}. In most implementations of the VA method, $\Gamma_{ijk} = V_{ijk}$ and $\mathbf{P}_{eff}^{VA}$ is then the volume average over the $\mathbf{P}_{\eta}\left[\mathbf{E}|_{ijk}\right]$, hence the name "volume-averaging". However, it shall be stressed, that this will lead to a particular interpretation of the update equations and that other choices for Γ_{ijk} are possible.

Although simple, the VA approach remains one of the most popular approaches to the material boundary problem in FDTD. Indeed, by averaging over the entire Yee cell, a small shift of a material boundary within a Yee cell will now affect the overall simulation result as is expected. This was not the case for the staircasing method and for a variety of systems the error of the simulation with the VA approach can be smaller than in the stair-casing case [79] which will also be confirmed in section 4.5.

4.1.3 Sub-pixel averaging

The success of the VA method is somewhat surprising as it can easily be shown that it is a bad approximation for the smoothing operation defined in equation 4.1.2, in

the sense that it does not converge with $\Delta V \to 0$. This is because the approximation 4.1.3 assumes

$$\mathbf{E}\left(\mathbf{r}', n\Delta t\right) \to \mathbf{E}\left(\mathbf{r}_{ijk}, n\Delta t\right) \text{ for any } \mathbf{r}', \mathbf{r}_{ijk} \in V_{ijk} \text{ and } \Delta V \to 0, \tag{4.1.6}$$

which is obviously incorrect at a material interface. The question arises if an approximation for the smoothing operation can be found that is not only compatible with the FDTD algorithm but also converges to the exact smoothing operation for $\Delta V \to 0$.

Although the above equation 4.1.6 is incorrect as stated, it *is* correct within a single material

$$\mathbf{E}\left(\mathbf{r}', n\Delta t\right) \to \mathbf{E}_\eta \text{ for any } \mathbf{r} \in V_\eta \text{ and } \Delta V \to 0,$$

where $\mathbf{E}_\eta$ is an electric field vector inside the material V_η. This is the case because the polarizations $\mathbf{P}_\eta$ were assumed to be local and not explicitly depend on $\mathbf{r}$.

With this, one can approximate the effective polarization response $\mathbf{P}_{eff}$ as follows

$$\begin{aligned}\mathbf{P}_{eff} = \frac{1}{\Delta\Gamma}\int\limits_{\Gamma_{ijk}} \mathbf{P}_{tot}\left(\mathbf{r}', n\Delta t\right) d^3r' &= \frac{1}{\Delta\Gamma}\int\limits_{\Gamma_{ijk}} \sum_\eta \mathbf{P}_\eta\left[\mathbf{E}\left(\mathbf{r}', t\right)\right]\Theta_\eta\left(\mathbf{r}\right) d^3r' \\ &\approx \frac{1}{\Delta\Gamma}\int\limits_{\Gamma_{ijk}} \sum_\eta \mathbf{P}_\eta\left[\mathbf{E}_\eta\right]\Theta_\eta\left(\mathbf{r}\right) d^3r'\end{aligned}$$

and with the definition 4.1.5 for the filling factors f_η, the approximate effective polarization response within the sub-pixel averaging method is found

$$\mathbf{P}_{eff}^{SA} = \sum_\eta f_\eta \mathbf{P}_\eta\left[\mathbf{E}_\eta\right]. \tag{4.1.7}$$

Although, an expression for the effective polarization response has now been found, which, in the limit of $\Delta V \to 0$, is equal to the smoothing operation defined in equation 4.1.2, the question arises of how to efficiently calculate the electric field vector $\mathbf{E}_\eta$ inside the η-th material. For this, one must additionally assume that the surfaces defined by the interfaces between the materials inside a specific Yee cell are planar and are all parallel to one another. In particular, it must be possible to uniquely split the electric field into parallel and perpendicular components

$$\mathbf{E}\left(\mathbf{r}, t\right) = \mathbf{E}_\parallel\left(\mathbf{r}, t\right) + \mathbf{e}_\perp E_\perp\left(\mathbf{r}, t\right),$$

where $\mathbf{e}_\perp$ is a unit vector perpendicular to the material boundaries. Note that it is

not required that each Yee cell has the same orientation $\mathbf{e}_\perp$ - and strictly $\mathbf{e}_\perp$ would require a ijk-suffix which is omitted for brevity.

An approximation for the parallel component of $\mathbf{E}_\eta$ can now be found as Gauss's Law states that the parallel component of the electric field is continuous across the material boundary

$$\mathbf{E}_{\parallel,\eta} \to \mathbf{E}_\parallel(\mathbf{r}', n\Delta t) \text{ for any } \mathbf{r} \in V_{ijk} \text{ and } \Delta V \to 0,$$

in particular, this is true for $\mathbf{r}' = \mathbf{r}_{ijk}$

$$\mathbf{E}_{\parallel,\eta} \to \mathbf{E}_\parallel\big|_{ijk} \text{ for } \Delta V \to 0.$$

An implicit equation can also be derived for the perpendicular component of the electric field $E_{\perp,\eta}$ inside the η-th material by observing that the perpendicular component of the displacement current $D_\perp$ is continuous through-out the Yee cell. This implies that for $\Delta V \to 0$

$$E_{\perp,\eta} + P_{\perp,\eta} \to D_\perp(\mathbf{r}) \text{ for any } \eta, \mathbf{r} \in V_{ijk}, \tag{4.1.8}$$

where the isotropy of the η-th material polarization was used in the following way

$$P_{\perp,\eta} \equiv \mathbf{n} \cdot \mathbf{P}_\eta[\mathbf{E}_\eta] = P[\mathbf{n} \cdot \mathbf{E}_\eta]. \tag{4.1.9}$$

With this, an implicit equation for $\mathbf{E}_\eta$ is found

$$\mathbf{E}_\eta \equiv \mathbf{E}_\parallel + (D_\perp - P_{\perp,\eta}[\mathbf{n} \cdot \mathbf{E}_\eta])\,\mathbf{n}. \tag{4.1.10}$$

Finally, an additional important relation within the sub-pixel averaging scheme shall be derived which is often used through-out this chapter. By averaging over all materials η on the LHS of equation 4.1.8 and considering that $\sum_\eta f_\eta = 1$

$$\sum_\eta f_\eta (E_{\perp,\eta} + P_{\perp,\eta}) \approx D_\perp\big|_{ijk}^n.$$

or with equation 4.1.7 this becomes

$$\sum_\eta f_\eta E_{\perp,\eta} \approx D_\perp\big|_{ijk}^n - P_{\perp,eff}.$$

Comparing this with the constituent relation between $\mathbf{E}(\mathbf{r}, t)$ and $\mathbf{D}(\mathbf{r}, t)$:

$$E_\perp = D_\perp - P_{\perp,eff}[E_{\perp,\eta}]$$

reveals the following relation

$$E_\perp \approx \sum_\eta f_\eta E_{\perp,\eta}. \tag{4.1.11}$$

Although not immediately evident, equations 4.1.11 and 4.1.10 fully specify $\mathbf{E}_\eta$ within the context of an FDTD algorithm. The exact steps to extract $\mathbf{E}_\eta$ will depend on the details of the numerical implementation and different approaches will be discussed in section 4.4. Nevertheless, this concludes the search for an effective polarization response in the sub-pixel averaging case and the relevant equations are repeated here

$$\mathbf{P}_{eff}^{SA} \equiv \sum_\eta f_\eta \mathbf{P}_\eta \left[\mathbf{E}_\eta|_{ijk}^n \right] \tag{4.1.12}$$

$$\mathbf{E}_\eta|_{ijk}^n \equiv \mathbf{E}_\parallel + \left(D_\perp|_{ijk}^n - P_{\perp,\eta} \left[\mathbf{n} \cdot \mathbf{E}_\eta|_{ijk}^n \right] \right) \mathbf{n} \tag{4.1.13}$$

$$\mathbf{E}|_{ijk}^n = \sum_\eta f_\eta \, \mathbf{E}_\eta|_{ijk}^n \, . \tag{4.1.14}$$

Finally, the last equation deserves some discussion, as it may seem disturbing, that it implies that the weighted sum of the electric field values evaluated at distinct points $\mathbf{r}_\eta$ in the η-th material should be equal to the electric field at a seemingly random point $\mathbf{r}_{ijk}$. However, this is the direct consequence of modifying Ampère's Law by "smoothing-out" the polarization response over a region centred at $\mathbf{r}_{ijk}$

$$\partial_t \mathbf{E}\left(\mathbf{r}_{ijk}, n\Delta t\right) = \partial_t \mathbf{D}\left(\mathbf{r}_{ijk}, n\Delta t\right) - \partial_t \frac{1}{\Delta\Gamma} \int\limits_{\Gamma_{ijk}} \mathbf{P}_{tot}\left(\mathbf{r}', n\Delta t\right) d^3 r'.$$

As the above equation is no longer the correct physical equation for Ampère's Law, it should not be surprising that the field it integrates can no longer be identified as the real physical electric field. Thus, the field integrated by the FDTD update equations may have properties that are unusual for physical fields. A more detailed discussion on this is given in section 4.3.

4.2 Application to static dielectric materials

In literature, the above derivations for an effective polarization functional are commonly given only for static dielectric materials [84, 83, 14, 15]. For the sake of comparing the above results to literature, it is interesting to investigate the case where the material polarization functionals $\mathbf{P}_\eta$ describe static dielectric materials

$$\mathbf{P}_\eta\left[\mathbf{E}\left(\mathbf{r}, t\right)\right] \equiv \left(\varepsilon_\eta - 1\right) \mathbf{E}\left(\mathbf{r}, t\right). \tag{4.2.1}$$

Stair-casing

The effective polarization response in the stair-casing method reads

$$\mathbf{P}_{eff}^{SC}\big|_{ijk}^{n} = \mathbf{P}_{\eta_{ijk}}\left(\mathbf{E}|_{ijk}^{n}\right) = \left(\varepsilon_{\eta_{ijk}} - 1\right)\mathbf{E}|_{ijk}^{n},$$

where $\varepsilon_{\eta_{ijk}}$ is the dielectric constant of the material that surrounds the point $\mathbf{r}_{ijk}$. Substituting the above equation into the constituent relation $\mathbf{E} = \mathbf{D} - \mathbf{P}_{eff}$ gives

$$\mathbf{E}|_{ijk}^{n} = \varepsilon_{\eta_{ijk}}^{-1}\,\mathbf{D}|_{ijk}^{n}$$

and consequently, in the stair-casing case, the effective dielectric constant $\varepsilon_{eff}^{-1}\big|_{ijk}$ is simply given by

$$\varepsilon_{SC,eff}^{-1}\big|_{ijk} \equiv \varepsilon^{-1}\left(\mathbf{r}_{ijk}\right).$$

Volume-averaging (VA)

Substituting the static dielectric polarization functional 4.2.1 into the effective polarization response of the VA method (equation 4.1.4) gives

$$\mathbf{P}_{eff}^{VA}\big|_{ijk}^{n} = \sum_{\eta} f_{\eta}\left(\varepsilon_{\eta} - 1\right)\mathbf{E}|_{ijk}^{n}$$

or by observing that $\sum f_{\eta} = 1$

$$\mathbf{P}_{eff}^{VA}\big|_{ijk}^{n} = \left(\langle\varepsilon\rangle|_{ijk} - 1\right)\mathbf{E}|_{ijk}^{n},$$

where

$$\langle\varepsilon\rangle|_{ijk} \equiv \sum_{\eta} f_{\eta}\varepsilon_{\eta} = \sum_{\eta}\varepsilon_{\eta}\frac{1}{\Delta\Gamma}\int\limits_{\Gamma_{ijk}}\Theta_{\eta}\left(\mathbf{r}'\right)d^{3}r' = \frac{1}{\Delta\Gamma}\int\limits_{\Gamma_{ijk}}\varepsilon\left(\mathbf{r}'\right)d^{3}r'$$

is the average dielectric value of $\varepsilon\left(\mathbf{r}\right)$ inside the region Γ_{ijk}. Once again, inserting the above into the constituent relation leads to

$$\mathbf{E}|_{ijk}^{n} = \langle\varepsilon\rangle^{-1}\big|_{ijk}\,\mathbf{D}|_{ijk}^{n}$$

and therefore

$$\varepsilon_{VA,eff}^{-1}\big|_{ijk} = \langle\varepsilon\rangle^{-1}\big|_{ijk},$$

which matches the expression found in the literature [83].

Sub-pixel averaging

Similarly, the static dielectric polarization functional 4.2.1 is substituted into the effective polarization response for the sub-pixel averaging method. The parallel component of the effective response is identical to the volume averaging method and therefore

$$\mathbf{E}_{\parallel}\big|_{ijk}^{n} = \langle\varepsilon\rangle^{-1}\big|_{ijk}\,\mathbf{D}_{\parallel}\big|_{ijk}^{n}\,.$$

For the perpendicular component, the static dielectric polarization response 4.2.1 is inserted into equation 4.1.13:

$$E_{\perp,\eta}|_{ijk}^{n} = D_{\perp}|_{ijk}^{n} - (\varepsilon_{\eta} - 1)\,E_{\perp,\eta}|_{ijk}^{n}$$

and then solved for $E_{\perp,\eta}|_{ijk}^{n}$:

$$E_{\perp,\eta}|_{ijk}^{n} = \varepsilon_{\eta}^{-1}\,D_{\perp}|_{ijk}^{n}\,,$$

which can then be substituted into the perpendicular component of the effective polarization response 4.1.12:

$$\begin{aligned} P_{\perp,eff}^{VA}\big|_{ijk}^{n} = \sum_{\eta} f_{\eta}\,(\varepsilon_{\eta} - 1)\,\varepsilon_{\eta}^{-1}\,D_{\perp}|_{ijk}^{n} &= \sum_{\eta} f_{\eta}\left(1 - \varepsilon_{\eta}^{-1}\right) D_{\perp}|_{ijk}^{n} \\ &= \left(1 - \left\langle\varepsilon^{-1}\right\rangle\big|_{ijk}\right) D_{\perp}|_{ijk}^{n}\,, \end{aligned}$$

where $\langle\varepsilon^{-1}\rangle|_{ijk}$ is now the average of the inverse dielectric constant over the region Γ (note that $\langle\varepsilon^{-1}\rangle|_{ijk} \neq \left(\langle\varepsilon\rangle|_{ijk}\right)^{-1}$). Inserting the above into the constituent relation gives

$$E_{\perp}|_{ijk}^{n} = \left\langle\varepsilon^{-1}\right\rangle\big|_{ijk}\,D_{\perp}|_{ijk}^{n}$$

and therefore the effective dielectric constant in the sub-pixel averaging case is given by the following tensor

$$\boldsymbol{\varepsilon}_{SA,eff}^{-1}\big|_{ijk} \equiv (\mathbf{1} - \mathbf{e}_{\perp} \otimes \mathbf{e}_{\perp})\,\langle\varepsilon\rangle|_{ijk}^{-1} + \mathbf{e}_{\perp} \otimes \mathbf{e}_{\perp}\left\langle\varepsilon^{-1}\right\rangle\big|_{ijk}\,. \tag{4.2.2}$$

where $\mathbf{e}_{\perp}$ is the unit vector perpendicular to the material interface, $\otimes$ denotes the outer product and $\mathbf{1}$ is the identity matrix. This expression is identical to the expression found in [84]. Table 4.1 lists a summary of the expressions for the effective dielectric constant in the various schemes.

	Effective polarization $\mathbf{P}_{eff}$	Effective inverse dielectric $\varepsilon_{eff}^{-1}\big\vert_{ijk}$
Stair-casing	$\mathbf{P}_{\eta_{ijk}}\big[\mathbf{E}\vert_{ijk}\big]$	$\varepsilon^{-1}\big(\mathbf{r}_{ijk}\big)$
VA	$\sum_\eta f_\eta \mathbf{P}_\eta\big[\mathbf{E}\vert_{ijk}\big]$	$\langle\varepsilon\rangle\vert_{ijk}^{-1}$
Sub-pixel	$\sum_\eta f_\eta^{\parallel}\mathbf{P}_{\parallel,\eta}\big[\mathbf{E}_{\parallel}\big\vert_{ijk}\big]+\sum_\eta f_\eta^{\perp}P_{\perp,\eta}\big[E_{\perp,\eta}\big]$	$(\mathbf{1}-\mathbf{e}_\perp\otimes\mathbf{e}_\perp)\,\langle\varepsilon\rangle\vert_{ijk}^{-1}+\mathbf{e}_\perp\otimes\mathbf{e}_\perp\,\big\Vert\varepsilon^{-1}\big\Vert\big\vert_{ijk}$

Table 4.1: Effective polarization response and inverse dielectric constant for various sub-pixel averaging schemes. Notes: 1) η_{ijk} is the index of the η-th material which contains the point $\mathbf{r}_{ijk}$ 2) $f_\eta^{\parallel}$, $f_\eta^{\perp}$ are filling factors ultimately defined by the averaging region Γ. Within the perturbation approach $f_\eta^{\parallel}=f_\eta^{\perp}$ are volume fractions. Within the integral form interpretation $f_\eta^{\parallel}\neq f_\eta^{\perp}$ and $f_\eta^{\parallel}$ is an area fraction and $f_\eta^{\perp}$ is a line-length fraction. 3) The notation $\langle\bullet\rangle$ and $\Vert\bullet\Vert$ stands for the smoothing operation defined by Γ. Within the perturbation $\langle\bullet\rangle=\Vert\bullet\Vert$ and indicates a volume average over $\bullet$. Within the integral form interpretation $\langle\bullet\rangle\neq\Vert\bullet\Vert$ and $\langle\bullet\rangle$, $\Vert\bullet\Vert$ is an area, line average respectively (see equations 4.3.3 and 4.3.4). 4) $\mathbf{e}_\perp$ is a unit vector which is perpendicular to the material interfaces 5) $\otimes$ denotes an outer-product

4.3 The choice of the smoothing region Γ and the resulting "representative field values"

The volume and sub-pixel averaging methods described above are found in the most popular commercial and non-commercial FDTD solvers and the success of these codes partly justifies their usage [86, 47, 87]. Both methods intend to smooth out the undesired behaviour of the stair-casing method by averaging the polarization response in the respective Yee cell. However, a thorough investigation on the consequences of this processes and how the smoothing region Γ effects the result has yet to be discussed.

In the derivation for the effective polarization response in the sub-pixel and volume averaging case, it was noted that the field, which is numerically integrated by the electric field update equation, can generally no longer be identified with the real physical electric field. This is because the update equation is based on a modified version of Ampère's Law where the total polarization response $\mathbf{P}_{tot}$ was replaced with an averaged $\mathbf{P}_{tot}$ over the region Γ:

$$\partial_t\tilde{\mathbf{E}}\left(\mathbf{r}_{ijk},n\Delta t\right)=\partial_t\tilde{\mathbf{D}}\left(\mathbf{r}_{ijk},n\Delta t\right)-\frac{1}{\Gamma}\partial_t\int\limits_{\Gamma_{ijk}}\mathbf{P}_{tot}\left(\mathbf{r}',n\Delta t\right)d^3r'. \tag{4.3.1}$$

where the $\tilde{\bullet}$ symbol now indicates that the above fields are merely some representation of the real physical fields. These quantities shall be referred to as "representative field values". Hence, the correct interpretation of the representative field values depends on the choice of the smoothing region Γ_{ijk}. Two possible choices for Γ_{ijk} and their resulting representative field values will be discussed here - each appropriate for different usage scenarios of the FDTD method.

4.3.1 Perturbation approach

One interpretation developed by Johnson et al. [88, 89] assumes that the location of the boundary between materials is only known within a given uncertainty. To illustrate the consequences, it is beneficial to assume that $\mathbf{P}_{tot}^{exp}(\mathbf{r})$ denotes the statistically expected polarization field of an interface region. The actual position of this region, however, is unknown and therefore the actual polarization $\mathbf{P}_{tot}^{act}(\mathbf{r})$ can be given as

$$\mathbf{P}_{tot}^{act}(\mathbf{r}_{ijk}) = \mathbf{P}_{tot}^{exp}(\mathbf{r}_{ijk} + \Delta\mathbf{r}),$$

where $\mathbf{\Delta r}$ is the difference in position between the actual and expected polarization field. Further, by assuming that the shift in position $\mathbf{\Delta r}$ is perfectly random, yet definitely within one Yee cell volume ΔV, the statistical average polarization field is given by

$$\mathbf{P}_{tot}^{avg}(\mathbf{r}_{ijk}) = \frac{1}{\Delta V}\int\limits_{V_{ijk}} \mathbf{P}_{tot}^{exp}(\mathbf{r}')\, d^3r', \tag{4.3.2}$$

which is identical to the smoothing operation defined in equation 4.1.2 for $\Gamma_{ijk} = V_{ijk}$ where V_{ijk} is the volume of the ijk-th Yee cell. In the absence of magnetic sources $\mathbf{M}$, the electric field $\mathbf{E}$ is completely defined by the polarization response $\mathbf{P}_{tot}$ and, together with the linearity of Maxwell's Equations, means that by using the above polarization response $\mathbf{P}_{tot}^{avg}$, the representative electric field $\tilde{\mathbf{E}}$ must be interpreted as a statistical average of the physical electric field $\mathbf{E}$ over many computational experiments with randomly shifted boundary locations.

It is more likely that the shift in position $\mathbf{\Delta r}$ of the interface region is not completely random within a certain region ΔV. Instead, points closer to the expected location of the boundary are expected to be more likely. However, Johnson et al. show that even if the integral on the RHS of equation 4.3.2 includes a smoothing function (denoted with g_s in [88]), the overall interpretation of the electric field as a perturbation to the interface position remains true for $\Delta V \to 0$.

4.3.2 Integral form of Maxwell's Equations

Another way to interpret the representative field values $\tilde{\mathbf{E}}$ and $\tilde{\mathbf{D}}$ is to assume that they are volume averages over the ijk-th Yee cell

$$\tilde{\mathbf{E}}\Big|_{ijk}^{n} \equiv \frac{1}{\Delta V}\int\limits_{V_{ijk}} \mathbf{E}(\mathbf{r}', n\Delta t)\, d^3r'$$

$$\tilde{\mathbf{D}}\Big|_{ijk}^{n} \equiv \frac{1}{\Delta V}\int\limits_{V_{ijk}} \mathbf{D}(\mathbf{r}', n\Delta t)\, d^3r'.$$

and that the smoothing region is once again equal to the volume of the ijk-th Yee cell $\Gamma_{ijk} = V_{ijk}$. With this definition, equation 4.3.1 is simply the result of integrating both sides of the constituent relations over the Yee cell volume centred at $\mathbf{r}_{ijk}$ which obviously leads to a physical correct constituent relation. In particular, equations that may have seemed strange during the derivation of the sub-pixel averaging method, now are easily understandable. For example, with the above definitions, the electric field vector $\mathbf{E}_\eta$ at a location inside the η-th material now reads

$$\mathbf{E}_\eta = \frac{1}{V_\eta} \int\limits_{V_\eta} \mathbf{E}\left(\mathbf{r}', n\Delta t\right) d^3r'$$

and equation 4.1.14, which previously needed some post-hoc justification, simply states the obvious:

$$\frac{1}{\Delta V} \int\limits_{V_{ijk}} \mathbf{E}\left(\mathbf{r}', n\Delta t\right) d^3r' = \sum_\eta f_\eta \frac{1}{V_\eta} \int\limits_{V_\eta} \mathbf{E}\left(\mathbf{r}', n\Delta t\right) d^3r',$$

where $f_\eta \equiv V_\eta / \Delta V_{ijk}$ is now defined as the volume fraction of the η-th region.

This interpretation is attractive due to its simplicity. However, it can be shown that it leads to inconsistencies with Faraday's Law:

$$\partial_t \tilde{\mathbf{H}}\left(\mathbf{r}, t\right) = -c^{-1} \nabla \times \tilde{\mathbf{E}}\left(\mathbf{r}, t\right)$$

and by substituting $\tilde{\mathbf{E}}$ with its definition

$$\partial_t \tilde{\mathbf{H}}\left(\mathbf{r}, t\right) = -c^{-1} \frac{1}{\Delta V} \nabla \times \int\limits_{V_{ijk}} \mathbf{E}\left(\mathbf{r}', t\right) d^3r'.$$

It is now tempting to swap the order of the spatial derivatives and the integral, which would then lead to the interpretation of $\tilde{\mathbf{H}}$ as a volume averaged quantity:

$$\partial_t \tilde{\mathbf{H}}\left(\mathbf{r}, t\right) = -c^{-1} \frac{1}{\Delta V} \int\limits_{V_{ijk}} \nabla \times \mathbf{E}\left(\mathbf{r}', t\right) d^3r'.$$

Unfortunately,

$$\int\limits_{V_{ijk}} \nabla \times \mathbf{E}\left(\mathbf{r}', t\right) d^3r' \neq \nabla \times \int\limits_{V_{ijk}} \mathbf{E}\left(\mathbf{r}', t\right) d^3r'$$

for discontinuous electric fields $\mathbf{E}$, which is obviously the case at a material boundary.

To find a set of consistent representative field values, it is beneficial to use the

integral form of Maxwell's Equations

$$\begin{aligned}\partial_t \int\limits_A \mathbf{E}(\mathbf{r}',t)\cdot d\mathbf{a} &= c^{-1}\oint\limits_{\partial A}\mathbf{H}(\mathbf{r}',t)\,d\mathbf{s} - \partial_t\int\limits_A \mathbf{P}(\mathbf{r}',t)\cdot d\mathbf{a}\\ \partial_t \int\limits_A \mathbf{H}(\mathbf{r}',t)\cdot d\mathbf{a} &= -c^{-1}\oint\limits_{\partial A}\mathbf{E}(\mathbf{r}',t)\cdot d\mathbf{s},\end{aligned}$$

where the area A is a surface of a Yee cell and $d\mathbf{a}$ is a vector perpendicular to this surface. To discretise the above equations, both sides of Faraday's Law and Ampére's Law are integrated over a single time step Δt. As the fields are assumed to be continuous in time, the Leibniz-Rule can be used. Ampère's Law then becomes

$$\int\limits_A \mathbf{E}(\mathbf{r}',(n+1)\Delta t)\cdot d\mathbf{a} - \int\limits_A \mathbf{E}(\mathbf{r}',n\Delta t)\cdot d\mathbf{a} = c^{-1}\int\limits_{(n-\frac{1}{2})\Delta t}^{(n+\frac{1}{2})\Delta t}\oint\limits_{\partial A}\mathbf{H}(\mathbf{r}',t')\cdot d\mathbf{s}dt' - \int\limits_A \mathbf{P}(\mathbf{r}',(n+1)\Delta t)\cdot d\mathbf{a} + \int\limits_A \mathbf{P}(\mathbf{r}',n\Delta t)\cdot d\mathbf{a},$$

and Faraday's Law reads

$$\int\limits_A \mathbf{H}(\mathbf{r}',(n+1)\Delta t)\cdot d\mathbf{a} - \int\limits_A \mathbf{H}(\mathbf{r}',n\Delta t)\cdot d\mathbf{a} = -c^{-1}\int\limits_{(n-\frac{1}{2})\Delta t}^{(n+\frac{1}{2})\Delta t}\oint\limits_{\partial A}\mathbf{E}(\mathbf{r}',t')\cdot d\mathbf{s}dt'.$$

Again, by using the assumption that the fields are continuous with respect to time, the temporal integrals can be approximated for $\Delta t \to 0$:

$$\int\limits_{(n-\frac{1}{2})\Delta t}^{(n+\frac{1}{2})\Delta t} F(\mathbf{r},t')\,dt' \approx \Delta t F(\mathbf{r}',n\Delta t)$$

The path integrals in Ampère's and Faraday's Law can be further split into integrals over straight lines. By doing this one obtains update equations which have an identical form to the FDTD update equations. To shorten equations, the following notation will be used

$$\langle F_\nu\rangle_{ijk}^n \equiv \iint\limits_{A_{ijk}^\nu}\mathbf{F}(\mathbf{r}',n\Delta t)\cdot d\mathbf{a} \tag{4.3.3}$$

$$\|F_\nu\|_{ijk}^n \equiv \int\limits_{l_{ijk}^\nu}\mathbf{F}(\mathbf{r}',n\Delta t)\cdot d\mathbf{r}', \tag{4.3.4}$$

where A_{ijk}^ν is an area centred at $\mathbf{r}_{ijk}$, with the normal vector $\mathbf{e}_\nu$ and an area of

$A = \Delta V/\Delta\nu$; and l^{ν}_{ijk} is a line centred at $\mathbf{r}_{ijk}$, pointing in the $\mathbf{e}_\nu$ direction and with a length of $\Delta\nu$ where ν is either the x,y,z component. The update equations now read

$$\langle E_x\rangle^{n+1}_{j,k-\frac{1}{2}} = \langle E_x\rangle^{n}_{j,k-\frac{1}{2}} + c^{-1}\Delta t\left(\|H_z\|^{n+\frac{1}{2}}_{j+\frac{1}{2},k-\frac{1}{2}} - \|H_z\|^{n+\frac{1}{2}}_{j+\frac{1}{2},k-\frac{1}{2}}\right) - \langle P_x\rangle^{n+1}_{j,k-\frac{1}{2}} + \langle P_x\rangle^{n+1}_{j,k-\frac{1}{2}}$$

$$\langle E_y\rangle^{n+1}_{j+\frac{1}{2},k} = \langle E_y\rangle^{n}_{j+\frac{1}{2},k} + c^{-1}\Delta t\left(\|H_z\|^{n+\frac{1}{2}}_{j+\frac{1}{2},k-\frac{1}{2}} - \|H_z\|^{n+\frac{1}{2}}_{j+\frac{1}{2},k+\frac{1}{2}}\right) - \langle P_y\rangle^{n+1}_{j+\frac{1}{2},k} + \langle P_y\rangle^{n+1}_{j+\frac{1}{2},k}$$

$$\begin{aligned}\langle H_z\rangle^{n+\frac{1}{2}}_{j+\frac{1}{2},k-\frac{1}{2}} = \langle H_z\rangle^{n-\frac{1}{2}}_{j+\frac{1}{2},k-\frac{1}{2}} - c^{-1}\Delta t\Big(&\|E_y\|^{n}_{j+\frac{1}{2},k} - \|E_y\|^{n}_{j+\frac{1}{2},k-1}\\ &+ \|E_x\|^{n}_{j,k-\frac{1}{2}} - \|E_x\|^{n}_{j+1,k-\frac{1}{2}}\Big),\end{aligned}$$

where the 2-D TM case was assumed for brevity only. Apart from the approximation regarding the temporal integrals, no approximations have been invoked so far. Therefore, for $\Delta t \to 0$, the above equations are exact for *any* ΔV. Unfortunately, the equations are uncoupled and cannot be used for a numerical scheme unless the following relationships are found:

$$\langle E_\nu\rangle_{ijk} \leftrightarrow \|E_\nu\|_{ijk}$$

$$\langle H_\nu\rangle_{ijk} \leftrightarrow \|H_\nu\|_{ijk}\,.$$

Assuming that there is no magnetic polarization response, the magnetic field $\mathbf{H}$ is continuous throughout the Yee cell and therefore the average value of the ν-th magnetic field component H_ν over any area A inside the Yee cell is approximately equivalent to the average over any line within the same Yee cell:

$$\frac{1}{\Delta A}\langle H_\nu\rangle_{ijk} = \frac{\Delta\nu}{\Delta V}\langle H_\nu\rangle_{ijk} \to \frac{1}{\Delta\nu}\|H_\nu\|_{ijk} \text{ for } \Delta V \to 0. \tag{4.3.5}$$

It is once again beneficial to investigate the perpendicular and parallel components of the electric field separately. With this, it remains to find the correct relationship between

$$\begin{aligned}\langle E_\parallel\rangle_{ijk} &\leftrightarrow \|E_\parallel\|_{ijk}\\ \langle E_\perp\rangle_{ijk} &\leftrightarrow \|E_\perp\|_{ijk}\,.\end{aligned}$$

The above relationships are depicted in figure 4.3.1.

Once again, the parallel component of the electric field is straightforward as Gauss's Law states that it is continuous across the interface. Therefore

$$\frac{\Delta\nu_\parallel}{\Delta V}\langle E_\parallel\rangle_{ijk} \approx \frac{1}{\Delta\nu_\parallel}\|E_\parallel\|_{ijk}\,, \tag{4.3.6}$$

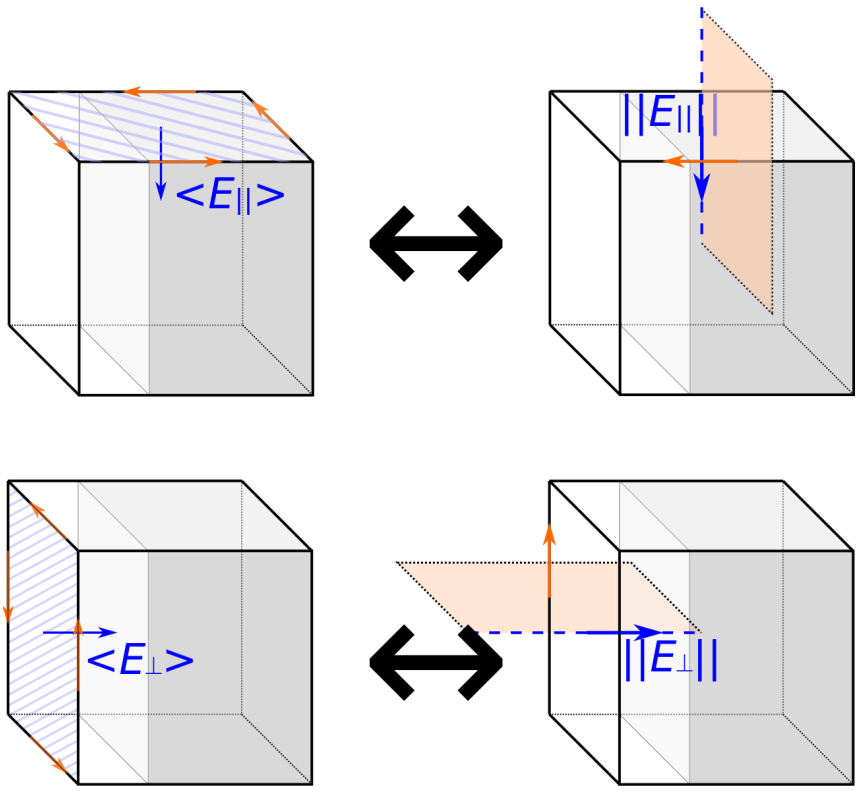

Figure 4.3.1: The relationship between the electric field averaged over a Yee cell surface (left) and over a line perpendicular to a Yee cell surface (right). Top: The electric field component is parallel to the material interface. In this case, $\langle E_{\parallel} \rangle_{ijk} = \|E_{\parallel}\|_{ijk}$ for $\Delta V \to 0$. Bottom: The electric field component is perpendicular to the material interface. The line average (right) will cross the boundary of the interface causing a discontinuity.

where $\Delta\nu_{\|}$ is the length of the Yee cell edge along the $\nu_{\|}$-coordinate and $\nu_{\|}$ refers to one of the two parallel coordinates.

As always, the perpendicular field is more involved. Starting with the line average of the perpendicular component of the electric field $\|E_{\perp}\|_{ijk}$, figure 4.3.1 shows that the integrand will cross the boundary and therefore have a discontinuity. However, $\|E_{\perp}\|_{ijk}$ can be split into two line integrals

$$\|E_{\perp}\| = \int_{l^{\nu}_{ijk}} \mathbf{D}_{\perp} \cdot d\mathbf{s} - \int_{l^{\nu}_{ijk}} \mathbf{P}_{\perp} \cdot d\mathbf{s},$$

where the integrand of the first term on the RHS $D_{\perp}$ is continuous throughout the Yee cell. In particular, for $\Delta V \to 0$

$$\frac{1}{\Delta\nu_{\|}} \|D_{\perp}\|_{ijk} \to \frac{\Delta\nu_{\|}}{\Delta V} \langle D_{\perp} \rangle_{ijk}$$

and therefore the above equation can be approximated with

$$\frac{1}{\Delta\nu_{\|}} \|E_{\perp}\|_{ijk} \approx \frac{\Delta\nu_{\|}}{\Delta V} \langle D_{\perp} \rangle_{ijk} - \frac{1}{\Delta\nu_{\|}} \|P_{\perp}\|_{ijk}$$

or

$$\frac{1}{\Delta\nu_{\|}} \|E_{\perp}\|_{ijk} \approx \frac{\Delta\nu_{\|}}{\Delta V} \langle E_{\perp} \rangle_{ijk} + \frac{\Delta\nu_{\|}}{\Delta V} \langle P_{\perp} \rangle_{ijk} - \frac{1}{\Delta\nu_{\|}} \|P_{\perp}\|_{ijk}.$$

Solving the above equation for $\langle E_{\perp} \rangle_{ijk}$ and substituting the result and equation 4.3.6 into the 2-D TM version of Ampère's Law gives:

$$\begin{aligned} \|E_x\|^{n+1}_{j,k-\frac{1}{2}} = \|E_x\|^{n}_{j,k-\frac{1}{2}} + c^{-1}\Delta t \left(\|H_z\|^{n+\frac{1}{2}}_{j+\frac{1}{2},k-\frac{1}{2}} - \|H_z\|^{n+\frac{1}{2}}_{j+\frac{1}{2},k-\frac{1}{2}} \right) \\ - \|P_x\|^{n+1}_{j,k-\frac{1}{2}} + \|P_x\|^{n}_{j,k-\frac{1}{2}} \end{aligned} \tag{4.3.7}$$

$$\begin{aligned} \|E_y\|^{n+1}_{j+\frac{1}{2},k} = \|E_y\|^{n}_{j+\frac{1}{2},k} + c^{-1}\Delta t \left(\|H_z\|^{n+\frac{1}{2}}_{j+\frac{1}{2},k-\frac{1}{2}} - \|H_z\|^{n+\frac{1}{2}}_{j+\frac{1}{2},k+\frac{1}{2}} \right) \\ - \langle P_y \rangle^{n+1}_{j+\frac{1}{2},k} + \langle P_y \rangle^{n+1}_{j+\frac{1}{2},k} \end{aligned} \tag{4.3.8}$$

where it was assumed that the x-axes lies perpendicular to the material boundary. With equation 4.3.5 Faraday's Law becomes

$$\begin{aligned} \|H_z\|^{n+\frac{1}{2}}_{j+\frac{1}{2},k-\frac{1}{2}} = \|H_z\|^{n-\frac{1}{2}}_{j+\frac{1}{2},k-\frac{1}{2}} - c^{-1}\Delta t \Big(\|E_y\|^{n}_{j+\frac{1}{2},k} - \|E_y\|^{n}_{j+\frac{1}{2},k-1} \\ + \|E_x\|^{n}_{j,k-\frac{1}{2}} - \|E_x\|^{n}_{j+1,k-\frac{1}{2}} \Big) \end{aligned}$$

and therefore both update equations are now coupled. Therefore, the following

representative field values have now been found [90]

$$\tilde{\mathbf{E}} = \|\mathbf{E}\| \, ; \, \tilde{\mathbf{H}} = \|\mathbf{H}\| \, .$$

along with the following, now orientation dependent smoothing region operation Γ_{ijk}:

$$\Gamma_{ijk} \equiv \begin{cases} A^{\nu}_{ijk} & \text{if component } \nu \text{ of the integrant is parallel to the interface} \\ l^{\nu}_{ijk} & \text{if component } \nu \text{ of the integrant is perpendicular to the interface} \end{cases}$$

With this, the filling factors f_η now also depend on the orientation and therefore, $f_\eta^\perp$ shall now denote a fraction of line-lengths and $f_\eta^\parallel$ an area-fraction. The results of the previous sections are summarized in table 4.1 using the new notation.

4.4 FDTD algorithms employing the sub-pixel averaging method

Although the theoretical foundations for a numerical algorithm to integrate Maxwell's Equations at a Yee cell containing a material boundary have been laid, some important details on the computational implementation of the theory have yet to be discussed. It was shown, that regardless of which smoothing region Γ_{ijk} is used, the polarization functional (or the dielectric constant) will generally become anisotropic as the effective polarization response depends on the orientation of the electric field vector. Therefore, a spatial interpolation must be used to apply the anisotropic polarization response as was discussed in section 2.4. Additionally, if the materials cannot be described by a static dielectric constant, then the implicit equations 4.1.12-4.1.14 for $E_{\perp,\nu}$ must be solved. Several different methods to achieve this have been developed of which some are presented here.

4.4.1 Direct method

The direct method implements the sub-pixel averaging equations 4.1.12-4.1.14 without any modifications. The method was developed by the author during the course of this thesis. As discussed above, a challenge with any implementation of the sub-pixel averaging method is that equation 4.1.13 is recursively defined, i.e. the RHS of the equation indirectly depends on the LHS via the polarization functional. However, if the polarization response of all materials inside the Yee cell is non-instantaneous, then the RHS of equation 4.1.13 only depends on the partial electric field $\mathbf{E}_\eta$ from the previous time step and hence the recursion is resolved. It is therefore beneficial

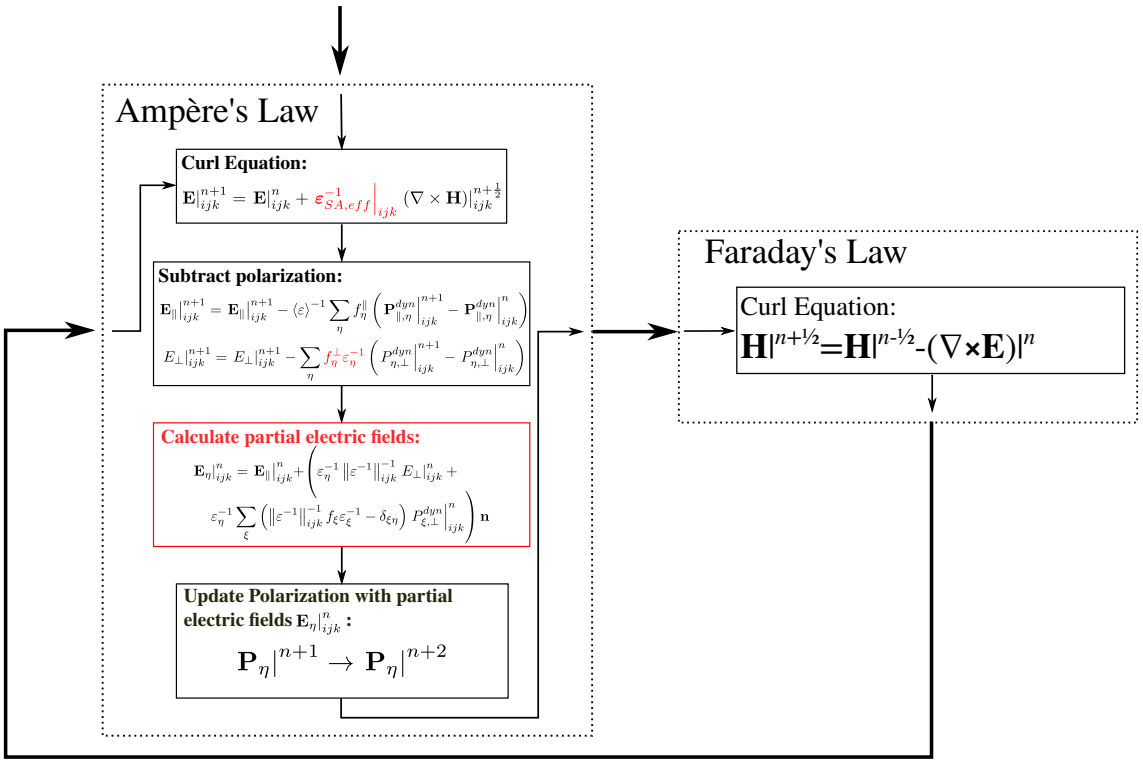

Figure 4.4.1: Diagram of the direct method. Steps which are different from the DVA method are highlighted in red. Details of the algorithm can be found in the text.

to temporarily assume that the polarization responses $\mathbf{P}_\eta$ are non-instantaneous and later discuss any alterations required to also include instantaneous static responses.

By inserting equation 4.1.12 into Ampère's Law, the update equation for the electric field within this method is

$$\mathbf{E}|_{ijk}^{n+1} = \mathbf{E}|_{ijk}^{n} + (\nabla \times \mathbf{H})|_{ijk}^{n+\frac{1}{2}} - \sum_\eta f_\eta \left(\mathbf{P}_\eta|_{ijk}^{n+1} \left[\mathbf{E}_\eta|_{ijk}^{n} \right] - \mathbf{P}_\eta|_{ijk}^{n} \left[\mathbf{E}_\eta|_{ijk}^{n} \right] \right), \quad (4.4.1)$$

where $\mathbf{P}_\eta|_{ijk}$ is the polarization response of the η-th material and that - within the integral form interpretation (see section 4.3.2) - the filling factors f_η will additionally depend on the orientation of the polarization. The above update equation implies the following constituent equation between the FDTD fields

$$\mathbf{E}|_{ijk}^{n} = \mathbf{D}|_{ijk}^{n} - \sum_\eta f_\eta \, \mathbf{P}_\eta|_{ijk}^{n} \quad (4.4.2)$$

As outlined in the derivation of the sub-pixel averaging method, the polarization response $\mathbf{P}_\eta|_{ijk}$ in the above equations is evaluated with the partial electric field $\mathbf{E}_\eta$ of previous time steps. $\mathbf{E}_\eta$ is given by equation 4.1.13

$$\mathbf{E}_\eta|_{ijk}^{n} \equiv \mathbf{E}_\parallel|_{ijk}^{n} + \left(D_\perp|_{ijk}^{n} - P_{\perp,\eta}|_{ijk}^{n} \right) \mathbf{n} \quad (4.4.3)$$

and by inserting the above constituent relation (equation 4.4.2) one finds

$$\mathbf{E}_\eta|_{ijk}^n \equiv \mathbf{E}_\parallel\big|_{ijk}^n + \left(E_\perp|_{ijk}^n + \sum_\xi \left(f_\xi - \delta_{\xi\eta}\right) P_{\perp,\xi}|_{ijk}^n \right) \mathbf{n}, \tag{4.4.4}$$

where $\delta_{\xi\eta}$ is the Kronecker delta. Equations 4.4.1 and 4.4.4 now fully specify the direct method.

The sequence of evaluation of these equations is as follows: firstly, the individual polarization responses of the materials are updated $\mathbf{P}_\eta|^{n-1} \rightarrow \mathbf{P}_\eta|^n$, which requires the calculation of the value of the electric field $\mathbf{E}_\eta|^{n-1}$ inside the η-th material from the previous time step. This can be calculated on-the-fly with equation 4.4.4 and does not require additional memory. However, as all of the polarization responses $\mathbf{P}_\xi|^{n-1}$ from the previous time steps are required to evaluate $\mathbf{E}_\eta|^{n-1}$, updating $\mathbf{P}_\eta|^{n-1} \rightarrow \mathbf{P}_\eta|^n$ must not overwrite the polarization from the previous time step in memory, as this will be required when evaluating the next material polarization update equation $\mathbf{P}_{\eta+1}|^{n-1} \rightarrow \mathbf{P}_{\eta+1}|^n$. This requires at least $N-1$ floating point values of temporary memory for each Yee cell containing a boundary, where N is the number of materials. However, for any polarization functional which is described by a recursive update equation (see chapter 2) - such as the Drude or Lorentzian responses - the previous polarization value is already stored in memory and therefore does not require any additional memory in these cases.

After all polarization responses have been updated, the electric field update equation can be executed, after which the magnetic field update equation is executed, completing a single FDTD time step. This sequence is depicted in figure 4.4.1 and pseudo-code for the direct implementation of the sub-pixel averaging method is given in section A.3.

The method shall now be extended to materials which contain an instantaneous dielectric response

$$\mathbf{P}_\eta\left[\mathbf{E}_\eta\right] \equiv \left(\varepsilon_\eta - 1\right)\mathbf{E}_\eta + \mathbf{P}_\eta^{dyn}\left[\mathbf{E}_\eta\right], \tag{4.4.5}$$

where $\mathbf{P}_\eta^{dyn}$ is the non-instantaneous dynamic response and ε_η is the dielectric constant of the η-th material. Inserting the above into the update equation of the electric field (equation 4.4.1) and following the derivation laid out in section 4.2 leads to the following new update equation for $\mathbf{E}|_{ijk}^n$:

$$\begin{aligned}\mathbf{E}|_{ijk}^{n+1} = \mathbf{E}|_{ijk}^n &+ \boldsymbol{\varepsilon}_{SA,eff}^{-1}\big|_{ijk} \left(\nabla \times \mathbf{H}\right)|_{ijk}^{n+\frac{1}{2}} \\ &- \langle\varepsilon\rangle^{-1} \sum_\eta f_\eta^\parallel \left(\mathbf{P}_{\parallel,\eta}^{dyn}\Big|_{ijk}^{n+1} - \mathbf{P}_{\parallel,\eta}^{dyn}\Big|_{ijk}^{n} \right) \\ &- \sum_\eta f_\eta^\perp \varepsilon_\eta^{-1} \left(P_{\eta,\perp}^{dyn}\Big|_{ijk}^{n+1} - P_{\eta,\perp}^{dyn}\Big|_{ijk}^{n} \right) \mathbf{n},\end{aligned} \tag{4.4.6}$$

where $\boldsymbol{\varepsilon}^{-1}_{SA,eff}\big|_{ijk}$ is the effective dielectric tensor given by equation 4.2.2. The above update equation implies the following new constituent equation between the FDTD fields

$$\mathbf{E}|^n_{ijk} = \boldsymbol{\varepsilon}^{-1}_{SA,eff}\big|_{ijk}\, \mathbf{D}|^n_{ijk} - \langle\varepsilon\rangle^{-1} \sum_\eta f^{\parallel}_\eta\, \mathbf{P}^{dyn}_{\parallel,\eta}\Big|^n_{ijk} - \sum_\eta f^{\perp}_\eta \varepsilon^{-1}_\eta\, P^{dyn}_{\eta,\perp}\Big|^n_{ijk}.$$

By substituting this and equation 4.4.5 into equation 4.4.3 gives the following new expression for the partial electric field $\mathbf{E}_\eta|^n_{ijk}$:

$$\mathbf{E}_\eta|^n_{ijk} = \mathbf{E}_\parallel\big|^n_{ijk} + \left(\varepsilon^{-1}_\eta \left\|\varepsilon^{-1}\right\|^{-1}_{ijk} E_\perp|^n_{ijk} + \varepsilon^{-1}_\eta \sum_\xi \left(\left\|\varepsilon^{-1}\right\|^{-1}_{ijk} f_\xi \varepsilon^{-1}_\xi - \delta_{\xi\eta} \right) P^{dyn}_{\xi,\perp}\Big|^n_{ijk} \right) \mathbf{n}.$$

An advantage of the direct method is that it places no restrictions on how the fields are split into parallel and perpendicular components. Essentially, the last two terms in the electric field update equation 4.4.6 can be treated as a single anisotropic polarization response and any spatial interpolation method described in section 2.4 can be used to apply them to the update equation. Further, the direct method can be applied to Yee cells containing any number of materials.

A disadvantage of the direct method is its significant increase in computational complexity compared to the traditional FDTD algorithm. This is due to two reasons: firstly, the update equations of the electric field have become anisotropic and therefore more computational operations are required per Yee cell to carry out any necessary spatial interpolation. Secondly, equation 4.4.4 must be evaluated N times for each Yee cell containing a material boundary, where N is the number of materials. As equation 4.4.4 in itself requires N computational operations the overall complexity of updating a single Yee cell is proportional to N^2.

4.4.2 Sub-pixel averaging for the static response (MEEP)

To avoid the computational complexity in evaluating the value of the electric field $\mathbf{E}_\eta$ within the η-th material, the popular and freely available, open-source solver MEEP [86] only applies the sub-pixel averaging method to the static instantaneous response. The VA method is applied to any remaining polarization response. With this the electric update equation simply becomes

$$\begin{aligned}\mathbf{E}|^{n+1}_{ijk} = \mathbf{E}|^n_{ijk} &+ \boldsymbol{\varepsilon}^{-1}_{SA,eff}\big|_{ijk}\, (\nabla\times\mathbf{H})|^{n+\frac{1}{2}}_{ijk} \\ &- \langle\varepsilon\rangle^{-1} \sum_\eta f_\eta \left(\mathbf{P}^{dyn}_\eta\big|^{n+1}_{ijk} \left[\mathbf{E}|^n_{ijk}\right] - \mathbf{P}^{dyn}_\eta\big|^n_{ijk} \left[\mathbf{E}|^{n-1}_{ijk}\right] \right).\end{aligned}$$

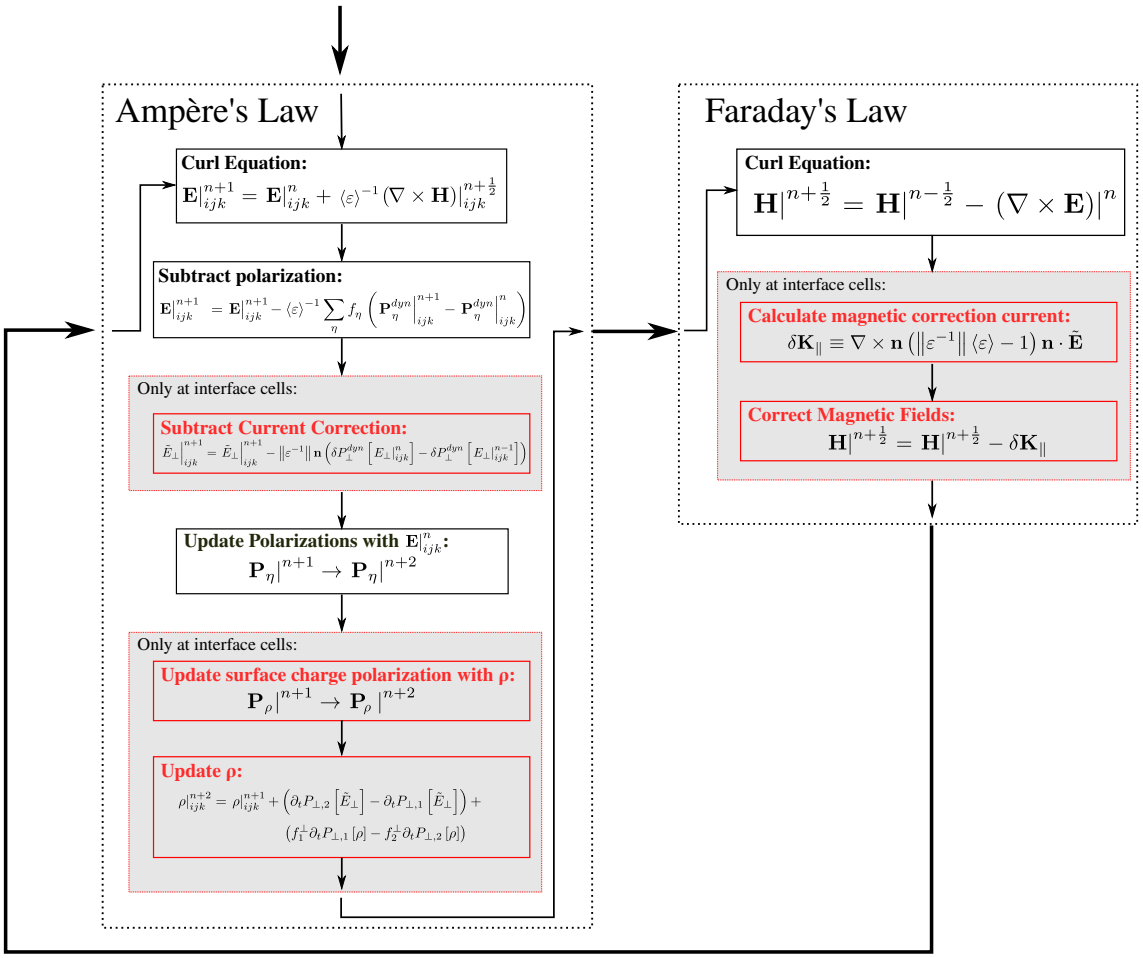

Figure 4.4.2: Diagram of the INCA (Induced Normal Current Approximation) method. Steps which are different from the DVA method are highlighted in red. Details of the algorithm can be found in the text.

In addition, the MEEP code uses the interpretation of the field values which leads to the perturbation approach (see section 4.3.1) and, therefore, all averages and fill-factors are volume averages or volume ratios respectively [91].

The success of MEEP is largely based on its well structured code-base and good computational efficiency. The approximations it uses is well suited for systems containing materials with strong differences in the static dielectric constant and relatively weak dynamic responses. This is because it correctly treats the static dielectric response of a Yee cell containing a material interface within the perturbation approach. It will be shown, however, that the nano-plasmonic system presented in chapter 5 also requires the correct treatment of the dynamic response.

4.4.3 The INCA Algorithm

Similar to the direct method, the INCA (Induced Normal Current Approximation) algorithm aims to also apply the sub-pixel averaging method to the dynamic material

response. The method was developed during the PhD of the author together with Dr. Joachim Hamm [92]. However, unlike the direct method, it aims to be compatible with the traditional *isotropic* FDTD update equations to reduce the computational complexity of the algorithm. It does this by first updating the electro-magnetic fields with the VA method, after which any errors are corrected at the interface cells only. As in the direct method, this derivation starts by assuming that all materials are non-instantaneous and later, will discuss any alterations required to also include instantaneous static responses. Furthermore, the INCA algorithm assumes that there are never more than two materials inside a single Yee cell - a valid assumption for most nano-plasmonic systems.

Within the VA approximation $\mathbf{P}_{eff} = \sum_\eta f_\eta \mathbf{P}_\eta$, the update equation for the electric field is as follows

$$\begin{aligned}\mathbf{E}|_{ijk}^{n+1} = \mathbf{E}|_{ijk}^{n} + (\nabla \times \mathbf{H})|^{n+\frac{1}{2}} \quad &- \quad \sum_{\eta=1}^{2} f_\eta^{\parallel} \left(\mathbf{P}_\eta \left[\mathbf{E}|_{ijk}^{n} \right] - \mathbf{P}_\eta \left[\mathbf{E}|_{ijk}^{n-1} \right] \right) \\ &- \quad \mathbf{n} \left(\delta P_\perp \left[E_\perp|_{ijk}^{n} \right] - \delta P_\perp \left[E_\perp|_{ijk}^{n-1} \right] \right) \end{aligned} \tag{4.4.7}$$

where $\sum_{\eta=1}^{2}$ indicates that there are never more than two materials at an interface cell and $\delta P_\perp$ is a correction term. Without this correction term, equations 4.1.12 and 4.1.13 show, that the above is correct for the parallel components of the electric field and therefore only the perpendicular component must be corrected by adding the following correction polarization to the perpendicular component of Ampère's Law

$$\delta P_\perp = f_1^\perp P_{\perp,1}\left[E_{\perp,1}\right] + f_2^\perp P_{\perp,2}\left[E_{\perp,2}\right] - f_1^{\parallel} P_{\perp,1}\left[E_\perp\right] - f_2^{\parallel} P_{\perp,2}\left[E_\perp\right]. \tag{4.4.8}$$

The first two terms above are the correct method for averaging over a perpendicular polarization response and the last two subtract the incorrectly averaged polarization responses from equation 4.4.7.

To now calculate the unknown quantities $E_{\perp,1}$, $E_{\perp,2}$, the INCA algorithm introduces a new quantity

$$\rho \equiv E_{\perp,2} - E_{\perp,1}$$

which, in the limit of $\Delta V \to 0$ is formally identical to the surface charge between both materials. With this and equation 4.1.14, the $E_{\perp,\nu}$ are uniquely defined

$$E_{\perp,1} = E_\perp - f_2^\perp \rho \tag{4.4.9}$$

$$E_{\perp,2} = E_\perp - f_1^\perp \rho \tag{4.4.10}$$

where $f_1^\perp$, $f_2^\perp$ are the perpendicular filling factors which depend on the selected

smoothing process Γ. It remains to find a method to efficiently calculate the surface charge ρ. This can be found by taking the time derivative of ρ and using equation 4.1.13, which leads to

$$\partial_t \rho = \partial_t P_{\perp,2}\left[E_{\perp,2}\right] - \partial_t P_{\perp,1}\left[E_{\perp,1}\right],$$

Further, by substituting equations 4.4.9, 4.4.10 into the above equation and assuming that the polarizations are linear, one finds the following update equation for ρ

$$\partial_t \rho = \left(\partial_t P_{\perp,2}\left[E_\perp\right] - \partial_t P_{\perp,1}\left[E_\perp\right]\right) + \left(f_1^\perp \partial_t P_{\perp,1}\left[\rho\right] - f_2^\perp \partial_t P_{\perp,2}\left[\rho\right]\right), \tag{4.4.11}$$

which can now be numerically integrated along side the FDTD update equations as an axillary equation. Once more, equations 4.4.9, 4.4.10 are substituted into the expression for the correction polarization $\delta P_\perp$ and the quantities $E_{\perp,1}$ and $E_{\perp,2}$ can be eliminated from the equations completely:

$$\delta P_\perp = \left(f_1^\perp - f_1^\parallel\right) P_{\perp,1}\left[E_\perp\right] + \left(f_2^\perp - f_2^\parallel\right) P_{\perp,2}\left[E_\perp\right] - f_1^\perp f_2^\perp P_{\perp,1}\left[\rho\right] - f_1^\perp f_2^\perp P_{\perp,2}\left[\rho\right] \tag{4.4.12}$$

which, together with equations 4.4.7 and 4.4.11, conclude the derivation of the INCA algorithm. As equation 4.4.7 is isotropic, it can be updated by one time step with an isotropic FDTD solver through-out the computational region, after which, the current correction 4.4.12 must be applied to the interface Yee cells only. This is because $f_\eta^\perp = f_\eta^\parallel$ and $f_1^\perp f_2^\perp = 0$ when there is no interface present in the Yee cell and therefore $\delta P_\perp$ is only non-zero at a Yee cell containing a material boundary.

It should be noted that, if the field values represent a statistical average as described in section 4.3.1, then the smoothing process $\langle \bullet \rangle$ is the same for the parallel and perpendicular components and therefore $f_\eta^\perp = f_\eta^\parallel$. Within this interpretation, the INCA algorithm becomes particularly elegant as the equation for the polarization correction $\delta P_\perp$ (equation 4.4.12) will only depend on the surface charge ρ.

It was assumed above that the polarization function is linear and therefore, strictly, the INCA algorithm cannot be used for the non-linear systems discussed in chapter 3. However, if the non-linear component is small compared to the linear response then the INCA algorithm is still a good approximations. This is typically true for the two- and four-level systems discussed in chapter 3, as the systems are modelled by Lorentzian resonance responses with a coupling determined by the occupation levels of the system. As the occupations typically vary only slowly compared to the oscillations of the polarization functional, the responses of the two- and four-level systems are nearly linear.

The INCA equations 4.4.11 and 4.4.12 require the decomposition of the electric

field $\mathbf{E}$ into a perpendicular component $E_\perp$ and parallel components $\mathbf{E}_\parallel$. As was discussed in section 2.4, this generally requires some form of spatial interpolation as the different field components of $\mathbf{E}$ are spread-out at different locations within the Yee cell. The INCA algorithm puts $E_\perp$ at the Yee cell centre, i.e. the electric field vector $\mathbf{E}$ is calculated at the cell-centre by linear interpolating each field component from the surrounding Yee cell locations

$$\begin{aligned} E_\perp = \frac{1}{2}\left(E_x|_{ij,k-\frac{1}{2}} + E_x|_{ij,k+\frac{1}{2}}\right)\mathbf{n}\cdot\mathbf{e}_x &+ \frac{1}{2}\left(E_y|_{i,j+\frac{1}{2},k} + E_y|_{i,j+\frac{1}{2},k}\right)\mathbf{n}\cdot\mathbf{e}_y \\ &+ \frac{1}{2}\left(E_z|_{i+\frac{1}{2},j,k} + E_z|_{i-\frac{1}{2},j,k}\right)\mathbf{n}\cdot\mathbf{e}_z. \end{aligned}$$

As the surface charge ρ and the correction polarization $\delta P_\perp$share the same location with $E_\perp$, all scalar quantities in the INCA algorithm are quantities which are defined at the Yee cell centre. Consequently, after the correction polarization $\delta P_\perp$ is calculated, it must be applied to the perpendicular component of the electric field, which requires $\delta P_\perp \mathbf{n}$ to be spread out to the original Yee cell positions, which requires an additional spatial interpolation.

Other spatial interpolation methods were introduced in section 2.4. However, each of these methods calculates the full vectorial electric-field $\mathbf{E}$ at multiple positions within in the Yee cell. This would be incompatible with the definition of ρ as scalar field, i.e. ρ has a single scalar value per Yee cell.

The INCA algorithm is now extended to allow the treatment of materials which include a static instantaneous response:

$$\mathbf{P}_\eta\left[\mathbf{E}\right] = \left(\varepsilon_\eta - 1\right)\mathbf{E} + \mathbf{P}^{dyn}\left[\mathbf{E}\right].$$

Inserting the above response into equations 4.4.7 and 4.4.8 gives the following new update equation

$$\begin{aligned} \mathbf{E}|_{ijk}^{n+1} = \mathbf{E}|_{ijk}^{n} &+ \langle\varepsilon\rangle^{-1}\left(\nabla\times\mathbf{H}\right)|_{ijk}^{n+\frac{1}{2}} \\ &- \langle\varepsilon\rangle^{-1}\sum_{\eta=1}^{2} f_1^{\parallel}\left(\mathbf{P}_\eta^{dyn}\left[\mathbf{E}|_{ijk}^{n}\right] - \mathbf{P}_\eta^{dyn}\left[\mathbf{E}|_{ijk}^{n-1}\right]\right) \\ &- \langle\varepsilon\rangle^{-1}\mathbf{n}\left(\delta P_\perp^{dyn}\left[E_\perp|_{ijk}^{n}\right] - \delta P_\perp^{dyn}\left[E_\perp|_{ijk}^{n-1}\right]\right) \\ &- \langle\varepsilon\rangle^{-1}\mathbf{n}\left(\left\|\varepsilon^{-1}\right\|^{-1} - \langle\varepsilon\rangle\right)\left(E_\perp|_{ijk}^{n+1} - E_\perp|_{ijk}^{n}\right) \end{aligned} \tag{4.4.13}$$

where $\langle\varepsilon\rangle \equiv f_1^{\parallel}\varepsilon_1 + f_2^{\parallel}\varepsilon_2$ and $\|\varepsilon^{-1}\| \equiv f_1^{\perp}\varepsilon_1^{-1} + f_2^{\perp}\varepsilon_2^{-1}$. The last term in the above equation re-affirms the interpretation of $\delta P_\perp$ as a correction for the perpendicular electric field. Yet, the electric field update equation still directly depends on current time step of $E_\perp$ on the RHS. Similar, to the approach in section 4.3, this is overcome

by redefining the quantity which is integrated by the FDTD update equations (the representative field value) $\tilde{\mathbf{E}}$, as a quantity which does not include the correction for the instantaneous response

$$\tilde{E}_\perp \equiv \langle\varepsilon\rangle^{-1} \left\|\varepsilon^{-1}\right\|^{-1} E_\perp$$

or, as the parallel component of the representative field value is already correct, the representative field value $\tilde{\mathbf{E}}$ is given by

$$\tilde{\mathbf{E}} = \mathbf{E}_\parallel + \langle\varepsilon\rangle^{-1} \left\|\varepsilon^{-1}\right\|^{-1} E_\perp \mathbf{n}. \tag{4.4.14}$$

Indeed, by solving the above quantity for $\mathbf{E}$ and inserting it into 4.4.13, the update equation for the representative field value $\tilde{\mathbf{E}}$ does not directly depend on $E_\perp$ any more, and, apart from the polarization correction term $\delta P_\perp$, is purely isotropic

$$\begin{aligned}\tilde{\mathbf{E}}\Big|_{ijk}^{n+1} = \tilde{\mathbf{E}}\Big|_{ijk}^{n} + \langle\varepsilon\rangle^{-1} (\nabla\times\mathbf{H})\big|_{ijk}^{n+\frac{1}{2}} &- \langle\varepsilon\rangle^{-1} \sum_{\eta=1}^{2} f_1^{\parallel} \left(\mathbf{P}_\eta^{dyn}\left[\tilde{\mathbf{E}}\Big|_{ijk}^{n}\right] - \mathbf{P}_\eta^{dyn}\left[\tilde{\mathbf{E}}\Big|_{ijk}^{n-1}\right]\right) \\ &- \langle\varepsilon\rangle^{-1} \mathbf{n}\left(\delta P_\perp^{dyn}\left[E_\perp|_{ijk}^{n}\right] - \delta P_\perp^{dyn}\left[E_\perp|_{ijk}^{n-1}\right]\right)\end{aligned}$$

Obviously, the update equation for the surface charge ρ (equation 4.4.11), the expression for the polarization correction $\delta P_\perp^{dyn}$ (equation 4.4.12) and Faraday's Law still depend on the real physical perpendicular electric field $E_\perp$, yet only the representative field value $\tilde{E}_\perp$ is stored in memory. Therefore, the physical electric field must be recovered by equation 4.4.14. In an attempt to not alter the original FDTD update equations, Faraday's Law is initially calculated with the incorrect representative field value $\tilde{\mathbf{E}}$ and then corrected with a corrective magnetic current density:

$$\partial_t \mathbf{H} = -\nabla\times\tilde{\mathbf{E}} - \delta\mathbf{K}_\parallel$$

and

$$\delta\mathbf{K}_\parallel \equiv \nabla\times\mathbf{n}\left(E_\perp - \tilde{E}_\perp\right) = \nabla\times\mathbf{n}\left(\left\|\varepsilon^{-1}\right\|\langle\varepsilon\rangle - 1\right)\mathbf{n}\cdot\tilde{\mathbf{E}}.$$

Similarly, equation 4.4.14 is solved for the physical electric field $E_\perp$ and then inserted into the update equation for the surface charge ρ and the polarization correction $\delta P_\perp^{dyn}$. Using the linearity of the polarization functionals and the following redefinitions

$$\rho \to \langle\varepsilon\rangle^{-1} \left\|\varepsilon^{-1}\right\|^{-1} \rho$$

$$\delta P_\perp^{dyn} \to \langle\varepsilon\rangle^{-1} \left\|\varepsilon^{-1}\right\|^{-1} \delta P_\perp^{dyn}$$

the expressions for the update equation of the surface charge ρ and the current correction $\delta P_\perp$ remain identical to equations 4.4.11 and 4.4.12, apart from now de-

pending on the perpendicular component of the representative field value $\tilde{E}_\perp$. Only, the update equation for the representative field value, requires a slight modification to accommodate the above redefinitions, which will be stated here along with all other equations which define the INCA algorithm with the presence of instantaneous material responses

$$\begin{aligned}\tilde{\mathbf{E}}\Big|_{ijk}^{n+1} = \tilde{\mathbf{E}}\Big|_{ijk}^{n} + \langle\varepsilon\rangle^{-1}\left(\nabla\times\mathbf{H}\right)\Big|_{ijk}^{n+\frac{1}{2}} &- \langle\varepsilon\rangle^{-1}\sum_{\eta=1}^{2} f_1^{\parallel}\left(\mathbf{P}_\eta^{dyn}\left[\tilde{\mathbf{E}}\Big|_{ijk}^{n}\right] - \mathbf{P}_\eta^{dyn}\left[\tilde{\mathbf{E}}\Big|_{ijk}^{n-1}\right]\right)\\ &- \left\|\varepsilon^{-1}\right\|\mathbf{n}\left(\delta P_\perp^{dyn}\left[E_\perp|_{ijk}^{n}\right] - \delta P_\perp^{dyn}\left[E_\perp|_{ijk}^{n-1}\right]\right)\end{aligned}$$

$$\partial_t\mathbf{H} = -\nabla\times\tilde{\mathbf{E}} - \delta\mathbf{K}_\parallel$$

$$\partial_t\rho = \left(\partial_t P_{\perp,2}\left[\tilde{E}_\perp\right] - \partial_t P_{\perp,1}\left[\tilde{E}_\perp\right]\right) + \left(f_1^\perp\partial_t P_{\perp,1}\left[\rho\right] - f_2^\perp\partial_t P_{\perp,2}\left[\rho\right]\right)$$

$$\delta P_\perp^{dyn} \equiv \left(f_1^\perp - f_1^\parallel\right)P_{\perp,1}\left[\tilde{E}_\perp\right] + \left(f_2^\perp - f_2^\parallel\right)P_{\perp,2}\left[\tilde{E}_\perp\right] - f_1^\perp f_2^\perp P_{\perp,1}\left[\rho\right] - f_1^\perp f_2^\perp P_{\perp,2}\left[\rho\right]$$

$$\delta\mathbf{K}_\parallel \equiv \nabla\times\mathbf{n}\left(\left\|\varepsilon^{-1}\right\|\langle\varepsilon\rangle - 1\right)\mathbf{n}\cdot\tilde{\mathbf{E}}$$

The steps of the algorithm are summarized in figure 4.4.2. For a Yee cell without a material boundary, all of the cell-centred quantities (ρ, $\delta P_\perp^{dyn}$) and the corrective magnetic current density $\delta\mathbf{K}_\parallel$ vanish, and therefore, the above equations reduce to the traditional FDTD update equations in the VA approximation. In the presence of a material boundary, three additional steps must be included in the sequence: after the material polarizations $\mathbf{P}_\eta^{n-1} \to \mathbf{P}_\eta^n$, but before the electric field is updated, the charge density ρ and its polarization $P_\eta\left[\rho\right]$ are updated and the polarization correction $\delta P_\perp^{dyn}$ can be calculated. This requires $\tilde{E}_\perp$ which in turn requires interpolating the representative electric field $\tilde{\mathbf{E}}$ to the cell-centre. After this, the current correction is spread-out, to the original Yee cell locations with an additional spatial interpolation. The traditional FDTD electric field update equation can now be executed, however, this time the current correction is included on the RHS. With the new representative E-field in place, the magnetic current correction can be calculated and the magnetic update equation is executed completing the sequence for a single FDTD time step at a material interface.

The INCA algorithm only requires the additional storage of the charge current ρ and the individual polarization response of the charge current $P_{\perp,1}\left[\rho\right]$ and $P_{\perp,2}\left[\rho\right]$. Thus adding three double-precision floating point values per interface Yee cell to the overall memory requirement of the FDTD algorithm. Additionally, it is useful to pre-calculate the fill-factors $f_1^\parallel, f_2^\parallel, f_1^\perp, f_2^\perp$and averaged dielectric constants $\langle\varepsilon\rangle$, $\|\varepsilon^{-1}\|$ adding additional memory requirements to Yee cells with a material boundary. However, as typically the fraction of boundary Yee cells is small, the overall memory increase is insignificant.

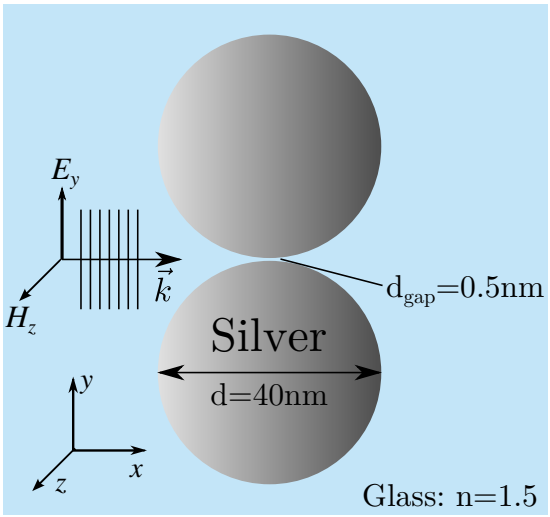

Figure 4.5.1: A pair of infinitely long silver nanowires excited by a trans-magnetic plane-wave excitation travelling in the $\mathbf{e}_x$-direction. This is system is used to compare the various methods of evaluating a Yee cell containing a material interface.

This is also true for the computation time: although the processing time of a boundary Yee cell significantly increases compared to a Yee cell without a boundary (see table 4.2), the low surface, volume ratio increases the total computation time by typically $< 50\%$.

4.5 Evaluation and comparison of methods

A pair of parallel, nearly touching silver nanowires was chosen to evaluate and compare the numerical methods discussed in this chapter. The silver nanowires have a radius of $R = 20$ nm and a gap of $d_{gap} = 0.5$ nm between them. Both nanowires are suspended in a glass substrate ($n = 1.5$). The nanowires are typically excited by plane-waves which travel parallel to and towards the gap and with their magnetic field component oriented along the nanowire axes. The recursion coefficients calculated in section 2.1.2.3 were used to model the silver material of the nanowires. The system's geometry along with its excitation configuration are depicted in figure 4.5.1.

This system resembles a well-known plasmonic dimer system which attracts continuous interest of the nano-plasmonics community [17, 18, 19, 20, 21] due to its ability to focus, confine and enhance light to and at scales down to just below one nanometre. Calculations based on transformation optics have shown (see chapter 5), that the electric field amplitudes can reach up to $\approx 1.5 \cdot 10^3$ of the incident field amplitude in the limit where both cylinders are infinitesimally close [17, 22]. This coincides with strong and sharp resonances in the absorption and scattering cross sections and strong field discontinuities in the gap region, which make the system

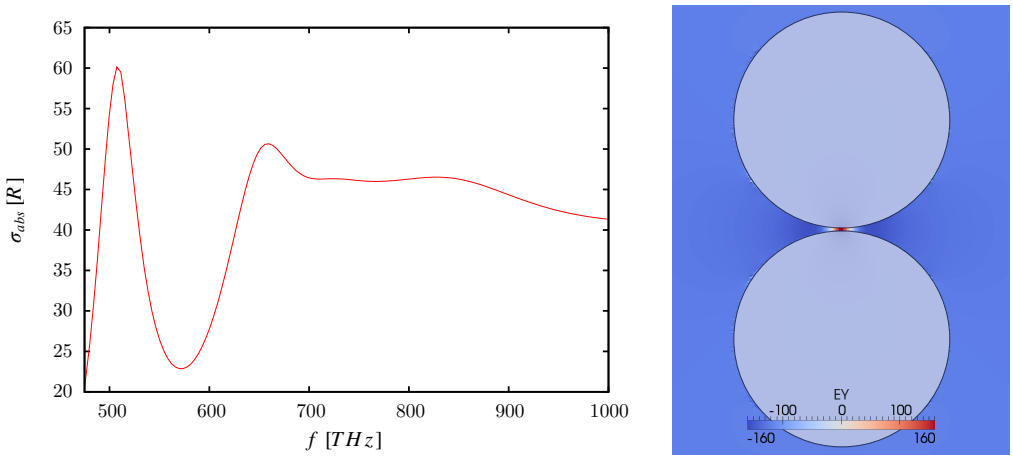

(a) (b)

Figure 4.5.2: (a) The absorption cross section of two nearly touching silver nanowires as calculated with a fully converged frequency based solver (COMSOL) and (b) the electric field profile of the resonance at $f = 512$ THz.

extremely demanding to simulate computationally.

A ground-truth absorption cross section spectrum of the system was obtained from a fully converged simulation which was calculated with the frequency based solver COMSOL[1]. This absorption cross section spectrum is depicted in figure 4.5.2a. The spectrum reveals two strong resonances at ≈ 512 THz and ≈ 659 THz. The field profile of the former, more intense resonance is also depicted in figure 4.5.2b. It can be seen that this resonance exhibits highly localised fields in the gap region indicating that there is a strong charge build-up of opposite sign on either side of the gap.

For each material boundary method, simulations were performed for various spatial resolutions varying from 0.25 pixels to 2 pixels at the centre of the gap. After this, the root mean square (RMS) error of the absorption cross section compared to the converged frequency-domain spectra (COMSOL) were calculated for every material boundary method and resolution. The results for the different methods are discussed individually.

4.5.1 Stair-casing method

Figure 4.5.3 shows the absorption cross section of the traditional or staircasing material interface method (see section 4.1.1) for various spatial resolutions. Within this method, the effective polarization response $\mathbf{P}_{eff}$ represents the physical polarization response $\mathbf{P}(\mathbf{r}_{ijk})$ at a single infinitesimal point $\mathbf{r}_{ijk}$. Therefore, as long as

[1] COMSOL calculations were done on the basis of COMSOL simulations conducted by Antonio Fernandez-Dominguez.

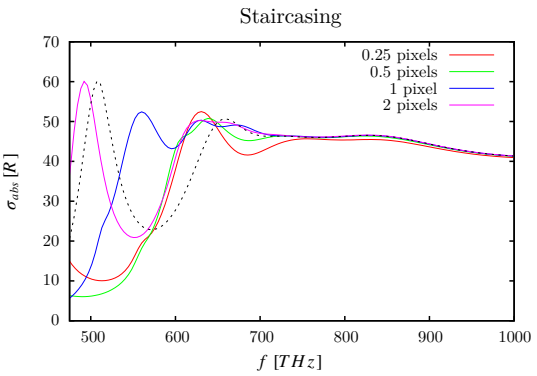

Figure 4.5.3: Absorption cross section for various spatial resolutions (pixels per gap) as calculated with the staircasing method. The black dotted line is the COMSOL reference simulation.

the gap between the cylinders is not resolved by the current resolution, the effective polarization response $\mathbf{P}_{eff}$ is indistinguishable from a system where the nanowires are "short-circuited" by a silver bridge at the centre of the gap. In such a system, charges can flow from one nanowire to the other so that opposite charges between both nanowires cannot build-up. Consequently, the strong dipole-like resonance discussed above cannot be sustained and thus, for resolutions $N_{gap} < 1$, this dipole-like resonance is not visible in the spectrum. Furthermore, even when the gap is resolved $N_{gap} \geq 1$ and the strong dipole-like resonance becomes visible, the stair-casing method does not predict the position of this resonance accurately. This is not surprising: as discussed in section 4.3, it is important to understand what physical quantity the representative field values stored in computer memory actually represent. Within the stair-casing method, the representative electric field values $\tilde{\mathbf{E}}$ represent the physical electric field at a single point. The electric field component perpendicular to the gap, however, will have strong discontinuities due to the strong fields and the material interfaces. This will significantly increase the error in the evaluation of the derivatives with a central difference scheme which was only derived for continuous fields in section 1.1.2.

4.5.2 Discrete Volume Averaging (DVA)

Figure 4.5.4a shows the absorption cross section of the DVA material interface method (see section 4.1.1) for various spatial resolutions. Similarly, to the stair-casing method, if the resolution does not resolve the gap $N_{gap} < 1$, then a charge transport between the nano-cylinders is possible. However, in contrast to the stair-casing method where the effective polarization response is indistinguishable from a system with a silver bridge, the DVA method has a bridge made of a less-conductive material than the stair-casing method. This is because the effective polarization

response of a gap cell at low resolutions will be a mixture of the silver and the background material. With increasing resolution the silver fraction will decrease and consequently the conduction between the nanowires decreases which will allow an increasing charge build-up between both nanowires. This can easily be seen in the absorption cross section. With increasing resolution, the dipole-like, symmetric mode slowly builds-up. Finally, when the gap is properly resolved, the resonance *intensity* of the symmetric mode reaches that of the fully converged system. Nevertheless, it was shown that the DVA method leads to inconsistencies in the update equations regarding the perpendicular component of the electric field. Therefore, even when the gap is resolved, the DVA method fails to predict the accurate location of the peak for all resolutions that were tested in this thesis.

4.5.3 Sub-pixel averaging

As discussed in section 4.3, both the DVA and sub-pixel averaging methods only specify the discretised polarization functional for a spatially averaged effective material response $\mathbf{P}_{eff} = \int_{\Gamma_{ijk}} \mathbf{P}(\mathbf{r}')\, d^3r'$. Strictly, it does not specify which averaging region Γ_{ijk} should be used. It was shown that the different averaging regions Γ_{ijk} correspond to different representative field values and two possible interpretations were introduced: the perturbation approach (see section 4.3.1) and the integral form representation of which only the latter shall be discussed here. Additionally, for each choice of representative field values, several computational implementations of the sub-pixel averaging method were discussed: the direct method, the MEEP method and the INCA algorithm. A quick summary of the method and their advantages and disadvantages along with the results shall be repeated here for the convenience of the reader.

MEEP method

The MEEP method only uses the sub-pixel averaging for the static dielectric response of the material. The dynamic response is evaluated with the DVA method. As discussed in section 4.2, the sub-pixel averaging of the static dielectric constants ε_i at an interface cell will be translated into an anisotropic effective dielectric tensor $\hat{\epsilon}^{eff}$. In general, applying this tensor to the FDTD update equations requires some form of spatial interpolation of which two methods were introduced and discussed in section 2.4. For the evaluation of the MEEP method the offset-spatial-averaging method (see section 2.4.1) was chosen as it is known to introduce less errors [61].

The results of the calculations are shown in figure 4.5.4b. The results are nearly identical to the discrete volume averaging method (figure 4.5.4a). This is not surprising as it was found that the conductive nature of the silver, which cannot be

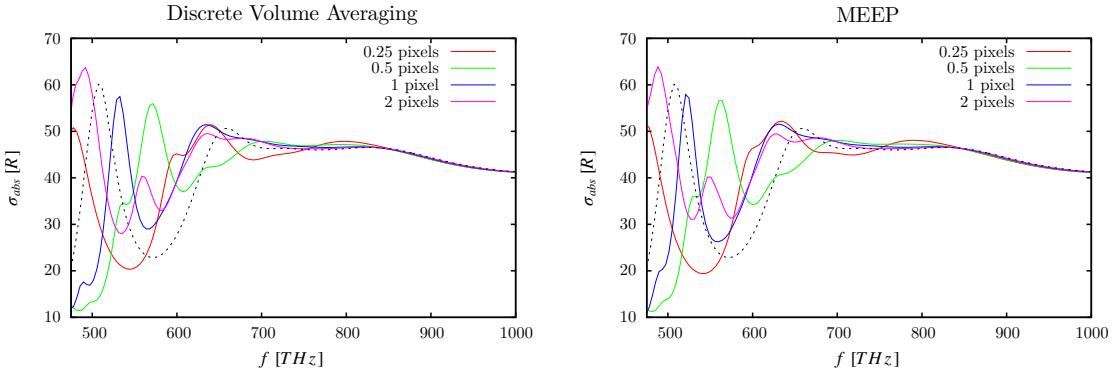

(a) (b)

Figure 4.5.4: Absorption cross section for various spatial resolutions (pixels per gap) as calculated with the (a) the DVA method and (b) the MEEP method. The black dotted line is the COMSOL reference simulation.

described by only a static dielectric response, is responsible for the charge build-up or short-circuiting of the gap and ultimately lead to the strong dipole resonance in the absorption cross section.

It must be noted however, that the MEEP method is a good approximation for many systems where the static dielectric response dominates the over-all material response. From the authors experience, the MEEP method can often yield identical results compared to the DVA method with only half the spatial resolution.

Direct method

As discussed more thoroughly in section 4.4.1, this method directly translates the sub-pixel averaging equations 4.1.12-4.1.14 into an FDTD algorithm without any further approximations. The advantage of the direct method is that it does not rely on the choice of a particular spatial averaging scheme and may include any number of materials in a Yee cell.

The results of the calculations are shown in figure 4.5.5a. It can easily be seen that this method shows the strong dipole resonance even if the gap is not resolved. This is because the direct method makes use of the fact that the perpendicular component of the displacement field $D_\perp$ is continuous and will specifically re-introduce the discontinuity of the electric field $E_\perp$ by subtracting the various polarizations $P_{\nu,\perp}$ that are contained in the Yee cell (see section 4.1.3). The absorption cross-sections for higher spatial resolutions quickly converge to the COMSOL calculation.

As noted above, in general, the direct method requires spatial averaging to split the electric field vector into its perpendicular and parallel components. However, this spatial averaging can be avoided if all the material boundaries within the system have the same orientation and are parallel to a single computational axes. In such

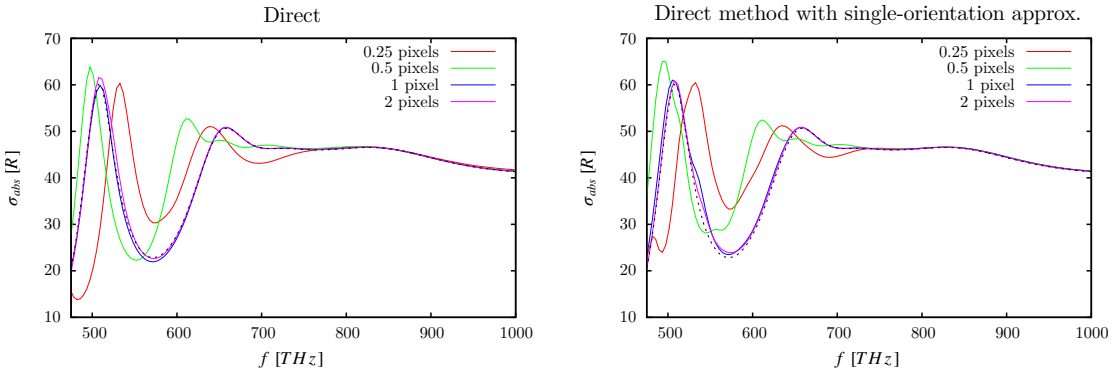

(a) (b)

Figure 4.5.5: The absorption cross section of two nearly touching silver nanowires as calculated with the (a) direct method and (b) the direct method assuming that the material interface orientations are all parallel to the gap. The absorption cross sections are shown for various spatial resolutions. The result of a frequency-based simulation COMSOL is shown with a black dotted line.

a system, the anisotropic material response tensor of the direct method becomes diagonal and will only involve a single electric field component in the Yee cell.

The response of the nanowire system is dominated by the strong fields in the gap region and one may argue that an accurate description of the material boundaries is only necessary in this region. Therefore, it is interesting to consider a numerical calculation with the assumption that all material boundary orientations are parallel to the gap with regards to the splitting of the electric field in the direct method. Such a numerical calculation will have the disadvantage of treating a large number of boundary cells incorrectly, yet will benefit from the decreased error as spatial interpolation is avoided altogether. This thesis refers to this method as the "single orientation approximation".

The absorption cross section of such a calculation is shown in 4.5.5b. The cross sections of the two methods are nearly identical and shows that the overall response of this particular system is dominated by the centre of the gap region to such a degree, that it seems beneficial to calculate this region more accurately (by avoiding spatial interpolation) at the cost of in-correctly updating the electric fields at many other Yee cells in the system. This is particularly useful as the single interface orientation approximation uses far less computational resources (see table 4.2) by avoiding the spatial averaging step *and* gives similarly accurate results.

INCA Algorithm

The INCA algorithm translates the sub-pixel averaging equations into an efficient computer algorithm without neglecting the sub-pixel averaging contribution of the

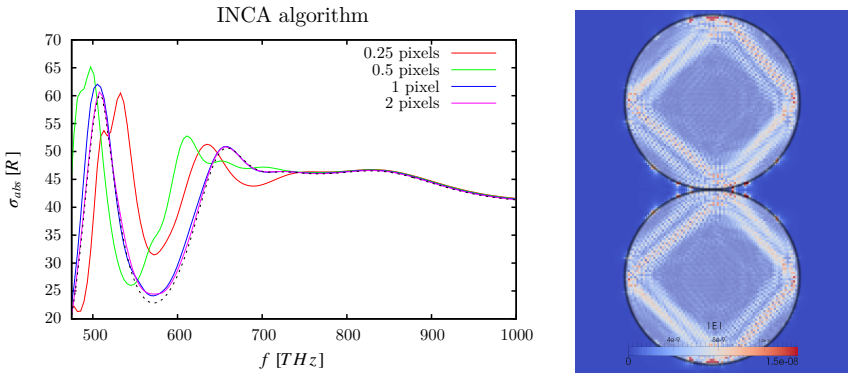

(a) (b)

Figure 4.5.6: (a) the absorption cross section of two nearly touching silver nanowires as calculated with the INCA algorithm and (b) the spatial profile of the absolute value of the electric field near the end of a numerical simulation of the silver nanowires. A weak numerical instability is clearly visible which predominantly travels along the diagonal axes of the computational domain. The absolute value of the electric field is given relative to the maximum electric field amplitude of the excitation field.

dynamic response (in contrast to the MEEP method). The algorithm requires a less-desirable spatial averaging scheme where *all* components of the electric field and the polarization responses need to be spatially interpolated (see section 2.4.2).

The results of the calculations are shown in figure 4.5.6a. In general, the INCA algorithm shows relatively good accuracy even for low resolutions. Similar to the direct method, the dipole resonance is visible even if the gap between both nanowires is not fully resolved ($N_{gap} < 1$). However, a field profile near the end of various simulations (shown in figure 4.5.6b) reveals the emergence of a weak spurious mode inside the nanowires which pre-dominantly travels along the diagonal axes of the computational domain. The intensity of this mode varies with spatial resolution, geometry and materials used in the system. Although the mode is very weak within the simulation durations conducted in this thesis, it does grow exponentially indicating that this is an unstable numerical artefact.

One hypothesis for the origin of this spurious mode is that the cell-centred spatial averaging causes a mismatch in the numerical dispersion relations between the update equations of the interface cells and the Yee cells containing only a single material. To understand this, it is illustrative to look at the case where the details of the INCA algorithm are neglected and the cell-centred spatial averaging is performed on Yee cell containing only vacuum.

After Ampère's Law is calculated for every component of the electric field at various positions in the Yee cell, the electric field components are gathered and

interpolated to the centre of the Yee cell:

$$\mathbf{E}|_{jk} = \tfrac{1}{2}\left(E_x|_{j,k-\frac{1}{2}} + E_x|_{j,k+\frac{1}{2}}\right)\mathbf{e}_x \quad + \tfrac{1}{2}\left(E_y|_{j+\frac{1}{2},k} + E_y|_{j-\frac{1}{2},k}\right)\mathbf{e}_y \ ,$$

where the 2-D trans-magnetic case and $\Delta x = \Delta y$ is considered for brevity. Inserting the electric field update equation into the above equation yields

$$\begin{aligned}\mathbf{E}|_{jk}^{n+1} = &\frac{1}{2}\left(E_x|_{j,k-\frac{1}{2}}^{n-1} + E_x|_{j,k+\frac{1}{2}}^{n-1}\right)\\ &+ \frac{\Delta t}{2\Delta x}\left(H_z|_{j+\frac{1}{2},k-\frac{1}{2}}^{n+\frac{1}{2}} - H_z|_{j-\frac{1}{2},k-\frac{1}{2}}^{n+\frac{1}{2}} + H_z|_{j+\frac{1}{2},k+\frac{1}{2}}^{n+\frac{1}{2}} - H_z|_{j-\frac{1}{2},k+\frac{1}{2}}^{n+\frac{1}{2}}\right)\mathbf{e}_x\\ &+ \frac{1}{2}\left(E_y|_{j+\frac{1}{2},k}^{n-1} + E_y|_{j-\frac{1}{2},k}^{n-1}\right)\\ &+ \frac{\Delta t}{2\Delta x}\left(H_z|_{j+\frac{1}{2},k-\frac{1}{2}}^{n+\frac{1}{2}} - H_z|_{j+\frac{1}{2},k+\frac{1}{2}}^{n+\frac{1}{2}} + H_z|_{j-\frac{1}{2},k-\frac{1}{2}}^{n+\frac{1}{2}} - H_z|_{j-\frac{1}{2},k+\frac{1}{2}}^{n+\frac{1}{2}}\right)\mathbf{e}_y\end{aligned} \tag{4.5.1}$$

After this, the electric field vector at the cell-centre $\mathbf{E}|_{jk}$ is spread-out again to the original positions of the electric field components in the Yee cell (see section 2.4.1):

$$E_x|_{j,k-\frac{1}{2}} = \frac{1}{2}\left(\mathbf{E}|_{j,k} + \mathbf{E}|_{j,k-1}\right)\mathbf{e}_x \tag{4.5.2}$$

$$E_y|_{j+\frac{1}{2},k} = \frac{1}{2}\left(\mathbf{E}|_{j,k} + \mathbf{E}|_{j+1,k}\right)\mathbf{e}_y, \tag{4.5.3}$$

after which Faraday's Law can be calculated

$$H_z|_{j+\frac{1}{2},k-\frac{1}{2}}^{n+\frac{1}{2}} = H_z|_{j+\frac{1}{2},k-\frac{1}{2}}^{n-\frac{1}{2}} - \frac{\Delta t}{\Delta x}\left(E_y|_{j+\frac{1}{2},k}^{n} - E_y|_{j+\frac{1}{2},k-1}^{n}\right) - \frac{\Delta t}{\Delta x}\left(E_x|_{j,k-\frac{1}{2}}^{n} - E_x|_{j+1,k-\frac{1}{2}}^{n}\right).$$

Inserting equation 4.5.2 and 4.5.3 into the above equations gives

$$\begin{aligned}H_z|_{j+\frac{1}{2},k-\frac{1}{2}}^{n+\frac{1}{2}} = H_z|_{j+\frac{1}{2},k-\frac{1}{2}}^{n-\frac{1}{2}} - \tfrac{\Delta t}{2\Delta x}\Big[&\left(\mathbf{E}|_{j,k} + \mathbf{E}|_{j+1,k} - \mathbf{E}|_{j,k-1} - \mathbf{E}|_{j+1,k-1}\right)\mathbf{e}_y\\ +\ &\left(\mathbf{E}|_{j,k} + \mathbf{E}|_{j,k-1} - \mathbf{E}|_{j+1,k} - \mathbf{E}|_{j+1,k-1}\right)\mathbf{e}_x\Big],\end{aligned}$$

and by now inserting equation 4.5.1 into the above equation and re-arranging, one finds the discretised Helmholtz Equation of a Yee cell where the electric fields were interpolated to the Yee cell centre:

$$\begin{aligned}H_z|_{j+\frac{1}{2},k-\frac{1}{2}}^{n+\frac{1}{2}} - 2\,H_z|_{j+\frac{1}{2},k-\frac{1}{2}}^{n-\frac{1}{2}} + H_z|_{j+\frac{1}{2},k-\frac{1}{2}}^{n-\frac{3}{2}} = &\\ \frac{\Delta t^2}{2\,(\Delta x)^2}\Big[&\left(H_z|_{j+\frac{3}{2},k+\frac{1}{2}}^{n+\frac{1}{2}} - 2\,H_z|_{j+\frac{1}{2},k-\frac{1}{2}}^{n+\frac{1}{2}} + H_z|_{j-\frac{1}{2},k-\frac{3}{2}}^{n+\frac{1}{2}}\right)\\ &+ \left(-H_z|_{j-\frac{1}{2},k+\frac{1}{2}}^{n+\frac{1}{2}} - 2\,H_z|_{j+\frac{1}{2},k-\frac{1}{2}}^{n+\frac{1}{2}} + H_z|_{j+\frac{3}{2},k-\frac{1}{2}}^{n+\frac{1}{2}}\right)\Big].\end{aligned}$$

By comparing the above Helmholtz equation with the Helmholtz equation of an FDTD algorithm without spatial averaging, one can easily see that they are identical

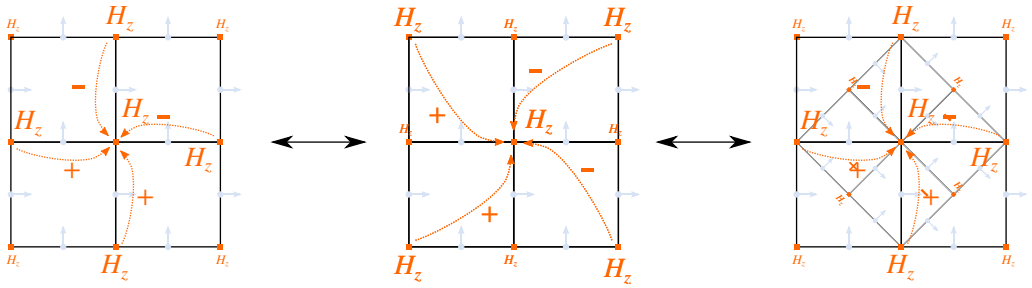

Figure 4.5.7: The effect of the cell-centred spatial averaging technique on Yee cells filled with vacuum: by inserting the electric field FDTD update equation into the magnetic field update equation, a discretised Helmholtz equation (see section 1.1.2) for the magnetic field component located at the centre of each of the above images can be found. This Helmholtz update equation involves only the nearest neighbours (left). However, if the cell-centred spatial averaging technique is used then the nearest neighbours cancel and only the second nearest neighbours are considered in the Helmholtz update equation (centre). Such an update equation is equivalent to the left image after a 45° rotation and by scaling down the geometry by $\frac{1}{\sqrt{2}}$ which was done for the right image (faint colours). The original Yee cell (left) was overlayed in dark colours on the right image to highlight the symmetry.

after a 45° spatial rotation and $\frac{1}{\sqrt{2}}$ spatial scaling. This is also shown in figure 4.5.7. As was discussed in section 1.1.6, the numerical dispersion relation depends on the angle of propagation of an electro-magnetic wave. Normally, in vacuum, the dispersion relation is constant for any given propagation direction. However, this is not the case, when Yee cells with cell-centred spatial averaging are present and therefore a wave with a constant propagation direction will experience an impedance mismatch at a Yee cell using this spatial-averaging techniques. This impedance mismatch will cause back-reflections which may sustain such a spurious mode as shown in figure 4.5.6b.

A more thorough investigation of this spurious mode has yet to be conducted and conclusive evidence that the above hypothesis is in fact the origin of the spurious mode - or if the mode is simply due to a yet unnoticed programming error - has yet to be found. Irrespective of the exact origin of the spurious mode, the mode grows so slowly that it does not seem to significantly affect the absorption cross-sections of the systems calculated through-out the course of the author's thesis.

As the simulation durations conducted in this thesis are long compared to other FDTD simulations of typical nano-plasmonic systems conducted in the author's research group, it is expected that the spurious mode will not affect the result of other similar simulations. Therefore, the INCA algorithm remains an attractive, computationally efficient algorithm to calculate cross sections of nano-plasmonic systems.

4.5.4 Comparison of the Root mean square (RMS) error and computational efficiency

The root mean square (RMS) error for various methods and resolutions is shown in figure 4.5.8. The RMS error was calculated by comparing the absorption cross sections of the various methods to the absorption cross section of the fully converged COMSOL simulation.

Unsurprisingly, the methods which ignore sub-pixel averaging for the dispersive currents (stair-casing, DVA, MEEP) are significantly less accurate than the sub-pixel averaging methods (Direct, Single Orientation Approximation, INCA). As expected, the direct method has the least errors as it uses a more favourable spatial averaging technique (as opposed to the INCA algorithm) and does not neglect the orientation of the material boundaries (as opposed to the single orientation approximation). However, as shown in table 4.2, the direct method is also the most computationally demanding in terms of computation time (see section 4.4.1). The INCA algorithm shows better computational performance compared to the direct method as it only calculates corrections at the Yee cell centre. The single orientation approximation, on the other hand, shows the best computational performance of the sub-pixel averaging methods as it avoids any spatial averaging steps all-together.

In summary, if the macroscopic response of the system is pre-dominantly defined by a region of Yee cells with interfaces of roughly identical orientations then the single orientation approximation gives the best trade-off between accuracy and computational efficiency. It typically requires only $\approx 10\%$ more computation time compared to the stair-casing method with significantly improved accuracy.

If a single orientation of the interfaces is not a good approximation, then the INCA algorithm is a good choice. However, the INCA algorithm cannot be used for systems which contain interface Yee cells with more than two materials, have strongly non-linear materials or are sensitive to the spurious mode discussed in section 4.5.3. In this case the direct method must be used.

4.6 Summary and Conclusion

This chapter investigated three different techniques - stair-casing, DVA, and sub-pixel averaging - to calculate the polarization response of a Yee cell containing a material boundary. It was shown that the traditional stair-casing method introduces discontinuities into the FDTD update equations which leads to large errors at material interfaces. One naïve approach to smooth out the response of interface Yee cells is to volume-average over the material response by evaluating the polarization responses with a volume-averaged electric field (DVA). It was shown, however,

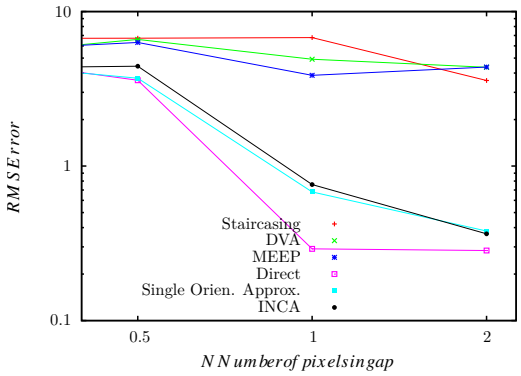

Figure 4.5.8: RMS error vs. the number of Yee cells in the gap region of two nearly touching nanowires for different methods to calculate the response of a Yee cell containing a material boundary.

	Stair-casing	**DVA**	**MEEP**
Dynamic fields	**E**, **H**, **P**	**E**, **H**, **P**	**E**, **H**, **P**
Static fields	ε	$\langle\varepsilon\rangle$, $f_{\parallel}$	$\langle\varepsilon\rangle$, $f_{\parallel}$, $\langle\varepsilon^{-1}\rangle$
Compute time of intf. cell	1.00	3.8	16.4
Typical compute time overall	1.00	1.02	1.11
	Direct	**Single Orien. Approx.**	**INCA**
Dynamic fields	**E**, **H**, **P**	**E**, **H**, **P**	**E**, **H**, **P**,ρ,$P\,[\rho]$
Static fields	$\langle\varepsilon\rangle$, $f_{\parallel}$, $\langle\varepsilon^{-1}\rangle$, $f_{\perp}$	$\langle\varepsilon\rangle$, $f_{\parallel}$, $\langle\varepsilon^{-1}\rangle$, $f_{\perp}$	$\langle\varepsilon\rangle$, $f_{\parallel}$, $\langle\varepsilon^{-1}\rangle$, $f_{\perp}$
Compute time of intf. cell	89.3	17.8	54.3
Typical compute time overall	1.63	1.12	1.38

Table 4.2: Computational efficiency of various methods to calculate the response of a Yee cell with a material interface. All computation times are relative to the computational time of the staircasing method and were acquired for a resolution of two-pixels per gap. The nearly touching nanowire system with a single Yee cell in the region was used as a test system.

that this leads to inconsistencies in the perpendicular component of the electric field; whereas the sub-pixel averaging approach correctly smooths out a polarization response over a given region Γ.

Further, it was found that the choice of the smoothing region Γ of the sub-pixel averaging technique further determines the interpretation of the field values stored in memory. If the smoothing region Γ is the volume average of the Yee cell, the field values must be interpreted within the perturbation approach described in section 4.3.1. If, though, Γ is a volume average for the parallel electric field components and a line average for the perpendicular field component, the interpretation of the field values stored in memory is consistent with discretised update equations of the integral form of Maxwell's curl equations.

Independently of the smoothing region Γ, several options for the computational implementation of the sub-pixel averaging scheme were presented in this chapter - MEEP, direct method, INCA, and single orientation approximation - with their respective approximations and assumptions. It was shown that the direct method, which was developed by the author, is the most accurate for a typical nano-plasmonic system consisting of two nearly touching nanowires but computationally also the most expensive. Hence, the INCA algorithm was developed to increase the computational efficiency by only calculating scalar corrections at the Yee cell centre. However, the unfavourable spatial averaging required by the INCA algorithm resulted in the algorithm being less accurate than the direct method and may also have been the origin of a spurious mode seen near the end of the simulations.

Finally, a third technique, single orientation approximation, was introduced, which is identical to the direct method but assumes that all interfaces have the same orientation. This avoids the problem of spatial interpolation as the anisotropic polarization response tensor is always diagonal. The key advantage of the single orientation approximation technique is that is has similar accuracy to the INCA algorithm while featuring the same favourable computational efficiency as the non sub-pixel averaging techniques. This makes the single orientation approximation a powerful technique to solve the nearly touching nanowire system. Consequently, in the following and final chapter of this thesis, this technique was used to investigate an active nano-plasmonic dimer system.

In conclusion, it was shown, that the algorithms using sub-pixel averaging techniques can improve the accuracy of nano-plasmonic simulations by roughly an order of magnitude for an only modest increase in computation time. Most freely available FDTD solvers [86][93] only apply the sub-pixel averaging equations to the static dielectric response of the materials (MEEP method). A few [94] also apply the sub-pixel averaging technique to the dispersive polarization currents. However, to the author's best knowledge, all of these solvers are limited to a set of fixed polarization

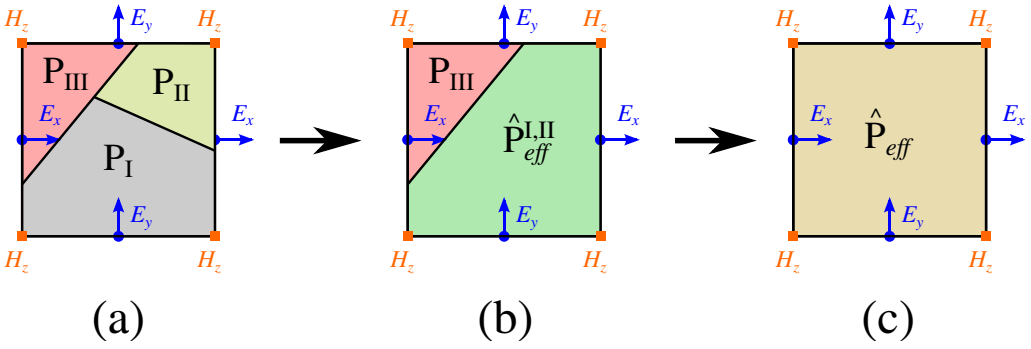

Figure 4.6.1: Iterative approach to describe the response of a Yee cell containing several materials. (a) A Yee cell containing three isotropic materials. Two of the materials can be combined to a single anisotropic material with an effective response $\hat{\mathbf{P}}^{I,II}_{eff}$ with the methods described in this thesis (b). The same approach *cannot* be used again to combine the remaining two materials (c) as an effective response for a Yee cell containing two anisotropic material responses has not been found yet.

responses - such as Drude responses, whereas the derivations of the sub-pixel algorithms in this chapter are generic and only require that the polarization functionals are linear and isotropic.

There are various opportunities for further research and investigations. For example, one major draw-back to the sub-pixel averaging technique in general is that it is limited to Yee cells containing material interfaces with a common orientation. To understand the origin of this limitation it is beneficial to consider the Yee cell depicted in figure 4.6.1 (a). By ignoring material III in this figure, one can apply the sub-pixel averaging technique to combine the isotropic polarization responses P_I, P_{II} of materials I and II, to an effective *an-isotropic* polarization response $\mathbf{P}^{eff}_{I,II}$. It is now tempting to also combine the effective polarization response $\mathbf{P}^{eff}_{I,II}$ with the polarization response P_{III} of material III. Unfortunately, the sub-pixel averaging technique was only derived for isotropic polarization responses. Further research into generalising the sub-pixel technique to an-isotropic media is therefore an obvious candidate for continuing work on this subject.

Although the FDTD solver developed during the course of this thesis was used to calculate the results of the next chapter, it must still be considered a prototype code. First and foremost, the solver is currently limited to only two dimensional systems. This is unfortunate as most of the code for calculating the response of materials and interface cells was written in such a way that it is independent of the number of dimensions. However, due to the limited time-frame of this thesis, it was not possible to extend *all* existing code (such as the PMLs and the TFSF-box) of the author's FDTD solver to three dimensions. It must be noted, however, that both the derivation of the sub-pixel averaging equations themselves and their implementation with various algorithms presented above, were not limited to two dimensions in

any way. Therefore, one may remain hopeful that the algorithms give similarly promising results also in three dimensions. Various other drawbacks associated with the prototype code exist, such as cumbersome usage and the potential for various further, more technical, computational optimizations, such as taking memory and cache locality into account and finding more efficient ways to iterate through interface cells. Finally, as already mentioned, the exact origin of the spurious mode found in the results of the INCA algorithm requires further investigations.

Further algorithms have been proposed for the FDTD method to improve the accuracy of describing interface cells. For example, the commercial FDTD solver Lumerical [47] uses an adaptive grid technique [95] which allows Yee cell sizes to vary. The edges of the Yee cells, however, must remain aligned throughout the simulation region and therefore any Yee cell side-length l may only vary along the axes parallel to l. This requirement limits the usefulness of the method to only a subset of systems with certain symmetries such as the nano-wire system presented in this chapter. Nevertheless, this adaptive meshing technique would be an obvious improvement to the current solver.

Another promising technique is to use the method of transformation optics to transform the geometry of the system to one that has less variation in length-scales [96]. In fact, renewed interest in the topic of transformation optics had its origins in improving the accuracy of computational electro-magnetic solvers [97]. In transformation optics [98], the chosen conformal transformation will not only transform space but also the material response at every point through-out the system. In general, this will transform a spatially independent material response into a response which continuously varies with position. Therefore, the sub-pixel averaging techniques become particularly interesting in this case, as it offers an averaged effective response of the continuously varying material responses inside the Yee cells of the transformed system.

Chapter 5

Gain Coated, nearly touching Nanowires

The previous chapters have laid the necessary theoretical foundations to embark on simulating a nano-plasmonic system coupled to a quantum mechanical dipole with an FDTD algorithm. The system - two nearly touching infinitely long silver nanowires - was already discussed in evaluating the different methods to correctly simulate material boundaries. However, in this chapter the nanowires will be coated with a non-linear system described by the two- or four-level model discussed in chapter 3. It will be shown that the unusually intense field confinement factors in the immediate vicinity of the centre of the gap facilitates the coupling between the plasmonic and non-linear system and a phenomena known as "strong-coupling" emerges.

The first part of this chapter will introduce the system and briefly discuss the properties of the purely plasmonic system, i.e. without the quantum mechanical gain molecules. After this, a non-linear quantum mechanical two-level system is added as a coating to the wires and a peak-splitting is observed in the numerically obtained spectra in the small-signal regime. We then compare this phenomena with the semi-classical model for Rabi splitting developed in section 3.3 which serves to both validate the model and confirm that the peak-splitting shown is indeed due to strong coupling effects.

By then increasing the amplitude of the incident field, we leave the small-signal regime behind, and non-linear phenomena such as saturation effects can be observed. We conclude the chapter by replacing the two-level quantum system with material roughly based on Rh800 laser dye molecules and simulate typical pump-probe experiments where enhanced pump rates and short laser bursts can be observed.

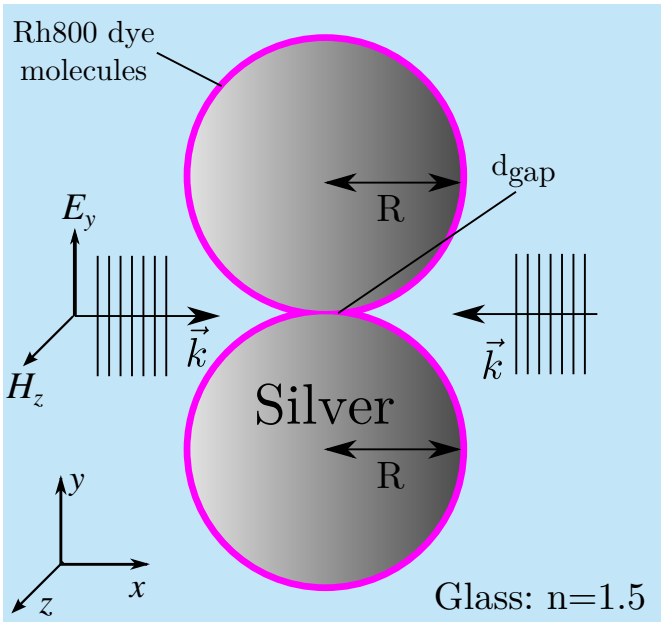

Figure 5.1.1: The nano-plasmonic dimer system investigated in this chapter: a pair of nearly touching, infinitely long, silver nanowires with a non-linear coating (two- and four-level systems are investigated). The dimer is excited by a plane-wave travelling parallel to the gap and with a magnetic field component along the axes of the wires.

5.1 The nanowire system

A pair of parallel, nearly touching, infinitely long, silver nanowires [17, 18, 19, 20, 21] surrounded with a dye coating was chosen to investigate the strong-coupling behaviour of a nano-plasmonic and a multi-level system. The entire system is suspended in an infinite glass substrate ($n = 1.5$). The nanowires are excited by plane-waves which travel parallel to the gap and with wavelengths significantly larger than the geometry (sub-wavelength regime). The nanowire geometry and the excitation configuration are depicted in figure 5.1.1. Just the cylinders - without the coating - resemble a well-known plasmonic dimer system which attracts continuous interest of the nano-plasmonics community due to its ability to focus, confine and enhance light to scales down to just below one nanometre. Calculations based on transformation optics have shown that, when the dimer is excited by a plane-wave travelling parallel to the gap and with a magnetic field component along the axes of the wires, the electric field amplitudes can reach up to $\approx 1.5 \cdot 10^3$ of the incident field amplitude in the limit where both cylinders are infinitesimally close [17, 22]. This coincides with strong and sharp resonances in the absorption and scattering cross sections, which can be exploited to achieve an intense coupling between the coating and the plasmonic dimer system.

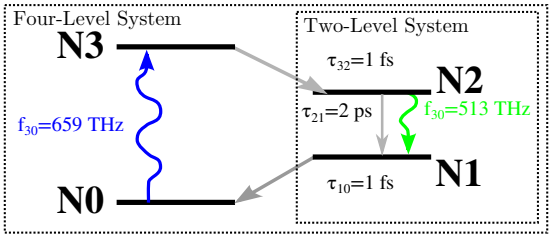

Figure 5.1.2: The energy levels of the two- and four-level system used as a coating in the system discussed in this chapter. Initially, only the energy levels $N1$ and $N2$ will be used to form a two-level system. Later, the energy levels $N0$ and $N3$ will be added to transform the two-level system into a four-level system.

5.1.1 Geometry and material of the nanowires

The following fixed ratio between the cylinders' radii R, the gap-size between the nanowires d_{gap} and the nanowire coating width $d_{coating}$ was chosen as

$$R = 40 \cdot d_{gap}; \quad d_{coating} = 4 \cdot d_{gap} \ ,$$

i.e., the entire geometry scales with d_{gap}.

The material of the silver nanowires was modelled with a superposition of a Drude and Lorentz response function to roughly match an experimentally derived dielectric function of silver $\varepsilon(\omega)$. A more detailed description of the superposition method along with the parameters of the Drude and Lorentzian response have been discussed in section 2.1.2.3.

5.1.2 Quantum model

In the first sections of this chapter, a coating consisting of dye molecules described by a two-level model with energy levels $N1$ and $N2$ will be added to the nanowires. The two-level system is described by the two-level model derived in section 3.2. Later, in section 5.3.4, additional energy levels $N0$ and $N3$ will be added to the quantum system, transforming it into a four-level system, which was also derived in section 3.2. The different energy levels and their notations for both the two- and four-level models are shown in figure 5.1.2.

As was shown in section 3.2, the polarization response of a four-level system is identical to the polarization response of two Lorentzians, which are coupled via update equations for the occupation densities (see equations 3.2.16). Therefore, the four-level system can be specified with the parameters of two Lorentzian responses (absorption frequency ω_{abs}, absorption decay-rate γ_{abs}, emission frequency ω_{ems}, emission decay rate γ_{ems}), the non-radiative decay times between the energy states τ_{30}, τ_{32}, τ_{21}, τ_{10}, and the microscopic dipole lengths for the absorption $|\mu_{abs}|$ and

emission $|\mu_{ems}|$. Additionally, a static refractive index n was assigned to the material.

In the interest of experimental feasibility, these parameters were chosen in such a way that the coating roughly resembles Rh800 laser-dye molecules [99, 100, 101, 102]:

$$\begin{array}{ccc} \omega_{ems} = 2 \cdot \pi \cdot 513 \text{ THz} & \gamma_{ems} = 0.05 \text{ ps}^{-1} & \frac{|\mu_{ems}|}{e} = 78.4 \text{ pm} \\ \omega_{abs} = 2 \cdot \pi \cdot 659 \text{ THz} & \gamma_{abs} = 0.05 \text{ ps}^{-1} & \frac{|\mu_{ems}|}{e} = 27.7 \text{ pm} \\ \tau_{21} = 2 \text{ ps} & \tau_{32} = \tau_{21} = 1 \text{ fs} & \tau_{30} = 0 \text{ ps} \end{array} \tag{5.1.1}$$

$$N_{QM}/V = 6 \times 10^{18} \text{ cm}^{-3}; \quad n = 1.5$$

where e denotes the elementary charge and N_{QM}/V is a realistic nominal density of the Rh800 dye molecules. Various different gain densities N/V are used through-out this chapter to understand the strong coupling behaviour. To improve readability, these gain densities are given in relation to the nominal gain density N_{QM}/V (for example $N/V = 2 \cdot N_{QM}/V$), which are not always experimentally feasible, but are none-the-less valuable for this chapter's discussion.

5.2 Analytic calculations based on the quasi-static approximation

To understand the general behaviour of the system, analytical calculations were performed on the purely plasmonic system (without the coating) to inform the parameter range of the numerical calculations. The system is always excited with a wavelength much larger than the dimensions of the scatterer (sub-wavelength regime) and therefore, one can invoke the quasi-static approximation [103, 4]. This approximation states that there is only negligible spatial variation of the incident field across the length scales of the scatterer and that fields vary slow enough, so that the system is in its electro-static equilibrium at any moment in time, i.e. retardation effects are negligible. An analytic, quasi-static calculation will typically first determine the polarizability α of the system by solving Laplace's equation in the static limit. It then replaces the scatterer with an infinitesimal dipole with the previously calculated polarizability α, for which the full time-varying, dynamic electro-magnetic solution is known [4]. It is important to note that, although the polarizability α is determined in the electro-static limit, it will already be frequency-dependent as it will depend on the frequency-dependent response $\varepsilon(\omega)$ of the materials in the system. In the quasi-static approximation, the frequency dependence of α is responsible for any resonant behaviour and - as all geometry parameters scale with d_{gap} - the frequency positions and decay rates of the resonances will not change when varying

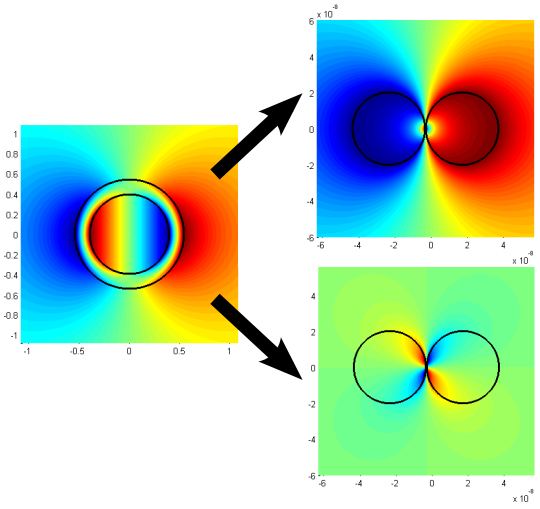

Figure 5.2.1: The electric scalar potential of the lowest frequency eigenmode as calculated with transformation optics calculations in the quasi-static limit. The profile of the electric potential in transformed space (left) corresponds to two modes with identical frequency and decay rate in real space due (right) to an ambiguity in the conformal transformation.

d_{gap}.

Although text-book analytic solutions for the electro-static potential of a single infinite cylinder exist [104], solving the two nearly touching, strongly coupled cylinders is surprisingly difficult. However, it is possible to use transformation optics [105, 106] to find a conformal mapping, which transforms the geometry of the problem into a geometry which is easier to solve. The transformed geometry of the system is depicted on the left of figure 5.2.1 and consists of an infinite cylinder at the origin, surrounded by a cylindrical gap which in turn is surrounded by a bulk material. Solving the Laplace equation in this system reveals that there is a strong eigenmode at $\approx$ 513 THz with a decay rate of $\gamma \approx 8$ ps^{-1}. The electric field at this resonant frequency is also shown in figure 5.2.1. In real space this resonance can be excited by two plane-wave with the magnetic component parallel to the nanowire axes, travelling parallel to and towards the gap yet from opposite sides of the computational domain as shown in figure 5.1.1.

Interestingly, the above transformation is ambiguous due to a hidden symmetry in the transformation: every solution to Laplace's equation in the transformed space has two solutions with a unique electric field configuration yet identical frequency and decay rate in real space. The electric field configuration of both solutions are shown in real space on the right side of figure 5.2.1 for the resonance at $\approx$ 513 THz. The symmetry of the incident field determines which of the two modes is excited: if the two incident plane-waves have the same sign (0° phase difference) then a strong

dipole-like field-configuration is found at the centre of the gap. This mode is therefore referred to as the "dipole" or "symmetric" mode. If, on the other hand, the two incident plane-waves have opposite signs (180° phase difference) then a quadrupole-like field configuration is found near the centre of the gap. This mode is therefore referred to as the "quadrupole" or "anti-symmetric" mode. The transformation optics calculations were performed by Dr. Yu Luo.

It should be noted here that the resonant frequency and decay rate of the symmetric and anti-symmetric modes are not expected to be identical when the quasi-static approximation is relaxed. This is can easily be seen for the decay rates γ: as the quasi-static approximation solves the potentials in the electro-static limit, all losses due to radiation are neglected. Therefore, the decay rate γ calculated within the quasi-static approximation can only include absorption losses due to, for example, Joule heating of the silver. However, it is well-known that quadrupole like excitations have significantly lower radiation losses than dipole modes [63]. Therefore one would expect that the symmetric mode has a higher decay rate than the anti-symmetric mode. Additionally, small differences between the resonant frequency of both modes can be expected due to retardation effects and it will be shown that this small frequency difference is responsible for some interesting phenomena.

5.3 Numerical calculations

5.3.1 Nanowires without the Coating

The nanowires without the coating were already simulated in section 4.5 to compare the different methods of evaluating the FDTD equations of a Yee cell containing a material interface. It was found that the direct method without spatial averaging gave the best trade-off between accuracy and computational efficiency and this method shall be used through-out this chapter.

The resulting absorption cross sections for both the symmetric, dipole-like (red) and anti-symmetric, quadrupole-like (green) excitations are shown in figure 5.3.1a for a gap-size of $d_{gap} = 0.5$ nm. The differences between both excitations is clearly visible and confirms our prediction that the quasi-static approximation fails to predict the detailed response of the system: not only do the positions of the resonances between the symmetric and anti-symmetric excitations differ slightly ($f_{sym} =$ 507.64 THz vs. $f_{anti} = 511.85$ THz), more importantly, the decay rates γ, are significantly larger for the symmetric mode ($\gamma_{sym} = 147.26$ ps^{-1} vs. $\gamma_{anti} = 55.00$ ps^{-1}) as was predicted above. The full-vectorial field profiles for the symmetric and anti-symmetric excitation are shown in figure 5.3.1b and 5.3.1c which confirm the dipole- and quadrupole-like nature of the resonance.

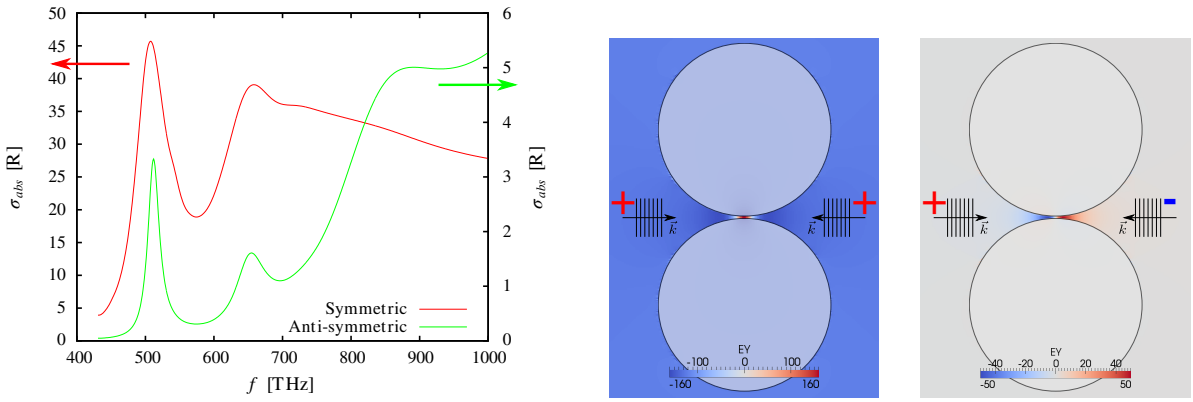

Figure 5.3.1: Absorption cross section (a) and spatial profile of the y-component of the electric field (b) + (c) of the symmetric (red, b) and anti-symmetric (green, c) mode of two infinitely long silver nanowires ($R = 20$ nm) with a gap size of $d_{gap} = 0.5$ nm. Both cross-sections are plotted on different y-axes as the antisymmetric mode couples significantly weaker to far-field radiation. The longer life-time of the anti-symmetric mode is also visible in the plot.

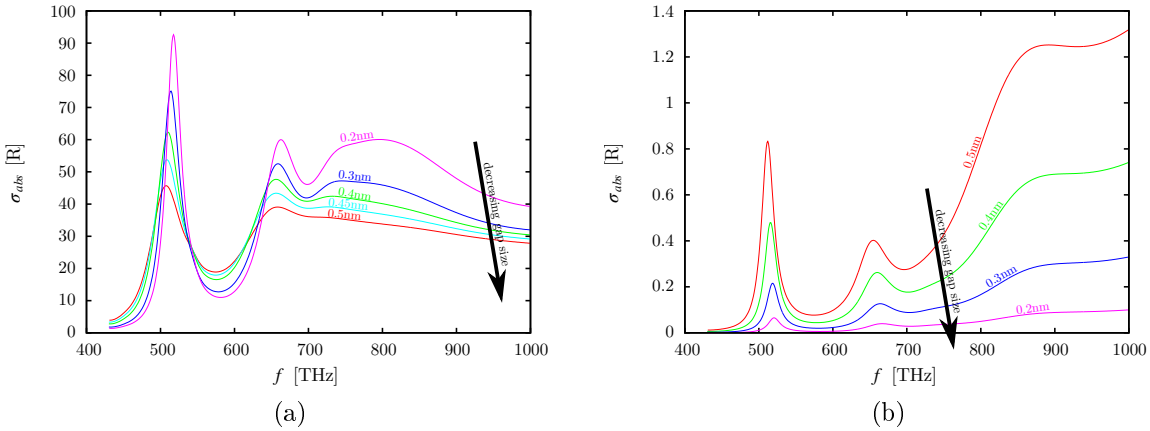

Figure 5.3.2: Absorption cross section for the symmetric (a) and anti-symmetric (b) mode for various gap-sizes d_{gap}.

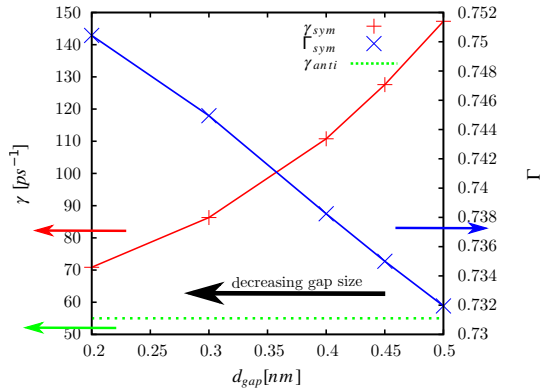

Figure 5.3.3: Decreasing decay rate γ_{symm} (red) and increasing confinement factor $\Gamma_{symmetric}$ (blue) of the symmetric mode. The decay rate γ_{anti} and the confinement factor Γ_{anti} (not shown) of the anti-symmetric mode did not vary significantly: $\gamma_{anti} \approx 55$ ps^{-1}, $\Gamma_{anti} \approx 0.85$.

The absorption cross sections for both the symmetric and anti-symmetric excitations were calculated and are depicted in figure 5.3.2a and 5.3.2b respectively for varying gap sizes d_{gap}. Additionally, the field confinement factors Γ_{sym}, Γ_{anti} (see equation 3.3.5 in section 3.3) and decay rates γ_{sym}, γ_{anti} were determined by performing simulations with a spectrally narrow excitation pulse centred around the frequency of the symmetric and anti-symmetric resonance.

Several interesting properties can be seen from these plots: firstly, as stated above, the radius of the cylinders relative to the gap size was kept constant ($R = 40 \cdot d_{gap}$) and, therefore, the position of the resonances is not significantly affected by the varying gap-size ($\Delta f < 10$ THz). Secondly, the quasi-static approximation becomes more and more valid, for example, the difference in the decay rates between the symmetric and anti-symmetric excitation becomes less $\gamma_{sym} \rightarrow \gamma_{anti}$, the smaller the overall size of the scatterer. This is shown in figure 5.3.3. And lastly, as the gap-size decreases, the decay-rates decrease and the field confinement factors Γ increase. Both of these properties are key quantities that enter the calculation of the size of the Rabi splitting and therefore, the gap-size offers excellent control over coupling between the quantum and plasmonic system.

Finally, it should be noted here that the canonical setup (see section 1.5) of measuring cross sections with the FDTD method uses a single plane-wave excitation originating from only one side. Using this setup for the nanowire system will excite both the symmetric and anti-symmetric eigenmodes[1] which have only slightly different resonant frequencies. Therefore, a temporal beating between both modes can be observed when excited from only one side. This is shown in figure 5.3.4 which plots the value of the component perpendicular to the gap of the electric field

[1]the term eigenmode is strictly only valid in the quasi-static limit as any external radiative coupling will cause a continuous spectrum

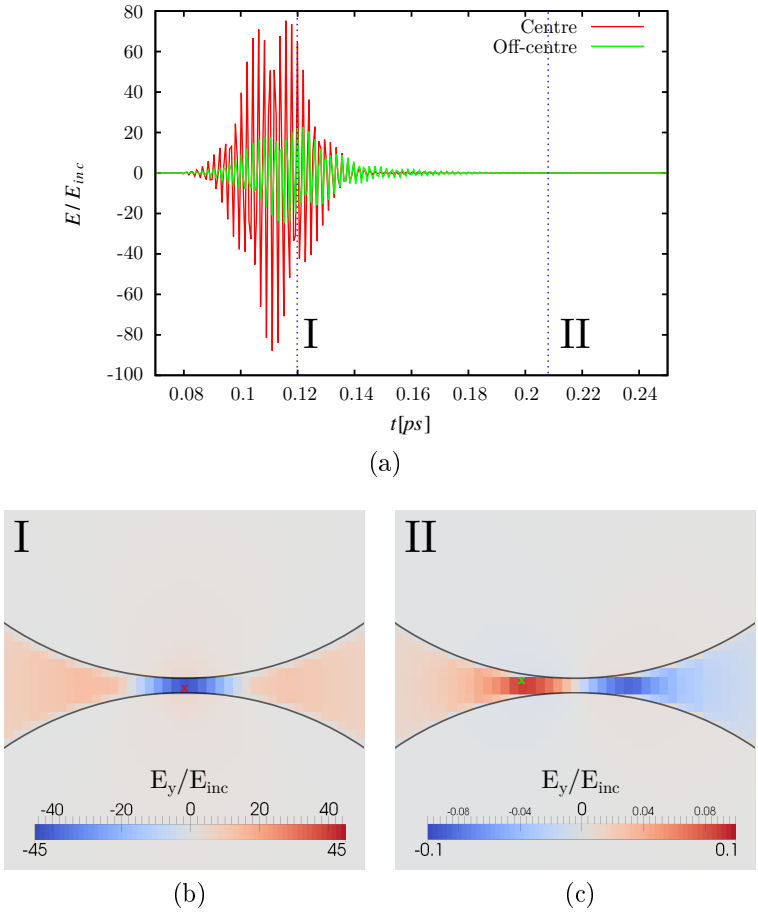

(a)

(b) (c)

Figure 5.3.4: Temporal evolution of the y-component of the electric field (a) and a close-up of the spatial profile (b)(c) recorded at two time points marked with I, II in (a). The red curve in (a) corresponds to the elctric field at the centre of the gap and the green curve to a location of maximum field value of the "anti-symmetric" mode (marked with "x" in (b) and (c)). The system was excited by a narrow probe pulse centred at the frequency of the strongest resonance and originated from only one side. The figure shows that such a mode is a superposition of the symmetric and anti-symmetric mode.

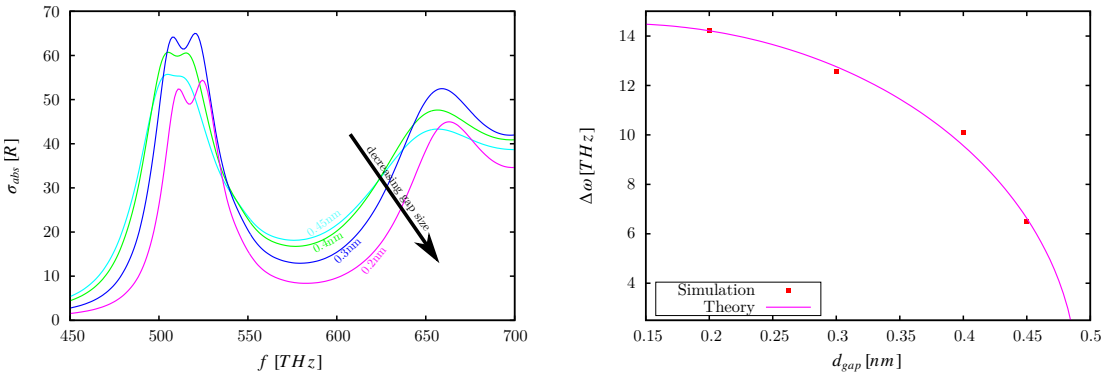

(a) (b)

Figure 5.3.5: The effect of adding a coating containing molecules described by a two-level model to the plasmonic system: (a) the absorption cross sections show a clear indication of strong-coupling. (b) The splitting of the peaks $\Delta\omega$ vs. the gap size d_{gap} as determined by numerical simulations (diamonds) and the theory developed in section 3.3 (magenta line). The peak-splitting for any gap-size $d_{gap} \geq 0.5$ nm could not be resolved and is therefore not shown here.

located at the centre of the gap along with snapshots of the field profile at various simulation times. It can be seen from this figure that eventually only the mode with the lower decay rate γ - the anti-symmetric mode - survives. This caused some confusion during the course of this thesis as the beating behaviour could not be reconciled with the results of the analytic calculation. Only after conducting FDTD calculations with extremely long simulation times was the beating sufficiently resolved to identify that a superposition of two eigenmodes was causing the unusual temporal behaviour, which in turn was the motivation to look more carefully for a missing mode in the analytical calculations.

5.3.2 Nanowires with a two-level Coating in the Small-signal Regime

A coating as described in section 5.1.2 is now added to the nanowires. Before embarking on a simulation with the complete four-level model enabled, we first study the response of the system with only the emission lines - effectively, reducing the four-level model to a two-level model. The simulations were performed with a two-level system of $N/V = 5 \cdot N_{QM}/V = 30 \times 10^{18}$ cm^{-3} (see equation 5.1.1).

Figure 5.3.5a show the absorption cross section of the system when excited with a symmetric excitation with only the two-level coating. It can easily be seen that the resonance frequency splits into two hybrid modes.

To confirm that the peak-splitting is indeed caused by strong coupling, we first check that the resonances of the system are in a regime where strong coupling is

expected. This is commonly defined as the region where the peak width of the resonances of the purely plasmonic system γ_p and quantum system γ_{QM} combined smaller than the Rabi frequency:

$$\frac{\gamma_{QM}}{2} + \frac{\gamma_p}{2} < \Omega,$$

where Ω is the semi-classical Rabi frequency (see equation 3.3.12 in section 5.1.2)

$$\Omega^2 = \frac{2N\omega_0}{3V_{eff}\epsilon_0\hbar} |\mu|^2 , \tag{5.3.1}$$

ω_0 is the circular frequency of the two-level transition, V_{eff} the effective mode volume (see equation 3.3.6 of section 3.3) and N/V is the density of the two-level system. The high electric field values in the gap lead to a strong field confinement factor Γ which in turn leads to a small effective mode volume V_{eff}.

With this and the other parameters for the quantum-model used, the Rabi frequency yields $\Omega \approx 90$ THz. The decay rate for the symmetric plasmonic resonance γ_{sym} were determined above $\gamma_{sym} \approx 70\ \text{ps}^{-1} - 150\ \text{ps}^{-1}$ (see figure 5.3.3). As $\gamma_{QM} \ll \gamma_{sym}$, we expect to see strong coupling phenomena when $\gamma_{sym} < 2 \cdot \Omega$, which is fulfilled for all geometries with a gap size smaller than $d_{gap} \leq 0.5$ nm.

The actual peak splitting $\Delta\omega$ of the dressed states further depends on the detuning of the frequencies and life-times of the plasmonic and quantum resonances. To simplify the calculation, the transition frequency of the two-level system ω_{QM} was adjusted slightly for each gap-size d_{gap} to match the plasmonic resonance of the passive system. Therefore the peak splitting of the dressed states is given by:

$$\Delta\omega = \sqrt{\Omega^2 - (\gamma_p - \gamma_{QM})^2}. \tag{5.3.2}$$

The excellent agreement of the numerical simulations with strong-coupling theory is shown in figure 5.3.5b.

In a further numerical experiment, the emission frequency of the two-level system was artificially detuned from the frequency of the plasmonic resonance f_{sym} and the absorption cross section was obtained. The gap size between the nanowires was $d_{gap} = 0.3$ nm and the incident field was such, that the symmetric plasmonic resonance was excited. The absorption cross sections of three detuning values δf is shown in figure 5.3.6a. As expected, the Rabi splitting only occurs if the frequency detuning is sufficiently small.

Figure 5.3.6b shows the frequency positions of the two resonances with the lowest frequencies which - in the limit of large frequency detuning - can be identified with the symmetric, dipolar-like, plasmonic resonance and the resonance due to the

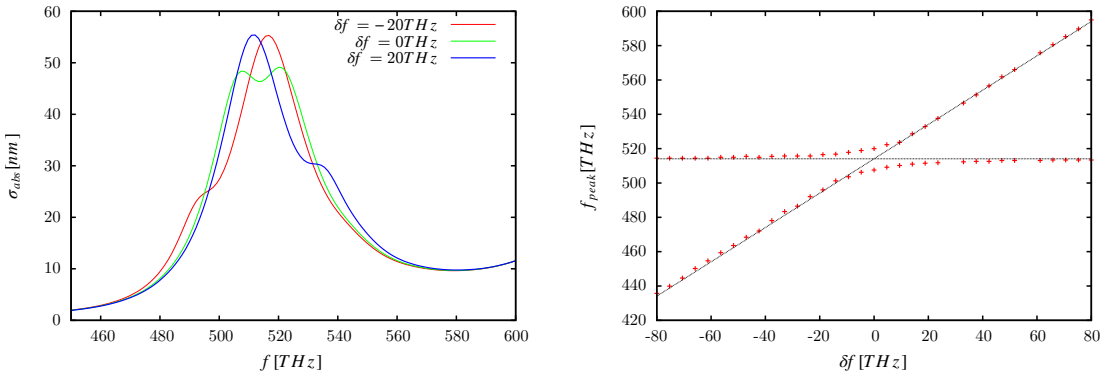

(a) (b)

Figure 5.3.6: (a) Absorption cross sections of the coated nanowire system with a gap size of $d_{gap} = 0.3$ nm and three different detuning frequencies $\delta f = -20$ THz (red), $\delta f = 0$ THz (green) and $\delta f = 20$ THz (blue). (b) Frequency positions of the resonances (red crosses) as obtained from the absorption cross sections of simulations with varying detuning parameters δf. The detuning frequency is varied by artificially detuning the emission frequency of the two-level system ω_{ems}. The black dotted lines indicate the frequency positions if both resonances were not coupled.

absorption of photons by the two-level systems. The frequency of both resonances were obtained from absorption cross sections of simulations with various detuning parameters δf of the two-level system. It can easily be seen that the positions of the resonances show the anti-crossing behaviour typically associated with Rabi splitting.

5.3.3 Nanowires with a two-level Coating beyond the Small-signal Regime

So far, the system has been excited in the small-signal regime. In this regime the coupling of the electro-magnetic fields with the two-level system is too weak to induce any significant changes in the occupation densities and, therefore, the overall response of the two-level coating is roughly linear. We now go beyond the small-signal regime by increasing the incident field amplitudes.

Figure 5.3.7a shows absorption cross sections of the nanowire system with a gap size of $d_{gap} = 0.3$ nm for various excitation field amplitudes. The excitation amplitude is given in units of the saturation amplitude E_{sat}: this is the amplitude at which a hypothetical system consisting only of a two-level system must be adiabatically pumped to reach exactly equal population of the ground and excited state ($N_2 = N_1$) after an infinite amount of time. The graph shows that the absorption cross section starts to be noticeably influenced for incident field amplitudes $E \geq 0.04 \cdot E_{sat}$. With increasing incident field amplitude E, the Rabi splitting decreases until the locations of the two separate peaks can no longer be accurately identified ($E \geq 0.2 \cdot E_{sat}$).

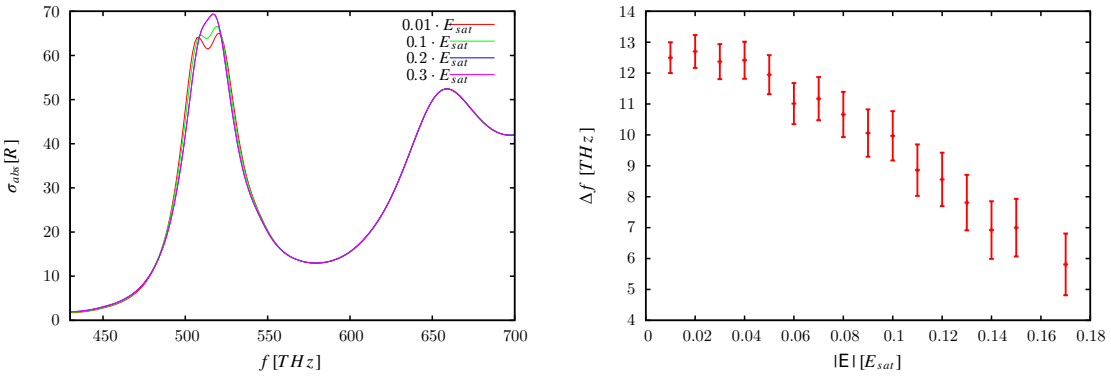

(a) (b)

Figure 5.3.7: (a) Absorption cross section for various simulations of the nearly touching nanowire system with increasing incident field amplitude E. The nanowires have a separation of $d_{gap} = 0.3$ nm. (b) Difference between the peak locations δf vs. the incident field amplitude E. The peak locations were determined by eye. The error bars show the maximum variation in peak difference when the same data-set was evaluated multiple times. With an increasing overlap of both peaks, the peak splitting becomes increasingly difficult to determine which is shown by the increasing height of the error bars. The exact definition of E_{sat} is given in the text.

This is also shown in figure 5.3.7b which shows the Rabi splitting over the various incident field amplitudes.

This saturation effect is a well-known phenomena in non-linear systems [107]: the two-level system becomes increasingly "harder" to excite as more and more carriers are pumped to the higher energy level. In the limit where the two-level system was adiabatically pumped to equal population in ground and excited state ($N_2 = N_1$), the two-level system becomes transparent and will no longer couple to an electro-magnetic field. This is because, an incoming photon will either stimulate the emission of another identical photon or the photon will be absorbed. When the ground and excited state population are identical, both processes happen with equal probability and therefore the net absorption is zero. This can also be seen in equation 3.2.12 in section 3.2. For $N_2 = N_1$, the coupling constant on the RHS of the equation will be zero $\Delta\varepsilon = 0$.

The inversion of the two-level system is spatially extremely inhomogeneous due to the large field enhancement (see, for example, the inset in figure 5.3.8b). Therefore, the two-level system will only saturate in a small regime at the centre of the gap. However, as was already shown in chapter 4, this gap region has a strong effect on the overall shape and characteristics of the absorption cross-section. Therefore, it is not surprising that a saturation of the two-level system in this region can result in the vanishing of the peak splitting.

5.3.4 Nanowires with a gain coating

The two-level system used in the previous sections will now be replaced with the four-level system introduced in section 5.1.2. This four-level system has an additional transition line (the absorption line) which is centred at the second strongest resonance located at roughly $f_{abs} = 659$ THz. The resonance can be seen in the absorption cross sections presented in section 5.3.1 (figure 5.3.1a and 5.3.2a). The electric field profile of this mode, when excited with a symmetric excitation configuration is shown in figure 5.3.8a. Similar to the symmetric mode discussed above, this mode also exhibits a strong, yet slightly weaker field enhancement at the centre of the gap. It also has an additional node on either side of the centre of the gap.

The presence of strong coupling in the previous sections is not the only consequence of the large field confinement factor Γ. A more obvious implication is a greatly enhanced pump rate of the four-level system. To highlight this effect, we compared the pump rate of the nearly touching nanowires system with a system consisting of only a single nanowire. The electric field amplitude for both cases is chosen so that a hypothetical system consisting of a pure four-level model (without any plasmonic elements) would be 10% inverted after an infinite amount of pump time.

The results for a system of two nanowires with a separation of $d_{gap} = 0.5$ nm and a four-level system density of $N/V = 5 \cdot N_{QM}/V = 30 \times 10^{18}$ cm^{-3} are shown in figure 5.3.8b. The pump rate of the nanowire pair is several orders of magnitude larger compared to a single nanowire with identical radius.

We turn our attention to the pumped system. The four-level system is in an inverted state and will amplify photons if they are in resonance with the emission line. In a similar effect as discussed in the previous section, the inversion flips the sign of the coupling constant of the Lorentzian resonance $\Delta\epsilon$ (negative coupling) of the emission line, along with the square of the Rabi frequency Ω^2 (see equation 3.3.12 in section 3.3). Consequently, equation 5.3.2 will no longer have any solutions and no splitting can be observed. This is confirmed in figure 5.3.9a which shows the scattering cross section of two nanowires with an inverted four-level system and a gap of $d_{gap} = 0.3$ nm for the symmetric excitation case (blue line). For comparison, the scattering cross section of an identical system with a two-level coating in its ground-state is shown (green) which shows the Rabi splitting. The amplification of photons which manifests itself as an increased scattering rate can also be seen by comparing the active, inverted system (blue line) with the purely plasmonic, passive system (red).

The scattering cross section of the nanowire system with the inverted four-level coating was calculated for various gap sizes and the result is shown in figure 5.3.9b.

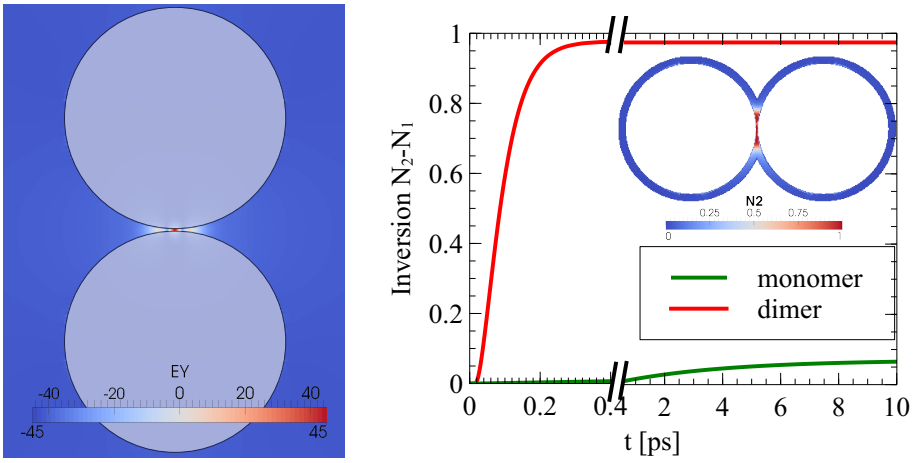

(a) (b)

Figure 5.3.8: (a) The spatial profile of the y-component of the electric field for the resonance at $f_{abs} \approx 659$ THz when pumped with a symmetric incident plane-wave. (b) The evolution of the inversion of a pump experiment (red line) for a nanowire system with a distance of $d_{gap} = 0.5$ nm and four-level density of $N/V = 5 \cdot N_{QM}/V = 30 \times 10^{18}$ cm^{-3} (red line). For comparison, the inversion of a system with a single nanowire is also shown (green line).

For comparison the scattering cross section of the purely passive system is shown in 5.3.9c. In both plots, the overall scattering of the system becomes weaker as we approach the quasi-static limit, however, the resonance at the emission frequency in the inverted system becomes increasingly sharp with smaller gap-sizes: as the gap-size becomes smaller the radiation losses decrease and therefore the system slowly approaches the lasing threshold, where more photons are amplified by the four-level system than are lost to radiation and Joule heating.

To confirm this, several simulations were performed with a nanowire spacing of $d_{gap} = 0.4$ nm and an increasing four-level system density N/V. This time, the system was excited with a plane-wave originating from only one side. Such an excitation is a superposition between the symmetric and anti-symmetric excitations which were used above.

The temporal evolution of the total electro-magnetic field energy in these simulations is shown in figure 5.3.10. It can clearly be seen that the system reaches the lasing threshold at a four-level system density of $N/V = 7 \cdot N_{QM}/V$ where a stimulated emission burst occurs. The energy of the system will increase exponentially until the inversion in the emission transition of the four-level system is depleted (not shown). The energy of the incident pulse at $t = 0.18$ ps can also be seen in this plot.

At first, it may seem surprising that the field energy of the lasing simulation ($N/V = 7 \cdot N_{QM}/V$) initially decreases before it increases again at $t \approx 0.22$ ps. However, electric field profiles (figure 5.3.11a, b and c) recorded at different time steps through-out the simulation (black dotted lines) reveal that only the anti-

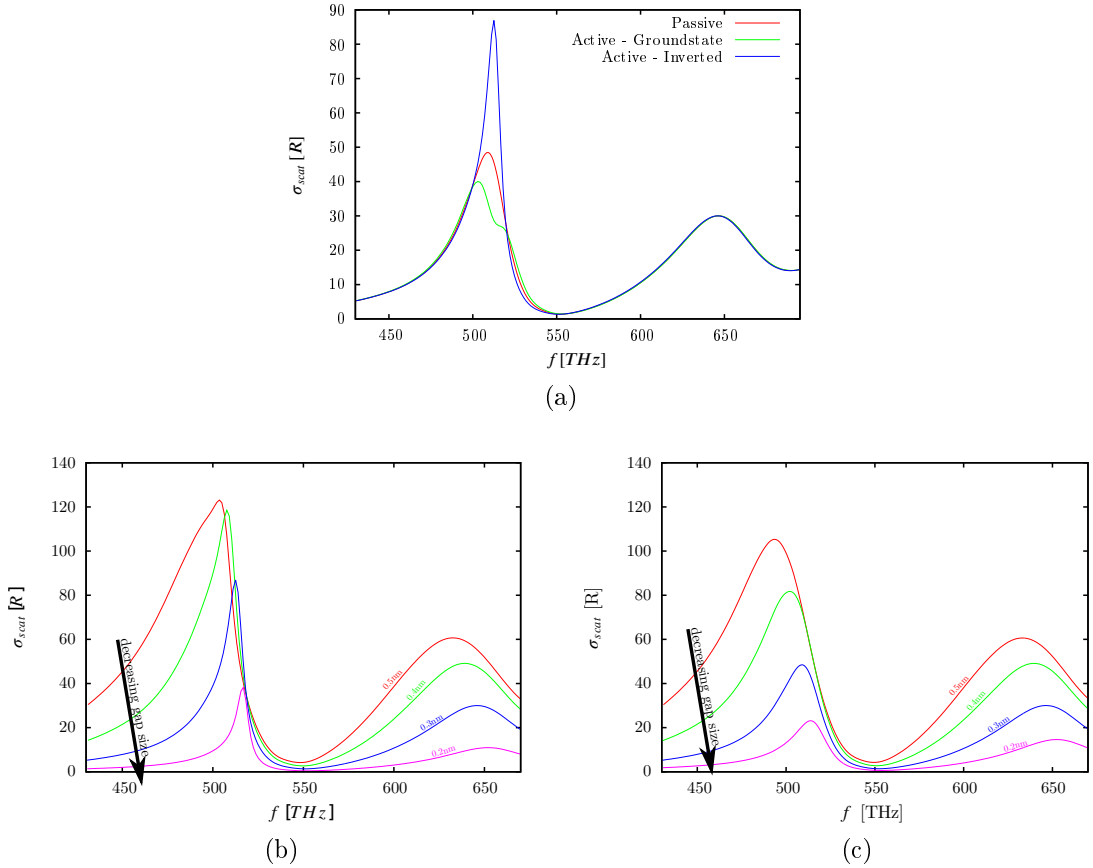

Figure 5.3.9: The Rabi splitting vanishes in the scattering cross-section of a nanowire system with an inverted four-level coating for a nanowire separation of $d_{gap} = 0.3$ nm (a) and various other gap sizes (b). The scattering cross section of the purely passive system is also shown for comparison for the nanowire separation $d_{gap} = 0.3$ nm (blue line in a) and various other gap sizes (c). The scattering cross section of a system which exhibits Rabi splitting (unpumped two-level coating, $d_{gap} = 0.3$ nm, see section 5.3.2) is also shown for comparison (green line in a).

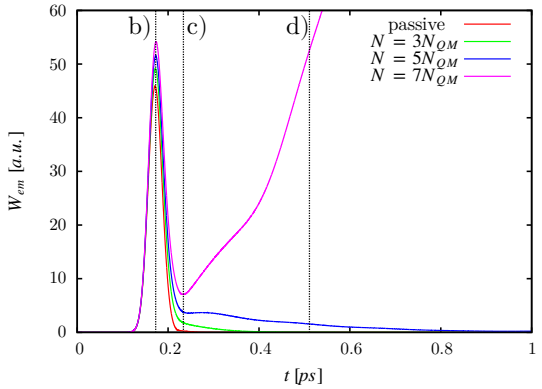

Figure 5.3.10: The temporal evolution of the total electro-magnetic field energy W_{em} of the nanowire system with various four-level densities N/V. Snapshots of the absolute electric field were recorded at several time-points (black dotted lines) and are shown in figure 5.3.11.

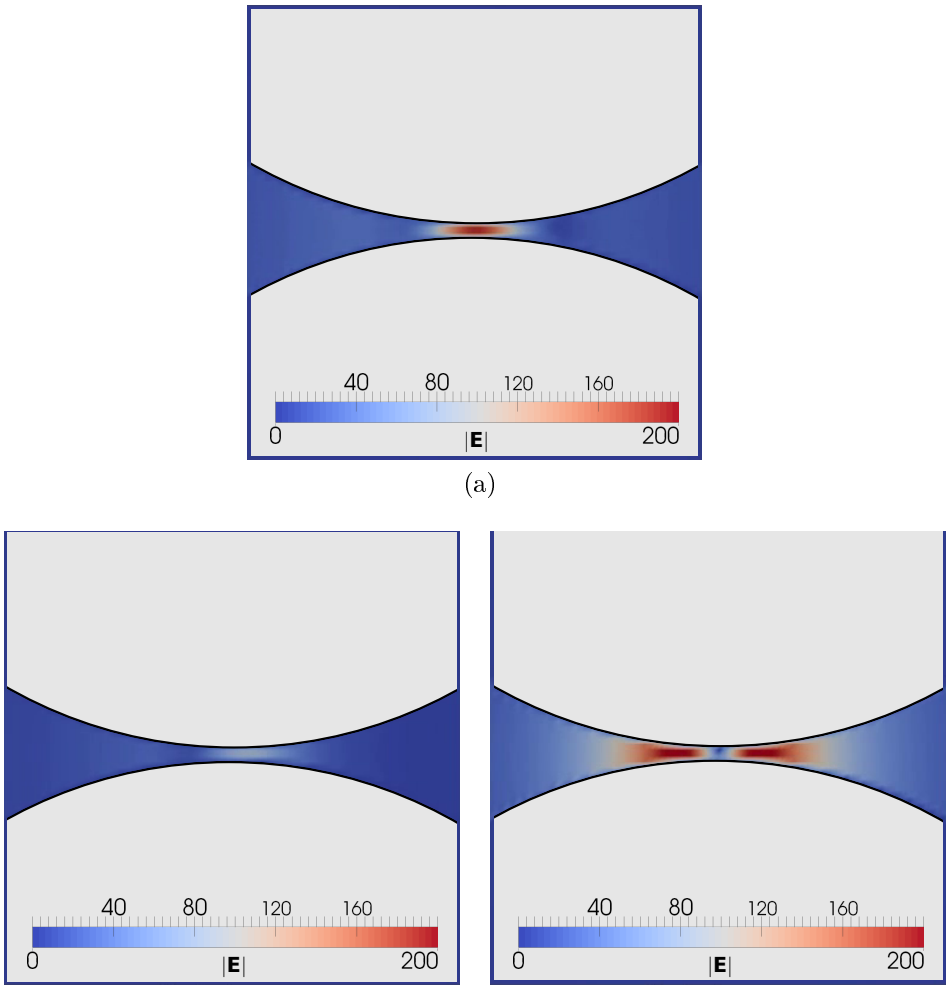

(a)

(b) (c)

Figure 5.3.11: Time-line of a stimulated emission burst of a nanowire system with a four-level coating and a gap-size of $d_{gap} = 0.4$ nm. Snapshots of the absolute electric field were recorded at several time-points (black dotted lines in figure 5.3.10) during the simulation of the lasing system ($N/V = 7 \cdot N_{QM}/V$).

symmetric mode is above the gain threshold due to its lower overall losses $\gamma_{anti} < \gamma_{sym}$. As the symmetric excitation pulse only couples weakly to the anti-symmetric mode, the total field energy in the first part of the simulation ($t \lesssim 0.22$ ps) is dominated by the symmetric mode. However, the energy of the anti-symmetric mode is steadily rising until it exceeds the energy of the symmetric mode at $t \gtrsim 0.22$ ps. As the lasing occurs on a dark, non-radiating mode, the coated nearly touching nanowire system is a spaser [108, 109] - a system which exhibits lasing behaviour on a non-radiating mode.

5.4 Summary and Conclusion

This chapter investigated the dynamics of a non-linear, nano-plasmonic system consisting of two nearly touching infinitely long silver nanowires with a two- or four-level coating. Numerical calculations performed on the purely plasmonic system revealed the presence of two strong resonances with nearly identical frequencies yet distinct spatial profiles. Both modes have high field enhancements in the gap region, yet, due to their spatial symmetry, significantly differ in their ability to couple to radiative modes. The nearly identical frequencies of both modes was explained by a hidden symmetry which was revealed by a transformation optics calculation.

A coating modelled with a two-level system was added to the nanowires. The emission frequency of the two-level system was chosen to match the frequency of the strong resonance of the plasmonic system. Due to the high field enhancements, both systems enter the strong coupling regime and Rabi splitting was observed. It was shown that by changing the gap size d_{gap} between the nanowires, the size of the Rabi splitting can be controlled. Additionally, non-linear saturation effects of the two-level were demonstrated by increasing the incident field energy beyond the small-signal regime: for high enough intensities the Rabi splitting in the absorption cross section vanishes.

Finally, the two-level coating was replaced by a four-level system and pump-probe experiments were conducted. The high field enhancement in the gap enhances the pump-rate of the system dramatically compared to a system consisting of only a single nanowire. After the pumping phase, the system was probed with a spectrally broad pulse. Once again, the Rabi splitting vanishes, however, this time, the inversion of the emission line results in the amplification of photons which is confirmed by an enhanced scattering rate at the emission frequency in the scattering cross section. By further increasing the density of the four-level system, the amplification of the photons reaches the lasing threshold. Lasing is observed on the mode with the lower losses - the non-radiating mode.

Although the system is interesting from a theoretical perspective alone, the ques-

tion must be asked if this system could be the basis of more practical applications. An obvious candidate are nano-lasers. Although the system as presented above results in stimulated emission on a dark, mostly non-radiating mode, modifications to the geometry and/or material properties may increase the radiative coupling. For example, the transformation optics calculations in the quasi-static limit show that the symmetry of the nanowires is the origin of the two orthogonal modes of which the spasing mode shows no radiative coupling. It is conceivable that by purposely introducing asymmetries into the system, the strict orthogonality of the two modes is broken - even in the quasi-static regime. This would allow control over how much the anti-symmetric mode couples to external radiation. The asymmetries could be introduced by varying the radius or material properties of only one nano-wire. This can also be achieved by replacing one nano-wire with a planar metallic surface. Such a system is only identical to the one presented in this chapter in the limit where the planar surface is a perfect electrical conductor. Therefore, any realistic metallic surface will automatically introduce asymmetries. In fact, a very similar system was experimentally realized by Oulton et al. [110] showing lasing behaviour on a mode confined to the gap region. Further research into the effect of asymmetries on the system dynamics is therefore well justified.

The dye coating was assumed to be a homogeneous distribution of collective dipoles (see 3.2). Another avenue of further research would be to understand how a discrete number of infinitesimal dye molecules in the vicinity of the nano-wires would affect the system. In such a system, strong coupling behaviour will occur between each individual molecule and the nanowires. Such a system was recently studied in [111].

Another opportunity for further research is to investigate the implications of the small gap-sizes d_{gap} between the nanowires. Obviously, for gap-sizes in the order of the lattice constant of silver, one would expect quantum effects such as electron tunnelling between the cylinders. Extensions to the FDTD method which phenomenologically account for such non-local effects have been formulated [112] and investigating the above nanowire system with such a solver is a consequent continuation of this research.

Chapter 6

Conclusion

The goal of this thesis was to computationally simulate a non-linear, nano-plasmonic system with the FDTD method. The simulation of such systems using FDTD bears two main challenges, which were identified in this thesis as follows.

The simulation of systems containing certain simple metals is already a standard feature in many modern FDTD solvers. As outlined in chapter 2, it is still challenging to find a computational efficient time-domain update equation for the electric or magnetic polarization $\mathbf{P}[\mathbf{E},\mathbf{H}]$, $\mathbf{M}[\mathbf{H},\mathbf{E}]$ fields for any given complex-valued, frequency-dependent permittivity $\varepsilon(\omega)$ or permeability $\mu(\omega)$. To overcome this limitation, an algorithm was developed which can autonomously find such update equations given an analytic or experimentally derived $\varepsilon(\omega)$,$\mu(\omega)$. It was found that the update equations found by this algorithm had a frequency response which was in excellent agreement to the desired permittivity $\varepsilon(\omega)$ or permeability $\mu(\omega)$ even for only a small number of recursion coefficients.

The second major challenge in extending the FDTD method to nano-plasmonic systems is the accurate description of Yee cells containing an interface between two materials. This problem was extensively studied in chapter 4 and several algorithms were proposed to overcome this limitation. It was shown that the algorithms using the sub-pixel averaging techniques - some of which were developed during the course of this thesis - can improve the accuracy of nano-plasmonic simulations by roughly an order of magnitude for an only modest increase in computation time.

In addition to investigating and proposing solutions to the above challenges, it was shown in chapter 3 that the FDTD method can naturally describe various non-linear materials and accompanying phenomena such as Rabi splitting. With this, the groundwork is laid to computationally investigate non-linear, strongly-coupled, nano-plasmonic systems.

Such a system was investigated in chapter 5: a pair of two nearly touching nanowires. It was shown that the purely plasmonic system shows two resonances with nearly identical frequencies, yet nearly orthogonal spatial field profiles. These

two resonances were illustratively explained by a hidden symmetry which is revealed by a transformation optics calculation. Adding a two-level coating to the nanowires results in the splitting of the dipole resonance. A comparison with the model developed in chapter 3 suggests that the splitting is due to Rabi splitting. The non-linear behaviour of the system is highlighted by increasing the excitation amplitude to such levels that the two-level system becomes saturated which results in the vanishing of the Rabi splitting phenomena.

By replacing the coating with an ensemble of four-level systems, it was shown that the high field enhancement dramatically improves the pump efficiency. Once inverted, the system exhibits a stimulated emission burst for sufficiently high four-level molecule densities. Due to the lower losses, the non-radiating mode is favoured by the four-level system and, consequently, the system is a spaser.

Various suggestions for further research were given in the outlook sections of the various chapters of this thesis. The most important being the extension of the author's FDTD solver to three dimensions and investigating the effect of asymmetries between the nanowires. The latter may pave the way to practical applications such as nano-lasers if other limitations are overcome such as the experimentally infeasibly high gain densities.

The most important result of this thesis, however, is the fact that it was possible to investigate such a computationally demanding system with a full-vectorial time-domain solver. Other full-vectorial numerical simulations of nano-plasmonic systems with gain have been published [113, 114, 1], yet, the author is unaware of any other time-domain numerical simulations of a non-linear, nano-plasmonic system with such high field enhancement factors and curved surface geometries. It is therefore the hope of the author, that by providing some of the methods described in this thesis, the accurate simulation of such systems will eventually become the new norm.

Appendix A

Pseudo-code Listings

Pseudo-code is listed here for various algorithms presented in this thesis. The notation of the pseudo-code language used below is roughly based on the C++ language and is a simplified version of the actual code used to implement a FDTD solver.

A.1 The basic FDTD algorithm

```
void UpdateE (tFieldType& Ex, tFieldType& Ey, tFieldType& Ez,
              const tFieldType& Hx, const tFieldType& Hy, const tFieldType& Hz)
{
    for (int i = imin; i <= imax; ++i)
    {
        for (int j = jmin; j <= jmax; ++j)
        {
            for (int k = kmin; k <= kmax; ++k)
            {
                Ex[i][j][k] += kCourant * ( ( Hz[i][j][k] - Hz[i][j-1][k] ) +
                                            ( Hy[i-1][j][k] - Hy[i][j][k] ) );
                Ey[i][j][k] += kCourant * ( ( Hx[i][j][k] - Hx[i-1][j][k] ) +
                                            ( Hz[i][j][k] - Hz[i][j][k+1] ) );
                Ez[i][j][k] += kCourant * ( ( Hy[i][j][k+1] - Hy[i][j][k] ) +
                                            ( Hx[i][j-1][k] - Hx[i][j][k] ) );
            }
        }
    }
}

void UpdateH (tFieldType& Hx, tFieldType& Hy, tFieldType& Hz,
              const tFieldType& Ex, const tFieldType& Ey, const tFieldType& Ez)
{
    for (int i = imin; i <= imax; ++i)
    {
        for (int j = jmin; j <= jmax; ++j)
        {
            for (int k = kmin; k <= kmax; ++k)
            {
                Hx[i][j][k] += kCourant * ( ( Ey[i+1][j][k] - Ey[i][j][k] ) +
                                            ( Ez[i][j][k] - Ez[i][j+1][k] ) );
                Hy[i][j][k] += kCourant * ( ( Ez[i][j][k] - Ez[i][j][k-1] ) +
                                            ( Ex[i][j][k] - Ex[i+1][j][k] ) );
                Hz[i][j][k] += kCourant * ( ( Ex[i][j+1][k] - Ex[i][j][k] ) +
                                            ( Ey[i][j][k-1] - Ey[i][j][k] ) );
            }
       }
    }
}

void AddMaterialCurrents (tFieldType& Ex, tFieldType& Ey, tFieldType& Ez,
```

```
                            const tMaterialsType& mat)
{
    /* cycle over all materials */
    for (int idx = 0; idx < mat.size(); ++idx)
    {
        for (int i = mat[idx].imin; i <= mat[idx].imax; ++i)
        {
            for (int j = mat[idx].jmin; j <= mat[idx].jmax; ++j)
            {
                for (int k = mat[idx].kmin; k <= mat[idx].kmax; ++k)
                {
                    Ex[i][j][k] -= mat[idx].Px[i][j][k][0] - mat[idx].Px[i][j][k][1];
                    Ey[i][j][k] -= mat[idx].Py[i][j][k][0] - mat[idx].Py[i][j][k][1];
                    Ez[i][j][k] -= mat[idx].Pz[i][j][k][0] - mat[idx].Pz[i][j][k][1];
                }
            }
        }
    }
}

void UpdatePolarizations (tMaterialsType& mat,
                            const tFieldType& Ex, const tFieldType& Ey, const tFieldType& Ez)
{
    /* cycle over all materials */
    for (int idx = 0; idx < mat.size(); ++idx)
    {
        /* do polarization specific update: this could be integrating a
           Lorentzian/Drude recursive equation or evaluating cascaded
           biquads, depending on the polarization functional of mat[idx].
        */
        mat [idx].update (Ex, Ey, Ez);
    }
}


void run()
{
    clear (Hx); clear (Hy); clear (Hz);
    clear (Ex); clear (Ey); clear (Ez);
    clear (mat);

    for (int n = 0; n < duration; ++n)
    {
        /* Electric Field Update */
        UpdateE (Ex, Ey, Ez, Hx, Hy, Hz);
        AddMaterialCurrents (Ex, Ey, Ez, mat);
        UpdatePolarizations (mat, Ex, Ey, Ez);

        /* Magnetic Field Update */
        UpdateH (Hx, Hy, Hz, Ex, Ey, Ez);
    }
}
```

A.2 Autonomous algorithm to find the coefficients a_m, b_m of a linear recursion equation for the polarization response of a material $\chi(\omega)$

```
template <typename function>
void rationalFit (const function& polarizability,
                  const unsigned int A, const unsigned int B,
                  std::vector<double>& a_coeffs, std::vector<double>& b_coeffs)
{
    const unsigned int N = (A + B) >> 1;

    boost::numeric::ublas::matrix<double> M (A + B, A + B);
    boost::numeric::ublas::vector<double> b (A + B);

    for (unsigned int i = 0; i < (A + B); ++i)
```

```
12      {
13          unsigned int row = i >> 1;
14          bool isImaginary = ((i & 1) != 0);
15
16          double freq = polarizability.min() +
17              ((polarizability.max() - polarizability.min()) *
18               static_cast<double> (row) / static_cast<double> (N - 1));
19
20          std::complex<double> chi = polarizability (freq);
21          std::complex<double> gamma =
22              exp (std::complex<double> (0.0,
23                                         2. * M_PI * freq * delta_t));
24
25          std::complex<double> bvalue = a0 * chi * pow (gamma, -1.0);
26          b (i) = isImaginary ? bvalue.imag() : bvalue.real();
27
28          unsigned int j;
29          for (j = 0; j < B; ++j)
30          {
31              unsigned int column = j;
32              std::complex<double> Mij = pow (gamma, static_cast<double> (column));
33
34              M (i,j) = isImaginary ? Mij.imag() : Mij.real();
35          }
36
37          for (; j < (B + A); ++j)
38          {
39              unsigned int column = j - B;
40              std::complex<double> Mij = pow (gamma, static_cast<double> (column)) * chi * -1.0;
41
42              M (i,j) = isImaginary ? Mij.imag() : Mij.real();
43          }
44      }
45
46      boost::numeric::ublas::permutation_matrix<size_t> pm(M.size1());
47      boost::numeric::ublas::lu_factorize(M, pm);
48      boost::numeric::ublas::lu_substitute(M, pm, b);
49
50      {
51          unsigned int j;
52          b_coeffs.push_back (0);
53          for (j = 0; j < B; ++j)
54              b_coeffs.push_back (b (j));
55
56          a_coeffs.push_back (a0);
57          for (; j < (B + A); ++j)
58              a_coeffs.push_back (b (j));
59      }
60  }
61
62  void findZerosAndPoles (const std::vector<double>& a_coeffs_,
63                          const std::vector<double>& b_coeffs_,
64                          std::vector<std::complex<double> >& zeros,
65                          std::vector<std::complex<double> >& poles)
66  {
67      const int base_order = -1;
68      std::vector<double> a_coeffs (a_coeffs_);
69      std::vector<double> b_coeffs (b_coeffs_);
70
71      /* normalize */
72      double a0 = a_coeffs[0] * -1.0;
73      for (auto&& a : a_coeffs)
74          a /= a0;
75      for (auto&& b : b_coeffs)
76          b /= a0;
77
78      std::cout << std::endl;
79
80      zeros.clear();
81      poles.clear();
82
83      std::vector<std::complex<double> > a_zeros_pre = poly_transform (a_coeffs);
84      zeros = poly_findzeros (b_coeffs);
85
86
87      for (int i = 0; i < a_zeros_pre.size(); ++i)
88      {
89          double diff = abs (1./a_zeros_pre [i]) - 1.0;
90
91          if (diff > 0.0)
```

```
92          {
93              if (diff <= 1e-5)
94              {
95                  std::cout << "WARNING: unstable filter due to round-off errors: correcting!" <<
96                      std::endl;
97
98                  a_zeros_pre[i] = (1.0 + (1.0 - abs(a_zeros_pre[i]))) *
99                      exp (std::complex<double> (0.0, atan2 (a_zeros_pre[i].imag(), a_zeros_pre[i↩
                            ].real())));
100
101                 std::cout << "new: " << abs (1./a_zeros_pre [i]) - 1.0 <<
102                     std::endl;
103             }
104         }
105         poles.push_back (a_zeros_pre [i]);
106     }
107 }
108
109 template <typename functional>
110 void findStableCoeffecients (const functional& chi,
111                              const unsigned int A, const unsigned int B,
112                              std::vector<double>& a_coeffs,
113                              std::vector<double>& b_coeffs)
114 {
115     std::vector<std::complex<double> > zeros, poles;
116
117     rationalFit (chi, A, B, a_coeffs, b_coeffs);
118     findZerosAndPoles (a_coeffs, b_coeffs, zeros, poles);
119
120     int originalNumPoles = poles.size();
121
122     // split into stable and unstable poly
123     std::vector<std::complex<double> > unstablePoles;
124     bool changed = true;
125     while (changed)
126     {
127         changed = false;
128         for (std::vector<std::complex<double> >::iterator it = poles.begin();
129              it != poles.end(); ++it)
130         {
131             if (abs (1./ (*it)) > 1.0)
132             {
133                 unstablePoles.push_back (*it);
134                 poles.erase (it);
135                 changed = true;
136                 break;
137             }
138         }
139     }
140
141
142     if (unstablePoles.size() != 0)
143     {
144         bool hadImaginaryCoeffecient = false;
145
146         std::vector<double> stable_a_coeffs =
147             poly_from_zeros (poles, hadImaginaryCoeffecient);
148         assert (hadImaginaryCoeffecient == false);
149         std::vector<double> stable_b_coeffs =
150             poly_from_zeros (zeros, hadImaginaryCoeffecient);
151         assert (hadImaginaryCoeffecient == false);
152
153         std::vector<double> denominator_poly =
154             poly_from_zeros (unstablePoles, hadImaginaryCoeffecient);
155         assert (hadImaginaryCoeffecient == false);
156         RationalPoly poly (denominator_poly, chi.min(), chi.max());
157
158         unsigned int newA = unstablePoles.size();
159         unsigned int newB = 1;
160
161         // something to end the recursion
162         if (unstablePoles.size() == originalNumPoles)
163         {
164             newA = newA - 1;
165             newB = newB + 1;
166         }
167
168         unsigned int N = newA + newB;
169         if ( N < 4 )
170             newB += 4 - N;
```

```
171
172         std::vector<double> new_a_coeffs;
173         std::vector<double> new_b_coeffs;
174         findStableCoeffecients (poly, newA, newB, new_a_coeffs, new_b_coeffs);
175
176         // combine both polys
177         a_coeffs = poly_multiply (new_a_coeffs, stable_a_coeffs);
178         b_coeffs = poly_multiply (new_b_coeffs, stable_b_coeffs);
179     }
180 }
181
182 template <typename function>
183 void recursionCoeffeceientsForMaxError(const function& polarizability,
184                                        std::vector<double>& a_coeffs,
185                                        std::vector<double>& b_coeffs,
186                                        double maxError)
187 {
188     // Try all combinations of A, B
189     for (int N = 3; error > maxError && N <= maxN; ++N)
190     {
191         for (unsigned int A = 2; (A < N && error > maxError); ++A)
192         {
193             unsigned int B = N - A;
194
195             a_coeffs.clear(); b_coeffs.clear();
196             findStableCoeffecients (polarizability, A, B, a_coeffs, b_coeffs);
197             error = rms (polarizability, a_coeffs, b_coeffs);
198
199         }
200     }
201
202 }
203
204 void findAndRemoveRealQuad (std::vector<std::complex<double> >& new_zeros,
205                             std::vector<std::complex<double> >& zeros)
206 {
207     if (zeros.size() > 1)
208     {
209         // add a zero
210         new_zeros.push_back (zeros[0]);
211         /* find a partner with which I can get a real result */
212         for (int i = 1; i < zeros.size(); ++i)
213         {
214             bool has_imaginary_coeffecients;
215             std::vector<std::complex<double> > quad;
216             quad.push_back (zeros [0]);
217             quad.push_back (zeros [i]);
218
219             poly_from_zeros (quad, has_imaginary_coeffecients);
220             if (has_imaginary_coeffecients == false)
221             {
222                 new_zeros.push_back (zeros [i]);
223                 zeros.erase (zeros.begin() + i);
224                 break;
225             }
226         }
227
228         // couldn't find a pair?
229         assert (i < zeros.size());
230
231         zeros.erase (zeros.begin());
232     }
233     else if (zeros.size() == 1)
234     {
235         // only one coeffecient, check if it is real
236         assert (zeros[0].imag() < 1e-6);
237         new_zeros.push_back (zeros [0]);
238     }
239 }
240
241
242 struct BiQuad
243 {
244     std::array<double, 3> a, b;
245 };
246
247 template <typename function>
248 std::vector<BiQuad> findBiquadsForMaxErrorAndChi(const function& polarizability,
249                                                  double maxError)
250 {
```

```
251     std::vector<BiQuad> retval;
252     std::vector<double> a_coeffs;
253     std::vector<double> b_coeffs;
254 
255     // calculate the a and b coeffecients
256     recursionCoeffeceientsForMaxError (polarizability, a_coeffs, b_coeffs, maxError);
257 
258     // translate a, b coeffecients into biquads
259     // we need to pair pole and zero pairs such
260     // that we only get real coeffecients
261     std::vector<std::complex<double> > a_zeros;
262     std::vector<std::complex<double> > b_zeros;
263     a_zeros = poly_findzeros (a_coeffs);
264     b_zeros = poly_findzeros (b_coeffs);
265 
266     while ((a_zeros.size() + b_zeros.size()) > 0)
267     {
268         std::vector<std::complex<double> > new_a_zeros, new_b_zeros;
269 
270         /* remove a single real quad and store it */
271         findAndRemoveRealQuad (new_a_zeros, a_zeros);
272         findAndRemoveRealQuad (new_b_zeros, b_zeros);
273 
274         BiQuad biquad;
275 
276         std::vector<double> new_a_coeffs;
277         std::vector<double> new_b_coeffs;
278 
279         bool ignore;
280 
281         if (new_a_zeros.size() > 0)
282         {
283             new_a_coeffs = poly_from_zeros (new_a_zeros, ignore);
284         }
285         else
286         {
287             new_a_coeffs.push_back (1.0);
288         }
289 
290         if (new_b_coeffs.size() > 0)
291         {
292             new_b_coeffs = poly_from_zeros (new_b_zeros, ignore);
293         }
294         else
295         {
296             new_b_coeffs.push_back (1.0);
297         }
298 
299         assert (new_a_coeffs.size() <= 3);
300         assert (new_b_coeffs.size() <= 3);
301 
302 
303         BiQuad biquad;
304 
305         for (int i = 0; i < biquad.a.size(); ++i)
306             biquad.a[i] = i < new_a_coeffs.size() ? new_a_coeffs[i] : 0.0;
307 
308         for (int i = 0; i < biquad.b.size(); ++i)
309             biquad.b[i] = i < new_b_coeffs.size() ? new_b_coeffs[i] : 0.0;
310 
311         retval.push_back (biquad);
312     }
313 
314     return retval;
315 }
```

A.3 Direct Method

```
1 void AddMaterialCurrents (tFieldType& E, const tMaterialsType& mat)
2 {
3     /* cycle over all materials */
4     for (int idx = 0; idx < mat.size(); ++idx)
```

```
5       {
6           for (int i = mat[idx].imin; i <= mat[idx].imax; ++i)
7           {
8               for (int j = mat[idx].jmin; j <= mat[idx].jmax; ++j)
9               {
10                  for (int k = mat[idx].kmin; k <= mat[idx].kmax; ++k)
11                  {
12                      double inv_avg_eps = 1.0 / getEpsSurfaceAvg (mat, i, j, k);
13                      vec3D n = getInterfaceNormal (i, j, k);
14
15                      /* calculate current */
16                      Vec3D J = mat[idx].P[i][j][k][0] - mat[idx].P[i][j][k][1];
17
18                      double Jperp = J * n;
19                      Vec3D Jpar = J - (n * Jperp);
20
21                      // parallel
22                      E[i][j][k] -= inv_avg_eps * mat[idx].area (i,j,k) * Jpar;
23                      // perpendicular
24                      E[i][j][k] -= ((1.0 / mat[idx].eps) * Jperp) * n;
25                  }
26              }
27          }
28      }
29  }
30
31  void UpdatePolarizations (tMaterialsType& mat, const tFieldType& E)
32  {
33      /* cycle over all materials */
34      for (int idx = 0; idx < mat.size(); ++idx)
35      {
36          for (int i = mat[idx].imin; i <= mat[idx].imax; ++i)
37          {
38              for (int j = mat[idx].jmin; j <= mat[idx].jmax; ++j)
39              {
40                  for (int k = mat[idx].kmin; k <= mat[idx].kmax; ++k)
41                  {
42                      double inv_avg_inveps = 1.0 / geInvEpsLineAvg (mat, i, j, k);
43                      vec3D n = getInterfaceNormal (i, j, k);
44
45                      // partial electric field in only one material
46                      vec3D Ei;
47                      clear (Ei);
48
49                      double Eperp = E[i][j][k] * n;
50                      vec3D Epar = E - (n * Eperp);
51
52                      // parallel part is easy
53                      Ei += Epar;
54
55                      // perpendicular part is harder
56                      double Ecorrection =
57                          (inv_avg_inveps / mat[idx].eps) * Eperp;
58
59                      for (int oth = 0; oth < mat.size(); ++oth)
60                      {
61                          double fac = mat[oth].length (i,j,k) * inv_avg_inveps *
62                              (1.0 / mat[oth].eps) - (oth == idx ? 1.0 : 0.0);
63
64                          Ecorrection += (fac * mat[oth].P[i][j][k][0] * n) / math[idx].eps;
65                      }
66
67                      Ei += Ecorrection * n;
68
69                      mat[idx].update (Ei);
70                  }
71              }
72          }
73      }
74  }
```

A.4 INCA Algorithm

```
Vec3D YeeToCellCentre (const tFieldType& F, int i, int j, int k)
{
    Vec3D retval (0.0);

    retval[0] = 0.5 * (F[i][j][k][0] + F[i][j][k+1][0]);
    retval[1] = 0.5 * (F[i][j][k][1] + F[i][j-1][k][1]);
    retval[2] = 0.5 * (F[i][j][k][2] + F[i+1][j][k][2]);

    return retval;
}

void SubtractCellCentreFromYee (Vec3D& F, const Vec3D& cc, int i, int j, int k)
{
    F[i][j][k][0] -= 0.5 * cc[0];
    F[i][j][k+1][0] -= 0.5 * cc[0];

    F[i][j][k][1] -= 0.5 * cc[1];
    F[i][j-1][j][1] -= 0.5 * cc[1];

    F[i][j][k][2] -= 0.5 * cc[2];
    F[i+1][j][k][2] -= 0.5 * cc[2];
}

void AddMaterialCurrents (tFieldType& E, const tMaterialsType& mat)
{
    /* cycle over all materials */
    for (int idx = 0; idx < mat.size(); ++idx)
    {
        for (int i = mat[idx].imin; i <= mat[idx].imax; ++i)
        {
            for (int j = mat[idx].jmin; j <= mat[idx].jmax; ++j)
            {
                for (int k = mat[idx].kmin; k <= mat[idx].kmax; ++k)
                {
                    /* do DVA */
                    double inv_avg_eps = 1.0 / mat[idx].getEpsSurfaceAvg (i,j,k);

                    /* calculate current */
                    Vec3D J = mat[idx].P[i][j][k][0] - mat[idx].P[i][j][k][1];
                    E[i][j][k] -= inv_avg_eps * mat[idx].area (i,j,k) * J;
                }
            }
        }
    }
}

void UpdatePolarizations (tMaterialsType& mat, const tFieldType& E)
{
    /* cycle over all materials */
    for (int idx = 0; idx < mat.size(); ++idx)
    {
        for (int i = mat[idx].imin; i <= mat[idx].imax; ++i)
        {
            for (int j = mat[idx].jmin; j <= mat[idx].jmax; ++j)
            {
                for (int k = mat[idx].kmin; k <= mat[idx].kmax; ++k)
                {
                    /* update P with polarization functional of material */
                    P[i][j][k] = mat[idx].update (E[i][j][k]);
                }
            }
        }
    }
}

void UpdateMaterialCurrentsIntfCells (tFieldType& E,
                                      const tMaterialsType& mat)
{
    for (int idx = 0; idx < mat.size(); ++idx)
    {
        const tFieldType& P_rho = mat[idx].P_rho;

        for ( i, j, k of mat[idx].interfaceCells)
        {
            vec3D n = getInterfaceNormal (i, j, k);

            Vec3D P_cell_centre = YeeToCellCentre (P, i, j, k);
            Vec3D J_cell_centre = P_cell_centre[0] - P_cell_centre[1];
            double J_cc_perp = J_cell_centre * n;
```

```
80              double J_rho  = P_rho[i][j][k][0] - P_rho[i][j][k][1];
81
82
83              double J_cor = ((mat[idx].length (i,j,k) - mat[idx].area (i,j,k)) * J_cc_perp)
84                  - ((mat[idx].length (i,j,k) * (1.0 - mat[idx].length (i,j,k))) * J_rho);
85
86              SubtractCellCentreFromYee (E, n * J_cor * mat[idx].getInvEpsAvg(i,j,k), i, j, k);
87          }
88      }
89  }
90
91  void UpdatePolarizationsIntfCells (tMaterialsType& mat,
92                                     const tFieldType& E)
93  {
94      for (int idx = 0; idx < mat.size(); ++idx)
95      {
96          tFieldType& P_rho = mat[idx].P_rho;
97          tFieldType& rho = mat[idx].rho;
98
99          for ( i, j, k of mat[idx].interfaceCells)
100         {
101             vec3D n = getInterfaceNormal (i, j, k);
102
103             Vec3D P_cell_centre = YeeToCellCentre (P, i, j, k);
104             Vec3D J_cell_centre = P_cell_centre[0] - P_cell_centre[1];
105             double J_cc_perp = J_cell_centre * n;
106
107             /* update P_rho with polarization functional of material */
108             P_rho = mat[idx].update (rho[i][j][k]);
109
110             double J_rho  = P_rho[i][j][k][0] - P_rho[i][j][k][1];
111
112             rho[i][j][k] += J_cc_perp - (mat[idx].length (i,j,k) * J_rho);
113         }
114     }
115 }
116
117 void UpdateHWitthDeltaK (tFieldType& H, const tMaterialsType& mat,
118                          const tFieldType& E)
119 {
120     for (int idx = 0; idx < mat.size(); ++idx)
121     {
122         for ( i, j, k of mat[idx].interfaceCells)
123         {
124             vec3D n = getInterfaceNormal (i, j, k);
125             double E_perp = YeeToCellCentre (E, i, j, k) * n;
126
127             Vec3D delE = n * E_perp *
128                 ((mat[idx].getInvEpsAvg(i,j,j) * mat[idx].getEpsSurfaceAvg (i,j,k)) - 1.0);
129
130             H[i][j][k][0]   += 0.5 * kCourant * (delE[0] - delE[1]);
131             H[i][j-1][k][0] -= 0.5 * kCourant * (delE[1] + delE[2]);
132             H[i-1][j][k][0] += 0.5 * kCourant * (delE[1] + delE[2]);
133
134             H[i][j][k][1]   += 0.5 * kCourant * (delE[2] + delE[0]);
135             H[i][j][k+1][1] += 0.5 * kCourant * (delE[0] - delE[2]);
136             H[i-1][j][k][1] += 0.5 * kCourant * (delE[2] - delE[0]);
137
138
139             H[i][j][k][2]   -= 0.5 * kCourant * (delE[0] + delE[1]);
140             H[i][j][k+1][2] += 0.5 * kCourant * (delE[1] - delE[0]);
141             H[i][j-1][k][2] += 0.5 * kCourant * (delE[0] - delE[1]);
142         }
143     }
144 }
```

Bibliography

[1] Sebastian Wuestner, Andreas Pusch, Kosmas L. Tsakmakidis, Joachim M. Hamm, and Ortwin Hess. Gain and plasmon dynamics in active negative-index metamaterials. *Philosophical Transactions of the Royal Society of London A: Mathematical, Physical and Engineering Sciences*, 369(1950):3525–3550, 2011.

[2] Mark L. Brongersma and Pieter G. Kik. *Surface plasmon nanophotonics*. Springer, 2007.

[3] Mark L. Brongersma. Introductory lecture: nanoplasmonics. *Faraday Discussions*, 178:9–36, 2015.

[4] Stefan Alexander Maier. *Plasmonics : fundamentals and applications*. Springer, New York, NY, 2007.

[5] Irene Ament, Janak Prasad, Andreas Henkel, Sebastian Schmachtel, and Carsten Sönnichsen. Single unlabeled protein detection on individual plasmonic nanoparticles. *Nano Letters*, 12(2):1092–1095, 2012. PMID: 22268768.

[6] Srdjan S. Aćimović, Mark P. Kreuzer, María U. González, and Romain Quidant. Plasmon near-field coupling in metal dimers as a step toward single-molecule sensing. *ACS Nano*, 3(5):1231–1237, 2009. PMID: 19385661.

[7] Alexandre G. Brolo. Plasmonics for future biosensors. *Nature Photonics*, 6(11):709–713, November 2012.

[8] A. V. Akimov, A. Mukherjee, C. L. Yu, D. E. Chang, A. S. Zibrov, P. R. Hemmer, H. Park, and M. D. Lukin. Generation of single optical plasmons in metallic nanowires coupled to quantum dots. *Nature*, 450(7168):402–406, November 2007.

[9] COMSOL Multiphysics, `https://www.comsol.com/comsol-multiphysics`.

[10] Christophe Geuzaine and Jean-François Remacle. Gmsh: A 3-D finite element mesh generator with built-in pre-and post-processing facilities. *International Journal for Numerical Methods in Engineering*, 79(11):1309–1331, 2009.

[11] Guy A. E. Vandenbosch. *Plasmonics - Principles and Applications*, chapter Computational Electromagnetics in Plasmonics, pages 23–48. InTech, 2012.

[12] Junuthula Narasimha Reddy. *An introduction to the finite element method*, volume 2. McGraw-Hill New York, 1993.

[13] AT Adams. Method of moments applications. volume 1 An introduction to the method of moments. Technical report, DTIC Document, 1974.

[14] Kane S Yee. Numerical solution of initial boundary value problems involving Maxwell's equations in isotropic media. *Antennas and Propagation, IEEE Transactions on*, 14(3):302–307, 1966.

[15] Allen Taflove and Susan C Hagness. *Computational electrodynamics*. Artech house, 2005.

[16] Johannes Hoffmann, Christian Hafner, Patrick Leidenberger, Jan Hesselbarth, and Sven Burger. Comparison of electromagnetic field solvers for the 3D analysis of plasmonic nanoantennas. *Proceedings of SPIE*, 7390:73900J–73900J–11, 2009.

[17] Alexandre Aubry, Dang Yuan Lei, Stefan A. Maier, and J. B. Pendry. Interaction between plasmonic nanoparticles revisited with transformation optics. *Physical Review Letters*, 105:233901, November 2010.

[18] Tatiana V. Teperik, Peter Nordlander, Javier Aizpurua, and Andrei G. Borisov. Quantum effects and nonlocality in strongly coupled plasmonic nanowire dimers. *Optics Express*, 21(22):27306–27325, November 2013.

[19] Giuseppe Toscano, Søren Raza, Antti-Pekka Jauho, N. Asger Mortensen, and Martijn Wubs. Modified field enhancement and extinction by plasmonic nanowire dimers due to nonlocal response. *Optics Express*, 20(4):4176–4188, February 2012.

[20] JeffreyM. McMahon, Anne-Isabelle Henry, KristinL. Wustholz, MichaelJ. Natan, R.Griffith Freeman, RichardP. Van Duyne, and GeorgeC. Schatz. Gold nanoparticle dimer plasmonics: finite element method calculations of the electromagnetic enhancement to surface-enhanced raman spectroscopy. *Analytical and Bioanalytical Chemistry*, 394(7):1819–1825, 2009.

[21] A. I. Fernández-Domínguez, A. Wiener, F. J. García-Vidal, S. A. Maier, and J. B. Pendry. Transformation-optics description of nonlocal effects in plasmonic nanostructures. *Physical Review Letters*, 108:106802, March 2012.

[22] Alexandre Aubry, Dang Yuan Lei, Antonio I. Fernández-Domínguez, Yannick Sonnefraud, Stefan A. Maier, and J. B. Pendry. Plasmonic light-harvesting devices over the whole visible spectrum. *Nano Letters*, 10(7):2574–2579, 2010. PMID: 20518545.

[23] P Törmä and W L Barnes. Strong coupling between surface plasmon polaritons and emitters: a review. *Reports on Progress in Physics*, 78(1):013901, 2015.

[24] T. Ciamulski, Mats Hjelm, and M. Sypniewski. Parallel FDTD calculation efficiency on computers with shared memory architecture. In *Computational Electromagnetics in Time-Domain, 2007. CEM-TD 2007. Workshop on*, pages 1–4, October 2007.

[25] C. Ong, M. Weldon, D. Cyca, and M. Okoniewski. Acceleration of large-scale FDTD simulations on high performance GPU clusters. In *Antennas and Propagation Society International Symposium, 2009. APSURSI '09. IEEE*, pages 1–4, June 2009.

[26] Shyh-Kang Jeng. An analytical expression for 3-D dyadic FDTD-compatible green's function in infinite free space via z-transform and partial difference operators. *Antennas and Propagation, IEEE Transactions on*, 59(4):1347–1355, April 2011.

[27] R. Kastner. A multidimensional z-transform evaluation of the discrete finite difference time domain green's function. *Antennas and Propagation, IEEE Transactions on*, 54(4):1215–1222, April 2006.

[28] *Heaviside-Lorentz system, McGraw-Hill Dictionary of Scientific & Technical Terms*. McGraw-Hill Professional, 6 edition, 2003.

[29] David Jeffrey Griffiths and Reed College. *Introduction to electrodynamics*, volume 3. prentice Hall Upper Saddle River, NJ, 1999.

[30] Zhang Bo, Xue Zheng-hui, Ren Wu, Li Wei-ming, and Sheng Xin-qing. Accelerating FDTD algorithm using GPU computing. In *Microwave Technology Computational Electromagnetics (ICMTCE), 2011 IEEE International Conference on*, pages 410–413, May 2011.

[31] S.E. Krakiwsky, L.E. Turner, and M.M. Okoniewski. Acceleration of finite-difference time-domain (FDTD) using graphics processor units (GPU). In *Microwave Symposium Digest, 2004 IEEE MTT-S International*, volume 2, pages 1033–1036Vol.2, June 2004.

[32] S. Adams, J. Payne, and R. Boppana. Finite difference time domain (FDTD) simulations using graphics processors. In *DoD High Performance Computing Modernization Program Users Group Conference, 2007*, pages 334–338, June 2007.

[33] D. De Donno, A. Esposito, L. Tarricone, and L. Catarinucci. Introduction to GPU computing and CUDA programming: A case study on FDTD [em programmer's notebook]. *Antennas and Propagation Magazine, IEEE*, 52(3):116–122, June 2010.

[34] Alan V Oppenheim, Ronald W Schafer, John R Buck, et al. *Discrete-time signal processing*, volume 2. Prentice-hall Englewood Cliffs, 1989.

[35] Alan V Oppenheim, Ronald W Schafer, John R Buck, et al. *Discrete-time signal processing*, volume 2, chapter 3.4, pages 119–126. Prentice-hall Englewood Cliffs, 2 edition, 1989.

[36] R. Courant, K. Friedrichs, and H. Lewy. Über die partiellen differenzengleichungen der mathematischen physik. *Mathematische Annalen*, 100(1):32–74, 1928.

[37] Dong-Hoa Lam. Finite difference methods for electromagnetic scattering problems. *Interaction Notes, Mississippi State University*, (44), August 1969.

[38] R. Holtzman and R. Kastner. The time-domain discrete green's function method (GFm) characterizing the FDTD grid boundary. *Antennas and Propagation, IEEE Transactions on*, 49(7):1079–1093, July 2001.

[39] M Wiktor and TP Stefanski. Examination of discrete green's function approach to absorbing boundary condition in FDTD method. *Session 3AK*, page 1035, 2013.

[40] Gerrit Mur. Absorbing boundary conditions for the finite-difference approximation of the time-domain electromagnetic-field equations. *Electromagnetic Compatibility, IEEE Transactions on*, EMC-23(4):377–382, November 1981.

[41] Jean-Pierre Berenger. A perfectly matched layer for the absorption of electromagnetic waves. *Journal of Computational Physics*, 114(2):185–200, 1994.

[42] D.S. Katz, E.T. Thiele, and Allen Taflove. Validation and extension to three dimensions of the berenger pml absorbing boundary condition for fd-td meshes. *Microwave and Guided Wave Letters, IEEE*, 4(8):268–270, August 1994.

[43] Tatsuya Kashiwa and Ichiro Fukai. A treatment by the fd-td method of the dispersive characteristics associated with electronic polarization. *Microwave and Optical Technology Letters*, 3(6):203–205, 1990.

[44] R. Luebbers, F.P. Hunsberger, Karl S. Kunz, R.B. Standler, and M. Schneider. A frequency-dependent finite-difference time-domain formulation for dispersive materials. *Electromagnetic Compatibility, IEEE Transactions on*, 32(3):222–227, August 1990.

[45] D.F. Kelley and R.J. Luebbers. Piecewise linear recursive convolution for dispersive media using FDTD. *Antennas and Propagation, IEEE Transactions on*, 44(6):792–797, June 1996.

[46] Dennis M. Sullivan. Z-transform theory and the FDTD method. *Antennas and Propagation, IEEE Transactions on*, 44(1):28–34, January 1996.

[47] Lumerical Solutions, Inc., `https://www.lumerical.com/tcad-products/fdtd/`.

[48] Lumerical Solutions. Material modeling. Powerpoint Presentation, 2011. Retrieved 6th of September 2015.

[49] A. Ditkowski, K. Dridi, and J.S. Hesthaven. Convergent cartesian grid methods for Maxwell's equations in complex geometries. *Journal of Computational Physics*, 170(1):39–80, 2001.

[50] Rose M. Joseph, Susan C. Hagness, and Allen Taflove. Direct time integration of Maxwell's equations in linear dispersive media with absorption for scattering and propagation of femtosecond electromagnetic pulses. *Optics Letters*, 16(18):1412–1414, September 1991.

[51] P. Drude. Zur elektronentheorie der metalle. *Annalen der Physik*, 306(3):566–613, 1900.

[52] P. Drude. Zur elektronentheorie der metalle; ii. teil. galvanomagnetische und thermomagnetische effecte. *Annalen der Physik*, 308(11):369–402, 1900.

[53] Edward N. Lorenz. Deterministic nonperiodic flow. *Journal of the Atmospheric Sciences*, 20(2):130–141, March 1963.

[54] H Haken. Analogy between higher instabilities in fluids and lasers. *Physics Letters A*, 53(1):77–78, 1975.

[55] P. B. Johnson and R. W. Christy. Optical constants of the noble metals. *Physical Review B*, 6:4370–4379, December 1972.

[56] Alan V Oppenheim, Ronald W Schafer, John R Buck, et al. *Discrete-time signal processing*, volume 2, chapter 8, pages 541–628. Prentice-hall Englewood Cliffs, 2 edition, 1989.

[57] MathRef Stack Exchange Post, Retrieved 26th February 2015, `http://math.stackexchange.com/questions/1645786`.

[58] E Ya Remez. Sur la détermination des polynômes d'approximation de degré donnée. *Communications of the Kharkov Mathematical Society*, 10:41–63, 1934.

[59] W. Fraser. A survey of methods of computing minimax and near-minimax polynomial approximations for functions of a single independent variable. *Journal of the ACM*, 12(3):295–314, July 1965.

[60] Bede Liu and T. Kaneko. Error analysis of digital filters realized with floating-point arithmetic. *Proceedings of the IEEE*, 57(10):1735–1747, October 1969.

[61] Gregory R. Werner and John R. Cary. A stable FDTD algorithm for non-diagonal, anisotropic dielectrics. *Journal of Computational Physics*, 226(1):1085–1101, 2007.

[62] Lukas Novotny and Bert Hecht. *Principles of nano-optics*. Cambridge university press, 2012.

[63] John David Jackson. *Classical electrodynamics*, volume 3. Wiley New York etc., 1962.

[64] M. Fujii, M. Tahara, I. Sakagami, W. Freude, and P. Russer. High-order fdtd and auxiliary differential equation formulation of optical pulse propagation in 2-d kerr and raman nonlinear dispersive media. *IEEE Journal of Quantum Electronics*, 40(2):175–182, Feb 2004.

[65] F. Bloch. Nuclear induction. *Physical Review*, 70:460–474, October 1946.

[66] Richard P. Feynman, Frank L. Vernon, and Robert W. Hellwarth. Geometrical representation of the schrödinger equation for solving maser problems. *Journal of Applied Physics*, 28(1):49–52, 1957.

[67] E.T. Jaynes and F.W. Cummings. Comparison of quantum and semiclassical radiation theories with application to the beam maser. *Proceedings of the IEEE*, 51(1):89–109, January 1963.

[68] C.L. Tang. 1. introductory concepts and results†. In C.L. Tang, editor, *Quantum Electronics*, volume 15, Part A of *Methods in Experimental Physics*, pages 1–30. Academic Press, 1979.

[69] E. M. Purcell. Spontaneous emission probabilities at radio frequencies. volume 69, pages 681+, 1946.

[70] Yong Xu, Reginald K. Lee, and Amnon Yariv. Quantum analysis and the classical analysis of spontaneous emission in a microcavity. *Physical Review A*, 61:033807, February 2000.

[71] Dr. Joachim Hamm. Private communication. 2015.

[72] S. L. McCall and E. L. Hahn. Self-induced transparency by pulsed coherent light. *Physical Review Letters*, 18:908–911, May 1967.

[73] F. Arecchi and R. Bonifacio. Theory of optical maser amplifiers. *Quantum Electronics, IEEE Journal of*, 1(4):169–178, July 1965.

[74] TD Visser, H Blok, Bart Demeulenaere, and D Lenstra. Confinement factors and gain in optical amplifiers. *Quantum Electronics, IEEE Journal of*, 33(10):1763–1766, 1997.

[75] Larry A Coldren, Scott W Corzine, and Milan L Mashanovitch. *Diode lasers and photonic integrated circuits*, volume 218, chapter A5, pages 565–577. John Wiley & Sons, 2012.

[76] Michael J Adams. *An introduction to optical waveguides.* UMI Books on Demand, 1981.

[77] Stefan A. Maier. Plasmonic field enhancement and sers in the effective mode volume picture. *Optics Express*, 14(5):1957–1964, March 2006.

[78] Richard L Liboff. *Introductory quantum mechanics.* Holden-Day San Francisco, 1980.

[79] CH Teng, A Ditkowski, and JS Hesthaven. Modeling dielectric interfaces in the FDTD-method: A comparative study. *Antennas and Propagation, IEEE Transactions on*, 2000.

[80] A. Akyurtlu, D.H. Werner, V. Veremey, D.J. Steich, and K. Aydin. Staircasing errors in FDTD at an air-dielectric interface. *Microwave and Guided Wave Letters, IEEE*, 9(11):444–446, November 1999.

[81] A.C. Cangellaris and D.B. Wright. Analysis of the numerical error caused by the stair-stepped approximation of a conducting boundary in FDTD simulations of electromagnetic phenomena. *Antennas and Propagation, IEEE Transactions on*, 39(10):1518–1525, October 1991.

[82] Richard Holland. Pitfalls of staircase meshing. *IEEE Transactions on Electromagnetic Compatibility*, 35(4):434–439, 1993.

[83] Kyu-Pyung Hwang and A.C. Cangellaris. Effective permittivities for second-order accurate FDTD equations at dielectric interfaces. *Microwave and Wireless Components Letters, IEEE*, 11(4):158–160, April 2001.

[84] A Farjadpour, David Roundy, Alejandro Rodriguez, M Ibanescu, Peter Bermel, JD Joannopoulos, Steven G Johnson, and GW Burr. Improving accuracy by sub-pixel smoothing in FDTD. In *SPIE Optics+ Photonics*, pages 63220G–63220G. International Society for Optics and Photonics, 2006.

[85] Wenhua Yu and R. Mittra. A conformal finite difference time domain technique for modeling curved dielectric surfaces. *Microwave and Wireless Components Letters, IEEE*, 11(1):25–27, January 2001.

[86] MEEP FDTD Engine, Retrieved 9th September 2015, `http://ab-initio.mit.edu/meep`.

[87] Microwave CST, `https://www.cst.com/Products/CSTMWS`.

[88] Steven G. Johnson, M. Ibanescu, M. A. Skorobogatiy, O. Weisberg, J. D. Joannopoulos, and Y. Fink. Perturbation theory for Maxwell's equations with shifting material boundaries. *Physical Review E*, 65:066611, June 2002.

[89] Steven G Johnson, ML Povinelli, M Soljačić, Aristeidis Karalis, S Jacobs, and JD Joannopoulos. Roughness losses and volume-current methods in photonic-crystal waveguides. *Applied Physics B*, 81(2-3):283–293, 2005.

[90] M Clemens T Weiland. Discrete electromagnetism with the finite integration technique. *Progress In Electromagnetics Research*, 32:65–87, 2001.

[91] Online. Meep Reference: Retrieved 9th September 2015, `http://ab-initio.mit.edu/wiki/index.php/Meep_Reference`.

[92] Joachim M. Hamm, Fabian Renn, and Ortwin Hess. Dispersive media subcell averaging in the FDTD method using corrective surface currents. *Antennas and Propagation, IEEE Transactions on*, 62(2):832–838, 2014.

[93] Thorsten Liebig. openems - open electromagnetic field solver. `http://openEMS.de`.

[94] Petr Klapetek. gsvit - open source FDTD solver. `http://gsvit.net/`.

[95] John A Svigelj. Efficient solution of Maxwell's equations using the nonuniform orthogonal finite difference time domain method. Technical report, DTIC Document, 1995.

[96] Ozlem Ozgun and Mustafa Kuzuoglu. Recent developments in transformation optics-aided cem. In *Forum for Electromagnetic Research Methods and Application Technologies, FERMAT*, volume 1, 2014.

[97] AJ Ward and JB Pendry. Refraction and geometry in Maxwell's equations. *Journal of Modern Optics*, 43(4):773–793, 1996.

[98] JB Pendry, A Aubry, DR Smith, and SA Maier. Transformation optics and subwavelength control of light. *Science*, 337(6094):549–552, 2012.

[99] Shumin Xiao, Vladimir P. Drachev, Alexander V. Kildishev, Xingjie Ni, Uday K. Chettiar, Hsiao-Kuan Yuan, and Vladimir M. Shalaev. Loss-free and active optical negative-index metamaterials. *Nature*, 466(7307):735–738, August 2010.

[100] Sebastian Wuestner, Andreas Pusch, Kosmas L. Tsakmakidis, Joachim M. Hamm, and Ortwin Hess. Overcoming losses with gain in a negative refractive index metamaterial. *Physical Review Letters*, 105:127401, September 2010.

[101] Roberto Marani, Antonella D'Orazio, Vincenzo Petruzzelli, Sergio G Rodrigo, Luis Martín-Moreno, Francisco J García-Vidal, and Jorge Bravo-Abad. Gain-assisted extraordinary optical transmission through periodic arrays of sub-wavelength apertures. *New Journal of Physics*, 14(1):013020, 2012.

[102] Yonatan Sivan, Shumin Xiao, Uday K. Chettiar, Alexander V. Kildishev, and Vladimir M. Shalaev. Frequency-domain simulations of a negative-index material with embedded gain. *Optics Express*, 17(26):24060–24074, December 2009.

[103] H. Haug and S. Schmitt-Rink. Electron theory of the optical properties of laser-excited semiconductors. *Progress in Quantum Electronics*, 9(1):3–100, 1984.

[104] Hendrik Christoffel Hulst and HC Van De Hulst. *Light scattering by small particles*. Courier Corporation, 1957.

[105] D. Schurig, J. B. Pendry, and D. R. Smith. Calculation of material properties and ray tracing in transformation media. *Optics Express*, 14(21):9794–9804, October 2006.

[106] J. B. Pendry, D. Schurig, and D. R. Smith. Controlling electromagnetic fields. *Science*, 312(5781):1780–1782, 2006.

[107] B. R. Mollow. Power spectrum of light scattered by two-level systems. *Physical Review*, 188:1969–1975, December 1969.

[108] Mark I Stockman. Spasers explained. *Nature Photonics*, 2(6):327–329, 2008.

[109] David J. Bergman and Mark I. Stockman. Surface plasmon amplification by stimulated emission of radiation: Quantum generation of coherent surface plasmons in nanosystems. *Physical Review Letters*, 90:027402, January 2003.

[110] Rupert F. Oulton, Volker J. Sorger, Thomas Zentgraf, Ren-Min Ma, Christopher Gladden, Lun Dai, Guy Bartal, and Xiang Zhang. Plasmon lasers at deep subwavelength scale. *Nature*, 461(7264):629–632, October 2009.

[111] A Delga, J Feist, J Bravo-Abad, and FJ Garcia-Vidal. Quantum emitters near a metal nanoparticle: strong coupling and quenching. *Physical review letters*, 112(25):253601, 2014.

[112] Jeffrey M. McMahon, Stephen K. Gray, and George C. Schatz. Nonlocal optical response of metal nanostructures with arbitrary shape. *Physical Review Letters*, 103:097403, August 2009.

[113] S Wuestner, EI Kirby, A Pusch, KL Tsakmakidis, JM Hamm, and O Hess. Gain in negative-index metamaterials and slow-light waveguides. In *SPIE NanoScience+ Engineering*, pages 775414–775414. International Society for Optics and Photonics, 2010.

[114] Ortwin Hess, Kosmas L Tsakmakidis, Jochaim M Hamm, and Sebastian Wuestner. Slow light amplification and nano-lasing in active plasmonic metamaterials. In *Laser Science*, page LWA1. Optical Society of America, 2011.